



NAVAL POSTGRADUATE SCHOOL

MONTEREY, CALIFORNIA

THESIS

**SIMULATION OF HYDRODYNAMIC RAM
PHENOMENON USING MSC DYTRAN**

by

Kangjie Roy Yang

September 2014

Thesis Advisor:

Young Kwon

Co-Advisor:

Christopher A. Adams

Approved for public release; distribution is unlimited

THIS PAGE INTENTIONALLY LEFT BLANK

REPORT DOCUMENTATION PAGE			<i>Form Approved OMB No. 0704-0188</i>	
Public reporting burden for this collection of information is estimated to average 1 hour per response, including the time for reviewing instruction, searching existing data sources, gathering and maintaining the data needed, and completing and reviewing the collection of information. Send comments regarding this burden estimate or any other aspect of this collection of information, including suggestions for reducing this burden, to Washington headquarters Services, Directorate for Information Operations and Reports, 1215 Jefferson Davis Highway, Suite 1204, Arlington, VA 22202-4302, and to the Office of Management and Budget, Paperwork Reduction Project (0704-0188) Washington, DC 20503.				
1. AGENCY USE ONLY (Leave blank)		2. REPORT DATE September 2014	3. REPORT TYPE AND DATES COVERED Master's Thesis	
4. TITLE AND SUBTITLE SIMULATION OF HYDRODYNAMIC RAM PHENOMENON USING MSC DYTRAN			5. FUNDING NUMBERS	
6. AUTHOR(S) Kangjie Roy Yang				
7. PERFORMING ORGANIZATION NAME(S) AND ADDRESS(ES) Naval Postgraduate School Monterey, CA 93943-5000			8. PERFORMING ORGANIZATION REPORT NUMBER	
9. SPONSORING /MONITORING AGENCY NAME(S) AND ADDRESS(ES) N/A			10. SPONSORING/MONITORING AGENCY REPORT NUMBER	
11. SUPPLEMENTARY NOTES The views expressed in this thesis are those of the author and do not reflect the official policy or position of the Department of Defense or the U.S. Government. IRB Protocol number ____N/A____.				
12a. DISTRIBUTION / AVAILABILITY STATEMENT Approved for public release; distribution is unlimited			12b. DISTRIBUTION CODE A	
13. ABSTRACT (maximum 200 words) Hydrodynamic ram (HRAM) refers to the damage process due to high pressures generated when a high-velocity projectile penetrates a compartment or vessel containing a fluid. A Finite Element model was developed using MSC Dytran to investigate the structural response during the initial phase of HRAM and conduct parametric studies on factors that could affect the tank wall response. The Lagrangian structural shell elements were coupled to the fluid Euler elements using the ALE coupling technique, whereas the projectile was coupled to the fluid using the general coupling technique. This study focused mainly on the structural back wall response where critical components or main structural members on the aircraft could be located. Results from this study show that initial shock wave pressure upon projectile impact is unlikely to have detrimental effects on the exit wall of tank due to its rapid extinction in the fluid. The presence of free surface with lower filling levels reduced both the initial shock pressure and subsequent drag phase pressure. Projectile mass was found to have a strong effect on the exit wall response during the shock phase, but once projectile penetrated the entry wall, results for the drag phase for different projectile mass investigated were inconclusive. Other factors examined included the tank's material properties and fluid density. Of all the factors being studied, projectile's velocity was found to have the strongest influence on exit wall response and fluid pressures. Therefore, the damage to exit wall of the tank could be greatly reduced if the entry wall is able to slow the projectile significantly.				
14. SUBJECT TERMS Hydrodynamic Ram, HRAM, Survivability, MSC, Dytran, Finite Element			15. NUMBER OF PAGES 205	
			16. PRICE CODE	
17. SECURITY CLASSIFICATION OF REPORT Unclassified	18. SECURITY CLASSIFICATION OF THIS PAGE Unclassified	19. SECURITY CLASSIFICATION OF ABSTRACT Unclassified	20. LIMITATION OF ABSTRACT UU	

THIS PAGE INTENTIONALLY LEFT BLANK

Approved for public release; distribution is unlimited

**SIMULATION OF HYDRODYNAMIC RAM PHENOMENON USING MSC
DYTRAN**

Kangjie Roy Yang
Civilian, Singapore Technologies Aerospace Limited
B.Eng., Nanyang Technological University (NTU), 2008

Submitted in partial fulfillment of the
requirements for the degree of

MASTER OF SCIENCE IN MECHANICAL ENGINEERING

from the

**NAVAL POSTGRADUATE SCHOOL
September 2014**

Author: Kangjie Roy Yang

Approved by: Young Kwon
Thesis Advisor

Christopher A. Adams
Co-Advisor

Garth V. Hobson, Ph.D.
Chair, Department of Mechanical and Aerospace
Engineering

THIS PAGE INTENTIONALLY LEFT BLANK

ABSTRACT

Hydrodynamic ram (HRAM) refers to the damage process due to high pressures generated when a high-velocity projectile penetrates a compartment or vessel containing a fluid. A Finite Element model was developed using MSC Dytran to investigate the structural response during the initial phase of HRAM and conduct parametric studies on factors that could affect the tank wall response. The Lagrangian structural shell elements were coupled to the fluid Euler elements using the ALE coupling technique, whereas the projectile was coupled to the fluid using the general coupling technique. This study focused mainly on the structural back wall response where critical components or main structural members on the aircraft could be located.

Results from this study show that initial shock wave pressure upon projectile impact is unlikely to have detrimental effects on the exit wall of tank due to its rapid extinction in the fluid. The presence of free surface with lower filling levels reduced both the initial shock pressure and subsequent drag phase pressure. Projectile mass was found to have a strong effect on the exit wall response during the shock phase, but once projectile penetrated the entry wall, results for the drag phase for different projectile mass investigated were inconclusive. Other factors examined included the tank's material properties and fluid density. Of all the factors being studied, projectile's velocity was found to have the strongest influence on exit wall response and fluid pressures. Therefore, the damage to exit wall of the tank could be greatly reduced if the entry wall is able to slow the projectile significantly.

THIS PAGE INTENTIONALLY LEFT BLANK

TABLE OF CONTENTS

I.	INTRODUCTION.....	1
A.	BACKGROUND	1
B.	OBJECTIVES.....	3
II.	UNDERSTANDING HRAM	5
A.	THE HRAM PHENOMENON	5
1.	The Shock Phase	6
2.	The Drag Phase.....	8
3.	The Cavitation Phase	11
B.	HISTORY AND OVERVIEW OF HRAM SIMULATION.....	14
1.	Evolution of Numerical Techniques for HRAM Simulation	14
2.	Overview of Recent HRAM Numerical Simulations	16
C.	FLUID STRUCTURE INTERACTION – DYTRAN.....	20
1.	Numerical Solvers	20
a.	<i>Lagrangian Solver</i>	21
b.	<i>Eulerian Solver</i>	22
2.	Coupling Techniques	23
a.	<i>General Coupling</i>	23
b.	<i>ALE Coupling</i>	24
III.	METHODOLOGY AND MODEL DEVELOPMENT	27
A.	MODELING PROCEDURES	27
B.	DESCRIPTION OF MODEL	28
1.	Projectile.....	28
2.	Tank	29
3.	Fluid	30
4.	Boundary Conditions	31
5.	Location of Tracer Elements.....	33
6.	Material Properties	34
IV.	RESULTS AND DISCUSSION	35
A.	TANK WALL RESPONSE TO HRAM LOADING	35
1.	Baseline Model 1.....	35
a.	<i>Entry Wall Response</i>	36
b.	<i>Left Wall Response</i>	38
c.	<i>Exit Wall Response</i>	41
2.	Baseline Model 2.....	46
a.	<i>Entry Wall Response</i>	47
b.	<i>Left Wall Response</i>	48
c.	<i>Exit Wall Response</i>	50
B.	PARAMETRIC STUDIES CONDUCTED FOR MODEL 1 AND MODEL 2	55
1.	Variation in Fluid Levels.....	56

2.	Variation in Projectile Mass	57
3.	Variation in Projectile Initial Velocity	60
4.	Variation in Tank Material Modulus.....	62
5.	Variation in Tank Material Density	64
6.	Variation in Fluid Density.....	66
V.	CONCLUSION AND FUTURE WORK	69
	APPENDIX A. GRAPHS FOR FLUID LEVELS VARIATION	71
	APPENDIX B. GRAPHS FOR PROJECTILE MASS VARIATION.....	87
	APPENDIX C. GRAPHS FOR PROJECTILE VELOCITY VARIATION	105
	APPENDIX D. GRAPHS FOR TANK MATERIAL MODULUS VARIATION	123
	APPENDIX E. GRAPHS FOR TANK MATERIAL DENSITY VARIATION	143
	APPENDIX F. GRAPHS FOR FLUID DENSITY VARIATION.....	161
	LIST OF REFERENCES.....	179
	INITIAL DISTRIBUTION LIST	181

LIST OF FIGURES

Figure 1.	Four phases of HRAM phenomenon, from [2].	5
Figure 2.	Extent of tank damage due to HRAM effect, from [5].	6
Figure 3.	Spark shadowgraph of pressure wave during the shock phase captured in McMillen experiment, from [6].	7
Figure 4.	Top: Pressure of drag phase recorded by transducer P3. Bottom: Video image as projectile nears transducer P3, from [8].	9
Figure 5.	Drag pressure comparison for different material measured by transducer P3, from [8].	10
Figure 6.	Pressure time history of spherical tungsten projectile impacting tank at 350 m/s, from [8].	12
Figure 7.	Experiment setup of spherical projectile impacting aluminum tank, from [13].	17
Figure 8.	ALE and SPH simulation of the different phases of HRAM, from [13].	18
Figure 9.	Left: Projectile velocity decay time history. Right: Pressure time history plot near impact point for 100% filled tube impacted at 900 m/s, from [13].	18
Figure 10.	Top Left: Lagrangian Tank shell element. Top Right: Eight node solid Eulerian fluid element. Bottom: Tank and projectile dimensions with pressure gage locations, from [14].	19
Figure 11.	Lagrangian solver mesh, from [17].	21
Figure 12.	Eulerian solver mesh, from [17].	22
Figure 13.	General coupling, from [4].	24
Figure 14.	ALE coupling, from [4].	25
Figure 15.	HRAM simulation modeling procedures.	27
Figure 16.	Spherical projectile Lagrangian solid element mesh.	29
Figure 17.	Left: Lagrangian tank model consisting 9,600 shell elements. Right: Lagrangian tank cutaway model.	30
Figure 18.	Left: Eulerian fluid model consisting 64,000 solid hexahedron elements. Right: Eulerian fluid cutaway model.	30
Figure 19.	Schematic of Model 1 and Model 2.	31
Figure 20.	Location of tracer elements	33
Figure 21.	Entry Wall X-Displacement (Model 1).	36
Figure 22.	Entry Wall X-Velocity (Model 1).	37
Figure 23.	Entry Wall Effective Stress (Model 1).	37
Figure 24.	Cutaway view of Model 1 Material Fraction plot at 0.6 ms.	39
Figure 25.	Left Wall Z-Displacement (Model 1).	40
Figure 26.	Left Wall Z-Velocity (Model 1).	40
Figure 27.	Left Wall Effective Stress (Model 1).	41
Figure 28.	Exit Wall X-Displacement (Model 1).	42
Figure 29.	Exit Wall X-Velocity (Model 1).	42
Figure 30.	Exit Wall Effective Stress (Model 1).	43

Figure 31.	Effective Stress Fringe Plot at 0.12 ms (Model 1).	44
Figure 32.	Effective Stress Fringe Plot at 0.2 ms (Model 1).	44
Figure 33.	Shock pressure propagating from impact point at 0.03 ms (Model 1).	45
Figure 34.	Shock pressure generated by 300 m/s spherical projectile (Model 1).	46
Figure 35.	Entry Wall X-Displacement (Model 2).	47
Figure 36.	Entry Wall X-Velocity (Model 2).	47
Figure 37.	Entry Wall Effective Stress (Model 2).	48
Figure 38.	Left Wall Z-Displacement (Model 2).	49
Figure 39.	Left Wall Z-Velocity (Model 2).	49
Figure 40.	Left Wall Effective Stress (Model 2).	50
Figure 41.	Exit Wall X-Displacement (Model 2).	51
Figure 42.	Exit Wall X-Velocity (Model 2).	51
Figure 43.	Exit Wall Effective Stress (Model 2).	52
Figure 44.	Effective stress fringe plot showing pre-stressed exit wall during drag phase (Model 2).	53
Figure 45.	Drag phase fluid pressure output from fluid gauge 2 (Model 2).	54
Figure 46.	Model 2 cavity evolution.	54
Figure 47.	Model 2 maximum cavity diameter measured from material fraction fringe plot.	55
Figure 48.	Material fraction plot of initial condition of Euler mesh for different fluid levels.	56
Figure 49.	Exit Wall X-Displacement for different projectile mass (Model 2).	59
Figure 50.	Exit wall X-displacement for different projectile velocity (Model 2).	61
Figure 51.	Drag phase pressure for different projectile velocities (Model 2).	62
Figure 52.	Exit wall X-displacement for different elastic modulus (Model 1).	64
Figure 53.	Exit Wall X-Displacement for different material density (Model 2).	66
Figure 54.	Exit wall X-Displacement for different fluid density (Model 1).	68
Figure 55.	Exit wall X-Displacement for different fluid density (Model 2).	68
Figure 56.	Entry wall resultant displacement for different fluid levels (Model 1). .	71
Figure 57.	Entry wall X-Displacement for different fluids levels (Model 1).	72
Figure 58.	Entry wall resultant velocity for different fluid levels (Model 1).	72
Figure 59.	Entry wall X-Velocity for different fluid levels (Model 1).	73
Figure 60.	Left wall resultant displacement for different fluid levels (Model 1).	73
Figure 61.	Left wall Z-Displacement for different fluid levels (Model 1).	74
Figure 62.	Left wall resultant velocity for different fluid levels (Model 1).	74
Figure 63.	Left wall Z-Velocity for different fluid levels (Model 1).	75
Figure 64.	Exit wall resultant displacement for different fluid levels (Model 1).	75
Figure 65.	Exit wall X-Displacement for different fluid levels (Model 1).	76
Figure 66.	Exit wall resultant velocity for different fluid levels (Model 1).	76
Figure 67.	Entry wall effective stress for different fluid levels (Model 1).	77
Figure 68.	Left wall effective stress for different fluid levels (Model 1).	77
Figure 69.	Exit wall effective stress for different fluid levels (Model 1).	78
Figure 70.	Fluid pressure for different fluid levels (Model 1).	78

Figure 71.	Entry wall resultant displacement for different fluid levels (Model 2).	79
Figure 72.	Entry wall X-Displacement for different fluid levels (Model 2).	79
Figure 73.	Entry wall resultant velocity for different fluid levels (Model 2).	80
Figure 74.	Entry wall X-Velocity for different fluid levels (Model 2).	80
Figure 75.	Left wall resultant displacement for different fluid levels (Model 2).	81
Figure 76.	Left wall Z-Displacement for different fluid levels (Model 2).	81
Figure 77.	Left wall resultant velocity for different fluid levels (Model 2).	82
Figure 78.	Left wall Z-Velocity for different fluid levels (Model 2).	82
Figure 79.	Exit wall resultant displacement for different fluid levels (Model 2).	83
Figure 80.	Exit wall X-Displacement for different fluid levels (Model 2).	83
Figure 81.	Exit wall X-Velocity for different fluid levels (Model 2).	84
Figure 82.	Entry wall effective stress for different fluid levels (Model 2).	84
Figure 83.	Left wall effective stress for different fluid levels (Model 2).	85
Figure 84.	Exit wall effective stress for different fluid levels (Model 2).	85
Figure 85.	Drag phase pressure for different fluid levels (Model 2).	86
Figure 86.	Drag phase pressure for different fluid levels (Model 2) - Enlarged.	86
Figure 87.	Entry wall resultant displacement for different projectile mass (Model 1).	87
Figure 88.	Entry wall X-Displacement for different projectile mass (Model 1).	88
Figure 89.	Entry wall resultant velocity for different projectile mass (Model 1).	88
Figure 90.	Entry wall X-Velocity for different projectile mass (Model 1).	89
Figure 91.	Left wall resultant displacement for different projectile mass (Model 1).	89
Figure 92.	Left wall Z displacement for different projectile mass (Model 1).	90
Figure 93.	Left wall resultant velocity for different projectile mass (Model 1).	90
Figure 94.	Left wall Z-Velocity for different projectile mass (Model 1).	91
Figure 95.	Exit wall resultant displacement for different projectile mass (Model 1).	91
Figure 96.	Exit wall X-Displacement for different projectile mass (Model 1).	92
Figure 97.	Exit wall resultant velocity for different projectile mass (Model 1).	92
Figure 98.	Exit wall X-Velocity for different projectile mass (Model 1).	93
Figure 99.	Entry wall effective stress for different projectile mass (Model 1).	93
Figure 100.	Left wall effective stress for different projectile mass (Model 1).	94
Figure 101.	Exit wall effective stress for different projectile mass (Model 1).	94
Figure 102.	Fluid pressure for different projectile mass (Model 1).	95
Figure 103.	Entry wall resultant displacement for different projectile mass (Model 2).	95
Figure 104.	Entry wall X-Displacement for different projectile mass (Model 2).	96
Figure 105.	Entry wall resultant velocity for different projectile mass (Model 2).	96
Figure 106.	Entry wall X-Velocity for different projectile mass (Model 2).	97
Figure 107.	Left wall resultant displacement for different projectile mass (Model 2).	97
Figure 108.	Left wall Z-Displacement for different projectile mass (Model 2).	98
Figure 109.	Left wall resultant velocity for different projectile mass (Model 2).	98
Figure 110.	Left wall Z-Velocity for different projectile mass (Model 2).	99

Figure 111.	Exit wall resultant displacement for different projectile mass (Model 2).	99
Figure 112.	Exit wall X-Displacement for different projectile mass (Model 2).	100
Figure 113.	Exit wall resultant velocity for different projectile mass (Model 2).	100
Figure 114.	Exit wall X-Velocity for different projectile mass (Model 2).	101
Figure 115.	Entry wall effective stress for different projectile mass (Model 2).	101
Figure 116.	Left wall effective stress for different projectile mass (Model 2).	102
Figure 117.	Exit wall effective stress for different projectile mass (Model 2).	102
Figure 118.	Drag phase pressure for different projectile mass (Model 2).	103
Figure 119.	Drag phase pressure for different projectile mass (Model 2). – Enlarged	103
Figure 120.	Exit wall resultant displacement for different projectile velocity (Model 1).	105
Figure 121.	Exit wall X-Displacement for different projectile velocity (Model 1)...	106
Figure 122.	Exit wall resultant velocity for different projectile velocity (Model 1). ..	106
Figure 123.	Exit wall resultant velocity for different projectile velocity (Model 1) – Enlarged.	107
Figure 124.	Exit wall X-Velocity for different projectile velocity (Model 1).	107
Figure 125.	Exit wall X-Velocity for different projectile velocity (Model 1) – Enlarged.	108
Figure 126.	Left wall resultant displacement for different projectile velocity (Model 1).	108
Figure 127.	Left wall Z-Displacement for different projectile velocity (Model 1)...	109
Figure 128.	Left wall resultant velocity for different projectile velocity (Model 1). ..	109
Figure 129.	Left wall Z-Velocity for different projectile velocity (Model 1).	110
Figure 130.	Exit wall resultant displacement for different projectile velocity (Model 1).	110
Figure 131.	Exit wall X-Displacement for different projectile velocity (Model 1)...	111
Figure 132.	Exit wall resultant velocity for different projectile velocity (Model 1). ..	111
Figure 133.	Exit wall X-Velocity for different projectile velocity (Model 1).	112
Figure 134.	Entry wall effective stress for different projectile velocity (Model 1)..	112
Figure 135.	Left wall effective stress for different projectile velocity (Model 1). ...	113
Figure 136.	Exit wall effective stress for different projectile velocity (Model 1). ...	113
Figure 137.	Fluid pressure for different projectile velocity (Model 1).	114
Figure 138.	Entry wall resultant displacement for different projectile velocity (Model 2).	114
Figure 139.	Entry wall X-Displacement for different projectile velocity (Model 2). ..	115
Figure 140.	Entry wall resultant velocity for different projectile velocity (Model 2).	115
Figure 141.	Entry wall X-Velocity for different projectile velocity (Model 2).	116
Figure 142.	Left wall resultant displacement for different projectile velocity (Model 2).	116
Figure 143.	Left wall Z-Displacement for different projectile velocity (Model 2)...	117
Figure 144.	Left wall resultant velocity for different projectile velocity (Model 2). ..	117
Figure 145.	Left wall Z-Velocity for different projectile velocity (Model 2).	118

Figure 146.	Exit wall resultant displacement for different projectile velocity (Model 2).	118
Figure 147.	Exit wall X-Displacement for different projectile velocity (Model 2)..	119
Figure 148.	Exit wall resultant velocity for different projectile velocity (Model 2).	119
Figure 149.	Exit wall X-Velocity for different projectile velocity (Model 2).....	120
Figure 150.	Entry wall effective stress for different projectile velocity (Model 2)..	120
Figure 151.	Left wall effective stress for different projectile velocity (Model 2). ...	121
Figure 152.	Exit wall effective stress for different projectile velocity (Model 2). ...	121
Figure 153.	Drag phase pressure for different projectile velocity (Model 2).....	122
Figure 154.	Drag phase pressure for different projectile velocity (Model 2) – Enlarged.	122
Figure 155.	Entry wall resultant displacement for different material modulus (Model 1).	123
Figure 156.	Entry wall X-Displacement for different material modulus (Model 1).	124
Figure 157.	Entry wall resultant velocity for different material modulus (Model 1).	124
Figure 158.	Entry wall X-Velocity for different material modulus (Model 1).	125
Figure 159.	Entry wall X-Velocity for different material modulus (Model 1) – Enlarged.	125
Figure 160.	Left wall resultant displacement for different material modulus (Model 1).	126
Figure 161.	Left wall Z-Displacement for different material modulus (Model 1)..	126
Figure 162.	Left wall resultant velocity for different material modulus (Model 1).	127
Figure 163.	Left wall Z-Velocity for different material modulus (Model 1).....	127
Figure 164.	Exit wall resultant displacement for different material modulus (Model 1).	128
Figure 165.	Exit wall X-Displacement for different material modulus (Model 1)..	128
Figure 166.	Exit wall resultant velocity for different material modulus (Model 1).	129
Figure 167.	Exit wall X-Velocity for different material modulus (Model 1).....	129
Figure 168.	Entry wall effective stress for different material modulus (Model 1)..	130
Figure 169.	Left wall effective stress for different material modulus (Model 1). ...	130
Figure 170.	Exit wall effective stress for different material modulus (Model 1). ...	131
Figure 171.	Fluid pressure for different material modulus (Model 1).	131
Figure 172.	Entry wall resultant displacement for different material modulus (Model 2).	132
Figure 173.	Entry wall X-Displacement for different material modulus (Model 2).	132
Figure 174.	Entry wall resultant velocity for different material modulus (Model 2).	133
Figure 175.	Entry wall resultant velocity for different material modulus (Model 2) – Enlarged.	133
Figure 176.	Entry wall X-Velocity for different material modulus (Model 2).	134
Figure 177.	Entry wall X-Velocity for different material modulus (Model 2) – Enlarged.	134
Figure 178.	Left wall resultant displacement for different material modulus (Model 2).	135

Figure 179.	Left wall Z-Displacement for different material modulus (Model 2)...	135
Figure 180.	Left wall resultant velocity for different material modulus (Model 2).	136
Figure 181.	Left wall Z-Velocity for different material modulus (Model 2).....	136
Figure 182.	Exit wall resultant displacement for different material modulus (Model 2).	137
Figure 183.	Exit wall X-Displacement for different material modulus (Model 2)...	137
Figure 184.	Exit wall resultant velocity for different material modulus (Model 2).	138
Figure 185.	Exit wall X-Velocity for different material modulus (Model 2).....	138
Figure 186.	Entry wall effective stress for different material modulus (Model 2)..	139
Figure 187.	Left wall effective stress for different material modulus (Model 2). ...	139
Figure 188.	Exit wall effective stress for different material modulus (Model 2). ...	140
Figure 189.	Drag phase pressure for different material modulus (Model 2).....	140
Figure 190.	Drag phase pressure for different material modulus (Model 2) - Enlarged.	141
Figure 191.	Entry wall resultant displacement for different material density (Model 1).	143
Figure 192.	Entry wall X-Displacement for different material density (Model 1). .	144
Figure 193.	Entry wall resultant velocity for different material density (Model 1).	144
Figure 194.	Entry wall X-Velocity for different material density (Model 1).....	145
Figure 195.	Left wall resultant displacement for different material density (Model 1).	145
Figure 196.	Left wall Z-Displacement for different material density (Model 1)....	146
Figure 197.	Left wall resultant velocity for different material density (Model 1)....	146
Figure 198.	Left wall Z-Velocity for different material density (Model 1).	147
Figure 199.	Exit wall resultant displacement for different material density (Model 1).	147
Figure 200.	Exit wall X-Displacement for different material density (Model 1)....	148
Figure 201.	Exit wall resultant velocity for different material density (Model 1)....	148
Figure 202.	Exit wall X-Velocity for different material density (Model 1).....	149
Figure 203.	Entry wall effective stress for different material density (Model 1)....	149
Figure 204.	Left wall effective stress for different material density (Model 1).	150
Figure 205.	Exit wall effective stress for different material density (Model 1).	150
Figure 206.	Fluid pressure for different material density (Model 1).....	151
Figure 207.	Entry wall resultant displacement for different material density (Model 2).	151
Figure 208.	Entry wall X-Displacement for different material density (Model 2). .	152
Figure 209.	Entry wall resultant velocity for different material density (Model 2).	152
Figure 210.	Entry wall resultant velocity for different material density (Model 2) – Enlarged.	153
Figure 211.	Entry wall X-Velocity for different material density (Model 2).....	153
Figure 212.	Entry wall X-Velocity for different material density (Model 2) – Enlarged.	154
Figure 213.	Left wall resultant displacement for different material density (Model 2).	154
Figure 214.	Left wall Z-Displacement for different material density (Model 2)....	155

Figure 215.	Left wall resultant velocity for different material density (Model 2)....	155
Figure 216.	Left wall Z-Velocity for different material density (Model 2).	156
Figure 217.	Exit wall resultant displacement for different material density (Model 2).	156
Figure 218.	Exit wall X-Displacement for different material density (Model 2)....	157
Figure 219.	Exit wall resultant velocity for different material density (Model 2)....	157
Figure 220.	Exit wall X-Velocity for different material density (Model 2).	158
Figure 221.	Entry wall effective stress for different material density (Model 2). ...	158
Figure 222.	Left wall effective stress for different material density (Model 2).	159
Figure 223.	Exit wall effective stress for different material density (Model 2).	159
Figure 224.	Drag phase pressure for different material density (Model 2).	160
Figure 225.	Drag phase pressure for different material density (Model 2) - Enlarged.	160
Figure 226.	Entry wall resultant displacement for different fluid density (Model 1).	161
Figure 227.	Entry wall X-Displacement for different fluid density (Model 1).	162
Figure 228.	Entry wall resultant velocity for different fluid density (Model 1).	162
Figure 229.	Entry wall X-Velocity for different fluid density (Model 1).	163
Figure 230.	Left wall resultant displacement for different fluid density (Model 1).	163
Figure 231.	Left wall Z-Displacement for different fluid density (Model 1).	164
Figure 232.	Left wall resultant velocity for different fluid density (Model 1).	164
Figure 233.	Left wall Z-Velocity for different fluid density (Model 1).	165
Figure 234.	Exit wall resultant displacement for different fluid density (Model 1).	165
Figure 235.	Exit wall X-Displacement for different fluid density (Model 1).	166
Figure 236.	Exit wall resultant velocity for different fluid density (Model 1).	166
Figure 237.	Exit wall X-Velocity for different fluid density (Model 1).	167
Figure 238.	Entry wall effective stress for different fluid density (Model 1).	167
Figure 239.	Left wall effective stress for different fluid density (Model 1).	168
Figure 240.	Exit wall effective stress for different fluid density (Model 1).	168
Figure 241.	Fluid pressure for different fluid density (Model 1).	169
Figure 242.	Entry wall resultant displacement for different fluid density (Model 2).	169
Figure 243.	Entry wall X-Displacement for different fluid density (Model 2).	170
Figure 244.	Entry wall resultant velocity for different fluid density (Model 2).	170
Figure 245.	Entry wall resultant velocity for different fluid density (Model 2) – Enlarged.	171
Figure 246.	Entry wall X-Velocity for different fluid density (Model 2).	171
Figure 247.	Entry wall X-Velocity for different fluid density (Model 2) – Enlarged.	172
Figure 248.	Left wall resultant displacement for different fluid density (Model 2).	172
Figure 249.	Left wall Z-Displacement for different fluid density (Model 2).	173
Figure 250.	Left wall resultant velocity for different fluid density (Model 2).	173
Figure 251.	Left wall Z-Velocity for different fluid density (Model 2).	174
Figure 252.	Exit wall resultant displacement for different fluid density (Model 2).	174
Figure 253.	Exit wall X-Displacement for different fluid density (Model 2).	175
Figure 254.	Exit wall resultant velocity for different fluid density (Model 2).	175

Figure 255.	Exit wall X-Velocity for different fluid density (Model 2).	176
Figure 256.	Entry wall effective stress for different fluid density (Model 2).	176
Figure 257.	Left wall effective stress for different fluid density (Model 2).	177
Figure 258.	Exit wall effective stress for different fluid density (Model 2).	177
Figure 259.	Drag phase pressure for different fluid density (Model 2).	178
Figure 260.	Drag phase pressure for different fluid density (Model 2) - Enlarged.	178

LIST OF TABLES

Table 1.	List of hardware and software for modeling and simulation.....	28
Table 2.	Loads and boundary conditions.....	32
Table 3.	Summary of material properties and constitutive model.....	34
Table 4.	Model 1 exit wall response to varying fluid levels.....	57
Table 5.	Model 2 exit wall response to varying fluid levels.....	57
Table 6.	Model 1 exit wall response to varying projectile mass.....	58
Table 7.	Model 2 exit wall response to varying projectile mass.....	58
Table 8.	Model 1 exit wall response to varying projectile initial velocity.....	60
Table 9.	Model 2 exit wall response to varying projectile initial velocity.....	60
Table 10.	Model 1 exit wall response for varying tank material modulus.....	62
Table 11.	Model 2 exit wall response for varying tank material modulus.....	63
Table 12.	Model 1 exit wall response for varying tank material density.....	65
Table 13.	Model 2 exit wall response for varying tank material density.....	65
Table 14.	Model 1 exit wall response to varying fluid density.....	66
Table 15.	Model 2 exit wall response to varying fluid density.....	67

THIS PAGE INTENTIONALLY LEFT BLANK

LIST OF ACRONYMS AND ABBREVIATIONS

ALE	Arbitrary Lagrange Euler
CEL	coupled Euler Lagrange
FE	Finite Element
HRAM	Hydrodynamic ram
LFT	live fire test
SPH	Smoothed Particle Hydrodynamics

THIS PAGE INTENTIONALLY LEFT BLANK

ACKNOWLEDGMENTS

I would like to express my deepest gratitude and appreciation to the following people for their advice, encouragement and support toward the successful completion of this thesis.

A sincere thank you goes to my thesis advisor, Distinguished Professor Kwon, who always put aside time for me despite his busy schedule to discuss my progress, giving me valuable technical insights and guidance along the way.

Many thanks to my thesis co-advisor, Professor Christopher Adams, for helping me come up with the thesis topic and for always being so friendly, encouraging, and approachable.

Milan Vukcevich, the IT specialist at the mechanical CAD lab, a big thank you for solving my IT-related problems and constantly updating me on any upcoming power outages and server maintenance at the lab when I was running my simulations.

Finally, I would like to thank my wife, Mei Ing, and daughter, Mikaela, for their unconditional love, encouragement, and support.

THIS PAGE INTENTIONALLY LEFT BLANK

I. INTRODUCTION

A. BACKGROUND

Hydrodynamic Ram (HRAM) refers to the damage process due to high pressures generated when a kinetic energy projectile penetrates a compartment or vessel containing a fluid [1]. The large internal fluid pressure that acts on the walls of the fluid filled tank can result in severe structural damage especially at the entrance and exit walls. The study of HRAM effects on fuel tanks used on military aircraft is vital as a tank that is designed to withstand HRAM loads can increase its survivability to threats from small arms when operating in a hostile environment.

Even as modern military aircraft become more survivable, due to technological advancements and considerations given to aircraft survivability during the development and design stages, HRAM remains a paramount damage process to today's combat aircraft, especially during the takeoff and landing phases of flight operations. Moreover, modern aircraft structures are moving away from all aluminum structures and utilizing greater amounts of lightweight composite material, which presents an added challenge to protect, especially against HRAM. Even though composites have a much better strength to weight ratio compared to aluminium, they were known to be more brittle when loaded to point of failure and are therefore more prone to abrupt failures.

Many types of threats can result in HRAM damage to aircraft fuel tanks, such as armor piercing rounds from small arms and fragments from missile warhead detonation. Statistics from Desert Storm indicated that 75% of aircraft losses were attributable to fuel system vulnerability with HRAM being one of the primary kill mechanisms [2]. An aircraft flying at low altitude in a hostile environment would be susceptible to small arms firing at them; and when these projectiles penetrate the aircraft's fuel tank, the HRAM effect could rupture the tank walls and damage structural components, eventually rendering the aircraft

incapable for flight. An aircraft's fuel tank is typically the most vulnerable component onboard, since it has the largest presented area. Ruptured aircraft fuel tanks and its damaged surrounding structures would require long downtime for depot level maintenance, as opposed to quick patch repairs of the entry wall panel, resulting in low aircraft availability and high cost of recovery. In some cases, HRAM could also lead to catastrophic attrition of the aircraft due to the cascading effect from a fuel tank failure [3].

To design structures to withstand the HRAM loads, or to develop the HRAM mitigation techniques for existing aircraft, it would be necessary to first predict the pressures and the distribution inside the tank throughout the different phases of the HRAM phenomenon. Understanding the source and magnitude of the pressure waves generated in the fluid could lead to improved methods of mitigation and attenuation to better protect aircraft. Live Fire Test (LFT), or experimental testing for such purposes, could be costly and impractical for parametric studies to be conducted. Therefore, in recent times, more emphasis has been placed on the development of numerical techniques to simulate this complex fluid structure interaction problem. For small projectile penetration into a fluid-filled tank, the classical Lagrangian finite element solver alone cannot resolve the large deformation in the fluid mesh. The high distortion in the fluid would have to be modeled using the Eulerian mesh, and solved using the Eulerian solver. For interaction to occur between the Lagrangian and Eulerian mesh, a coupling surface would be necessary to define the interaction between the fluid and structure mesh. MSC Dytran provides two types of coupling techniques, known as General Coupling and Arbitrary Lagrange Euler Coupling (ALE) [4].

The ultimate goal for HRAM analysis and research is to develop ways to eliminate the extensive damage to the entry and exit walls of the fuel tank immediately after being impacted by a projectile such as a bullet. A well-designed fuel tank would be able to withstand HRAM loading and keep the damage to a mere small hole at the entry and exit walls. Such damage levels would be

considered acceptable, as the subsequent fuel loss would be minimal leading to increased survivability of the aircraft to such threats. The small hole on the entry wall of the tank could also be repaired more rapidly resulting in better aircraft availability.

B. OBJECTIVES

The objective of this thesis was to develop a Finite Element (FE) model using MSC Dytran to analyze the dynamic response of tank structure, and conduct parametric studies on factors that could affect tank wall response during the initial phase of HRAM event. The model would enable a better understanding of how various parameters affect the pressure waves generated in the fluid, as well as the dynamic response of the coupled structure. MSC Patran is used as the pre-processor for developing the FE model and boundary conditions for this complex fluid structure interaction problem. The Lagrangian structural shell elements were coupled to the fluid Euler elements using the ALE coupling technique whereas the projectile was coupled to the fluid using the general coupling technique. For the parametric studies conducted, the emphasis would mainly be on the structural exit wall response where critical components or main structural members on the aircraft are located.

Chapter I presents the background and objective of this thesis. Chapter II introduces the different phases of the HRAM phenomenon by looking at some of the previous studies and experiments conducted. It also gives a brief history and overview of the HRAM simulation follow by the different techniques used by MSC Dytran for fluid structure interaction problems. Chapter III provides a description of the model development and its boundary conditions. Chapter IV presents the results and discussions of baseline Model 1 and 2 followed by the parametric studies that were conducted on the two baseline models. Finally, the conclusion and some possible future work are provided in Chapter V.

THIS PAGE INTENTIONALLY LEFT BLANK

II. UNDERSTANDING HRAM

A. THE HRAM PHENOMENON

In most non-exploding projectile impacts with penetration and traversing through a fluid-filled tank, the HRAM phenomenon can be described in four distinct phases as follows [2]:

- Shock phase: initial impact of projectile into entry wall of fuel tank
- Drag phase: movement of projectile through fluid
- Cavitation phase: development of cavity behind projectile as it moves through the fluid and the subsequent cavity oscillation and collapse
- Exit phase: projectile penetrates the exit wall and leaves the tank only when there is sufficient energy remaining.

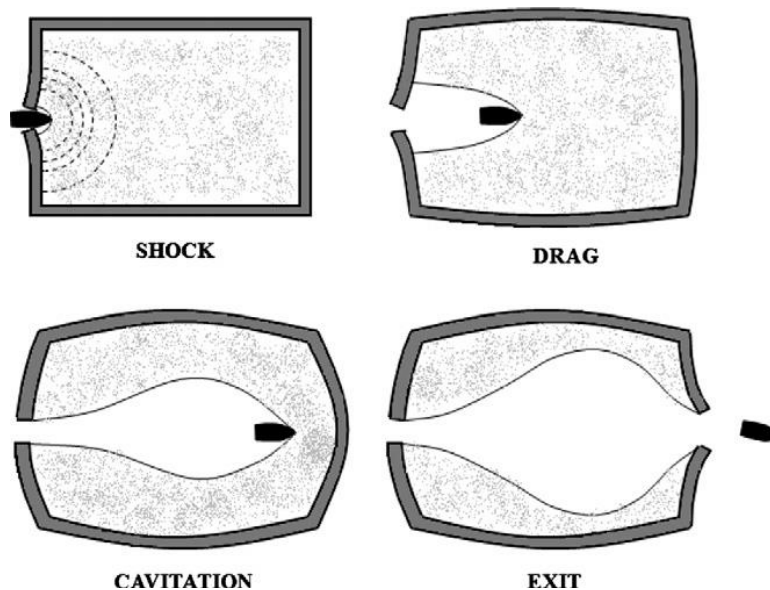


Figure 1. Four phases of HRAM phenomenon, from [2].

As depicted in Figure 1, each phase contributes to structural damage of the tank walls via a different mechanism and the extent of damage depends on numerous factors such as projectile shape and velocity, fluid level in impacted tank, obliquity of impact and material of fuel tank. The amount of structural

damage, shown in Figure 2, could be significant, with large-scale petalling and tearing of the entry and exit walls. Fuel tank failure could lead to numerous modes of aircraft attrition [5]. The following sub-sections detail the first three phases of HRAM phenomenon.

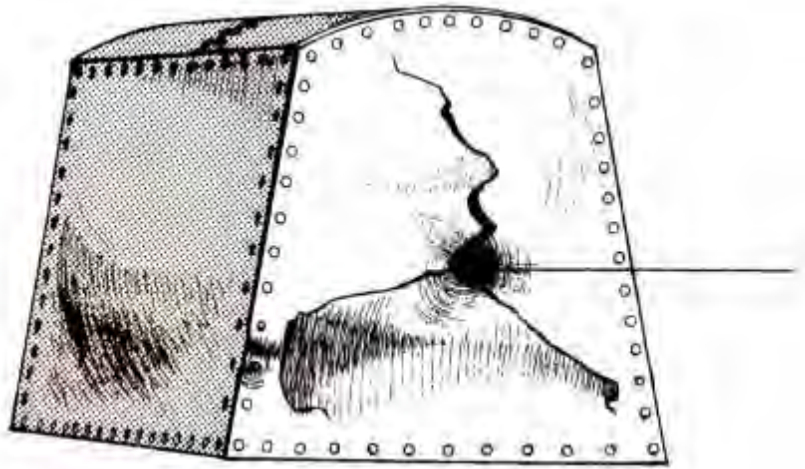


Figure 2. Extent of tank damage due to HRAM effect, from [5].

1. The Shock Phase

The HRAM phenomenon begins with the shock phase as the projectile first impacts and penetrates the tank wall. A hemispherical shock wave propagates from the point of impact and traverses through the fluid due to the rapid transfer of energy from the projectile to the fluid, as shown in one of the earliest experiments conducted by McMillen [6] and McMillen and Harvey [7]. The shadowgraph technique was used to capture the shock wave shown in Figure 3, for a 3.2 mm steel sphere being propelled into the tank at an impact velocity of 1073 m/s. The shock front propagated away from the impact point and its strength diminished rapidly as it traveled away from the impact point. Since the projectile moved at a velocity below the speed of sound in water, as it is retarded by forces after entering water, the shock wave was observed to be ahead of the projectile.

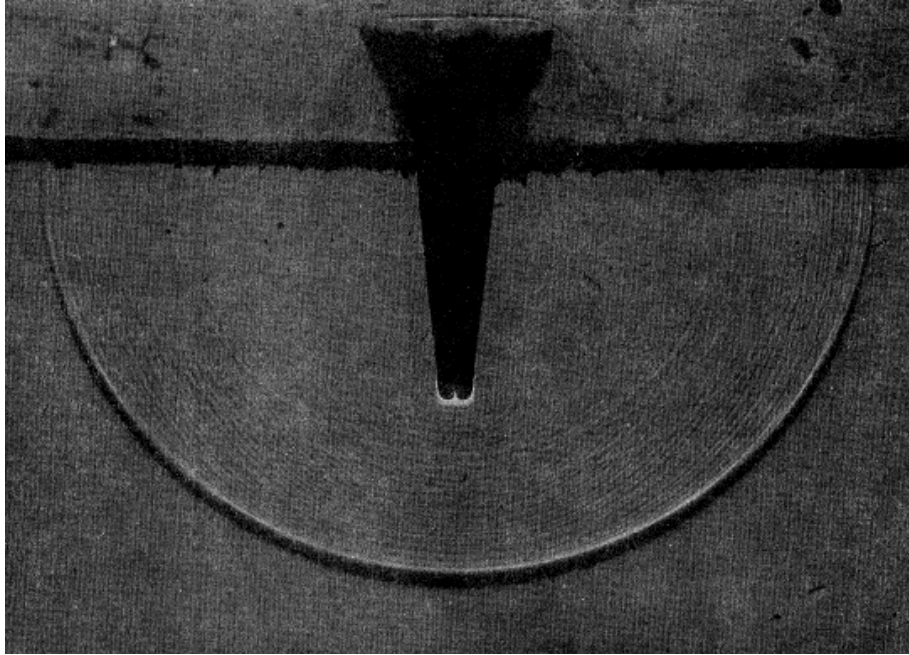


Figure 3. Spark shadowgraph of pressure wave during the shock phase captured in McMillen experiment, from [6].

Besides capturing the initial shock wave visually, McMillen [6] also concluded that the wave pressure was proportional to the impact velocity of projectile raised to the power of 2.17, and it varied linearly with the projectile's projected area based on the dark band thickness captured by the shadowgraph.

Several studies were done to record the initial impact and shock wave pressure of the shock phase using pressure transducers at different locations in the fluid filled tank, with the more recent experiment conducted by Disimile [8]. For the shock phase, Disimile found that the initial impact wave resulted in a sharp pressure rise of short duration. Tests were also conducted with spherical projectiles of the same size but made of different materials and it was concluded that the magnitude and duration of the initial wave pressure did not vary with the projectile material, which was consistent with the findings from Morse and Stepka [9]. The wave pressure was also found to have the greatest value near the shot line, and decreased with angles away from the shot line.

Equations 2.1 and 2.2 [10] attempted to provide analytical prediction for the shock phase of HRAM event.

- Rankine-Hugoniot relations

$$u_s = c_l + S_l u_p \quad (2.1)$$

where,

u_s = shock front velocity (m/s)

c_l = sound velocity in fluid (m/s)

S_l = Hugoniot slope coefficient of fluid

u_p = projectile velocity after impact (m/s)

- Impact pressure

$$p = \rho_l c_l u_p + \rho_l S_l u_p^2 \quad (2.2)$$

where,

p = impact pressure (Pa)

ρ_l = fluid density (kg/m³)

c_l = sound velocity in fluid (m/s)

u_p = projectile velocity after impact (m/s)

S_l = Hugoniot slope coefficient of fluid

2. The Drag Phase

As the projectile moves through the fluid, it is slowed by viscous drag and its energy is transformed into the kinetic energy of fluid motion. A pressure field is generated in front of the projectile along its path, as fluid is being displaced. Since the fluid is accelerated gradually rather than impulsively unlike the shock phase, the peak pressure would be much lower but occurred over a longer duration [5].

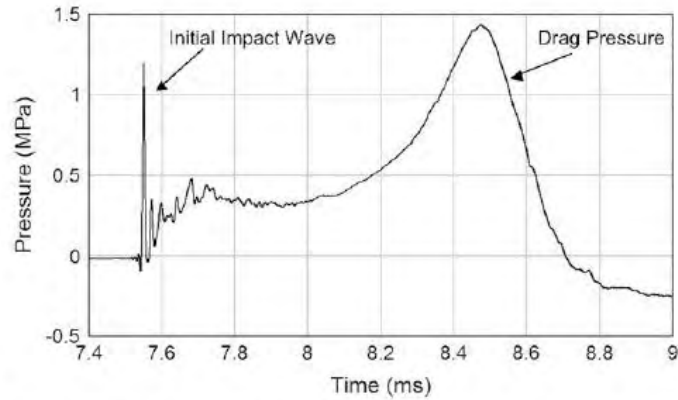


Figure 4. Top: Pressure of drag phase recorded by transducer P3. Bottom: Video image as projectile nears transducer P3, from [8].

In the Disimile experiment [8], the drag phase pressure rise is compared to the high-speed video image of the projectile path, to map the drag pressure recorded by the pressure transducer to the location of the projectile as it traverses through the fluid. The pressure time history of one of the transducers is shown in Figure 4, together with the captured video image during the drag pressure rise. The pressure recorded by the transducer P3 was found to increase gradually as the projectile approached the transducer, and then decreased as it passed the transducer. This phenomenon indicated that the projectile pressure field was responsible for the gradual pressure rise. In this study, projectile material and its effect on the drag pressure was also investigated. The comparison of the drag pressure time history of three different projectiles is shown in Figure 5. The aluminum projectile was found to produce the lowest drag

pressure followed by steel and then tungsten. It was determined that heavier projectiles maintained a greater velocity through the tank, demonstrating the effect of projectile mass and kinetic energy [8].

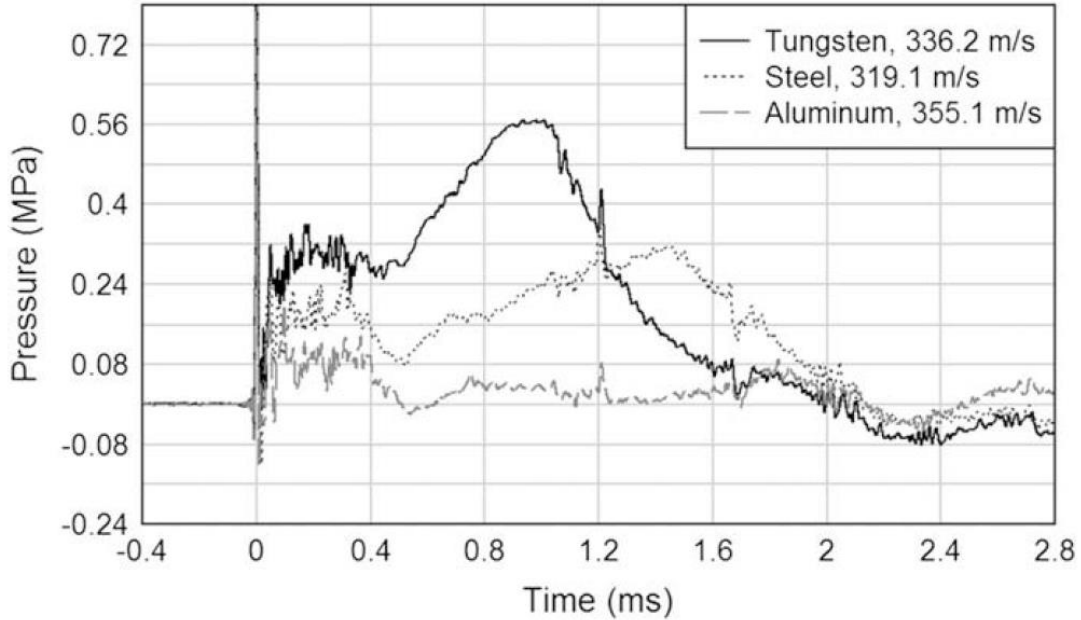


Figure 5. Drag pressure comparison for different material measured by transducer P3, from [8].

Equations 2.3 and 2.4 for the analytical predictions of the drag phase [10] are given as such:

- Drag Force on projectile

$$F_D = -C_D A_p \rho \frac{u_0^2}{2} \quad (2.3)$$

where,

F_D = Drag force (N)

C_D = Drag coefficient of projectile

A_p = Cross sectional area of projectile (m²)

u_0 = projectile velocity after impact (m/s)

- Newton's second law on projectile

$$\frac{u}{u_0} = \frac{1}{\left[1 + \frac{3}{4} C_D \left(\frac{\rho u_0}{\rho_p d_p} \right) t \right]^2} \quad (2.4)$$

where,

u = velocity of projectile after impact (m/s)

u_0 = velocity of projectile before impact (m/s)

C_D = Drag coefficient of projectile

ρ = Fluid density (kg/m³)

ρ_p = Projectile density (kg/m³)

d_p = Projectile diameter (m)

t = time (s)

3. The Cavitation Phase

The cavitation phase is the most complex and least understood phase of a HRAM event. As the projectile moved through the fluid, a region of low pressure is developed in its wake as the flow accelerates past the surface of the projectile. This low pressure region could result in vaporization of the fluid behind, and air from the penetrated hole in the entry wall could also fill the cavity. The displaced fluid from the formation of an air cavity would eventually seek to regain its undisturbed condition and oscillate before collapsing. The oscillation and collapsing of the cavity is known as the cavitation phase [5]. Besides increasing the pressure in the tank, the collapsing of the cavity could also result in the violent ejection of fuel from the entry and exit holes, thereby increasing the risk of fire and damaged to surrounding critical component. Pressure pulses generated from the cavitation phase for a tungsten spherical projectile impacting the tank at 350 m/s, have been found in the Disimile experiment to be much greater than the initial pressure wave from the impact phase, as illustrated in Figure 6 [8].

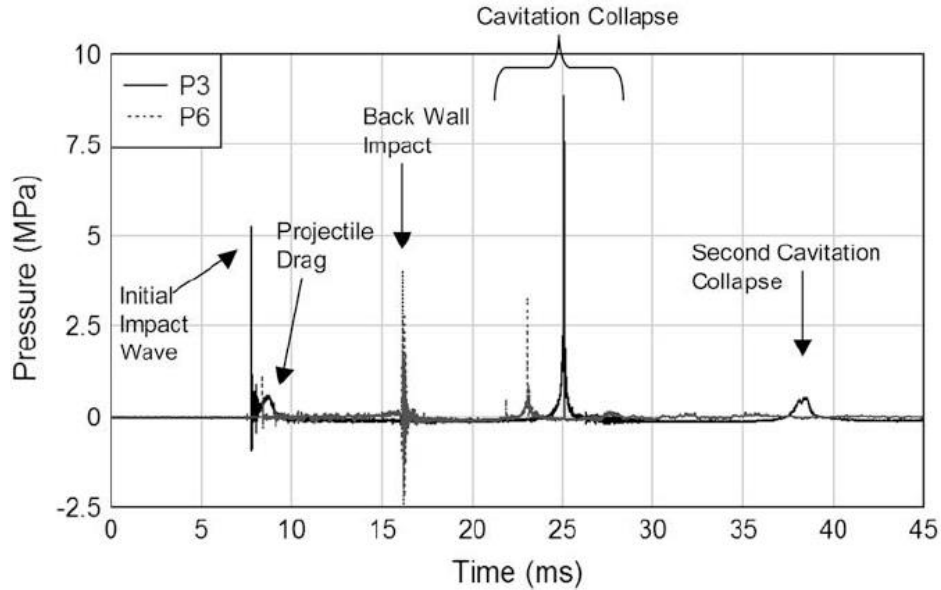


Figure 6. Pressure time history of spherical tungsten projectile impacting tank at 350 m/s, from [8].

The cavitation collapse was found to occur approximately 20 ms after the initial impact. The largest cavitation collapse pressure, occurring at approximately 25 ms, corresponded to the smallest size of the cavity captured in the video image, and reached a peak value of approximately 10 MPa.

Equations 2.5–2.10 for the analytical predictions of the cavitation phase [10] are given as such:

- Cavitation parameter

$$k = \frac{p_0 - p_v}{\frac{1}{2} \rho u_p^2} \quad (2.5)$$

where,

p_0 = initial static pressure at axis level of projectile (Pa)

p_v = liquid vapor pressure (Pa)

ρ = Fluid density (kg/m³)

u_p = projectile velocity after impact (m/s)

- Drag coefficient

$$C_D = C_0(1+k) \quad (2.6)$$

where,

C_0 = Drag coefficient without cavitation

k = Cavitation parameter

- Relation between drag and maximum cavity diameter

$$\frac{d_{\max}}{d_p} = \sqrt{\frac{C_D}{k\left(1-0.132k^{\frac{1}{2}}\right)}} \quad (2.7)$$

where,

d_{\max} = Cavity maximum diameter (m)

d_p = Projectile diameter (m)

C_D = Drag coefficient

k = Cavitation parameter

- Rate of growth of cavity

$$\frac{dr_c}{dt} = \sqrt{A \frac{u_0^2}{r_c^2(1+Bt)^2} - 2gh} \quad (2.8)$$

where,

$$A = \frac{d_p^2}{4 \left(1 + \sqrt{\frac{\rho}{\rho_p}}\right)^2} \quad (2.9)$$

and

$$B = \frac{3u_0 C_D \rho}{4\rho_p d_p} \quad (2.10)$$

r_c = Cavity diameter (m)

u_0 = Projectile velocity before impact (m/s)

g = Gravitational acceleration (m/s^2)

h = Height of fluid at shot level (m)

B. HISTORY AND OVERVIEW OF HRAM SIMULATION

1. Evolution of Numerical Techniques for HRAM Simulation

The high cost of performing experiments for extracting useful data to understand HRAM phenomenon has led to extensive efforts in developing numerical techniques for computational simulation. Such efforts had been attempted for the past thirty years with the earlier efforts trying simplify the phenomenon into a structural response problem with boundary conditions representing the applied loads from the pressure field generated by ram effects. Subsequent efforts attempted to solve the nonlinear sets of hydrodynamic equations using numerical techniques by coupling the fluid and structure interaction.

The first method for the HRAM simulation was an approximate theory developed by Robert Ball at the Naval Postgraduate School, known as the piston theory [11]. This method allowed the solution for fluid pressures to be obtained separately from solution of wall response, which greatly simplified the problem as it ignored the effects of complex fluid and structure interaction during the HRAM event. Ball modified two structural response codes, known as BR-1 and SATANS, to include the piston theory and called it the BR-1HR. Simulating the fluid structure interaction is necessary as the high pressure in the fluid caused by the penetrating projectile loads and displaces the tank walls, while the displacement in turn also affects the pressure profile of the fluid. Due to the simplification and separation of fluid and structural analysis, the predicted entry and exit wall strains were found to be much lower than the actual data collected from experiments.

In 1980, Kimsey became the first to simulate the HRAM problem by solving the nonlinear set of hydrodynamic equations together with material constitutive model [1]. Dynamic analysis of a projectile penetrating a fluid-filled cylinder was performed using the two dimensional EPIC-2 code, which is a Lagrangian Finite Element solver. Since the elements in the Lagrangian Finite Element mesh move together with the deformation of the structure, this method, when applied to the HRAM problem, will result in massive distortion of the mesh, and will compromise the numerical accuracy of the results. However, Kimsey concluded that the use of EPIC-2 code in understanding the HRAM phenomenon was promising, even though mesh distortions and computational power might be a potential downside. Moreover, no validation to the numerical model was performed, due to the lack of experimental data [1].

Due to the limitations of Lagrangian codes for simulating the HRAM problem, and because of the high-mesh distortion, a new method was needed. The Eulerian method that uses a fixed-grid system managed to mitigate the problem of high-mesh distortion, but still require massive computational power. This led to the development of a new generation of computer codes in the early 1990s that incorporated the Lagrangian and Eulerian methods together with higher-order numerical algorithms. These new codes, sometimes referred to as hybrid codes, allow for the coupling of Lagrangian and Eulerian formulations that are required for fluid and structure interaction problems in the HRAM simulation. Different numerical techniques for coupling, such as Coupled Euler-Lagrange (CEL) and Arbitrary Lagrange Euler (ALE) methodology, will be introduced in later sections. Most of these codes are still in the validation and verification phase, but have shown great potential in simulating fluid structure interaction problems. In particular, MSC Dytran and LS-DYNA had been verified to be capable of accurately predicting the response of structures to HRAM events, and are currently used by leading aerospace defense contractors like Boeing, Lockheed Martin, and Northrop Grumman [12].

More recently, the Smoothed Particle Hydrodynamics (SPH) methodology, initially created by Lucy and Gingold and Monaghan to study astrophysical events, has been applied to the HRAM simulation. SPH is a mesh-free method where particles containing individual material properties replaced the mesh, but have its motion still governed by the general conservation equations. Since the particles are not constraint, they can move freely and deform in any manner, making SPH suitable for simulating processes where large deformation will occur in the case of HRAM [12].

Even though ALE and SPH methods have shown promising results in the simulation of the HRAM, modeling fluid structure interaction problems has proven to be a complicated task. The suitability and predictive capabilities of both methods have not been fully solved, and are currently still being investigated.

2. Overview of Recent HRAM Numerical Simulations

Most of the recent studies conducted on the HRAM simulation served to investigate the capabilities and shortfalls of different techniques such as CEL, ALE, and SPH. Due to the intensive computational time required for HRAM models, most research conducted was on simplified, small, and generic tanks and projectile. Some studies also involved the actual firing of projectiles into water tanks for the purpose of model validation and verification.

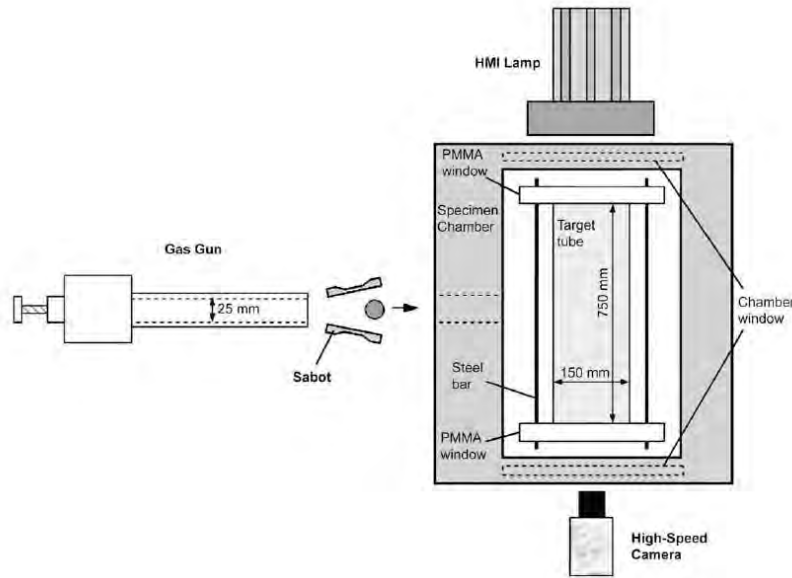


Figure 7. Experiment setup of spherical projectile impacting aluminum tank, from [13].

In his research, Varas [13] utilized the commercial code LS-DYNA to simulate an HRAM event created by steel spherical projectiles, impacting a fluid-filled aluminum square tank. Two different formulations, ALE and SPH, were used to recreate the actual experiment that was conducted. The experiment setup is shown in Figure 7, which provide data such as pressure in different points in the fluid, deformation of the tank walls, and cavity evolution for different impact velocities.

Subsequently, the numerical results were compared to experimental data to determine the capabilities of the two techniques in reproducing such a complex phenomenon. Both ALE and SPH methods were able to qualitatively reproduce the HRAM phenomenon appropriately, as shown in Figure 8. Three important variables, the pressure time history in the fluid, the cavity evolution and the final deformation of the aluminum tank, are found to have good correlation to experimental test results, as illustrated in Figure 9. However, modeling of the shock wave propagation required fine mesh and particles, which resulted in a very long computational time.

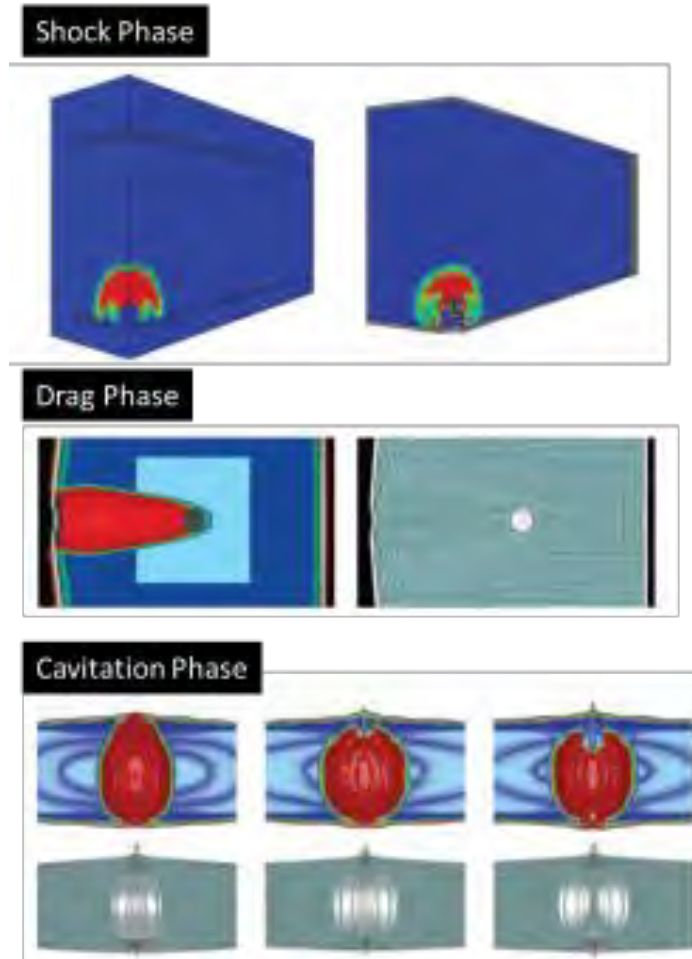


Figure 8. ALE and SPH simulation of the different phases of HRAM, from [13].

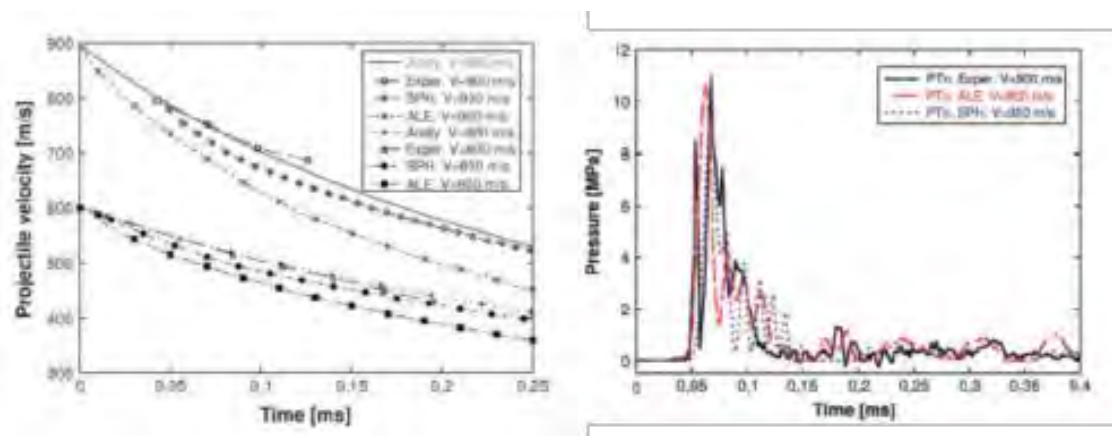


Figure 9. Left: Projectile velocity decay time history. Right: Pressure time history plot near impact point for 100% filled tube impacted at 900 m/s, from [13].

MSC Dytran was used in [14] to simulate the HRAM effects where a high-velocity projectile is shot into a fluid filled tank. ALE coupling was used to define the interaction between the structure and fluid mesh while a general coupling is defined between the penetrating projectile and fluid mesh. In this study, the velocity of the projectile and density of the fluid was varied to study its effect on the ram pressure in a 36" x 36" x 36" cubic aluminum tank of thickness 0.125." The tank was modelled with Lagrangian shell element while the fluid was modelled with eight nodes solid element, as shown in Figure 10.

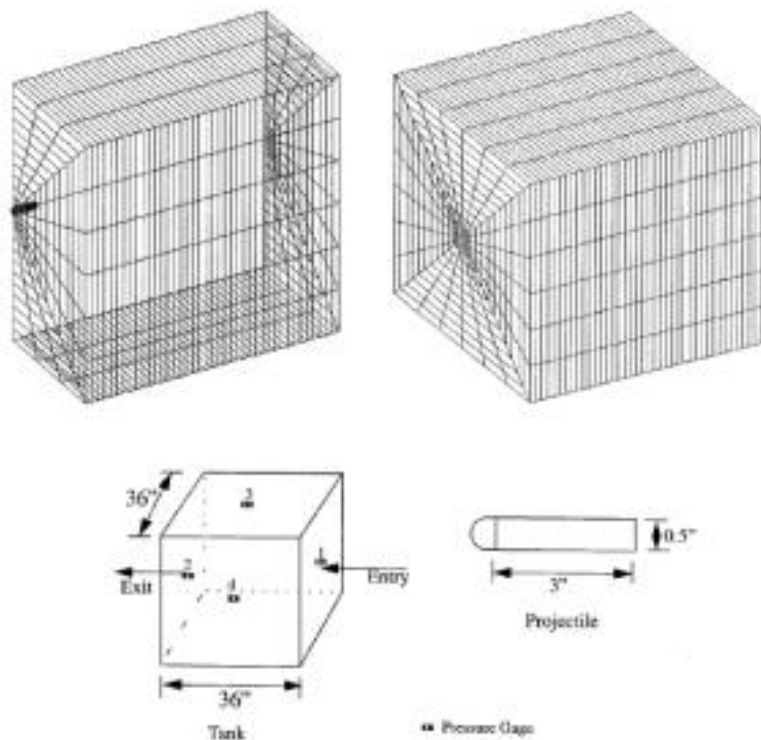


Figure 10. Top Left: Lagrangian Tank shell element. Top Right: Eight node solid Eulerian fluid element. Bottom: Tank and projectile dimensions with pressure gage locations, from [14].

It was concluded that higher projectile velocities translated to an increased displacement of the tank walls. The tank wall stresses were also higher for higher projectile velocities, but the duration of load application was shorter. When the densities of the fluid was varied, data collected from the simulation model

seemed to indicate no discernible effect on the deformation of the tank, but it was indicated that further analysis needed to be performed due to the lack of a consistent pattern. Additionally, the simulation model was not validated, as no experiment was conducted for comparison.

Some of the more recent research into HRAM simulation involved the meshless SPH technique, which is currently still in the research phase even though some preliminary studies in [13], [15] and [16] have shown that SPH is capable of reproducing some of the physics of the HRAM and its different phases.

C. FLUID STRUCTURE INTERACTION – DYTRAN

MSC Dytran is a three-dimensional, explicit, finite, element analysis software program for simulating and analyzing complex, short-duration events involving severe deformation of structural materials, and the interaction of fluids and structures. This makes MSC Dytran a suitable platform for the simulation of HRAM phenomenon. The following sections summarize the solution techniques used by MSC Dytran detailed in [4] that are necessary for the modeling of HRAM events.

1. Numerical Solvers

MSC Dytran provides two solvers and two coupling techniques summarized in the following section [4], [17]. The Lagrangian solver is the most common finite element solution technique for engineering applications whereas the Eulerian solver is most frequently used for analyzing fluids or materials that undergo large deformation. The Lagrangian and Eulerian mesh can be coupled together to analyze fluid structure interaction problems, such as HRAM phenomenon, by means of a coupling surface in MSC Dytran: General Coupling and ALE Coupling.

a. Lagrangian Solver

When the Lagrangian solver is used, grid points are fixed to locations on the body being analyzed. Elements of material are created by connecting the grid points together, and the collection of elements produces a mesh. When the body deforms due to loads, the numerical mesh moves and distorts together with the elements containing materials, as shown in Figure 11. Therefore, the Lagrangian solver is computing the motion of elements of constant mass bounded by the grid points at every time step.

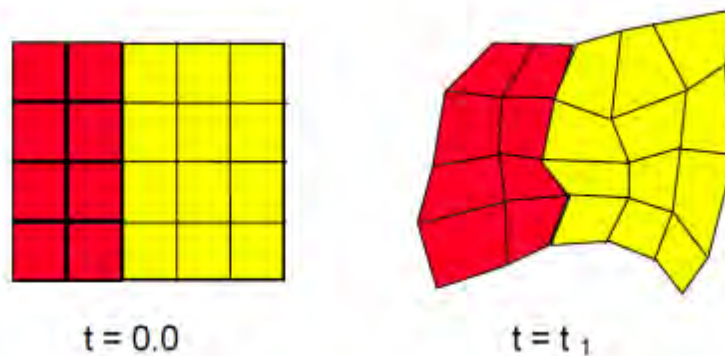


Figure 11. Lagrangian solver mesh, from [17].

This solver is widely used in engineering applications as it is able to effectively and accurately track material interfaces and incorporate complex material models. However, its application is only suited for simulations where the material undergo relatively small deformations because large deformations will result in small time steps due to mesh distortion and entangling. Even though some numerical codes are able to handle such problems, it is computationally costly and might also cause the loss of accuracy. In the case of the HRAM simulation where the elements become highly distorted, a pure Lagrangian solver will not be sufficient.

b. Eulerian Solver

In the Eulerian solver, the grid points are fixed in space and the elements are simply partitions of the space defined by connected grid points. The Eulerian mesh is a fixed reference frame where the grid points will not move. The physical material of a body under analysis moves through the Eulerian mesh; where the mass, momentum, and energy of the material are transported from element to element, as illustrated in Figure 12. The Eulerian solver, therefore, calculates the motion of material through elements of constant volume.

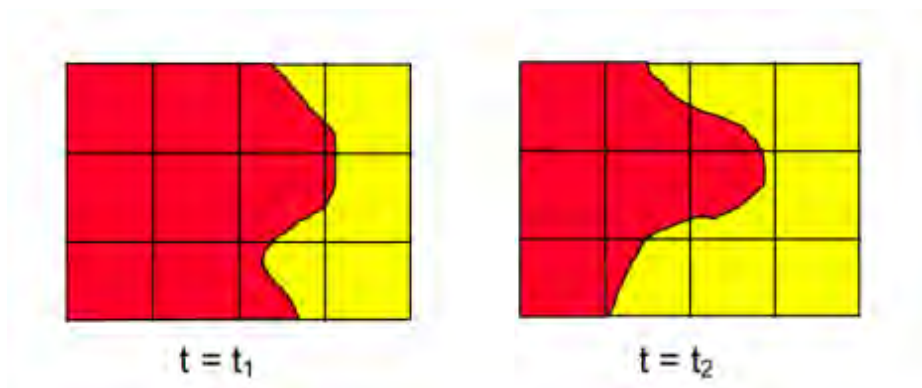


Figure 12. Eulerian solver mesh, from [17].

This solver is commonly used to represent fluids and gases, usually for the analysis of flow problems that involve multi-material properties with one finite element cell. Free surfaces and material interfaces can move through the fixed mesh and therefore it is also necessary that void spaces be modeled. The advantage for using Eulerian solver is that there will not be any mesh distortion problems as the mesh does not move even when there are large deformation. When modeling with the Eulerian technique, it is important for the mesh to be sufficiently big enough to contain the material after deformation. Since the Eulerian mesh acts like a container, the material cannot leave the boundary of the mesh, and stress waves reflection and pressure build-up can occur if the Eulerian mesh is too small for analysis.

A HRAM simulation will likely require both Lagrangian and Eulerian solvers, with the tank structure and projectile modeled using a Lagrangian mesh and the fluid domain inside the tank, using an Eulerian mesh. The two meshes will then be coupled together, either with the General Coupling or ALE Coupling techniques, by defining the coupling surface that acts as a boundary to the flow of material in the Eulerian mesh, while the stresses in the Eulerian material exerts forces on the surface, causing the Lagrangian mesh to distort.

2. Coupling Techniques

The coupling algorithm enabled the material modelled in the Eulerian and Lagrangian mesh to interact in the case of fluid structure interaction problem such as HRAM simulation. Without the coupling algorithm, the two solvers are entirely separate. This means that the Lagrangian elements that lie within an Eulerian mesh do not affect the flow of the Eulerian material and no forces are transferred from the Eulerian material back to the Lagrangian structure.

a. General Coupling

In order to create a coupling condition between the Eulerian and Lagrangian domain of the model, a surface had to be created on the Lagrangian structure. This surface was created to enable the transfer of forces between the two solver domains as shown in Figure 13. The coupling surface acts as a boundary to the flow of material in the Eulerian mesh. Concurrently, the stresses in the Eulerian elements also cause forces to act on the coupling surface, resulting in the distortion of the Lagrangian elements. MSC Dytran allows for a few methods to define the coupling surface, either by element numbers, property numbers, or material numbers. Users can also define whether the inside or outside domain is covered by the coupling surface by setting the COVER field on the entry. This entry means that the Euler domain cannot contain material where it is covered by the outside or inside of the Lagrangian structure.

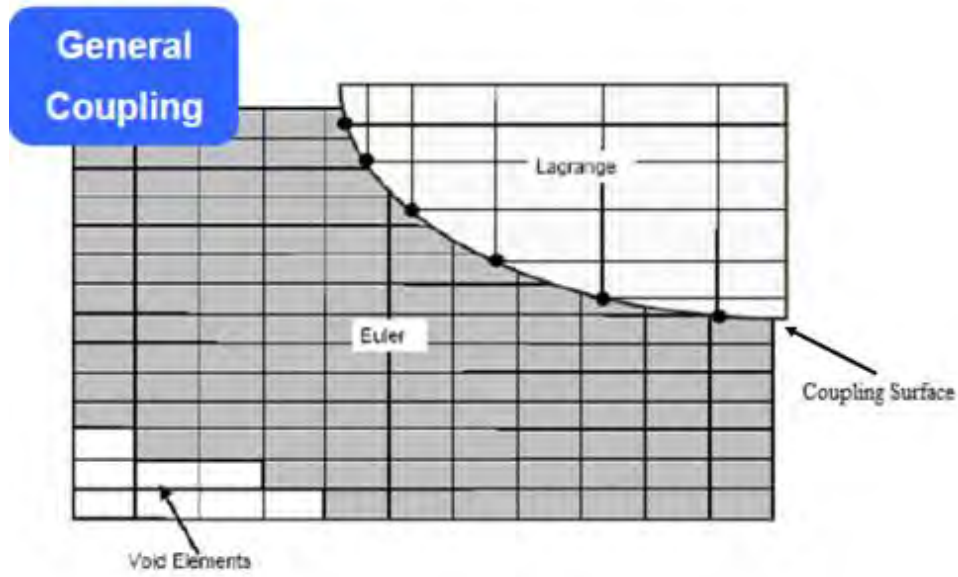


Figure 13. General coupling, from [4].

For the HRAM simulation, the Lagrangian tank model is to be filled with fluid likely being modeled with a Eulerian mesh; therefore, when coupling the tank mesh to the fluid mesh, the COVER field should be set to the outside, since the Eulerian elements outside the coupling surface must be covered. When coupling the projectile to the fluid, the COVER field should be set to the inside. In order for general coupling to work, the coupling surface must form a close volume, which means that there cannot be any holes in the coupling surface and the surface must be closed. Additionally, the closed volume formed by the coupling surface must intersect at least one Euler element in order for the coupling surface to be recognized by the Eulerian mesh.

b. ALE Coupling

The ALE coupling can be considered a hybrid method and a trade-off between pure Lagrangian and pure Eulerian formulation. In the ALE coupling approach, the Eulerian mesh is no longer fixed, but is allowed to follow the motion of the Lagrangian mesh at the coupling surface. The nodes of the structural Lagrangian mesh are physically connected to the nodes of the fluid

Eulerian mesh, as shown in Figure 14. When the tank starts to move and deform due to projectile impact in a HRAM simulation, the Eulerian mesh that is attached to the tank nodes at the coupling surface also start to move. Due to the movement of the coupling surface, fluid in the adjacent Eulerian elements becomes compressed, and exerts a pressure load back onto the structural tank wall elements.

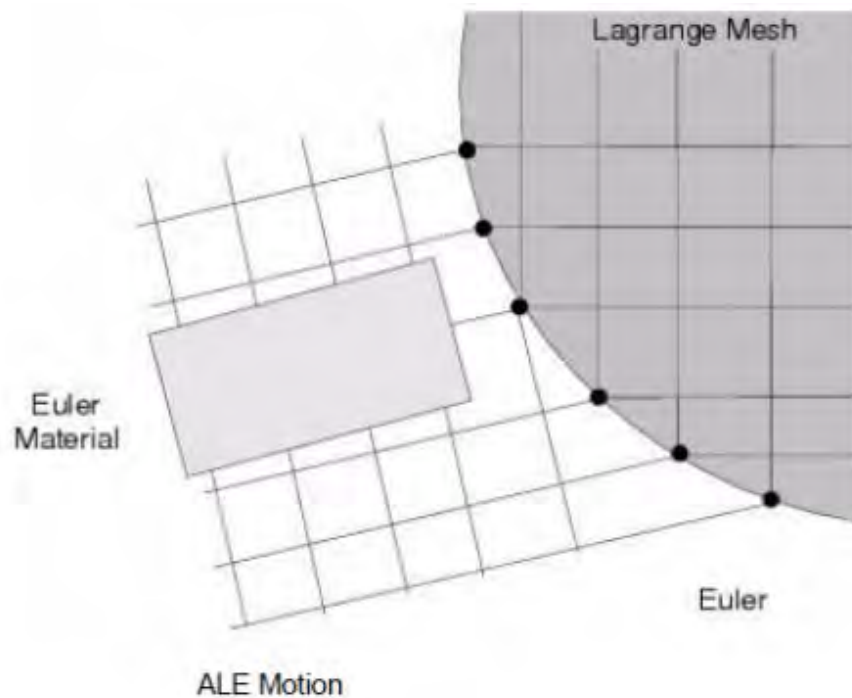


Figure 14. ALE coupling, from [4].

To preserve the original Eulerian mesh and have it follow the structural motion, the Eulerian grid points can be defined as ALE grid points. This will allow the motion of the ALE coupling surface to propagate through the Eulerian mesh by the ALE motion algorithm. In the ALE formulation, the Eulerian material flows through the mesh, but the mesh can also move due to the coupling with the Lagrangian mesh.

THIS PAGE INTENTIONALLY LEFT BLANK

III. METHODOLOGY AND MODEL DEVELOPMENT

A. MODELING PROCEDURES

This study was conducted using the commercial FE software MSC Patran and MSC Dytran.

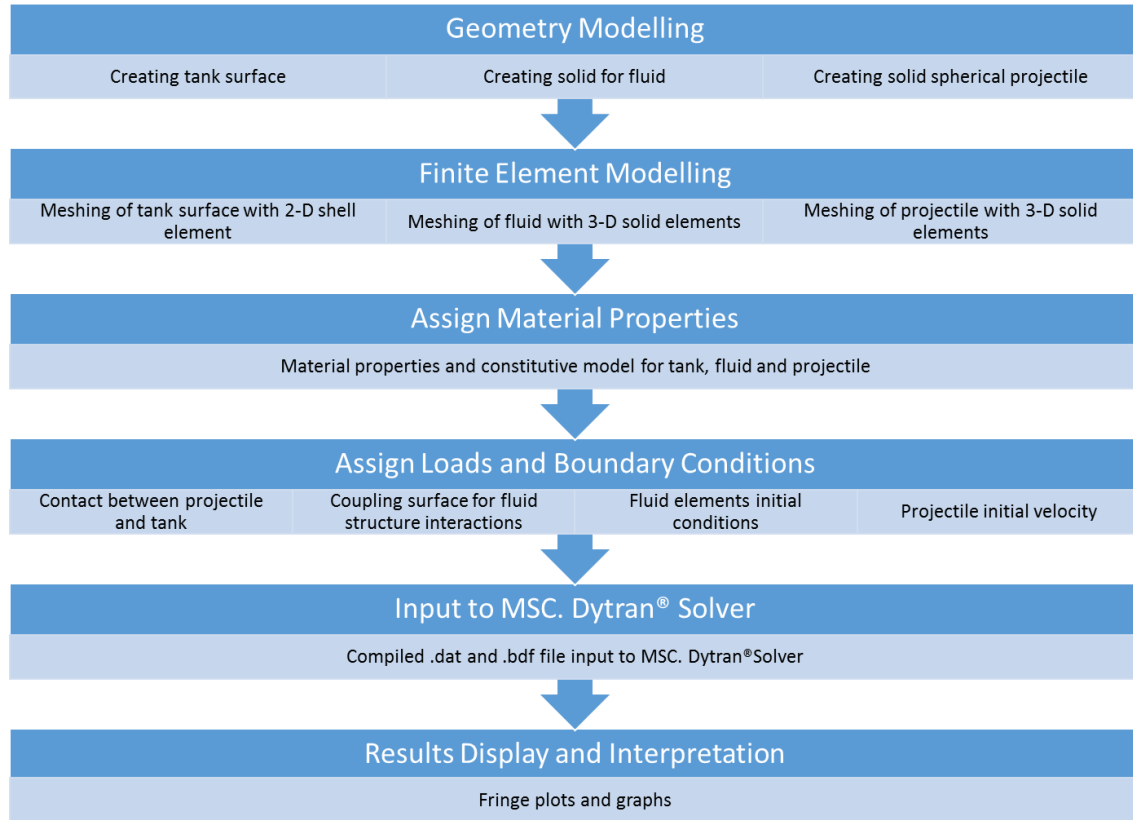


Figure 15. HRAM simulation modeling procedures.

The modeling procedures for HRAM simulation are detailed in Figure 15. The MSC Patran was the pre-processor, where the tank, fluid, and projectile geometry were modeled and FE mesh created. The Patran interface to the Dytran input deck was utilized as a tool to create and assign material properties to the elements together with the assignments of loads and boundary conditions. The modeling and analysis were input and computed in S.I units by the MSC Dytran solver. Results archive file output from Dytran explorer was attached and

post-processed by MSC Patran. Table 1 lists the hardware and software tools for performing the analysis:

Table 1. List of hardware and software for modeling and simulation.

Hardware	Specifications
Computer	Intel® Xeon® CPU E5606 @ 2.13Ghz Dual Processor, 24Gb Ram (8 core)
Software	Versions
MSC. Patran®	2012.2 64 bit, Build: 19.1.164499
MSC. Dytran®	Dytran Explorer 2012.1.2

B. DESCRIPTION OF MODEL

This section details the definition of the model and the interactions between the various parts in the simulation for the different phases of HRAM. The HRAM model consisted of three main parts: Lagrangian mesh for the tank and projectile and Eulerian mesh for the fluid inside the tank.

The simulation of HRAM required a very fine Euler mesh and small sampling times to capture the propagation of shock waves in the fluid; thereby resulting in large files and long computational times. For a computational model simplification, a generic cubic tank of dimensions 200 mm x 200 mm x 200 mm, impacted by a 10 mm diameter spherical projectile was developed. Subsequent parametric studies on the tank wall response and fluid pressures during the different phases of the HRAM event will be conducted with this simplified fluid-filled tank model.

1. Projectile

The projectile impacting at the center of the tank's entry wall was a solid steel sphere weighing 4 grams, and with diameter 10mm. It was discretized with 160 solid eight nodes hexahedron Lagrangian elements, as shown in Figure 16.

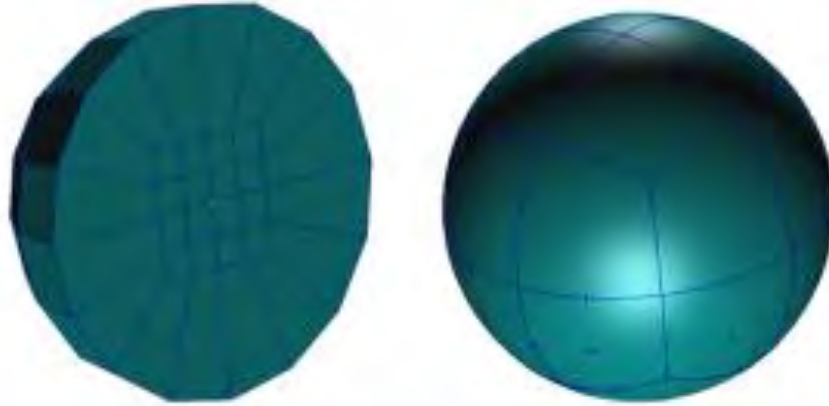


Figure 16. Spherical projectile Lagrangian solid element mesh.

Since the deformation of the projectile was not of interest in this study, the projectile was modeled as a rigid body defined using the material constitutive form MATRIG. One reason for selecting a projectile with a spherical surface was to prevent the tumbling of the projectile during the drag phase which would have resulted in significant pressure fluctuations in the fluid causing erratic response to the coupled tank walls.

2. Tank

The 200 mm cubic tank was discretized with 9,600 2-D quadrilateral shell element with four grid points, as shown in Figure 17. The element's global edge length was set to 5 mm and was assigned properties defined with material constitutive form DMATEP in Dytran for the different cases investigated and detailed in Chapter IV. The DMATEP entry describes an isotropic, elastic-plastic material with a failure criterion.

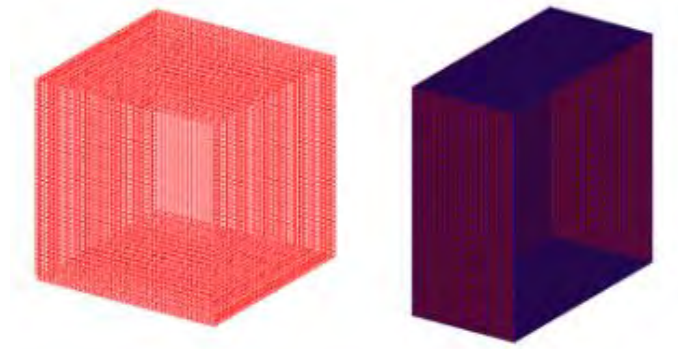


Figure 17. Left: Lagrangian tank model consisting 9,600 shell elements.
Right: Lagrangian tank cutaway model.

3. Fluid

The fluid in the tank was discretized with 3-D solid eight nodes hexahedron Eulerian elements, as shown in Figure 18. A total of 64,000 Eulerian elements, with a global edge length of 5 mm, made up the Euler box. The fluid level and properties were varied for the different cases being investigated. The mesh size for the Eulerian fluid elements was chosen to be similar to the Lagrangian tank shell elements, so that the nodes are coincident to one another at the coupling surface. This condition is necessary for proper coupling of the Lagrangian and Eulerian elements to avoid unnecessary problems that could arise from the failure of the coupling surfaces.

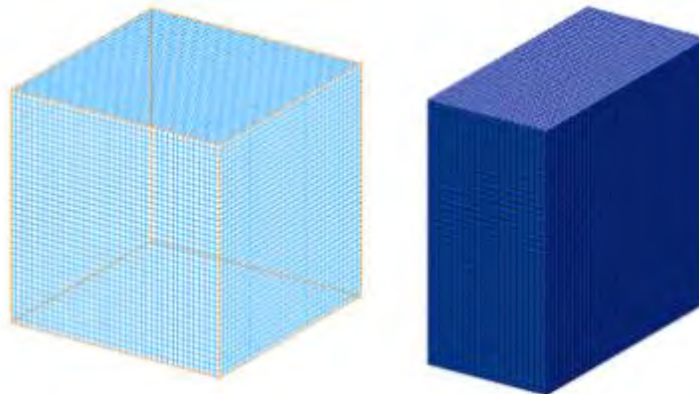


Figure 18. Left: Eulerian fluid model consisting 64,000 solid hexahedron elements. Right: Eulerian fluid cutaway model.

4. Boundary Conditions

As shown in Figure 19, two models were constructed for the purpose of this study. The first model was for the investigation of the shock phase of the HRAM with the projectile outside the tank, impacting the entry wall at a prescribed velocity. For this model, hereby referred to as Model 1, the displacement of the tank walls due to projectile impact and the subsequent ram pressure of the propagating hemispherical shock wave in the fluid from the impact point would be of interest.

For the second model, hereby referred to as Model 2, the projectile initial starting position will be flush against the inner surface of the entry wall at the impact point to simulate the projectile's position just after penetrating the entry wall. The initial velocity of the projectile will be lesser, at 250 m/s, due to retardation of the projectile by the entry wall. Model 2 would be used to study the fluid pressures and the tank wall response during the drag phase.

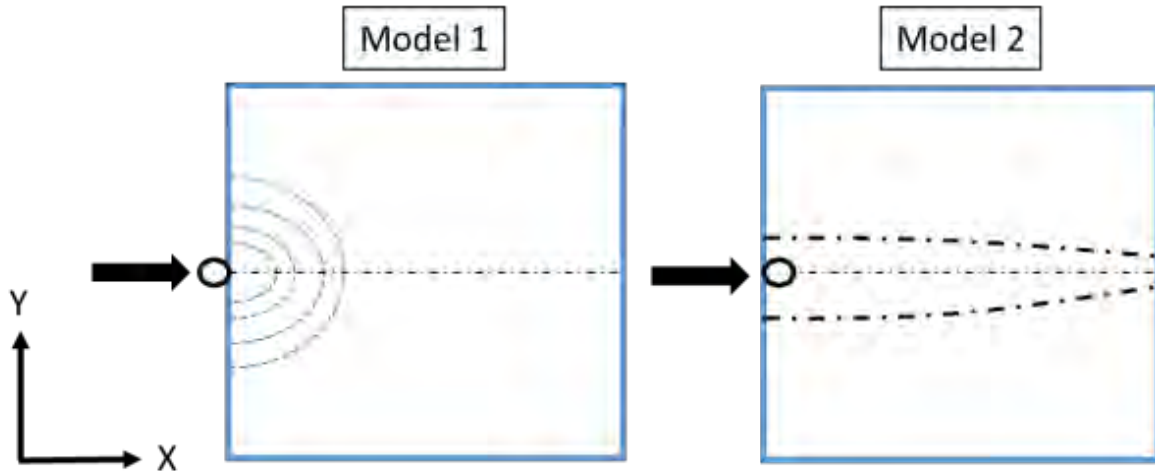


Figure 19. Schematic of Model 1 and Model 2.

The initial loads and boundary conditions for the two models are tabulated in Table 2.

Table 2. Loads and boundary conditions.

Loads and Boundary Conditions	Description
Displacement	Model 1: Bottom surface of tank is fixed. Model 2: Bottom surface of tank is fixed.
Projectile Initial Velocity	Model 1: 300 m/s Model 2: 250 m/s
Contact	Model 1: Master-slave surface contact between projectile and tank Model 2: Adaptive master-slave contact between projectile and tank
Coupling (between fluid and projectile)	Model 1: Nil Model 2: General Coupling
Coupling (between fluid and tank)	Model 1: ALE Coupling Model 2: ALE Coupling

An important aspect of fluid structure interaction problem is the coupling of the surfaces between the structure and fluid mesh. For Model 2, the projectile was coupled to the fluid by the general coupling technique while the fluid and tank surfaces was coupled together using the ALE coupling technique. In MSC Dytran, the general coupling mode allows the motion of a structure through a fixed Eulerian mesh, such as the movement of the projectile through the fluid. The Lagrangian structure, which is the projectile in this case, acts as a moving flow boundary for the fluid in the Eulerian domain while the fluid in turns acts as a pressure load boundary on the projectile. For the ALE coupling technique used to define the interaction between the tank and fluid, the Eulerian mesh is now allowed to move and follow the motion of the Lagrangian mesh at the interface, since the nodes between the two meshes are now physically coupled together. When the tank walls start to displace, the fluid Euler mesh also move together. Due to the motion of the Euler mesh, a compressive force would be exerted on the adjacent fluid element. The compressed fluid element in turn would exert a pressure load back on the structural tank wall elements [14].

5. Location of Tracer Elements

Tracer elements were defined at various locations within the model to collect data required for time history plots of the tank wall displacement, velocity and stresses, and the fluid pressures for analysis. Location of the tracer elements were illustrated in Figure 20. There were nine tank shell element across the entry, left, and exit walls, and three fluid hex element tracers.

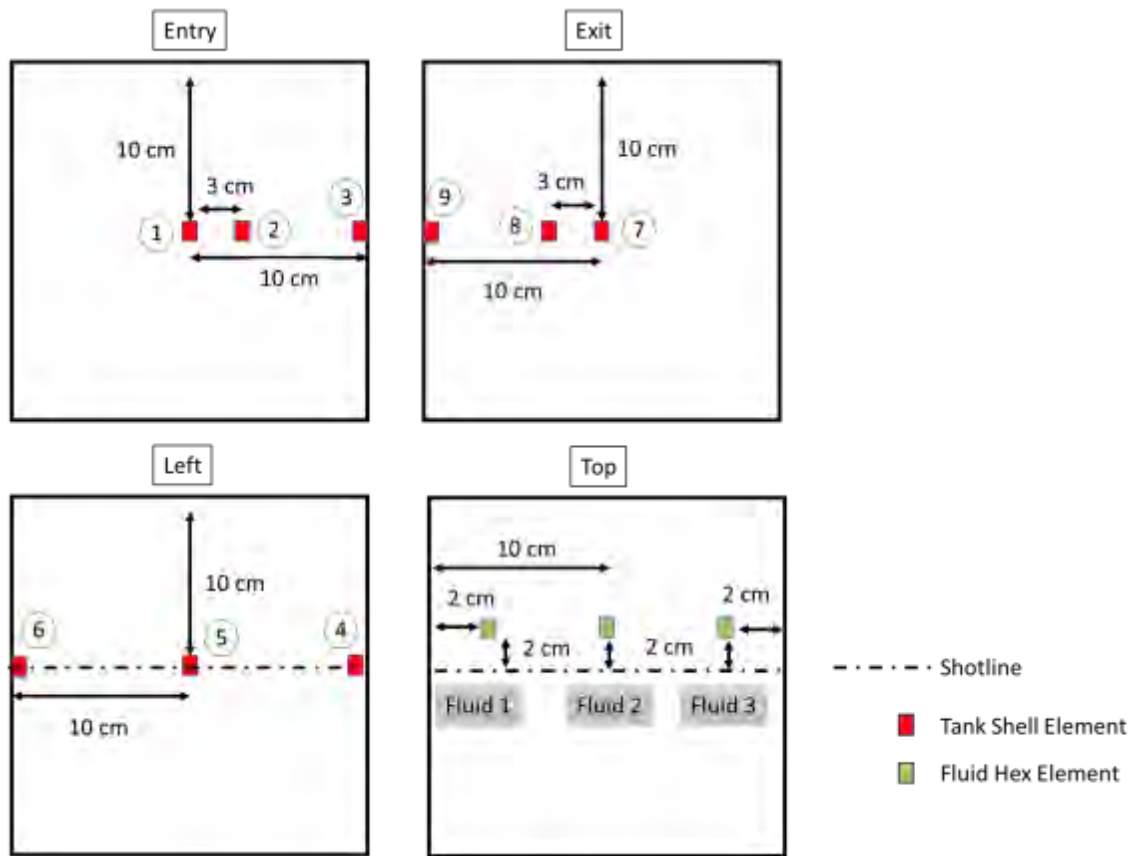


Figure 20. Location of tracer elements

For ease of comparison and analysis, the graphs plotted in Chapter IV were obtained from the middle node and element of each wall, labeled No. 1, 5, and 7 for the tank structure, and Fluid 2 for the fluid pressures output.

6. Material Properties

The material properties and constitutive models for baseline Model 1 and 2 are summarized in Table 3.

Table 3. Summary of material properties and constitutive model

	Tank	Fluid	Projectile
Material	Aluminium	Water	Steel
Material Model	DMATEP	LINFLUID	MATRIG
Density (kg/m³)	2700	1000	N.A.
Elastic Modulus (GPa)	70	N.A.	N.A.
Bulk Modulus (GPa)	N.A.	2.2	N.A.
Von Mises Yield Strength (GPa)	20	N.A.	N.A.
Mass (kg)	N.A.	N.A.	0.004
Thickness (m)	0.002	N.A.	N.A.
Poisson Ratio	0.33	N.A.	N.A.

Initially, the tank shell elements were assigned a linear elastic material model DMAT. This material constitutive model does not output the Von Mises stress that was necessary for analysis; therefore, it was decided to use DMATEP to model the tank structure. Since DMATEP is used for describing an elastic-plastic material with failure criteria, the yield strength for the aluminum tank was artificially given a large value so that the failure and penetration of the tank structure, due to projectile impact, would not be simulated.

IV. RESULTS AND DISCUSSION

A. TANK WALL RESPONSE TO HRAM LOADING

The first step to better protect aircraft fuel tanks from the drastic consequences of the HRAM is to understand the structural dynamic responses of the tank during the HRAM events. Baseline Model 1 and Model 2 were developed for this purpose. Even though a typical HRAM event consists of four phases, as discussed earlier in Chapter II, it was decided to analyze the impact phase separately using Model 1, as the failure process of projectile penetration and the subsequent material failure is still not well modeled at present. To avoid the unclear nature and the possible ambiguity in the results, it was decided that the modeling of projectile penetration into and out of the tank be omitted from the simulation. Data collected to plot the time history for the tank wall's displacement, velocity, and effective stress were taken from the nodes and elements output at the center of each wall. The gauges corresponded to shell element gauge no. 1, 5, and 7, as shown in Figure 20. Similarly, the fluid pressures generated during the shock and drag phase were plotted using data collected from fluid gauge no. 2, whose location was also shown in Figure 20.

1. Baseline Model 1

The baseline Model 1 simulation was set up for a 100% water filled aluminium tank of 2 mm thickness, impacted without penetration at the center of the entry wall by a spherical steel projectile of mass 4 grams, diameter 10 mm and with an initial velocity of 300 m/s. Even though this is a hypothetical situation, since the projectile would likely penetrate the entry wall in an actual experiment, this simulation provided some insight to the tank wall behavior during the initial shock phase of the HRAM event. The event was simulated for 1 ms with a sampling rate of 20 μ s for data collection, to plot the event time history. A high frequency of sampling was required to capture the propagation of the ram pressure wave across the fluid upon projectile impact. For comparison purposes,

the following discussion compares Model 1 to an empty tank impacted under the same conditions.

a. Entry Wall Response

Entry wall X-displacement, X-velocity and effective stress plots are shown in Figures 21, 22, and 23, respectively. The X-direction corresponds to the major component of the entry wall, since the direction of projectile velocity impacting the entry wall is in the positive X-direction.

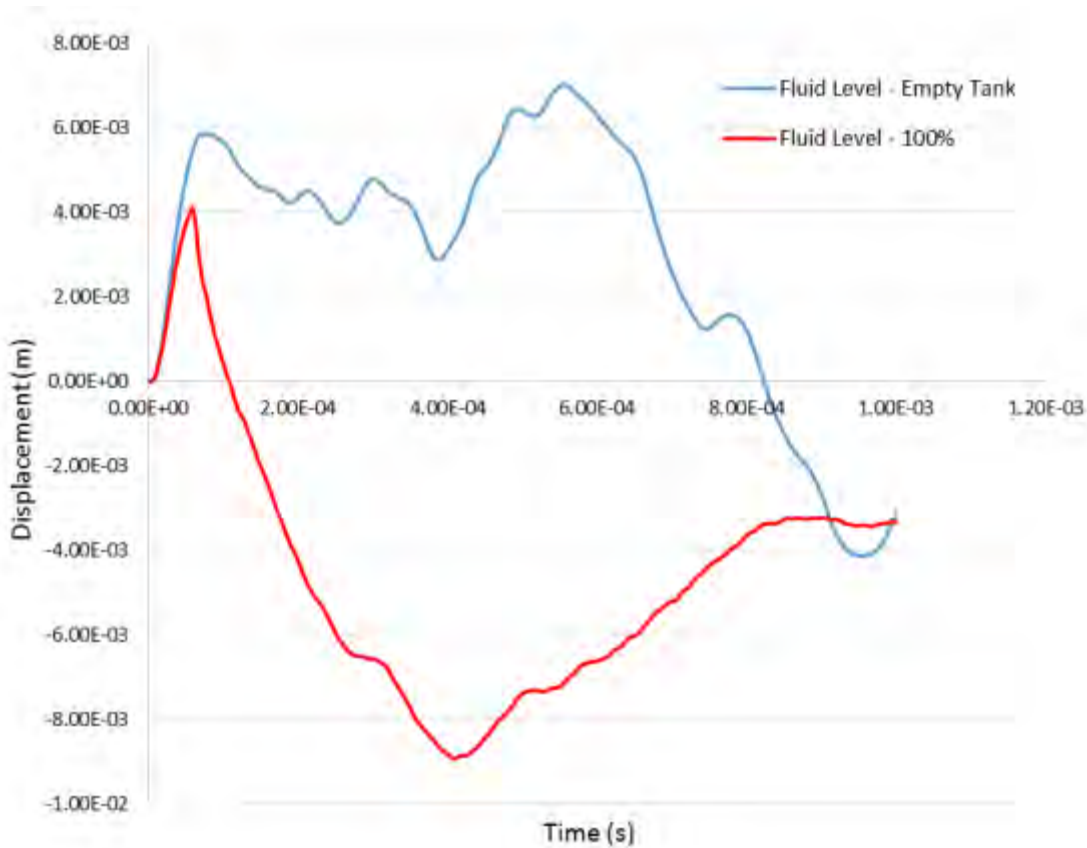


Figure 21. Entry Wall X-Displacement (Model 1).

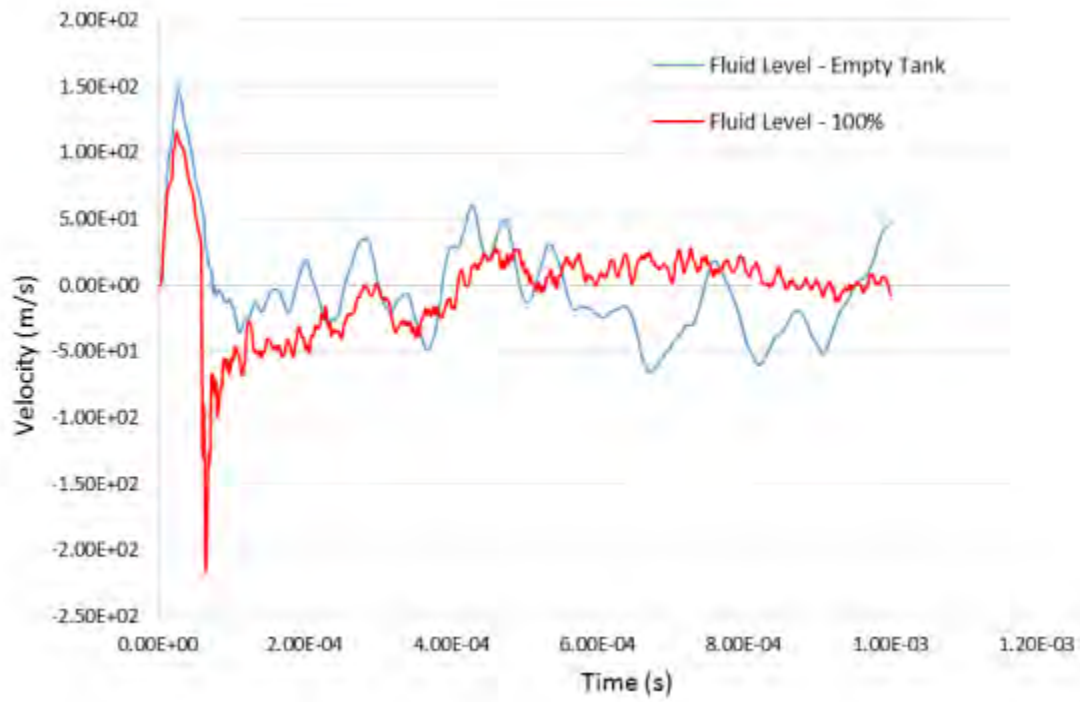


Figure 22. Entry Wall X-Velocity (Model 1).

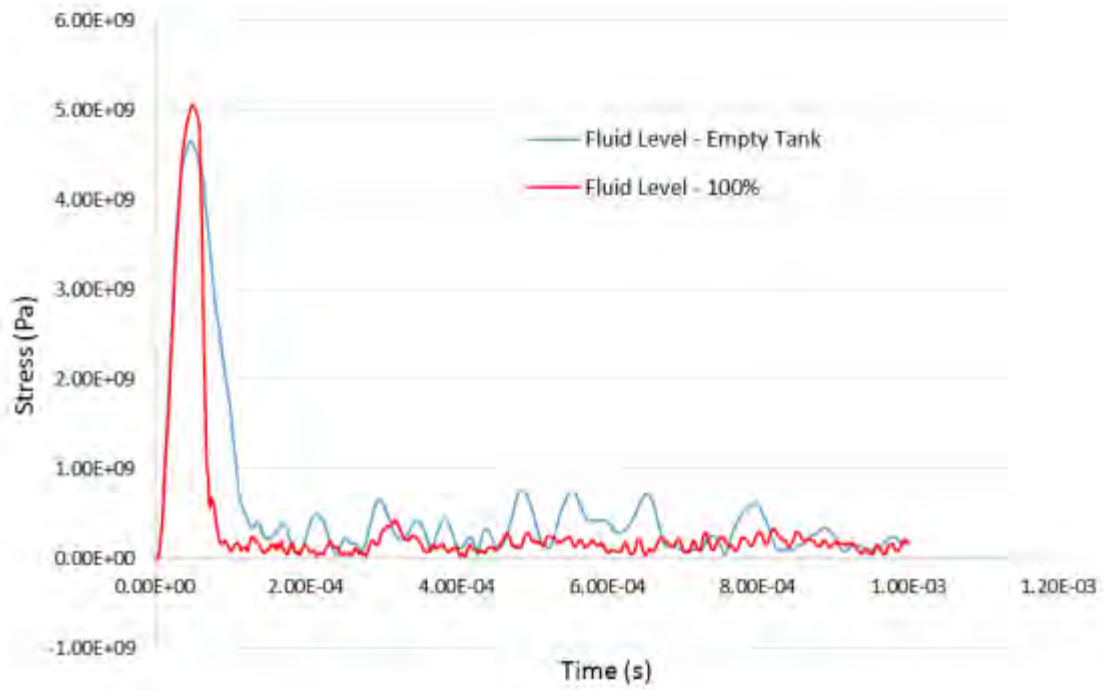


Figure 23. Entry Wall Effective Stress (Model 1).

It can be observed that the peak displacement of the entry wall for the 100% filled baseline Model 1 is higher at around 9 mm as compared to 7 mm for the empty tank. An interesting phenomenon observed for Model 1 was the entry wall displacing in the negative X-direction at around 0.06 ms after impact, which indicated the entry wall bulging outwards. The X-component velocity time history plot shown in Figure 22 indicated a much larger peak value of around 210 m/s in the negative X-direction right after projectile impact. This corresponded to the time where the entry wall starts to bulge. The subsequent velocity of the entry wall after deforming outwards was lower compared to that of the empty tank.

The effective entry wall stress, also known as the Von Mises Stress, reached a higher peak value of 5 GPa for Model 1 but over a shorter duration of time. Once the entry wall started to bulge outwards in response to the impact, the effective stress decreased significantly to a stabilised value of around 0.3 GPa. For the empty tank, the peak stress is slightly lower at 4.7 GPa but tapered off after a longer time at around 0.13 ms. Subsequent peak stress for the empty tank was observed to be higher at around 0.9 GPa.

b. Left Wall Response

The Z-direction corresponded to the major component of the left wall since the projectile impact onto the entry wall would displace the fluid near the impact point forming a cavity as shown in Figure 24. The displaced fluid pushed the walls of the tank outwards causing it to deform. The Left wall Z-displacement, Z-velocity and effective stress plots are shown in Figures 25, 26 and 27, respectively.

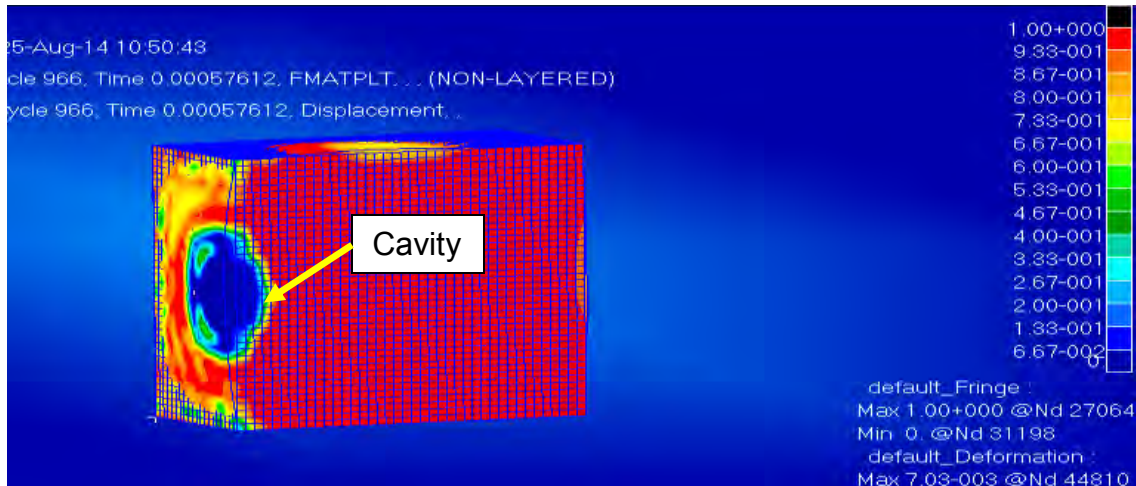


Figure 24. Cutaway view of Model 1 Material Fraction plot at 0.6 ms.

Model 1 left wall Z-displacement plot shown in Figure 25 indicated the left wall displacing in the negative Z-direction. The peak displacement of around 3.5 mm was much lesser than that of the entry wall, which registered a peak displacement of 9 mm. Similarly, the left wall experienced a much greater displacement as compared to an empty tank but with lesser oscillations due to the presence of fluid to damp out the fluctuations. The left wall Z-velocity plot shown in Figure 26, registered a peak value of around 15 m/s and stabilized to around 5 m/s whereas the empty tank had a larger peak value of 38 m/s with wild fluctuations. The left wall effective stress was observed to peak at around 0.15 GPa, close to its nominal value of 0.05 GPa while a much higher peak value of 0.42 GPa was observed for the empty tank.

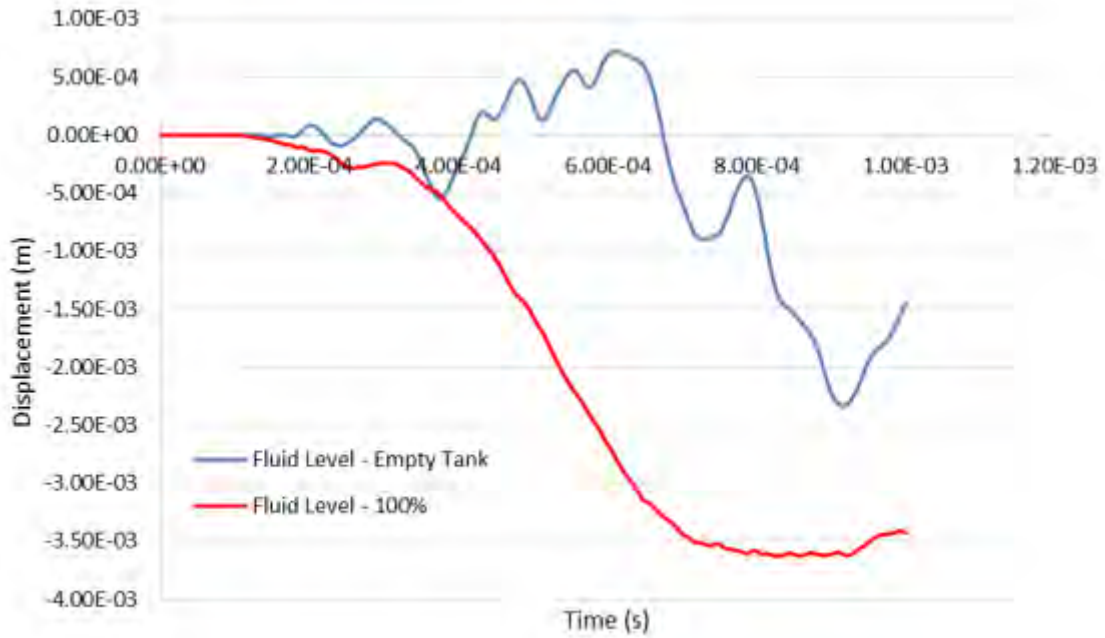


Figure 25. Left Wall Z-Displacement (Model 1).

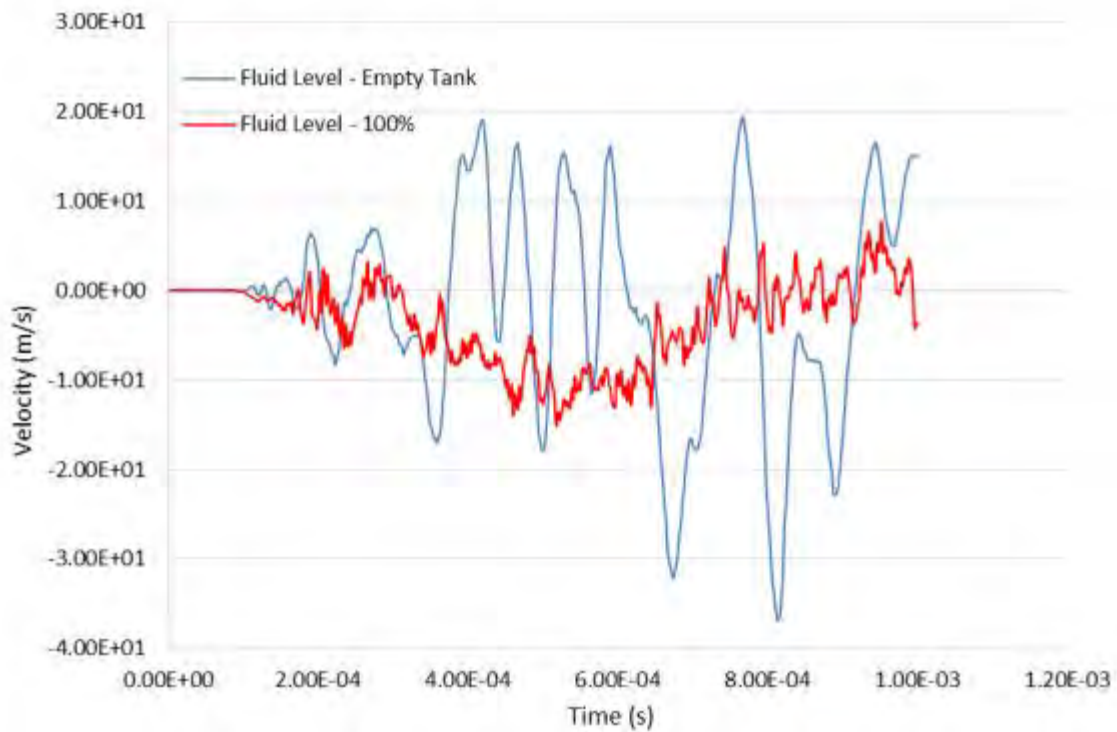


Figure 26. Left Wall Z-Velocity (Model 1).

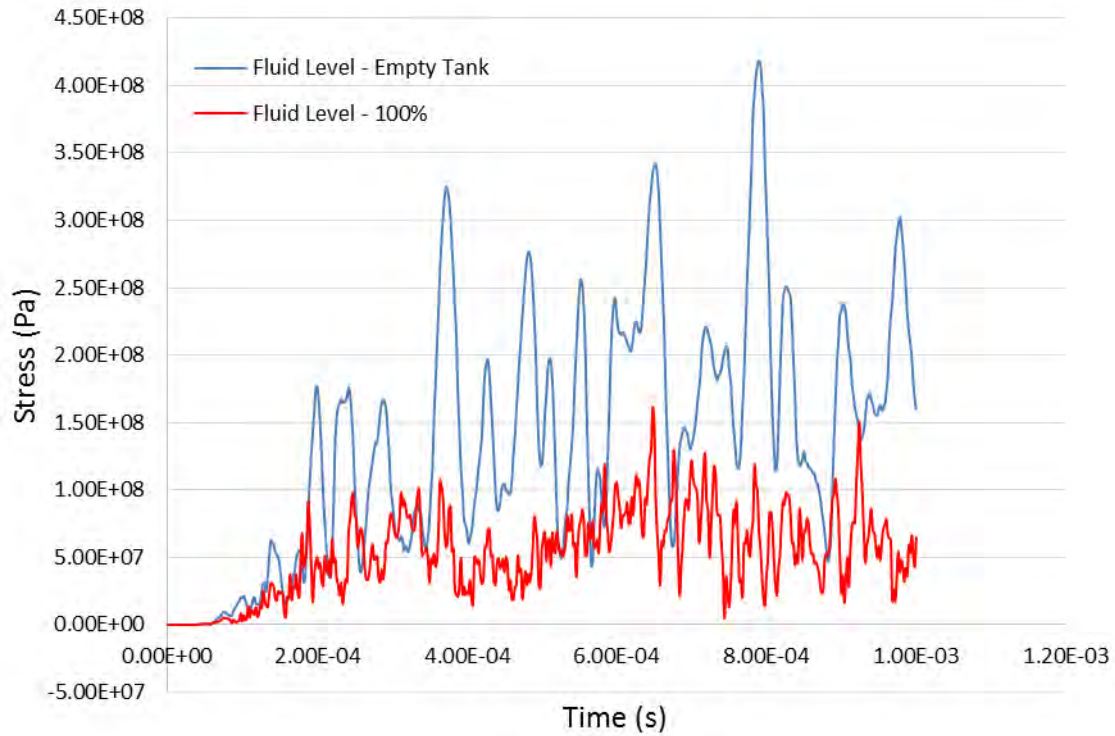


Figure 27. Left Wall Effective Stress (Model 1).

c. Exit Wall Response

Exit wall response to HRAM is of main interest in this study as it is an area on the aircraft where main structural components and load bearing members are likely to be located. Graphs for exit wall response plotted from data collected from the center node of the exit wall panel are shown in Figures 28, 29 and 30.

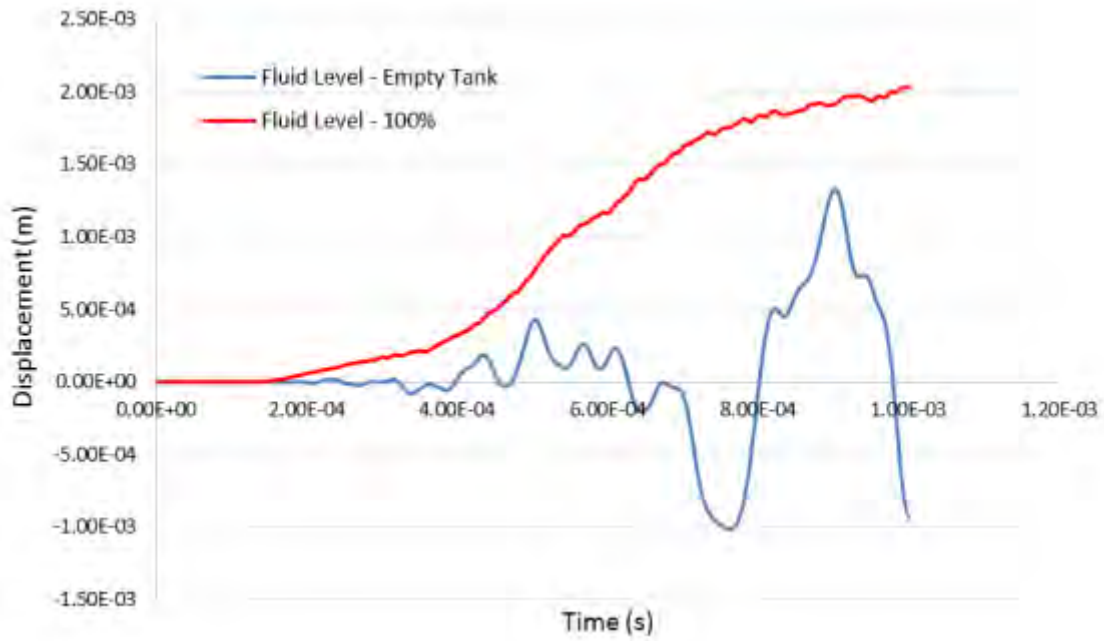


Figure 28. Exit Wall X-Displacement (Model 1).

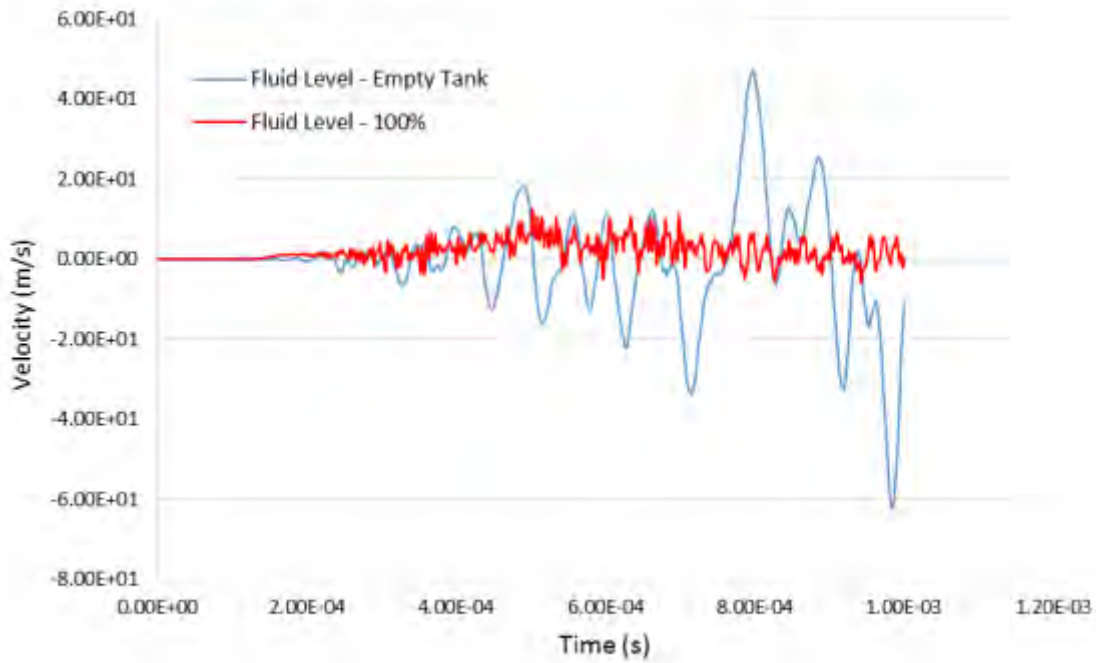


Figure 29. Exit Wall X-Velocity (Model 1).

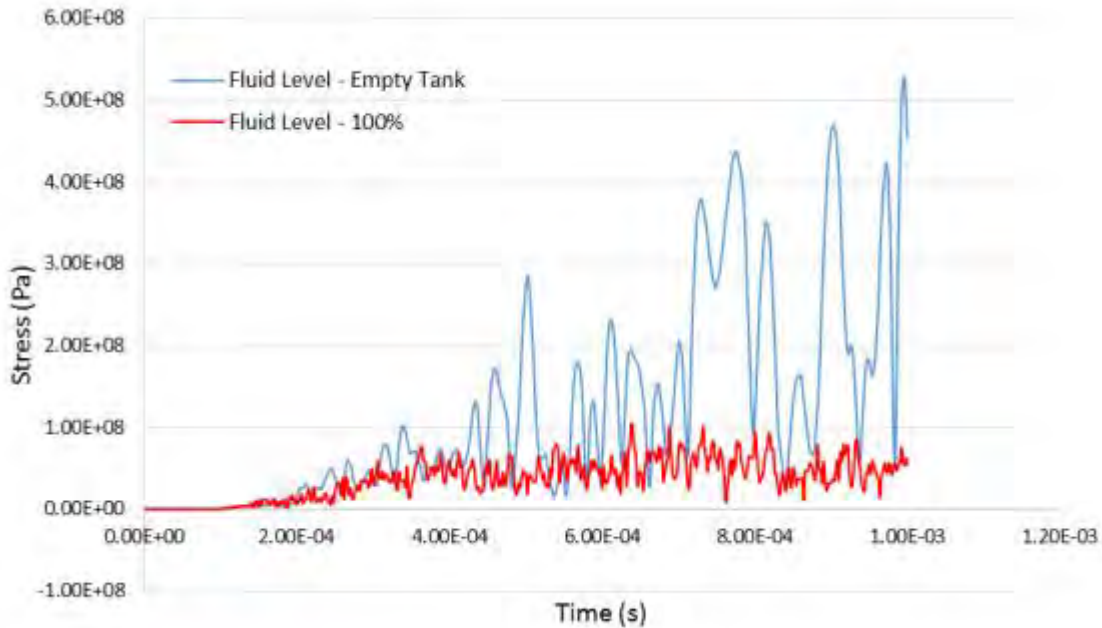


Figure 30. Exit Wall Effective Stress (Model 1).

The X-displacement plot in Figure 28 showed a peak displacement of around 2 mm experienced by the exit wall at the end of the simulation, a value which is much higher than that experienced by the empty tank. The exit wall for Model 1 started deforming earlier at approximately 0.13 ms. This is approximately the time where the initial shock wave due to projectile impact at the entry wall impinged onto the exit wall causing it to displace. The presence of fluid in the tank actually resulted in a much smaller velocity and effective stress at the exit wall. Peak stress at the center of the exit wall registered a much lower value of approximately 100 MPa as compared to 500 MPa for the empty tank. Fringe plot of entry wall effective stress at 0.12 ms and 0.2 ms shown in Figures 31 and 32 indicated the stress wave on the aluminium tank structure propagating radially outwards from the point of impact towards the edges of the entry wall where there would be a region of stress concentration before propagating to other panels of the tank.

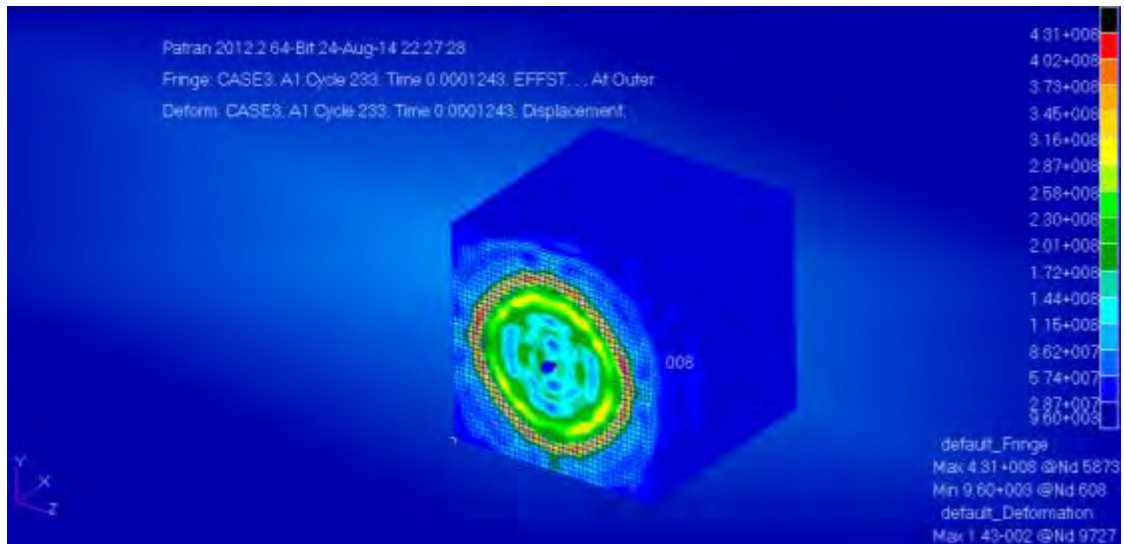


Figure 31. Effective Stress Fringe Plot at 0.12 ms (Model 1).

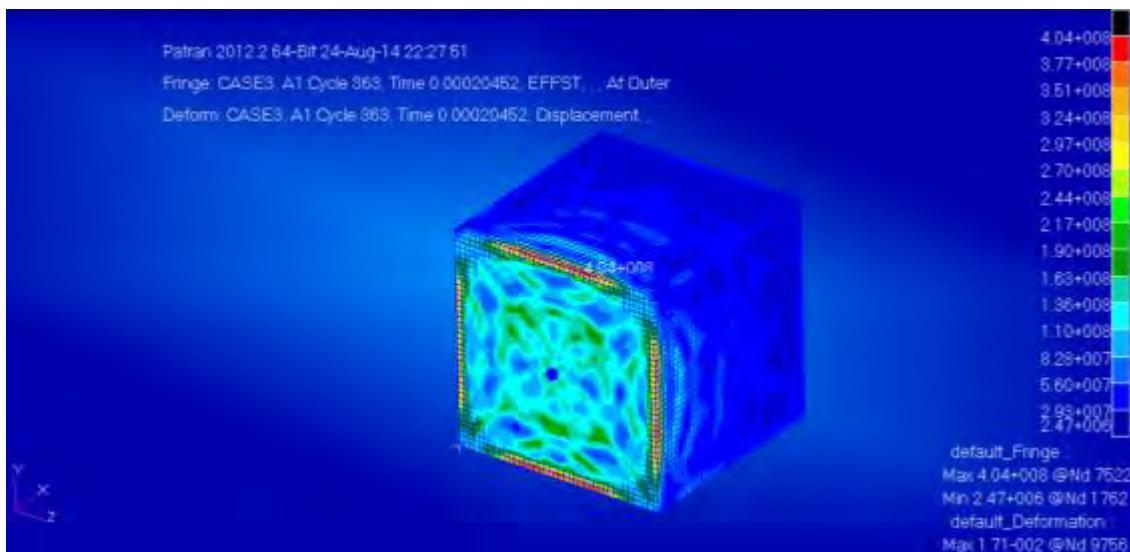


Figure 32. Effective Stress Fringe Plot at 0.2 ms (Model 1).

Besides the propagation of shock wave through the aluminium tank structure, a hemispherical shock wave was observed to propagate in the fluid towards the exit wall. This ram pressure generated by the impact of the projectile in the shock phase was recorded by the three fluid tracer elements whose locations were shown in Figure 20 previously.

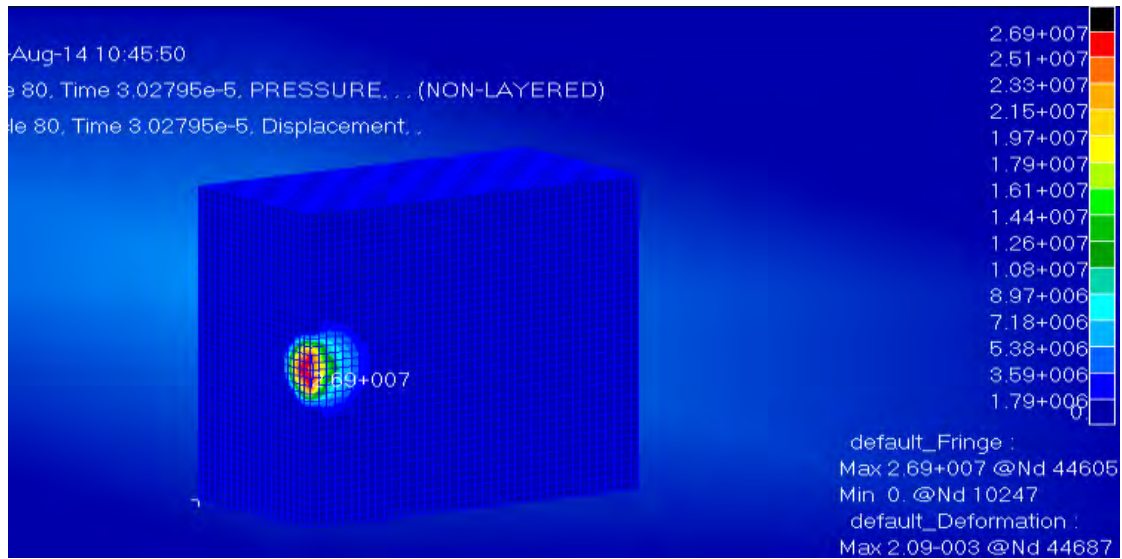


Figure 33. Shock pressure propagating from impact point at 0.03 ms (Model 1).

A pressure fringe plot of the shock wave propagation from the impact point is shown in Figure 33. Data for the ram pressure collected by the fluid element pressure tracer were plotted in Figure 34. The graph showed a peak pressure of 7 MPa recorded by fluid Gauge 1 located nearest to the impact point. This ram pressure was found to weaken significantly as it propagated through the fluid medium, reducing to a magnitude of 0.9 MPa near the exit wall recorded by fluid gauge 3. As the shock wave moved across the fluid towards the exit wall, its energy would be dissipated across a larger volume of fluid thereby resulting in a drastic reduction in ram pressure. The rapid weakening of the initial shock wave due to geometric expansion about the impact point and its short duration indicated that the left and exit walls of the tank are unlikely to experience significant pressures from the impact shock wave.

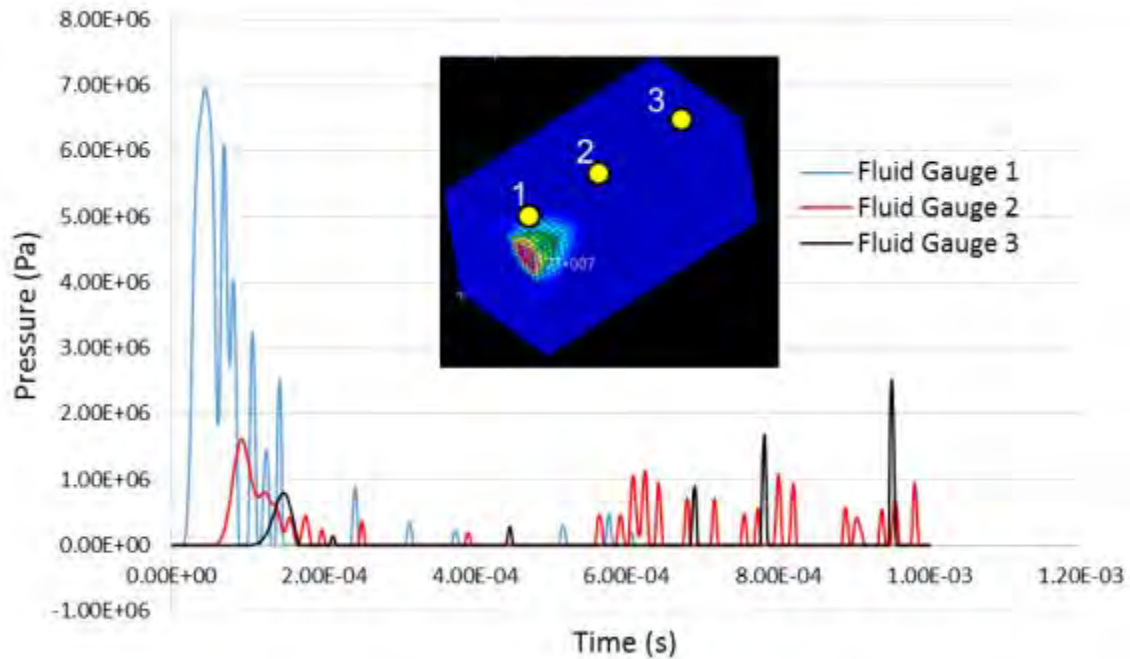


Figure 34. Shock pressure generated by 300 m/s spherical projectile (Model 1).

2. Baseline Model 2

Simulation for baseline Model 2 was set up for a 100% water filled aluminium tank of 2 mm thickness, with initial position of the spherical steel projectile of mass 4 grams and diameter 10 mm, centered and flushed against the inner surface of the entry wall, given an initial velocity of 250 m/s. Model 2 was developed to assist in understanding the structural response of the tank walls during the drag and cavitation phase of HRAM. The event was simulated for real time of 2 ms with a sampling rate of 2 μ s. All displacement, velocity and effective stress values plotted were obtained from the center node or element of the tank walls. Since the collapse of the cavity would most likely occur at a much later time, the cavitation collapse pressure and its subsequent effect on the tank walls would be omitted from this study. Instead, the effects on tank walls due to drag phase pressure and the formation of cavity in the fluid would be of main interest.

a. Entry Wall Response

The entry wall response for Model 2 is shown in Figures 35, 36 and 37.

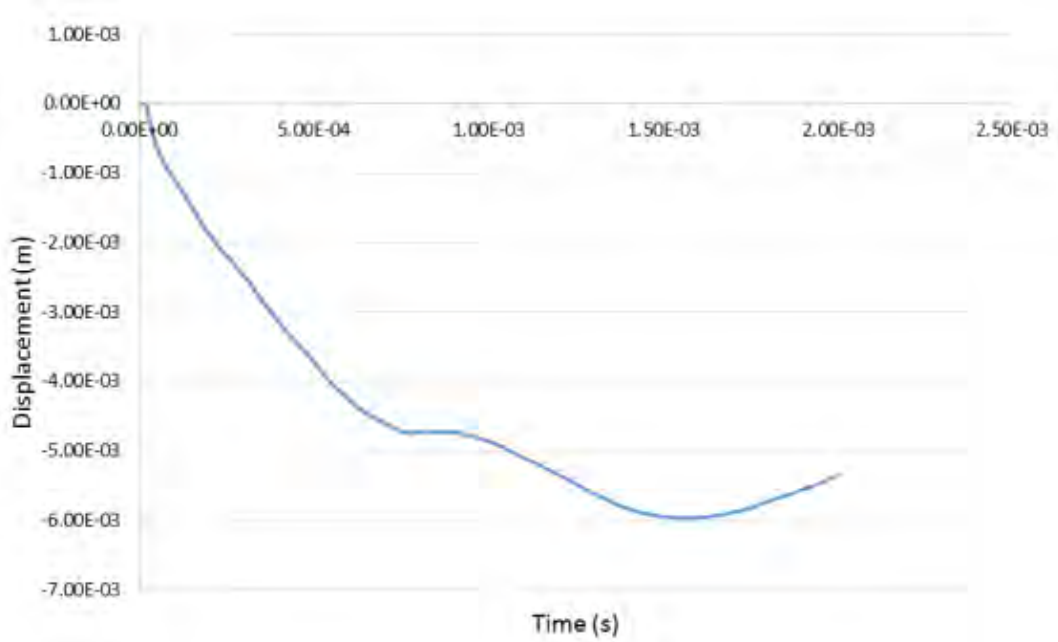


Figure 35. Entry Wall X-Displacement (Model 2).

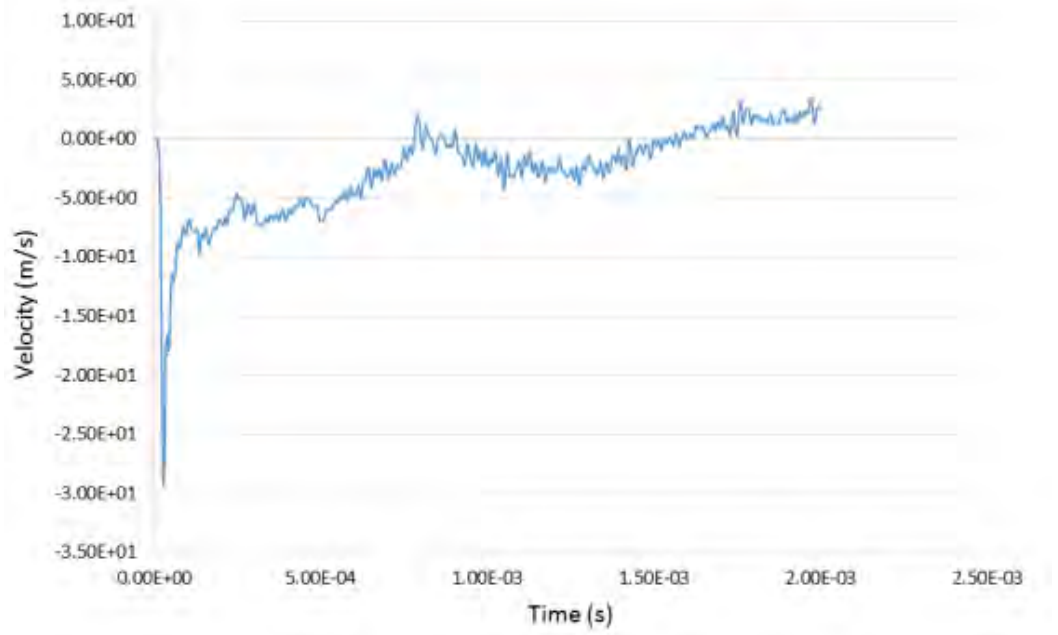


Figure 36. Entry Wall X-Velocity (Model 2).

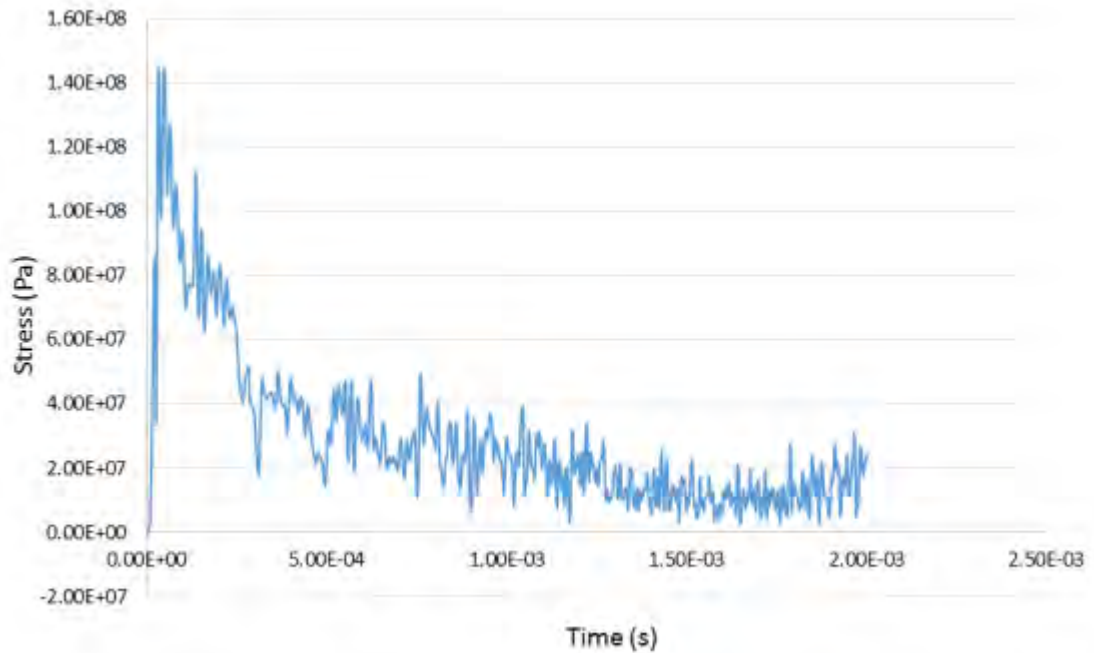


Figure 37. Entry Wall Effective Stress (Model 2).

As the projectile moved towards the exit wall in the positive X-direction, the fluid is being accelerated towards the entry wall after flowing over the projectile in the opposite direction. A peak displacement of 6 mm was experienced by the entry wall, occurring at approximately 1.5 ms into the simulation. The X-velocity of the entry wall shown in Figure 36 is pretty similar to that of Model 1, with velocity peaking at around 30 m/s for a short duration at the start of the simulation with the projectile initial velocity of 250 m/s. Subsequently, the velocity of the entry wall was reduced to below 5 m/s as the projectile moves closer to the exit wall of the tank. Similarly for effective stress, the entry wall experienced a peak stress of around 145 MPa initially for a very short duration before decreasing to around 20 MPa as the projectile reaches the exit wall.

b. Left Wall Response

Figures 38, 39 and 40 show the left wall Z-displacement, Z-velocity and effective stress at the center of the wall for Model 2.

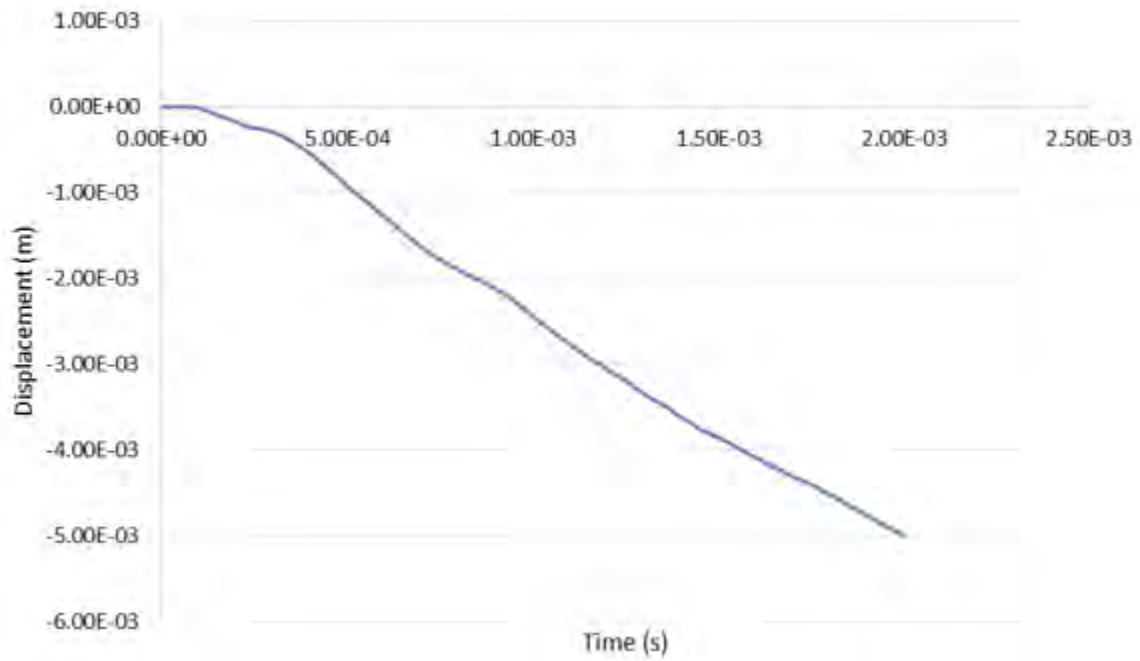


Figure 38. Left Wall Z-Displacement (Model 2).

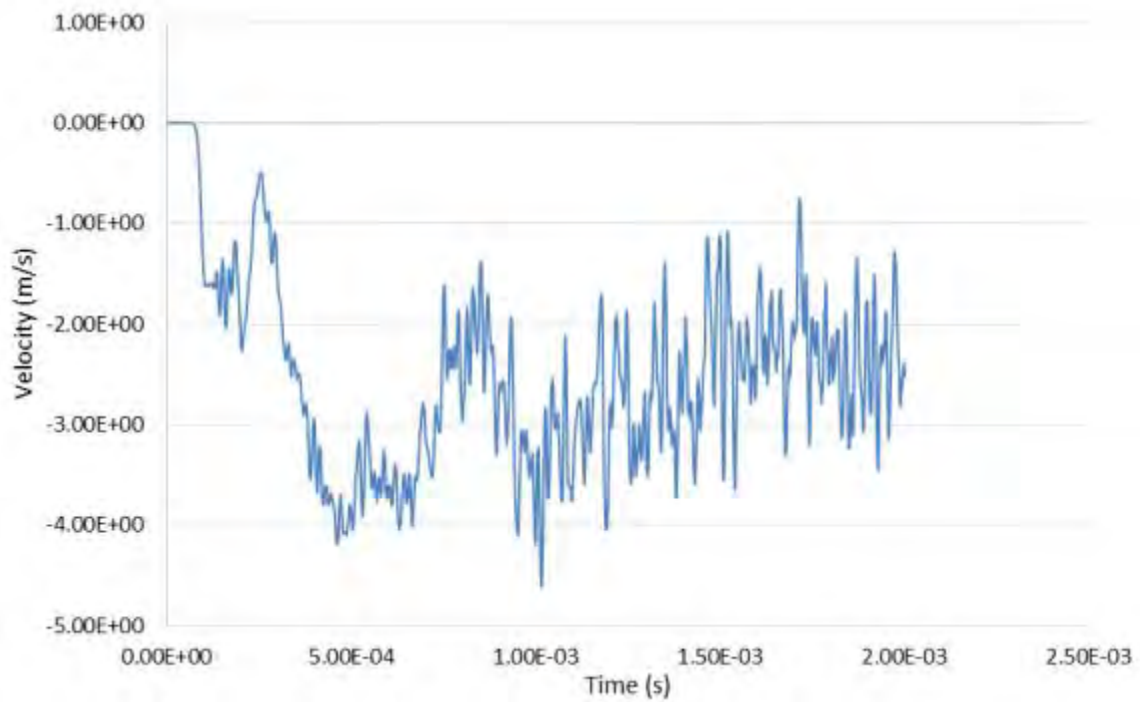


Figure 39. Left Wall Z-Velocity (Model 2).

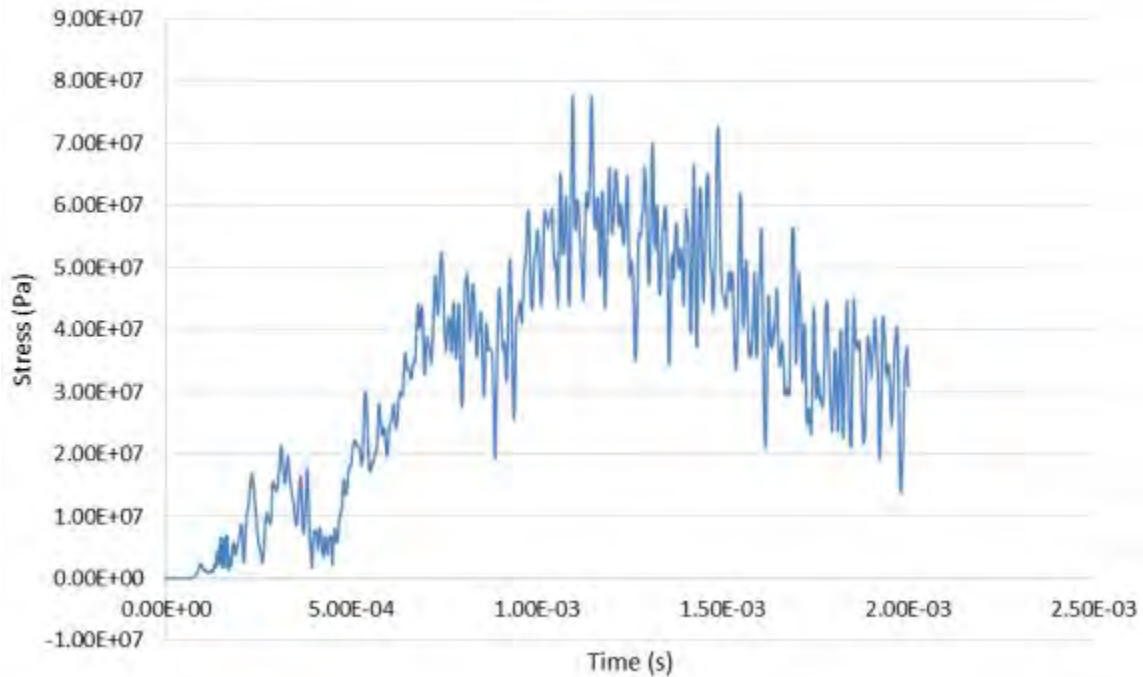


Figure 40. Left Wall Effective Stress (Model 2).

With the growth of the cavity as the projectile traverse through the fluid, the left wall was pushed outwards, resulting in a peak negative Z-displacement of 5 mm. The left wall started to deform slightly later than the entry wall at approximately 0.15 ms. The left wall Z-velocity recorded a value of around 3 m/s throughout the drag phase. The effective stress at the middle of the left wall had a peak value of 80 MPa occurring at 1.2 ms, which corresponded to the time where the projectile is in the middle of the tank. Subsequently as the projectile passed the middle mark, the effective stress decreased to around 40 MPa.

c. Exit Wall Response

Figures 41, 42 and 43 showed the exit wall X-displacement, X-velocity and effective stress time history plot, respectively. The exit wall response graphs were plotted from start of simulation up to 1.5 ms just before the projectile impact the exit wall.

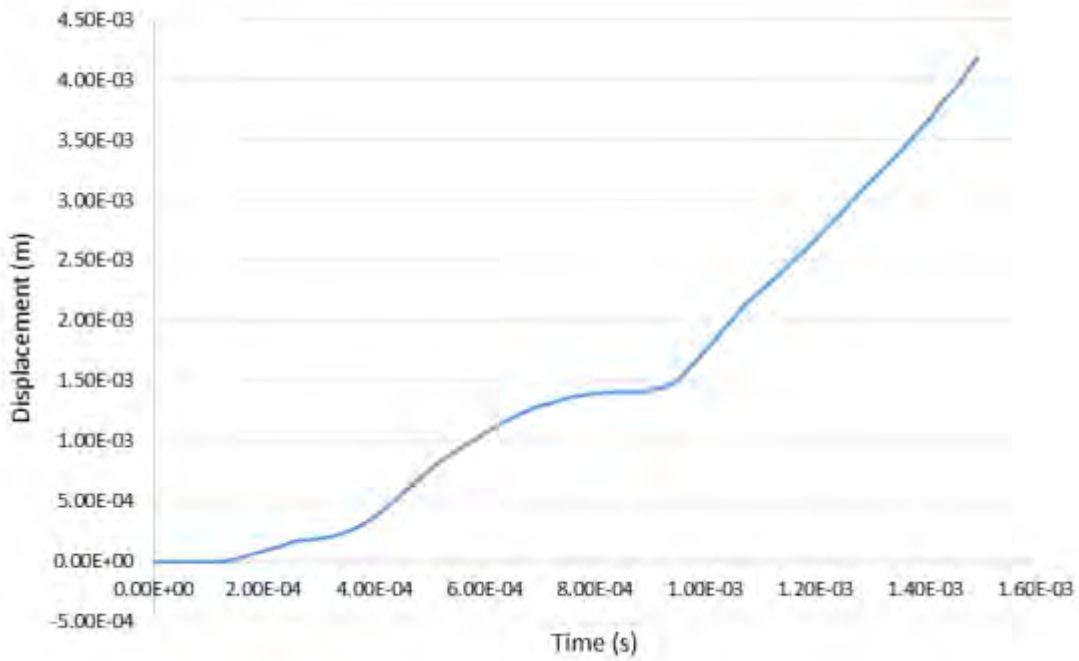


Figure 41. Exit Wall X-Displacement (Model 2).

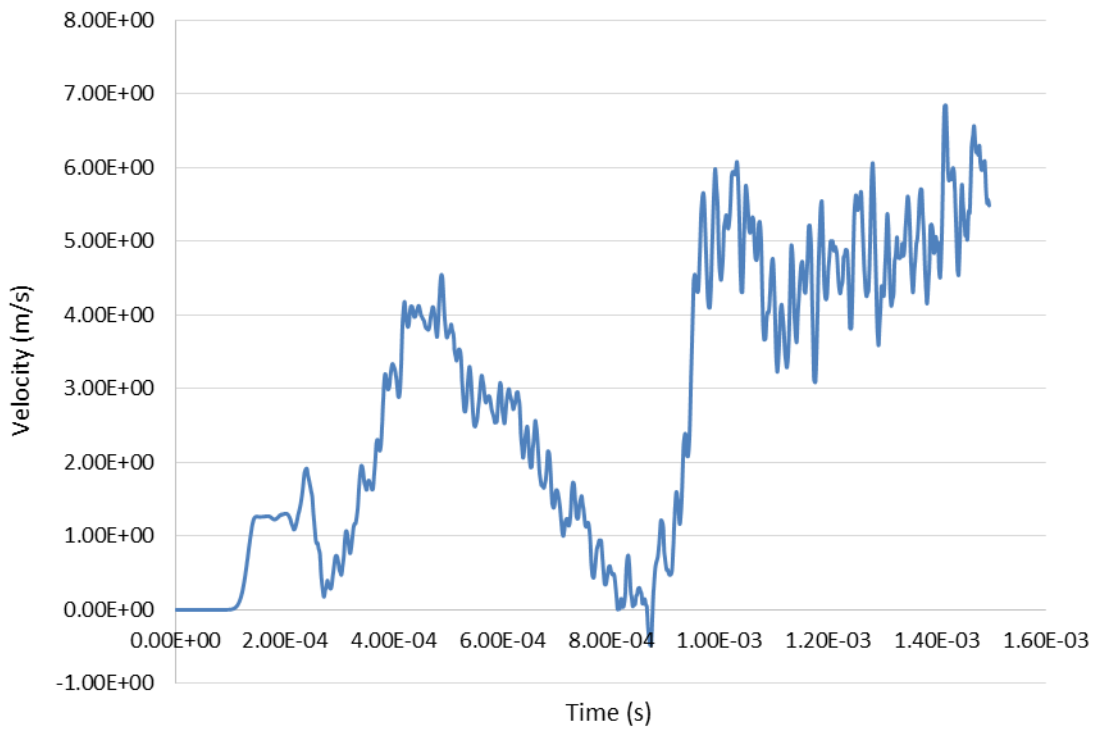


Figure 42. Exit Wall X-Velocity (Model 2).

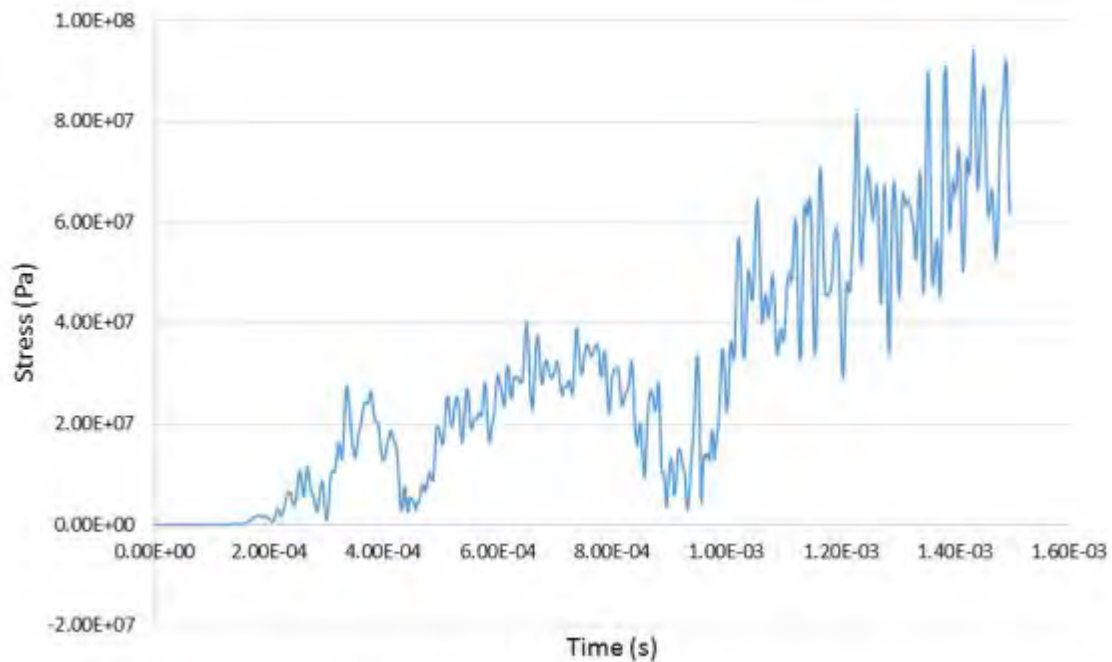


Figure 43. Exit Wall Effective Stress (Model 2).

Exit wall started to move and deform at approximately 0.13 ms into the simulation due to the initial shock wave impinging onto the exit wall as shown in Figure 41. At approximately 1 ms into the simulation, the rate of displacement of the exit wall registered an increase as can be observed from the steeper gradient of the displacement time-history plot of the exit wall. Correspondingly, there was a sharp increase in exit wall X-velocity after 1 ms as illustrated in Figure 42. This is due to the projectile approaching the exit wall and the high pressure region in front of the projectile during the drag phase exerting a greater pressure and pre-stressing the exit wall before projectile impact. The pre-stressing of the exit wall before the projectile impact is further illustrated in Figure 44. Likewise for the exit wall velocity and effective stress shown in Figures 42 and 43, respectively, the peak value occurred after 1 ms when the projectile approached the exit wall. The exit wall registered a peak velocity of 7 m/s and a peak stress of around 94 MPa prior to projectile impact.

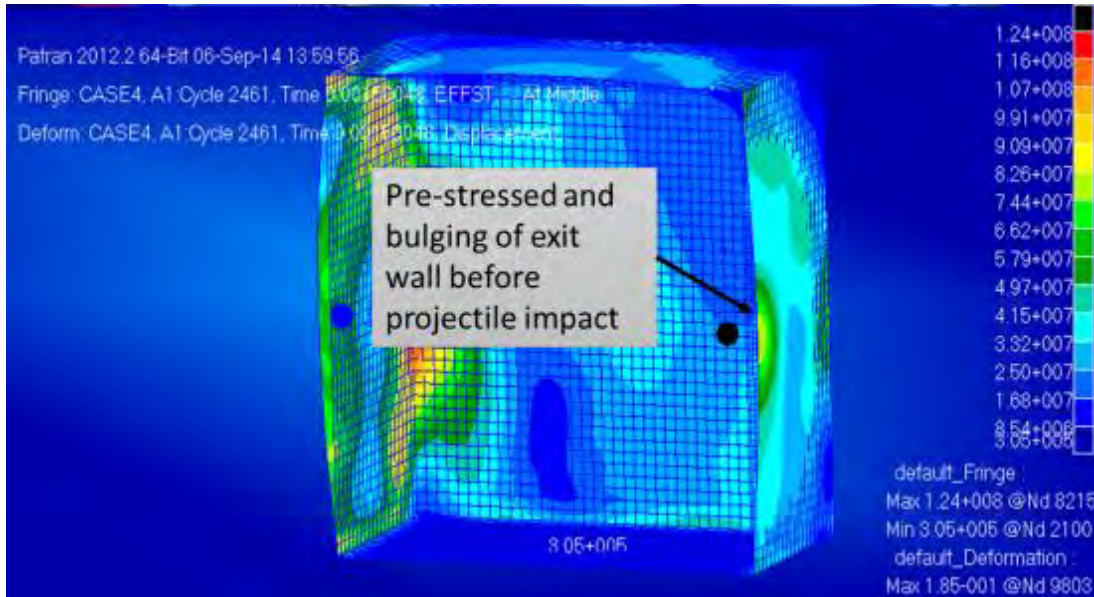


Figure 44. Effective stress fringe plot showing pre-stressed exit wall during drag phase (Model 2).

Figure 45 shows the drag phase fluid pressure recorded by fluid gauge 2 located in the middle of the tank near the shot line. A peak pressure of around 5 MPa was registered as the projectile approached fluid gauge 2 at around 0.5 ms. As observed from Figure 45, the drag phase pressure rise was gradual and occurred over a longer period of time as compared to the initial shock phase pressure. As the projectile moved past fluid gauge 2, the pressure recorded went to zero, indicating the formation of a cavity behind the projectile path. The cavitation phase of HRAM, which include the oscillation and the subsequent collapse of the cavity is not part of this study since it would occur at a later time after the simulation had ended.

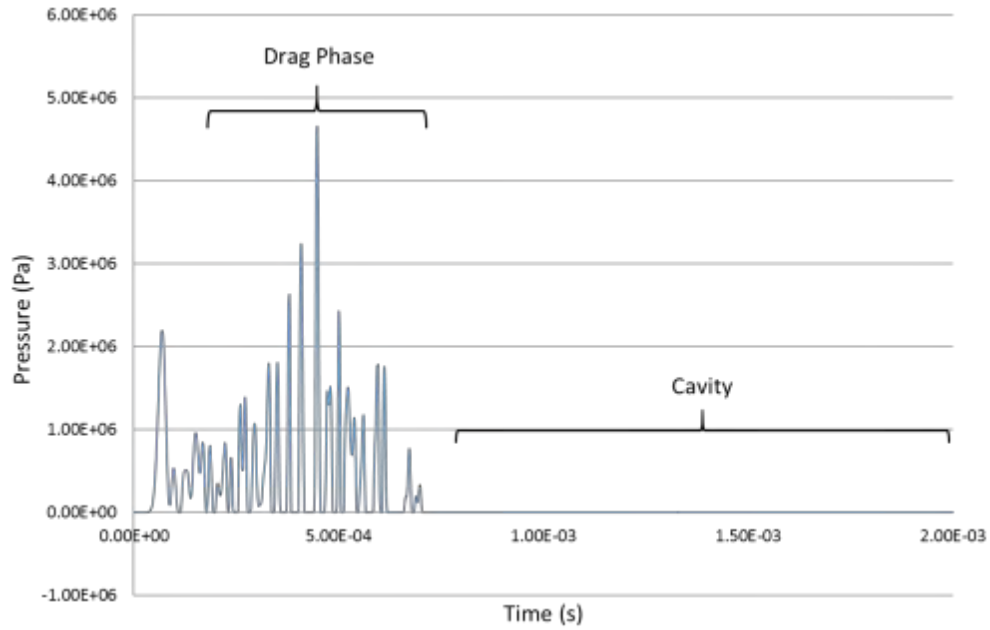


Figure 45. Drag phase fluid pressure output from fluid gauge 2 (Model 2).

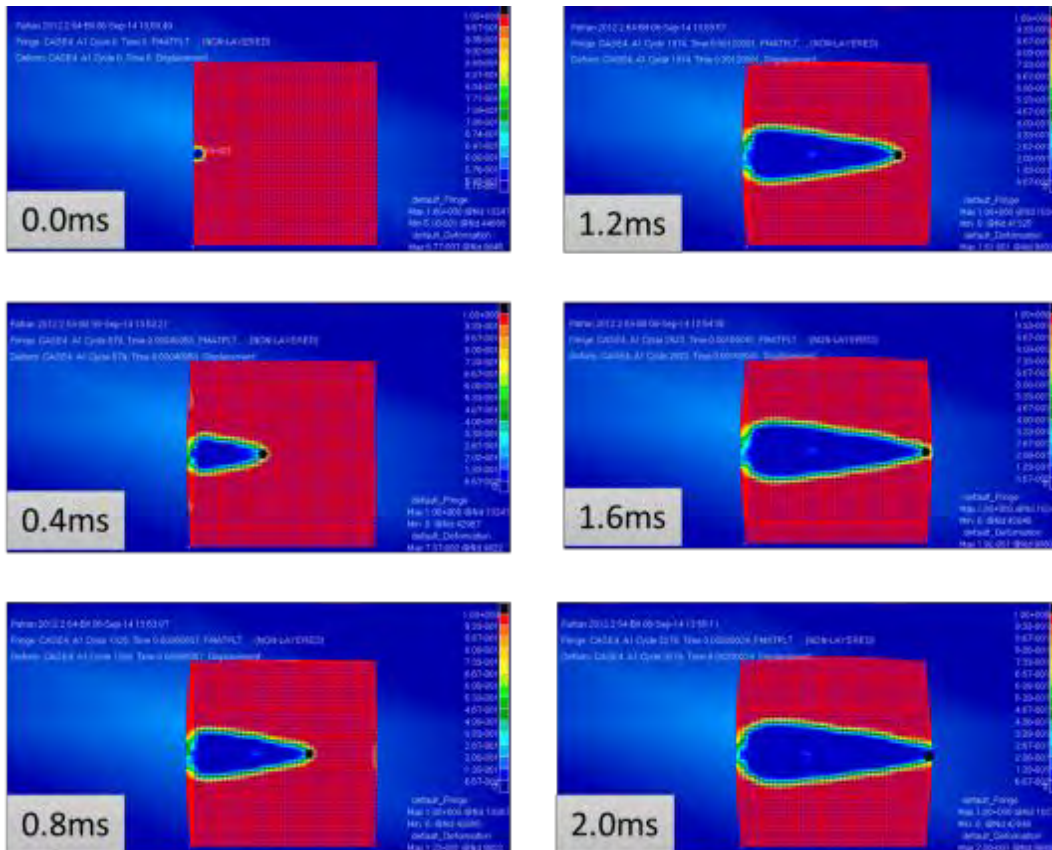


Figure 46. Model 2 cavity evolution.

An interesting parameter that the numerical simulation provided for drag phase analysis was the cavity evolution when the projectile traverses the fluid towards the exit wall. The Model 2 simulation fringe plot of material fraction in the fluid Euler mesh obtained at 0.4 ms interval is presented in Figure 46. The maximum cavity diameter measured from the fringe plot at 2ms was found to be approximately 60 mm as illustrated in Figure 47. The bulging of the entry and exit wall can also be observed in Figure 47.

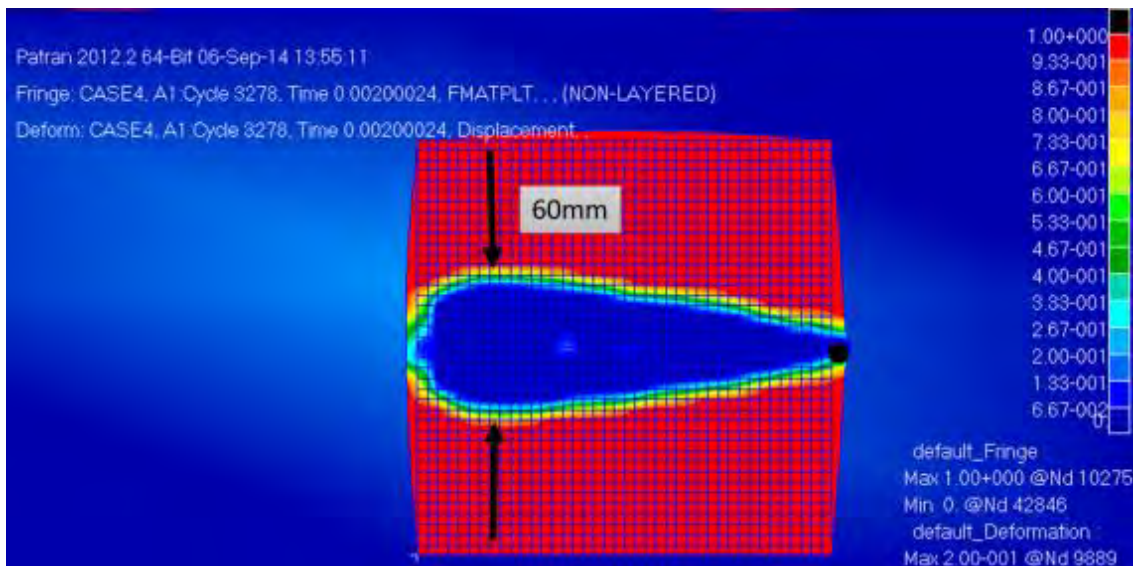


Figure 47. Model 2 maximum cavity diameter measured from material fraction fringe plot.

B. PARAMETRIC STUDIES CONDUCTED FOR MODEL 1 AND MODEL 2

As part of the objective of this thesis, parametric studies were conducted on Model 1 and 2 to understand how different factors could affect the exit wall response. For Model 2, even though the simulation end time was set at 2 ms, peak values that were tabulated were chosen from the start of simulation up till the point before the projectile impact the exit wall. All graphs generated for the entry, left and exit wall response together with the fluid pressures obtained from fluid gauge 2 for the different impact conditions were attached in Appendix A to Appendix F for reference.

1. Variation in Fluid Levels

The fluid level was varied for Model 1 and 2 to study the effects of free surface on the shockwave propagation and the resultant exit wall response. With the rest of the parameters and impact conditions kept constant, the fluid level was varied for 80% and 60% fluid levels. This was made possible by adjusting the initial condition of the Euler elements that would be filled with water as shown in Figure 48.

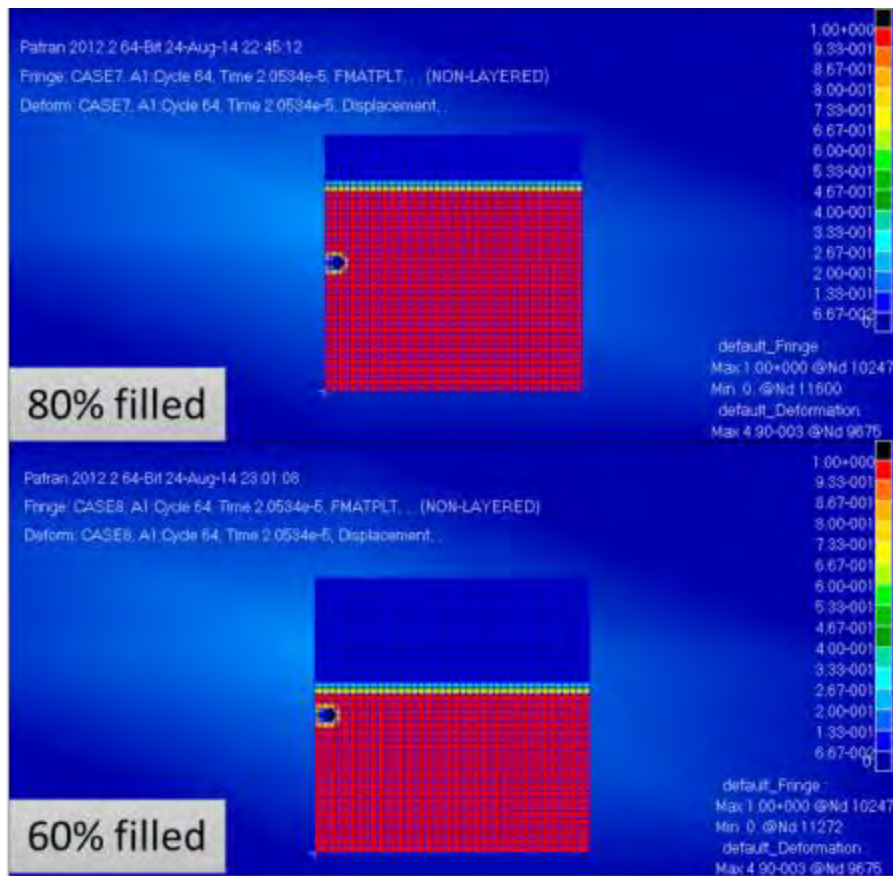


Figure 48. Material fraction plot of initial condition of Euler mesh for different fluid levels.

The exit wall response and fluid pressures for Model 1 and Model 2 were tabulated in Table 4 and Table 5, respectively.

Table 4. Model 1 exit wall response to varying fluid levels

Parameters	% Filling Level	Maximum Displacement (m)	Peak Stress (MPa)	Shock phase Ram Pressure from Fluid Gauge 2 (MPa)	Peak Velocity (m/s)
Fluid Level Variation	100	0.002035	104.802	1.61365	12.7263
	80	0.002027	170.765	1.3469	19.1264
	60	0.001714	240.244	0.45185	19.2642

Table 5. Model 2 exit wall response to varying fluid levels

Parameters	% Filling Level	Maximum Displacement (m)	Peak Stress (MPa)	Peak Fluid Drag Pressure from Fluid Gauge 2 (MPa)	Peak Velocity (m/s)
Fluid Level Variation	100	0.00471648	94.074	4.64315	6.85024
	80	0.00398923	102.79	4.27619	6.23109
	60	0.00274174	109.94	3.0948	4.98805

For Model 1, it was observed that lower fluid levels resulted in a lower exit wall displacement but higher velocity and stress. The shock phase ram pressure was also reduced significantly from 1.61 MPa in the fully filled tank to a mere 0.45 MPa in the 60% filled tank. This was due to the presence of free surface distorting the hemispherical formation of the shock wave at the impact point.

The reduction of exit wall displacement is more evident in Model 2 from 4.7 mm for the fully filled tank to 2.7 mm for the 60% filled tank. The peak stress at the exit wall for the three different fluid levels see a lesser variation as compared to Model 1. Peak drag phase pressure was also observed to be higher for 100% filled tank at 4.63 MPa compared to 3.09 MPa for 60% filling level.

2. Variation in Projectile Mass

Projectile mass was varied from two grams to six grams to study its effect on exit wall response. Results were tabulated in Tables 6 and 7.

Table 6. Model 1 exit wall response to varying projectile mass

Parameters	Mass (g)	Maximum Displacement (m)	Peak Stress (MPa)	Shock phase Ram Pressure from Fluid Gauge 2 (MPa)	Peak Velocity (m/s)
Projectile Mass	2	0.00128098	70.5868	1.0475	7.32631
	4	0.00203513	104.802	1.61365	12.7263
	6	0.00243127	172.462	2.02303	16.4221

Table 7. Model 2 exit wall response to varying projectile mass

Parameters	Mass (g)	Maximum Displacement (m)	Peak Stress (MPa)	Peak Fluid Drag Pressure from Fluid Gauge 2 (MPa)	Peak Velocity (m/s)
Projectile Mass	2	0.00295588	68.2312	2.68013	4.07203
	4	0.00471648	125.866	4.64315	8.3379
	6	0.00478961	170.508	4.52462	13.4958

Model 1 results presented in Table 6 showed that projectile mass have a strong effect on the exit wall response during the initial shock phase. Peak displacement, stress, velocity and ram pressures were all found to increase significantly even though the difference in projectile mass for each case was only two grams. By increasing the mass from four grams to six grams, the peak stress recorded a considerable increase from 105 MPa to 172 MPa.

However for Model 2, the variation in projectile mass on exit wall response was not entirely conclusive. Figure 49 showed the exit wall X-displacement plot for Model 2 comparison for the different projectile mass. The dotted line indicated the moment just before the projectile impact the exit wall. It can be observed that the peak displacement of the exit wall just before projectile impact registered only a minute difference, 4.79 mm compared to 4.72 mm between the four and six grams projectile. The only difference that could be observed from Figure 49 is that the heavier six grams projectile reaches the exit wall earlier than the lighter

four grams projectile. The two grams projectile most likely did not have enough momentum to overcome the drag of the fluid to reach the exit wall at the end of the simulation at 2 ms and was omitted from this discussion. The six grams projectile was observed to reach the exit wall at 1.28 ms whereas the four grams projectile took 1.6 ms to travel the same distance.

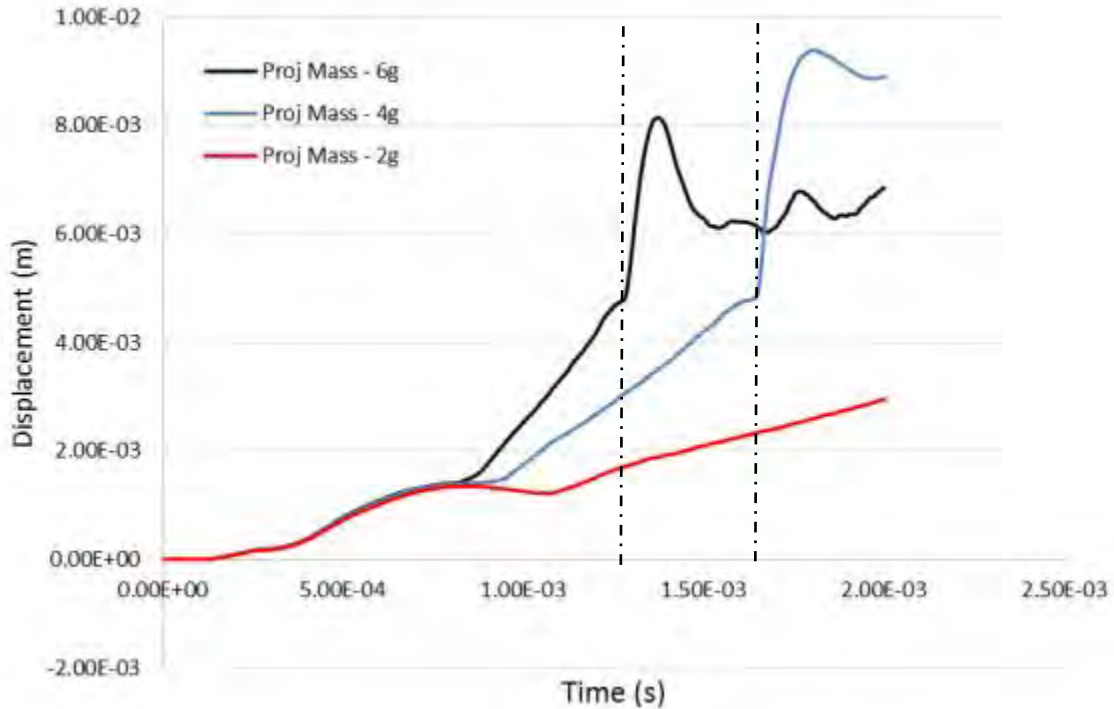


Figure 49. Exit Wall X-Displacement for different projectile mass (Model 2).

The peak fluid drag pressure was also found to be of similar magnitude for the four grams and six grams projectile. Nevertheless, some correlation was observed for the peak stress and velocity at the exit wall for Model 2 where a higher projectile mass resulted in a higher peak stress and velocity.

3. Variation in Projectile Initial Velocity

In this parametric study, the initial velocity of the projectile was varied from 100 m/s to 500 m/s. The results for Model 1 and 2 exit wall response were tabulated in Tables 8 and 9, respectively.

Table 8. Model 1 exit wall response to varying projectile initial velocity.

Parameters	Projectile Velocity (m/s)	Maximum Displacement (m)	Peak Stress (MPa)	Shock phase Ram Pressure from Fluid Gauge 2 (MPa)	Peak Velocity (m/s)
Projectile Velocity	100	0.000660054	29.5669	0.46631	2.78716
	300	0.00203509	104.802	1.61365	12.7263
	500	0.00255664	406.831	2.39176	34.2576

Table 9. Model 2 exit wall response to varying projectile initial velocity.

Parameters	Projectile Velocity (m/s)	Maximum Displacement (m)	Peak Stress (MPa)	Peak Fluid Drag Pressure from Fluid Gauge 2 (MPa)	Peak Velocity (m/s)
Projectile Velocity	100	0.00123423	32.48	2.72262	1.61611
	250	0.00471674	125.866	4.64315	8.3379
	500	0.00589209	157.726	10.6443	20.3856

Model 1 results indicated a strong influence of projectile velocity on the exit wall response and fluid ram pressures. A projectile impacting the tank at a higher velocity of 500 m/s resulted in a drastic increase in peak stress and velocity at the exit wall. The ram pressure from projectile impact saw an increase from 1.61 MPa for the baseline Model to 2.39 MPa for 500 m/s projectile.

The exit wall X-displacement and drag phase pressure for different projectile velocities was shown in Figure 50 and 51, respectively. The dotted line in Figure 50 corresponded to the time where the projectile reached the exit wall.

The projectile with velocity of 100 m/s did not have sufficient momentum to reach the exit wall at the end of simulation. It was evident that the exit wall response and fluid pressure were even more sensitive to projectile velocity for Model 2. With an increase in velocity from 250 m/s to 500 m/s, the displacement of the exit wall saw an increase from 4.72 mm to 5.89 mm. Similarly, drag phase pressure was more than doubled due to the increasing projectile velocity from 250 m/s to 500 m/s.

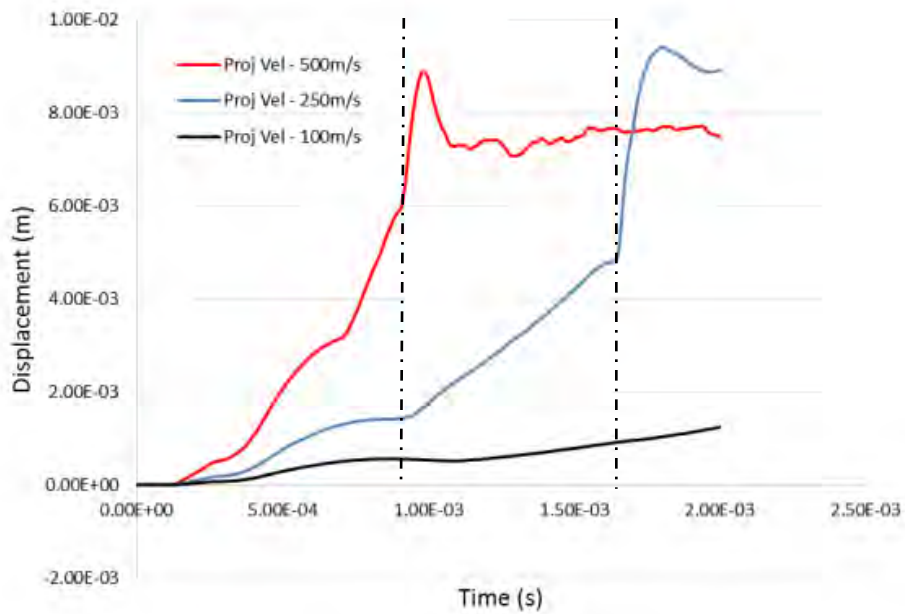


Figure 50. Exit wall X-displacement for different projectile velocity (Model 2).

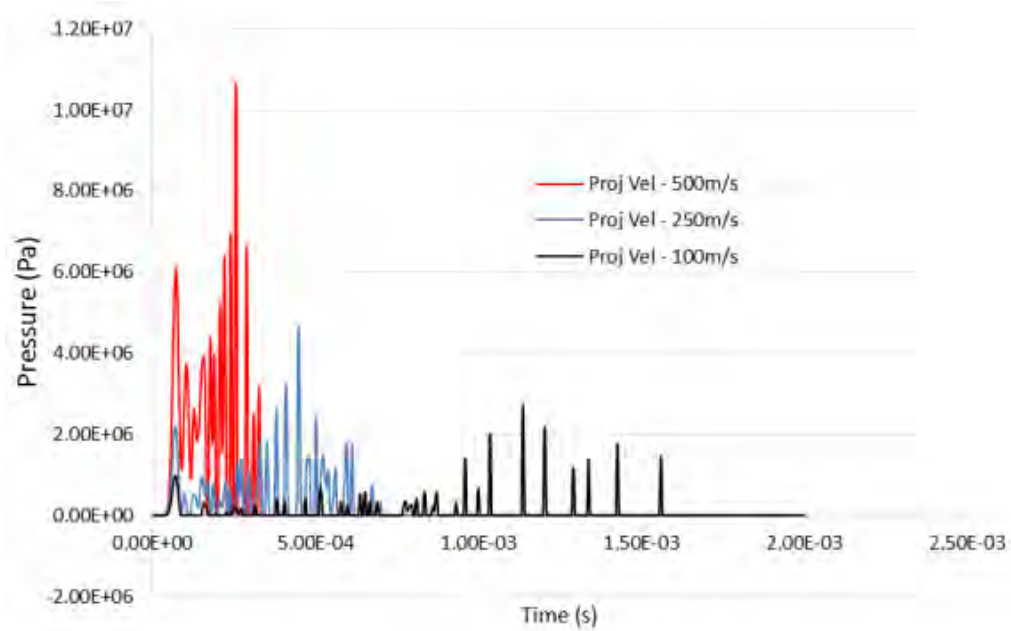


Figure 51. Drag phase pressure for different projectile velocities (Model 2).

4. Variation in Tank Material Modulus

Tank material elastic modulus was varied for this study, while keeping the rest of the parameters constant. Elastic modulus E was varied from 40 GPa to 70 GPa, and results were tabulated in Tables 10 and 11.

Table 10. Model 1 exit wall response for varying tank material modulus.

Parameters	Elastic Modulus (GPa)	Maximum Displacement (m)	Peak Stress (MPa)	Shock phase Ram Pressure from Fluid Gauge 2 (MPa)	Peak Velocity (m/s)
Tank Material Modulus	40	0.00180311	72.9672	1.04987	11.6687
	70	0.00203509	104.802	1.61365	12.7263
	100	0.00181285	142.944	2.0287	9.30065

Table 11. Model 2 exit wall response for varying tank material modulus.

Parameters	Elastic Modulus (GPa)	Maximum Displacement (m)	Peak Stress (MPa)	Peak Fluid Drag Pressure from Fluid Gauge 2 (MPa)	Peak Velocity (m/s)
Tank Material Modulus	40	0.00502539	73.4471	5.35703	9.39117
	70	0.00471648	125.866	4.64315	8.3379
	100	0.00435498	152.739	3.00561	7.25874

Examination of the data presented in Table 10 revealed no particular trend for displacement and velocity for the different elastic modulus. The X displacement plot for the exit wall, illustrated in Figure 52, showed that the 100 GPa tank had a larger displacement initially but was eventually overtaken by tanks with lower modulus. This is an interesting phenomenon, which warrants further investigation. Values for peak stress and shock phase ram pressure for Model 1 did see a correlation with the stiffer tank with modulus of 100 GPa experiencing a higher stress and larger ram pressure at 143 MPa and 2.03 MPa, respectively.

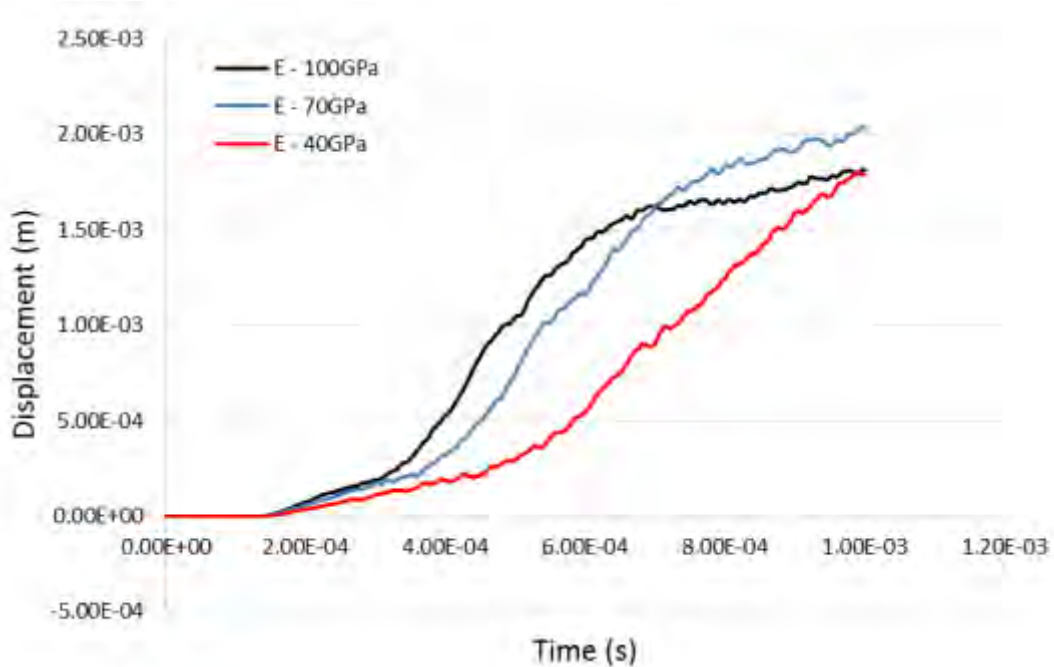


Figure 52. Exit wall X-displacement for different elastic modulus (Model 1).

Moving to Model 2, the effect of varying Young’s modulus was minimal for the exit wall displacement and velocity. However, the correlation for peak stresses and drag phase pressures was more apparent, with the stiffer tank experiencing a larger stress but smaller drag pressures.

5. Variation in Tank Material Density

The next parametric study conducted on Model 1 and 2 was the variation in the density of the tank’s material. With the baseline Model 1 and 2 having the density of aluminum at 2,700 kg/m³, material density was changed to 1,500 kg/m³ and 4,500 kg/m³ to evaluate its effect on the structural response at the exit wall. Results obtained were summarized in Tables 12 and 13.

Table 12. Model 1 exit wall response for varying tank material density.

Parameters	Density (kg/m ³)	Maximum Displacement (m)	Peak Stress (MPa)	Shock phase Ram Pressure from Fluid Gauge 2 (MPa)	Peak Velocity (m/s)
Tank Material Density	1500	0.00187647	93.5504	2.08677	13.448
	2700	0.00203509	104.802	1.61365	12.7263
	4500	0.00151676	98.4064	1.08979	10.6776

Table 13. Model 2 exit wall response for varying tank material density.

Parameters	Density (kg/m ³)	Maximum Displacement (m)	Peak Stress (MPa)	Peak Fluid Drag Pressure from Fluid Gauge 2 (MPa)	Peak Velocity (m/s)
Tank Material Density	1500	0.00466953	124.526	4.70424	9.52921
	2700	0.00471648	125.866	4.64315	8.3379
	4500	0.00465953	109.789	5.27148	7.03468

Data from Table 12 indicated no discernible effect of material density on displacement and stress. It was observed that the baseline Model 1 has the highest displacement and stress, but the difference in value for the different material density was small. Some correlations were observed for shock ram pressure and velocity, with the denser material at 4,500 kg/m³ having a smaller ram pressure of 1.09 MPa and peak velocity of 10.7 m/s.

For Model 2, the simulation model found that varying material density has almost negligible effects on the exit wall displacement, as illustrated in Figure 53. The dotted line shows that the projectile reached the exit wall at almost the same time with small difference in peak displacement for the three cases. A slight difference in the exit wall response was noted at an earlier time, with higher displacement observed for the less dense tank structure. Peak stress and velocity also see small changes even though density was varied from 1,500 kg/m³ to 4,500 kg/m³.

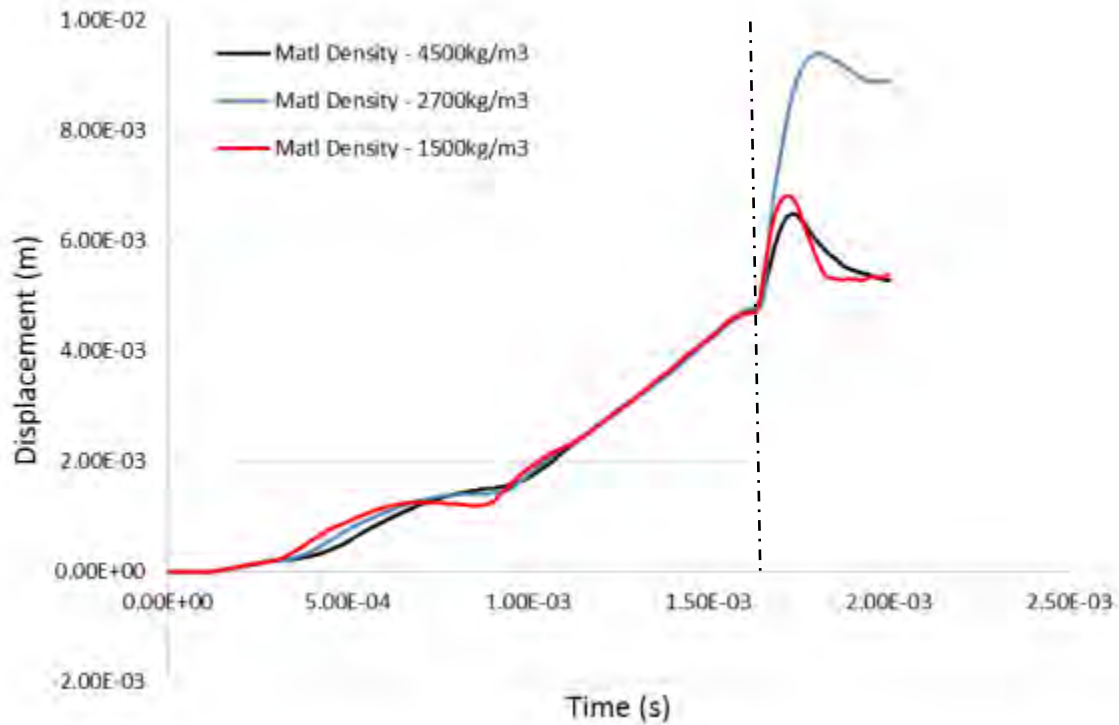


Figure 53. Exit Wall X-Displacement for different material density (Model 2).

6. Variation in Fluid Density

For the final investigative choice, the density of the fluid was varied from 800 kg/m³ to 1,200 kg/m³, with the baseline Model 1 and 2 having the density of water at 100 kg/m³. Results for this study are tabulated in Tables 14 and 15.

Table 14. Model 1 exit wall response to varying fluid density.

Parameters	Density (kg/m ³)	Maximum Displacement (m)	Peak Stress (MPa)	Shock phase Ram Pressure from Fluid Gauge 2 (MPa)	Peak Velocity (m/s)
Fluid Density	800	0.00208119	126.662	1.16409	14.1915
	1000	0.00203512	104.802	1.61365	12.7263
	1200	0.00178056	105.41	1.5171	14.2918

Table 15. Model 2 exit wall response to varying fluid density

Parameters	Density (kg/m ³)	Maximum Displacement (m)	Peak Stress (MPa)	Peak Fluid Drag Pressure from Fluid Gauge 2 (MPa)	Peak Velocity (m/s)
Fluid Density	800	0.00463453	129.618	3.99885	10.0071
	1000	0.00471674	125.866	4.64315	8.3379
	1200	0.00475732	142.476	5.35016	13.8578

The effect of fluid density on the shock phase of the HRAM for Model 1 saw no consistent trend at the exit wall, especially for stress, velocity, and ram pressure. Even though displacement of the exit wall for lower fluid density seemed to be higher, the difference is perceived to be small, as illustrated in Figure 54. Results for shock phase ram pressure were also inconsistent where the more dense and less dense fluid both having a smaller ram pressure than the baseline Model 1.

As for the drag phase analysis for Model 2, varying fluid density was observed to have little effect on the exit wall displacement. However, the less dense fluid allowed the projectile to reach the exit wall earlier, as illustrated in Figure 55, where the dotted line represented the time just before impact. With lower fluid density of 800 kg/m³, the projectile reached the exit wall after 1.4 ms, approximately 0.5 ms faster than the denser fluid with a density of 1,200 kg/m³.

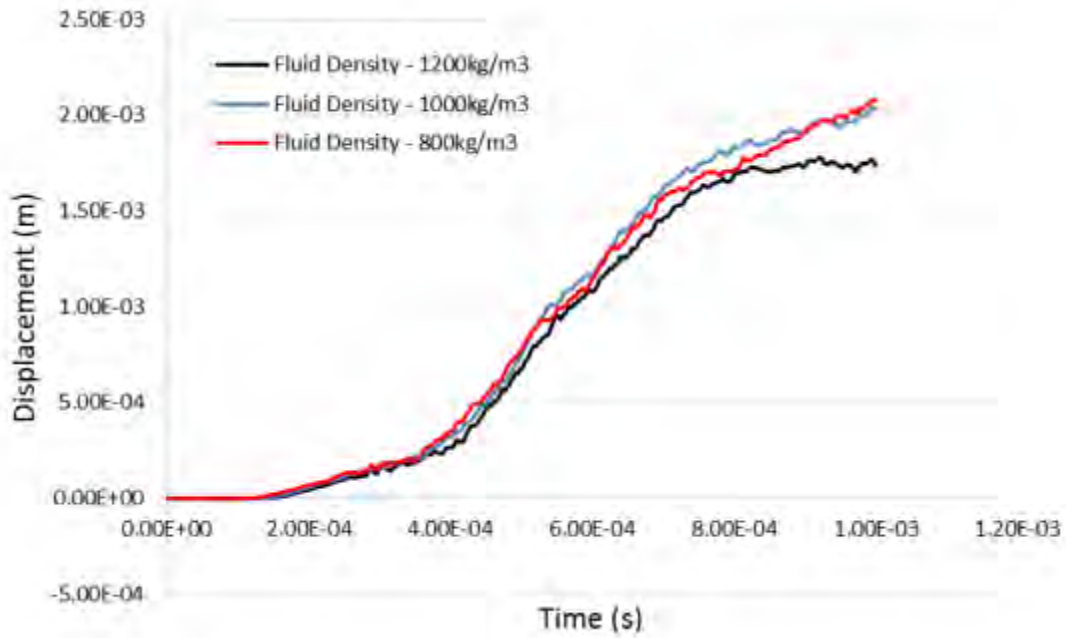


Figure 54. Exit wall X-Displacement for different fluid density (Model 1).

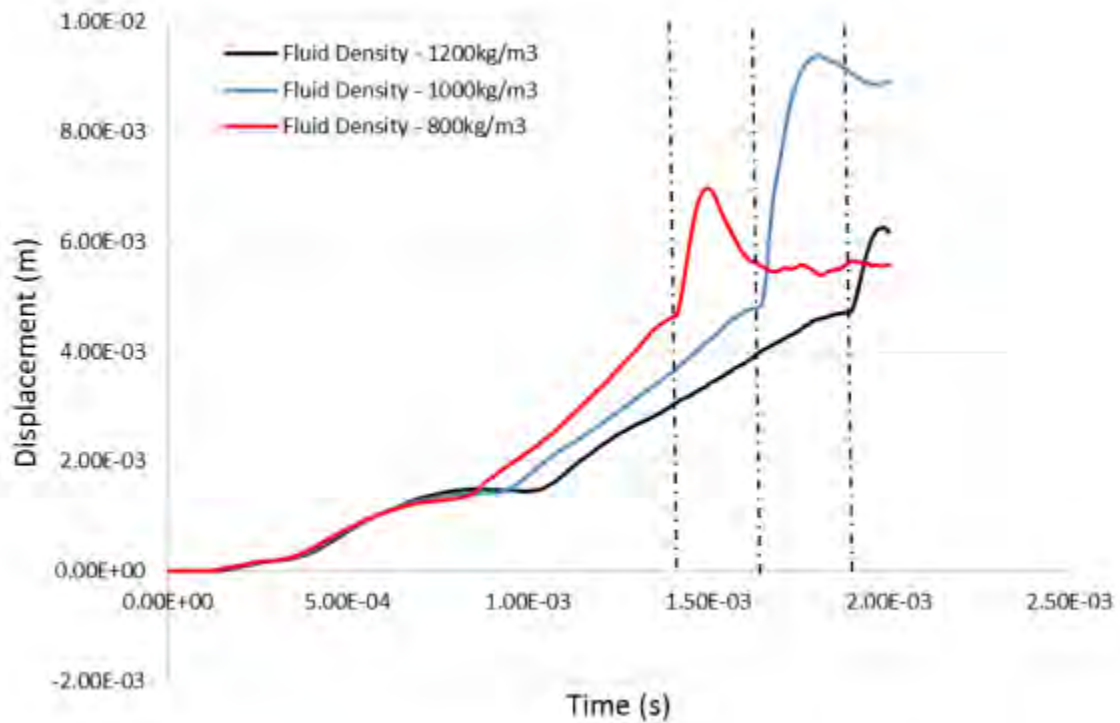


Figure 55. Exit wall X-Displacement for different fluid density (Model 2).

V. CONCLUSION AND FUTURE WORK

HRAM is a complex phenomenon which is still not well understood at present. Computational models can now provide an alternative to experimental testing in the understanding of HRAM by coupling the tank mesh to fluid mesh to simulate the fluid structure interaction. FE Models 1 and 2 developed using MSC Dytran, provided some insights into the dynamic response of the tank structure and fluid pressures at the early phases of the HRAM phenomenon. Key features of HRAM phenomenon such as the shock wave propagation through the fluid upon impact, drag phase pressures, cavity evolution and tank walls deformation could be observed from the model.

For the studies conducted with Models 1 and 2, the examination and analysis of the data collected revealed the following observations:

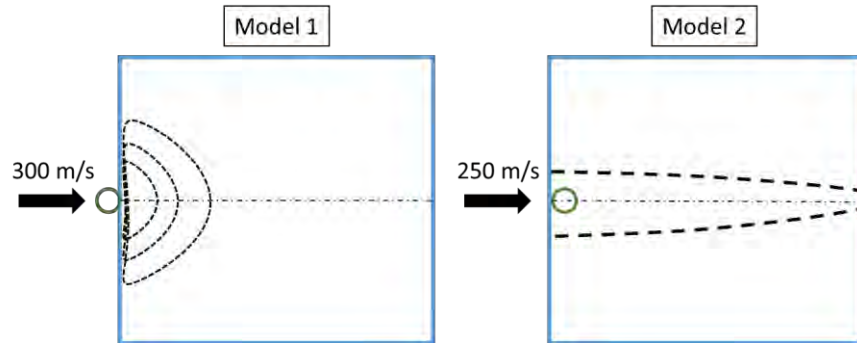
- Initial shock wave pressure upon projectile impact is unlikely to have detrimental effects on the exit wall of tank due to its rapid extinction in the fluid.
- Presence of free surface with lower filling levels reduced both the initial shock pressure and subsequent drag phase pressures.
- Projectile mass has a strong effect on the exit wall response during the shock phase, but once projectile penetrates the entry wall, the drag phase for different projectile mass investigated was inconclusive.
- Velocity of the projectile had the largest influence on the exit wall response and fluid pressures, since the kinetic energy of the projectile is proportional to the square of its velocity. Therefore, when projectile velocity was increase to 500 m/s, all data collected for analysis observed a huge increase especially during the drag phase. From this observation, damage to exit wall of the tank could

be greatly reduced if the projectile velocity could be reduced significantly by the entry wall after penetration.

- Tank material with a higher Young's modulus resulted in a larger shock pressure but smaller drag phase pressures. Effective stress experienced by the exit wall was significantly greater for the stiffer tank.
- Varying tank material density had little effect on the exit wall response during the drag phase.
- Increasing the density of fluid in the tank resulted in higher drag phase pressures. The projectile was observed to reach the exit wall at a later time with increased fluid density. Deformation at the exit wall remained unchanged with varying fluid densities.

Validation of the HRAM model is extremely challenging due to the lack of experimental data and the many factors that could affect the results. Some of the data that were collected for tank deformation and fluid pressures were compared to Varas [2] experiment, and found to be of the same order of magnitude; however, further verification is required in the future. Future development of the model could also investigate the effects of the cavitation phase on the tank wall response, which would entail an increase of simulation end time.

APPENDIX A. GRAPHS FOR FLUID LEVELS VARIATION



- Fluid levels investigated: 100% filled, 80% filled, 60% filled and empty.

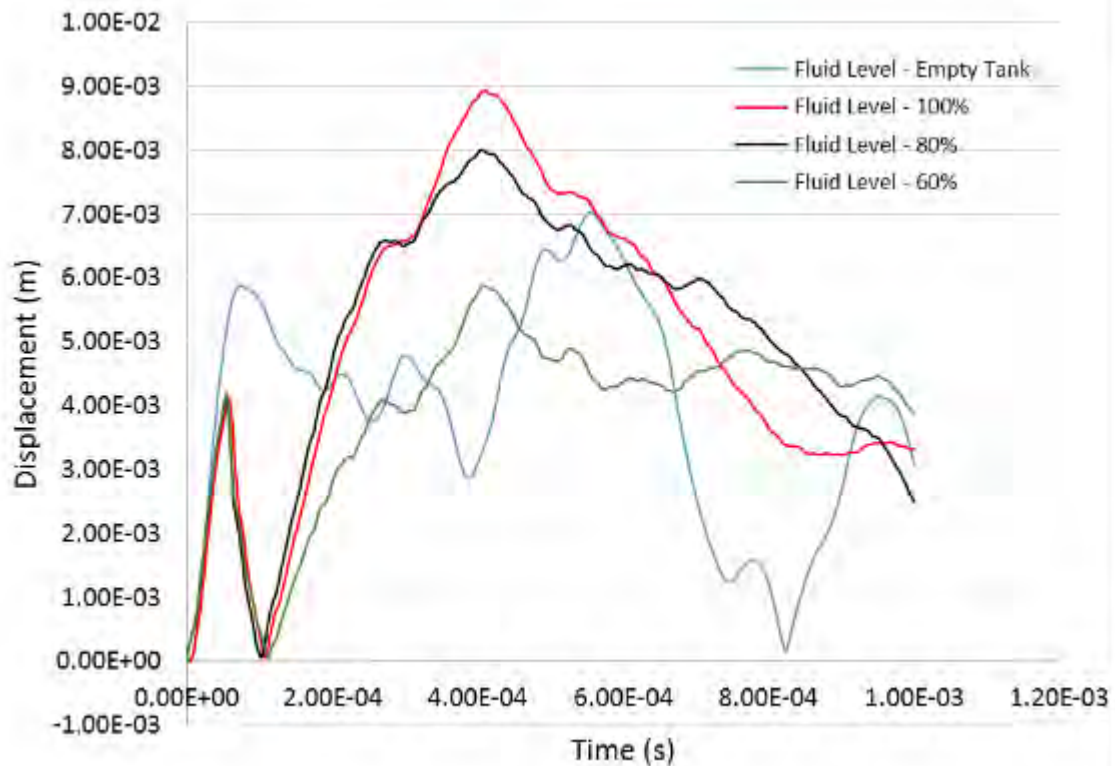


Figure 56. Entry wall resultant displacement for different fluid levels (Model 1).

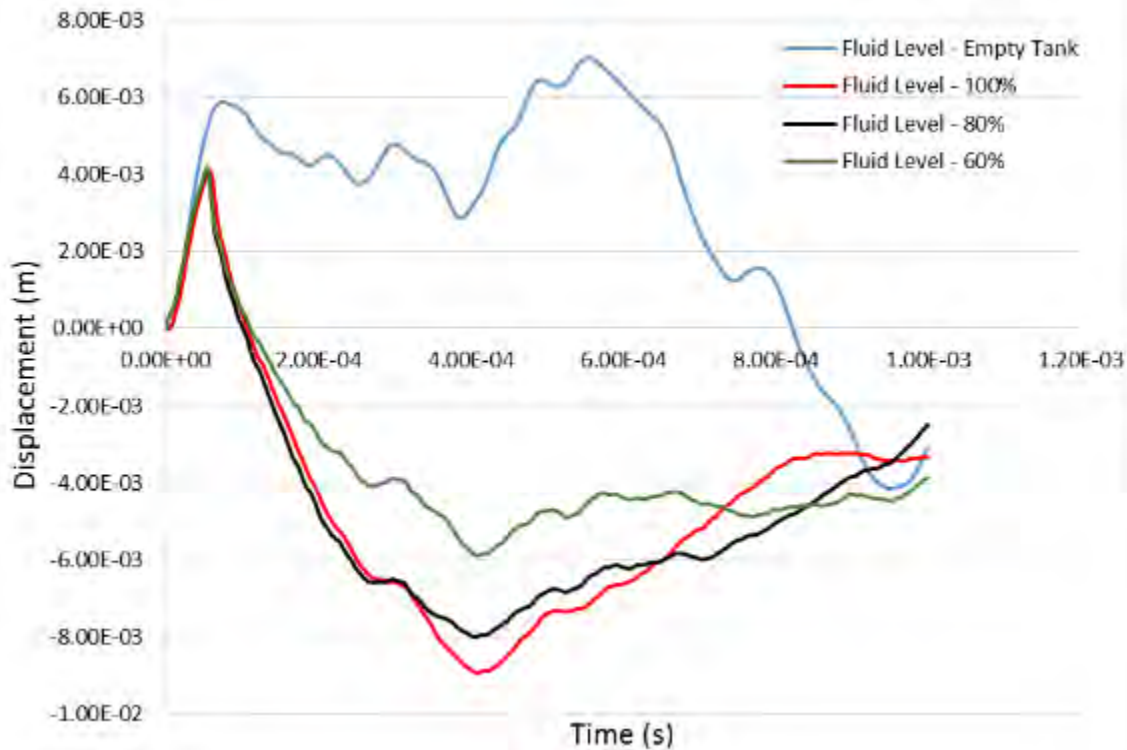


Figure 57. Entry wall X-Displacement for different fluids levels (Model 1).

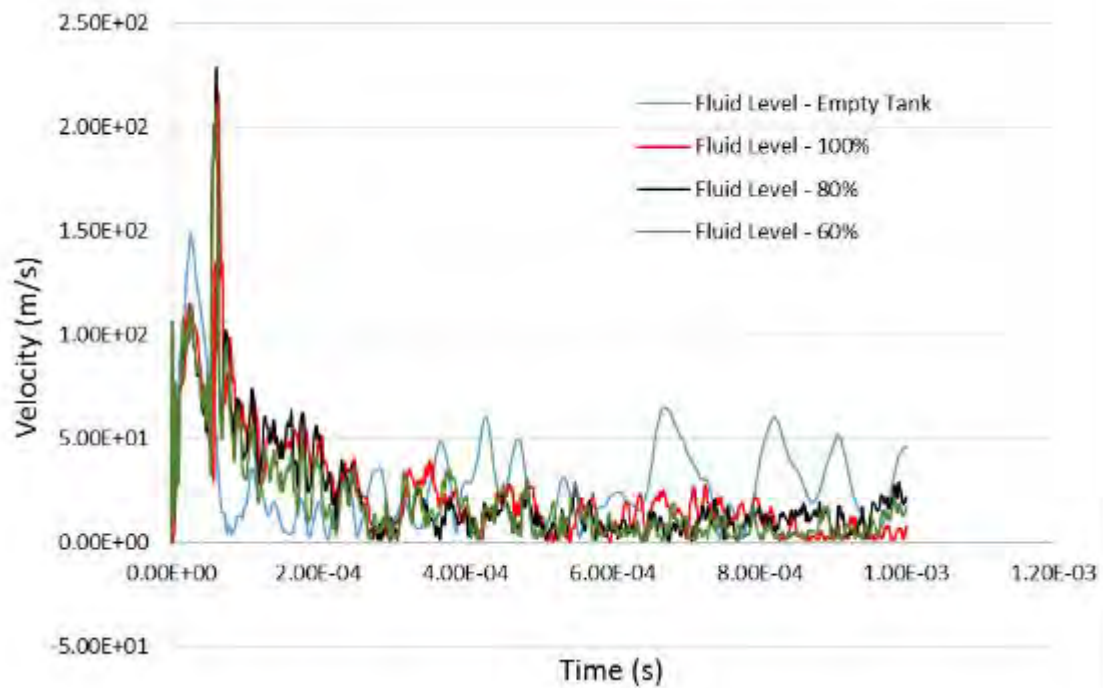


Figure 58. Entry wall resultant velocity for different fluid levels (Model 1).

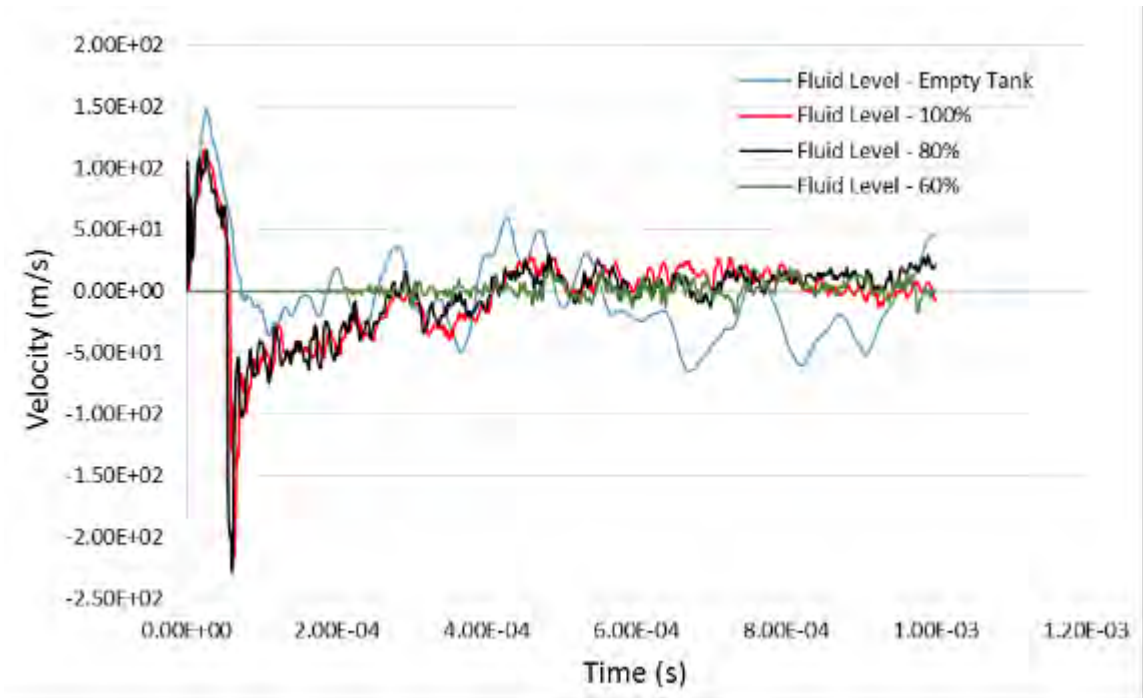


Figure 59. Entry wall X-Velocity for different fluid levels (Model 1).

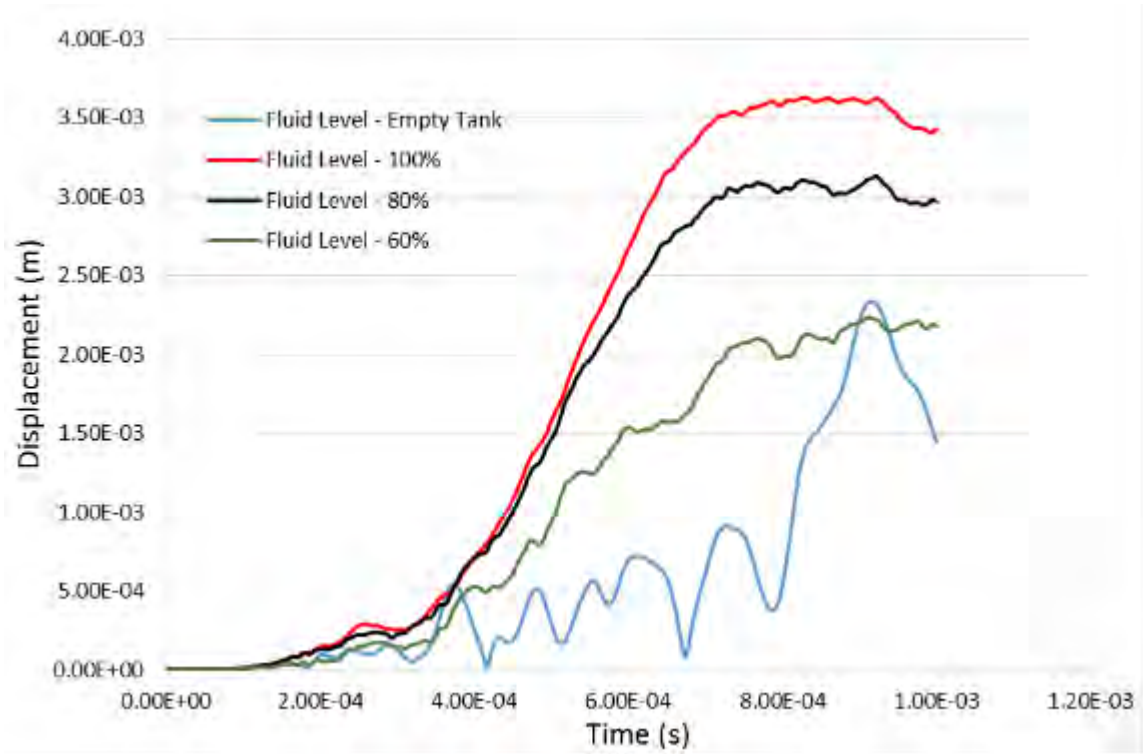


Figure 60. Left wall resultant displacement for different fluid levels (Model 1).

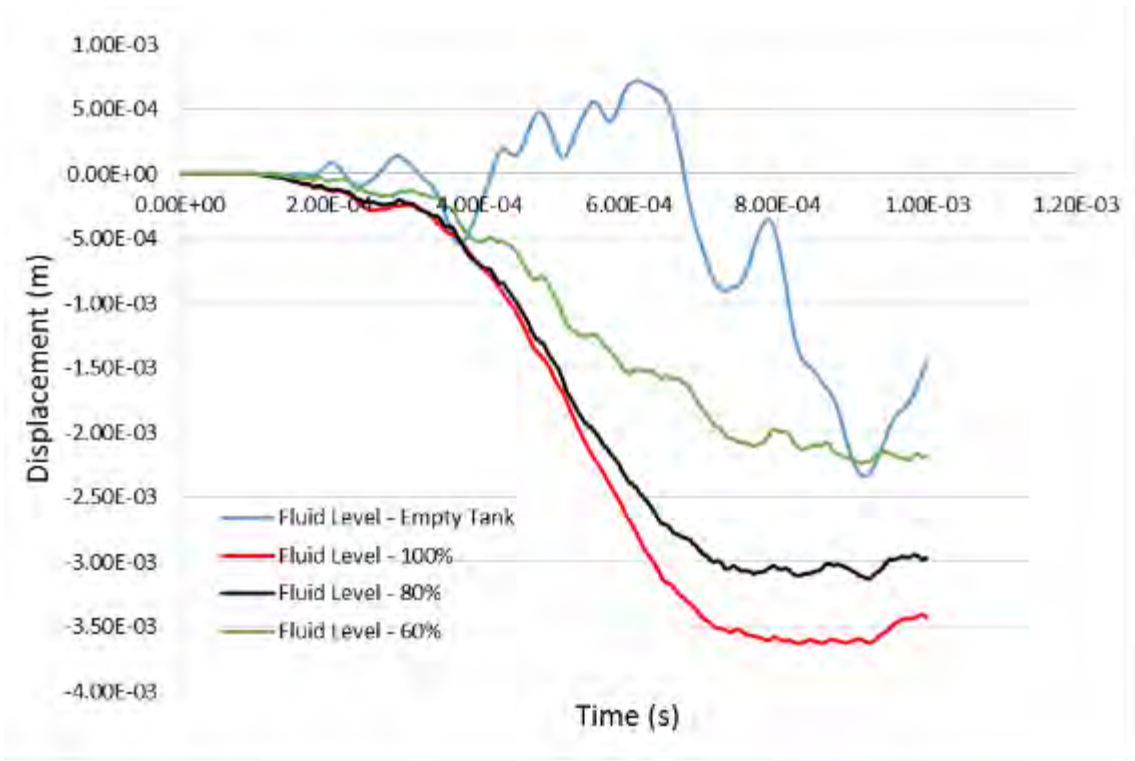


Figure 61. Left wall Z-Displacement for different fluid levels (Model 1).

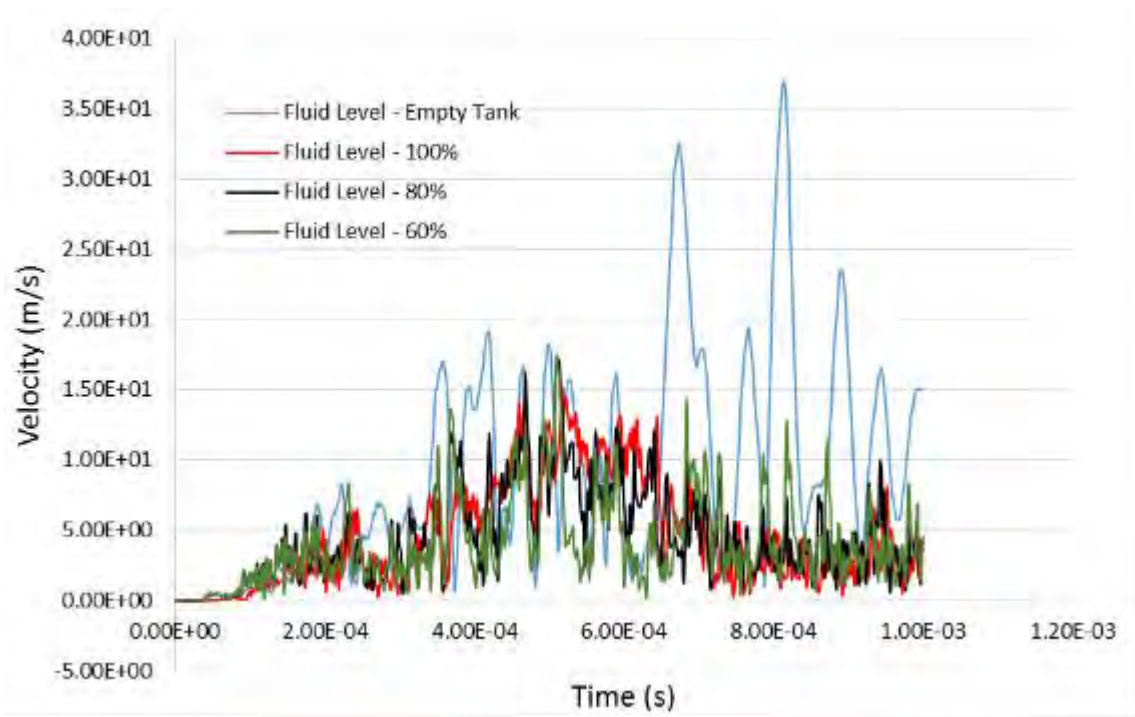


Figure 62. Left wall resultant velocity for different fluid levels (Model 1).

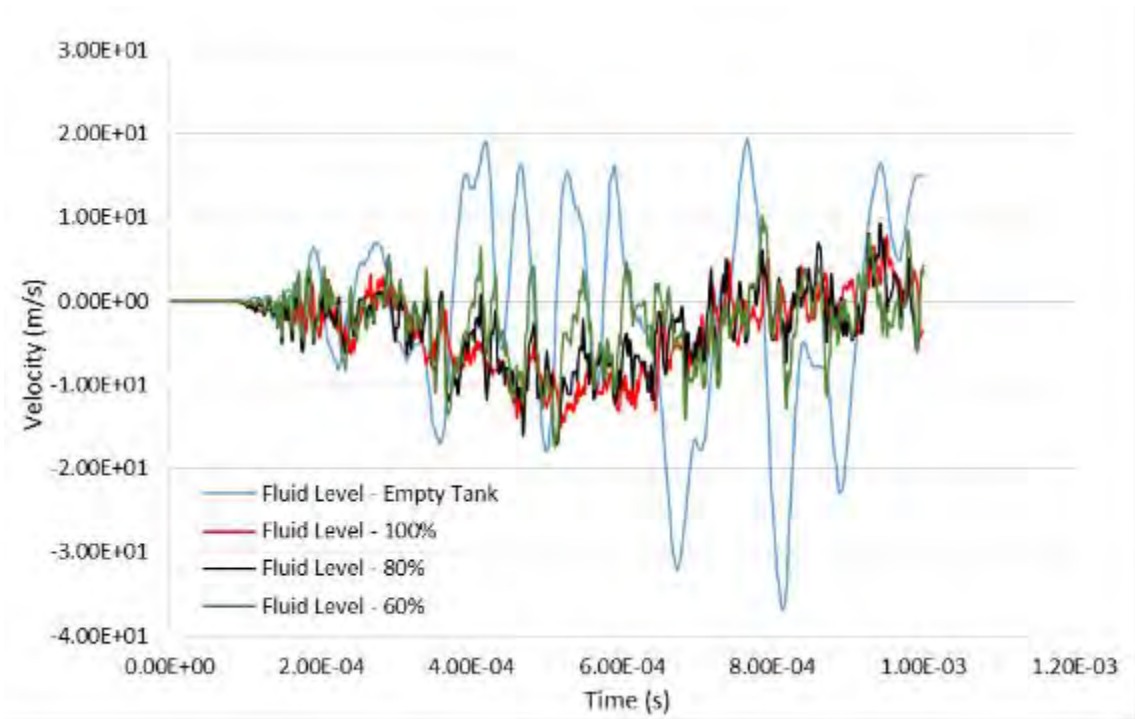


Figure 63. Left wall Z-Velocity for different fluid levels (Model 1).

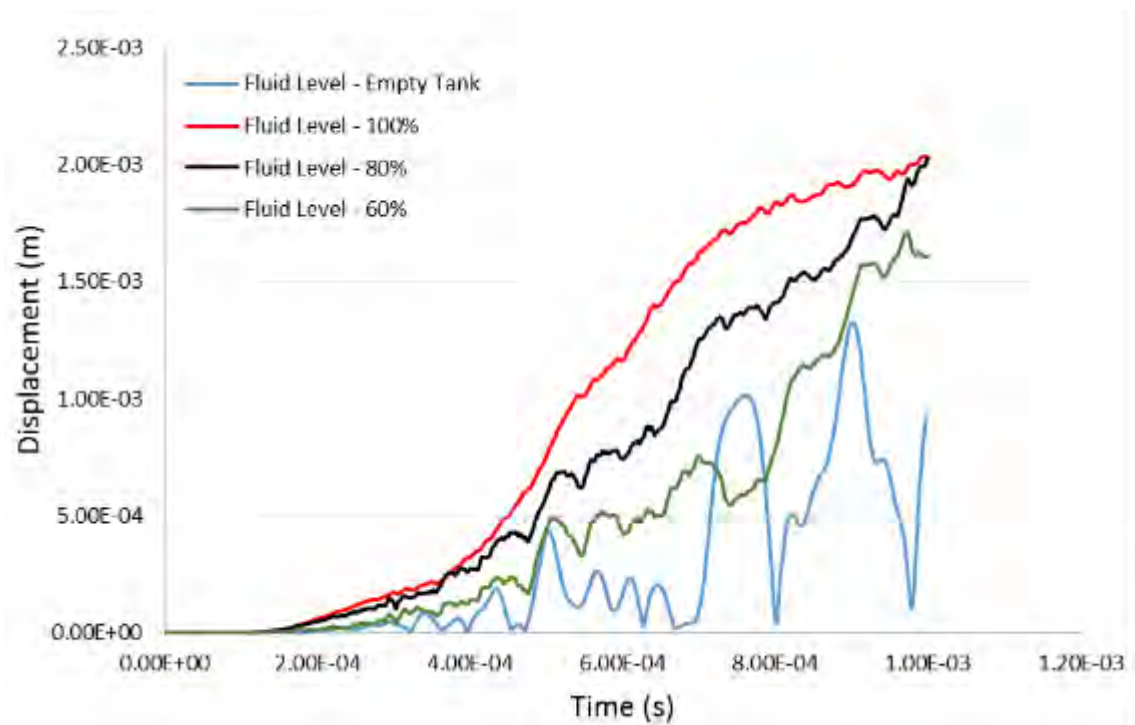


Figure 64. Exit wall resultant displacement for different fluid levels (Model 1).

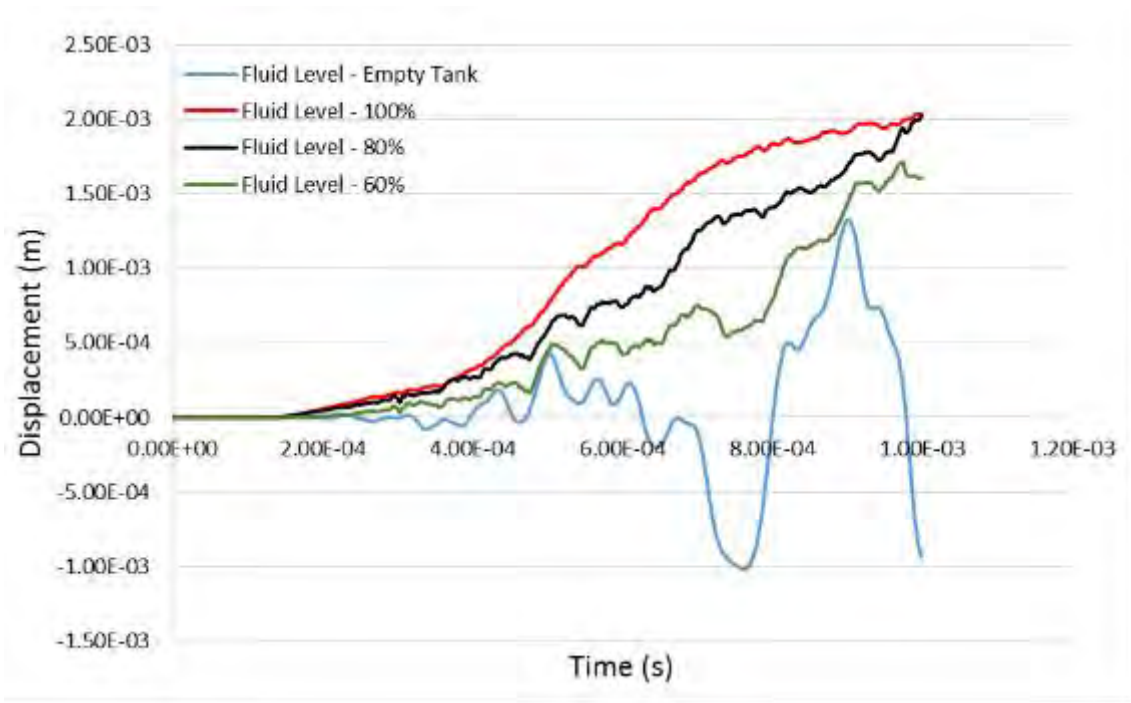


Figure 65. Exit wall X-Displacement for different fluid levels (Model 1).

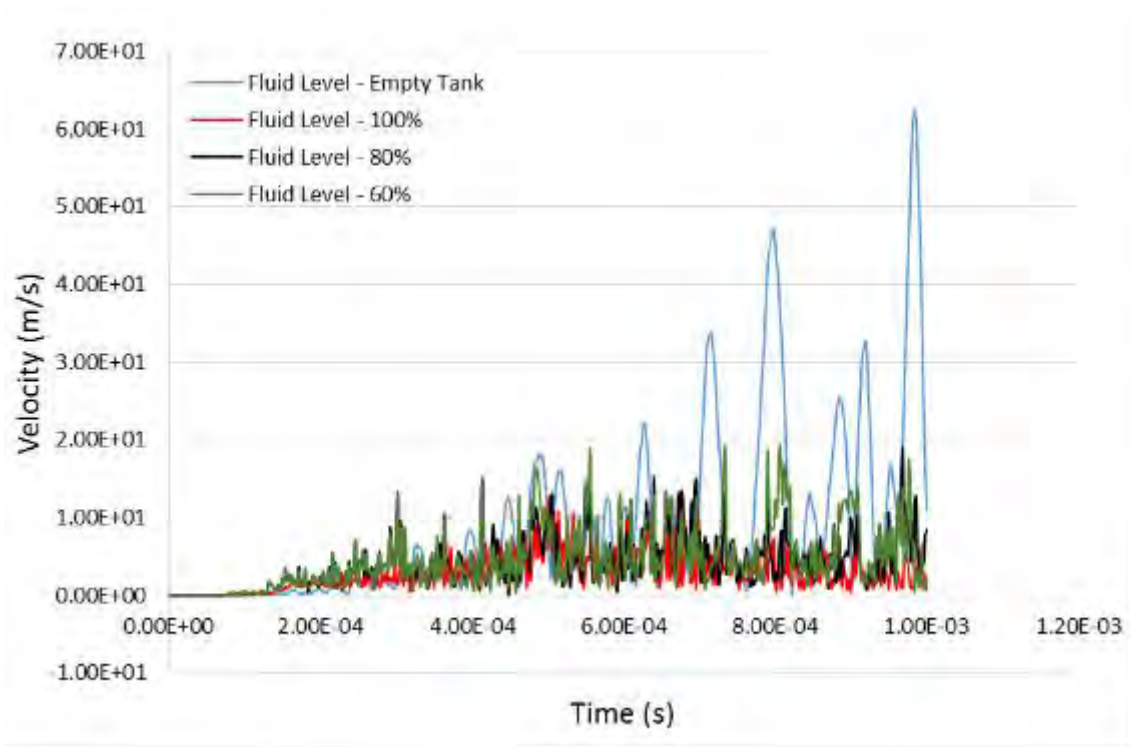


Figure 66. Exit wall resultant velocity for different fluid levels (Model 1).

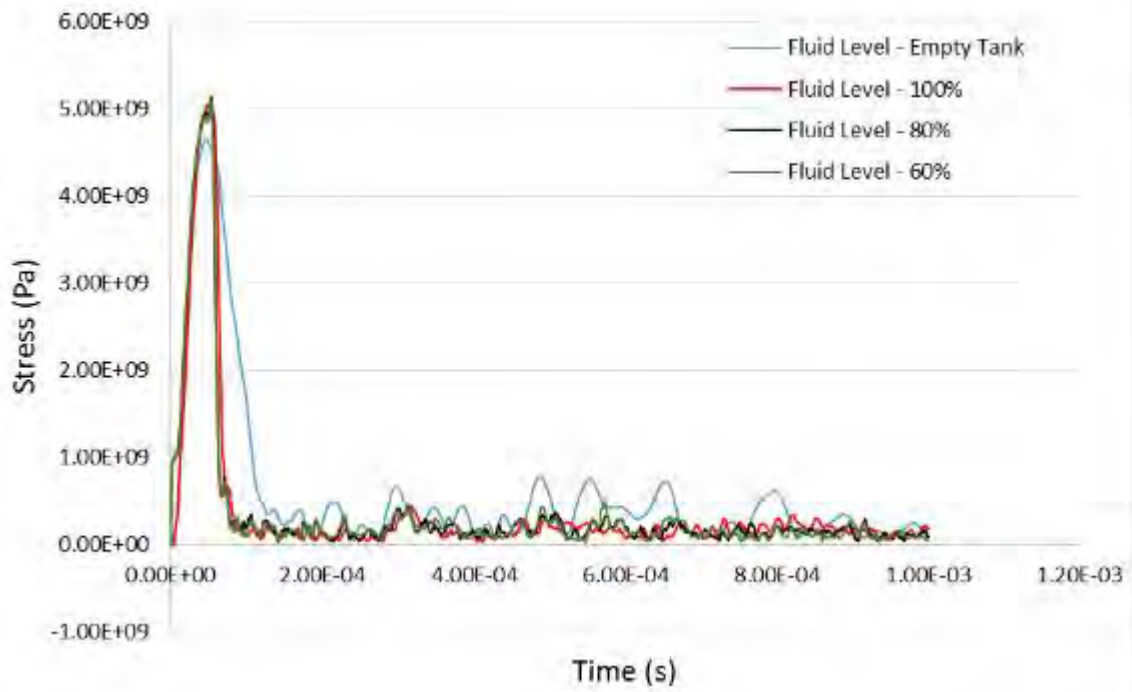


Figure 67. Entry wall effective stress for different fluid levels (Model 1).

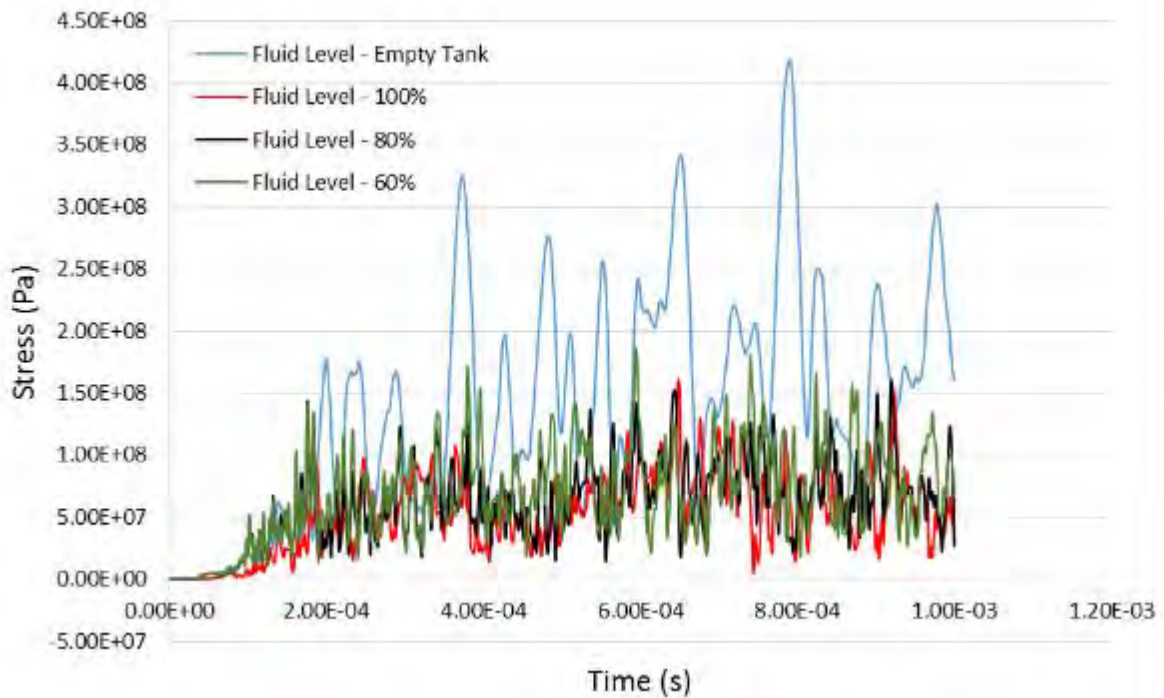


Figure 68. Left wall effective stress for different fluid levels (Model 1).

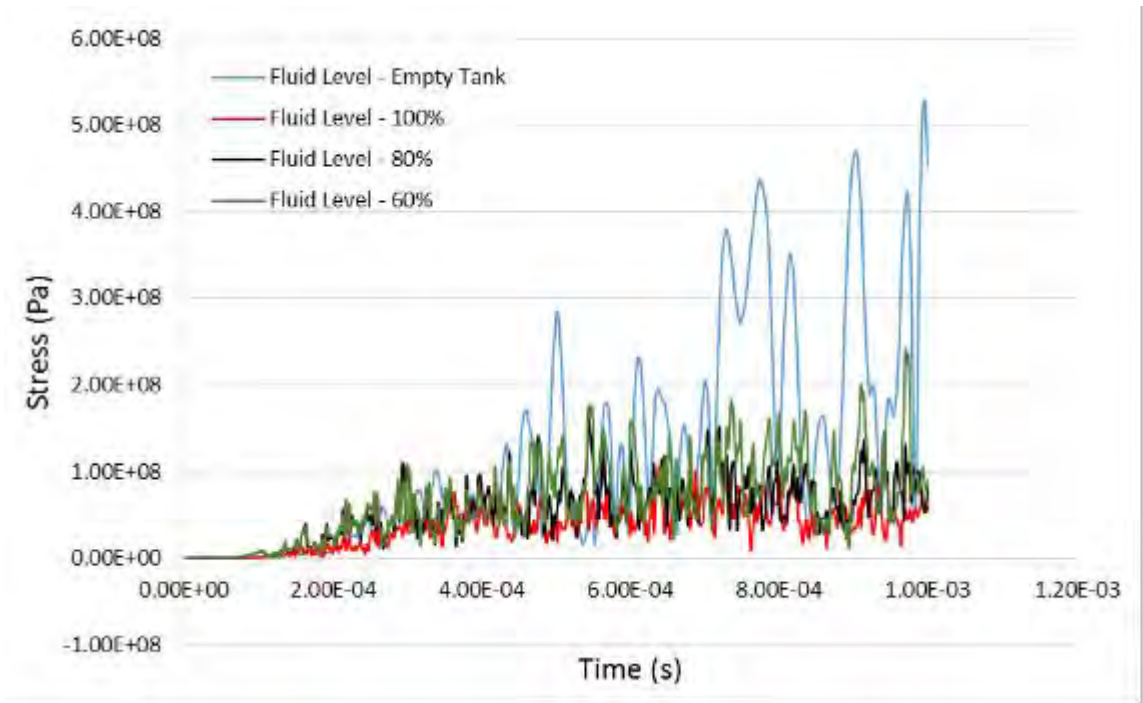


Figure 69. Exit wall effective stress for different fluid levels (Model 1).

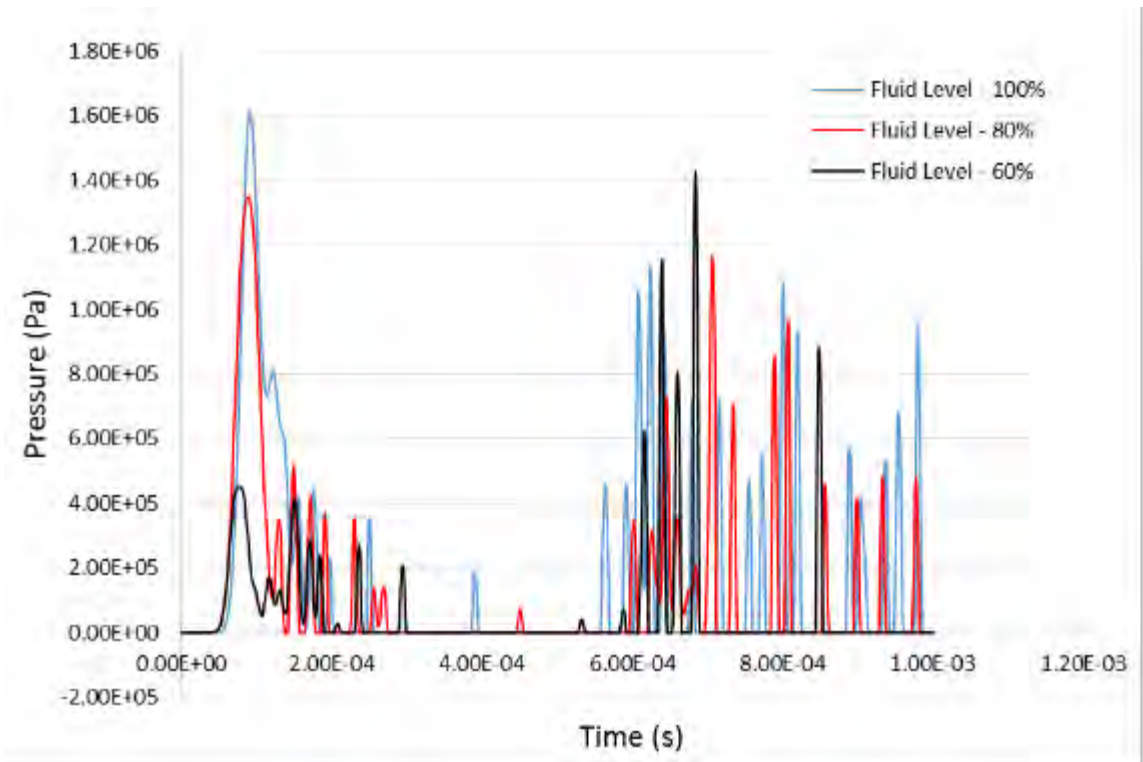


Figure 70. Fluid pressure for different fluid levels (Model 1).

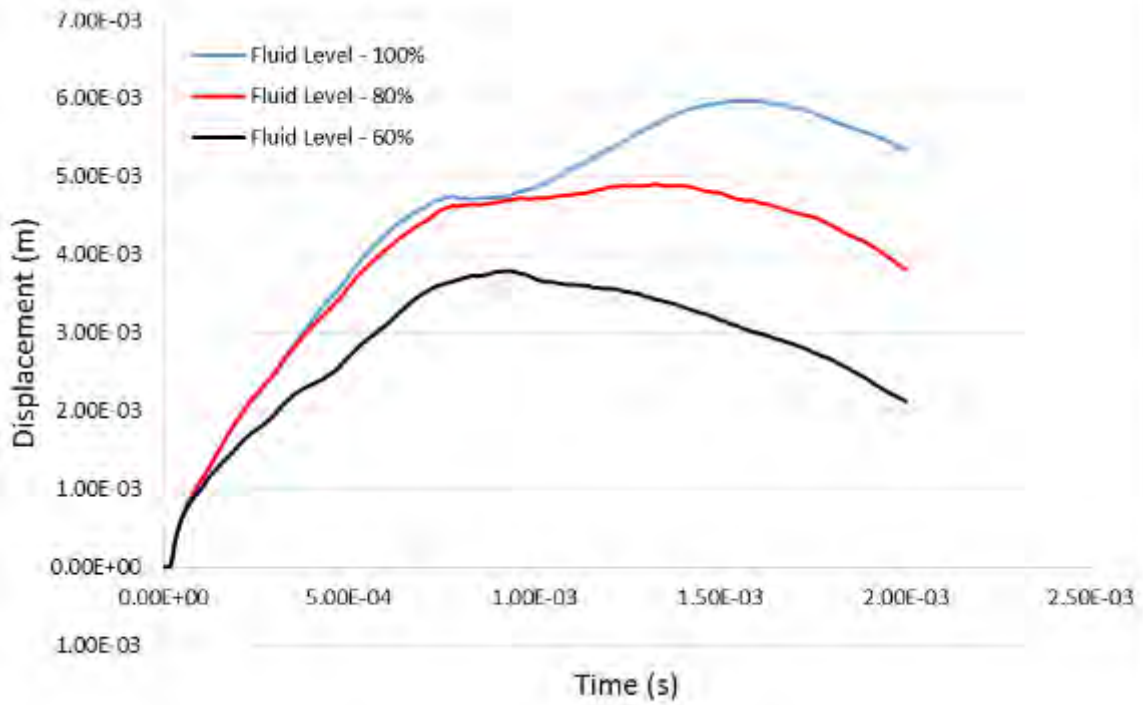


Figure 71. Entry wall resultant displacement for different fluid levels (Model 2).

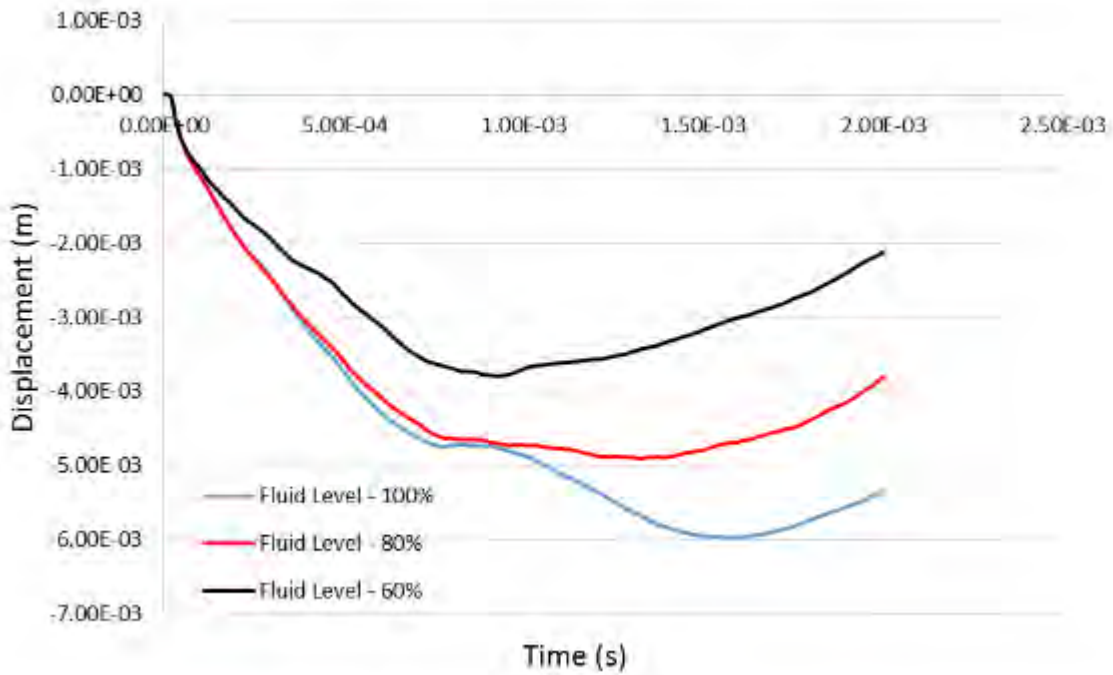


Figure 72. Entry wall X-Displacement for different fluid levels (Model 2).

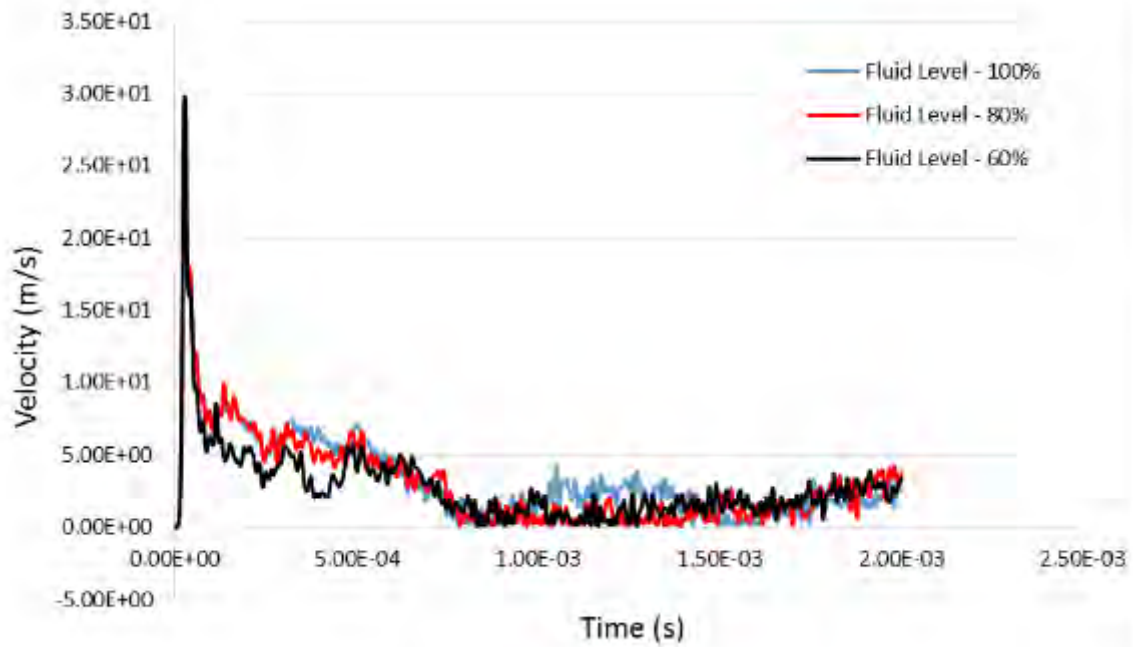


Figure 73. Entry wall resultant velocity for different fluid levels (Model 2).

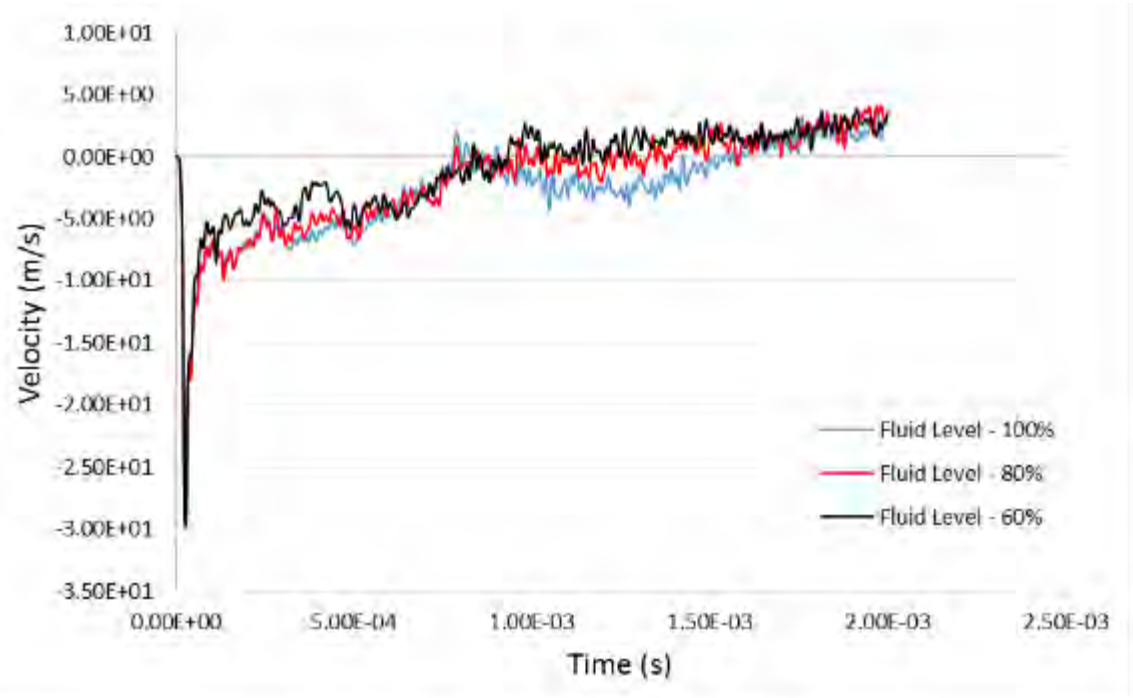


Figure 74. Entry wall X-Velocity for different fluid levels (Model 2).

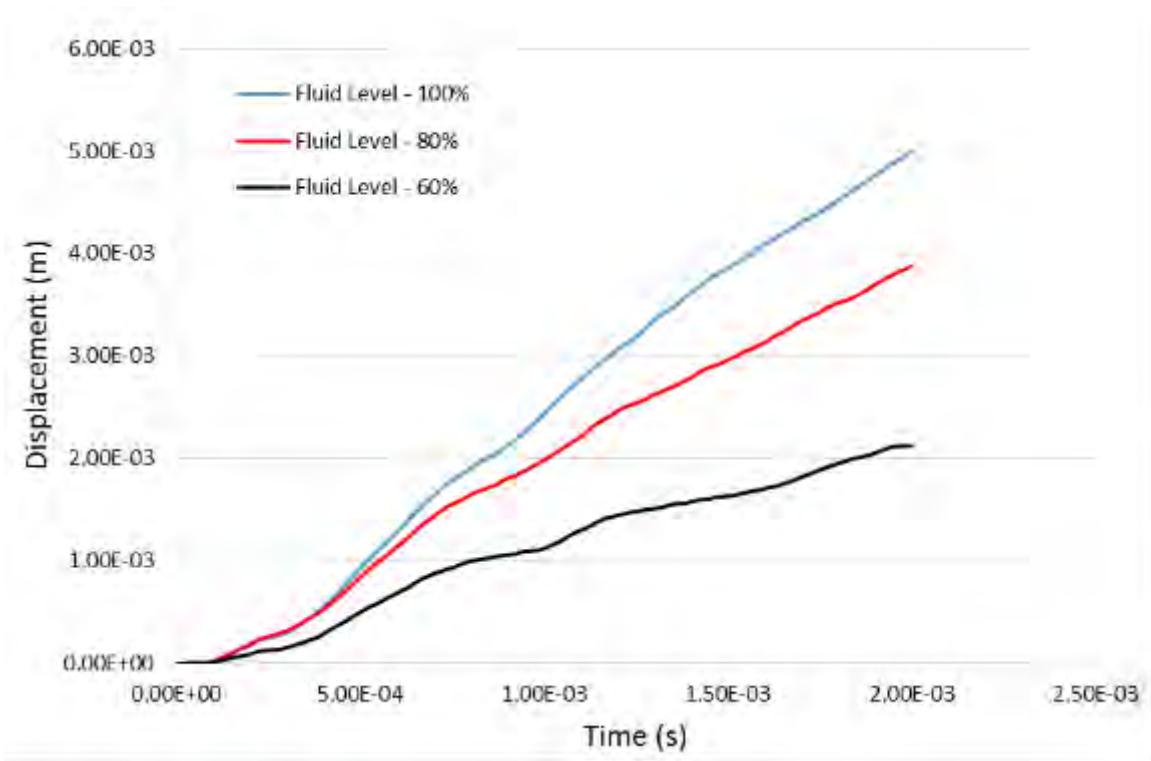


Figure 75. Left wall resultant displacement for different fluid levels (Model 2).

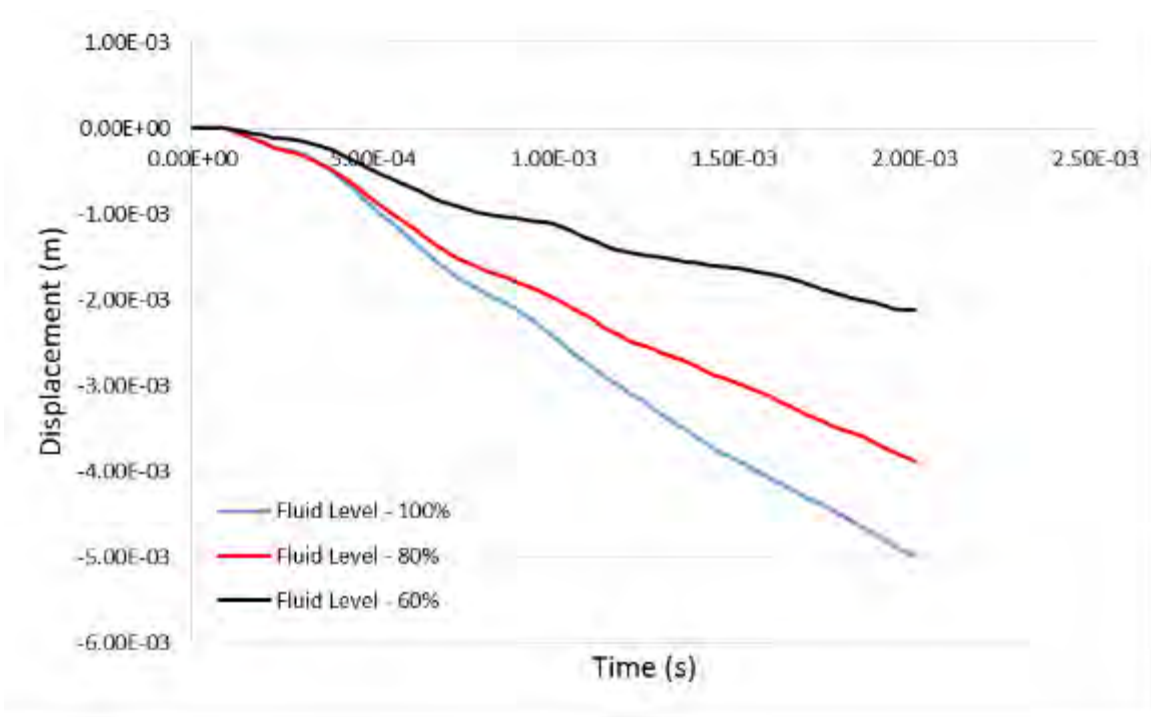


Figure 76. Left wall Z-Displacement for different fluid levels (Model 2).

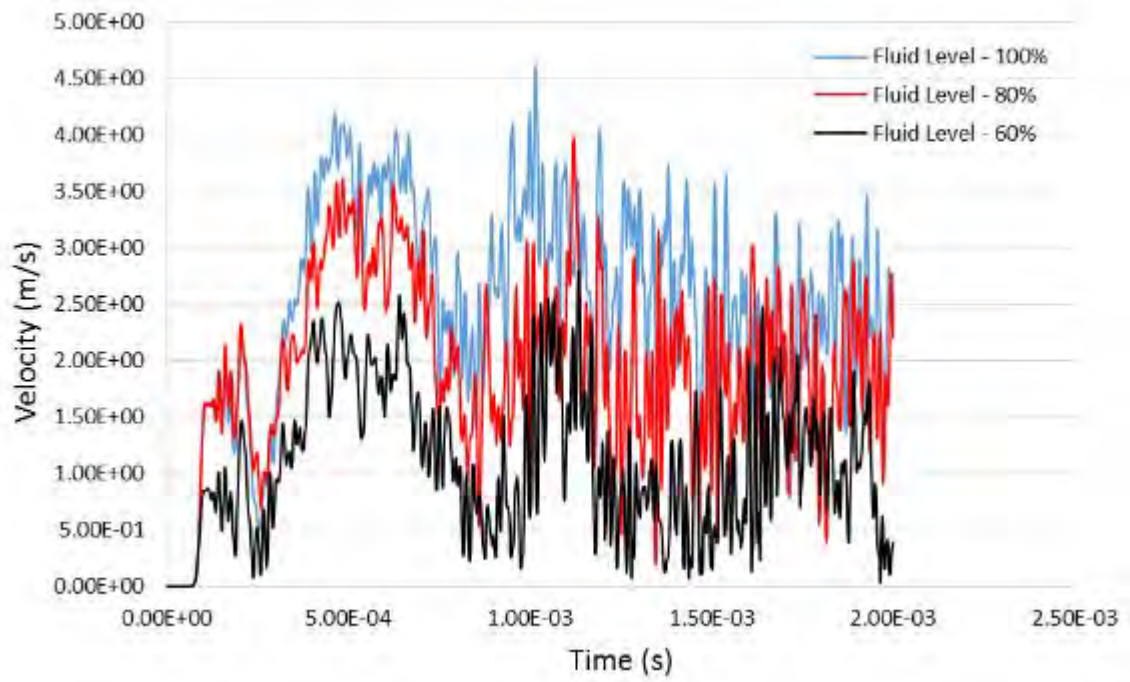


Figure 77. Left wall resultant velocity for different fluid levels (Model 2).

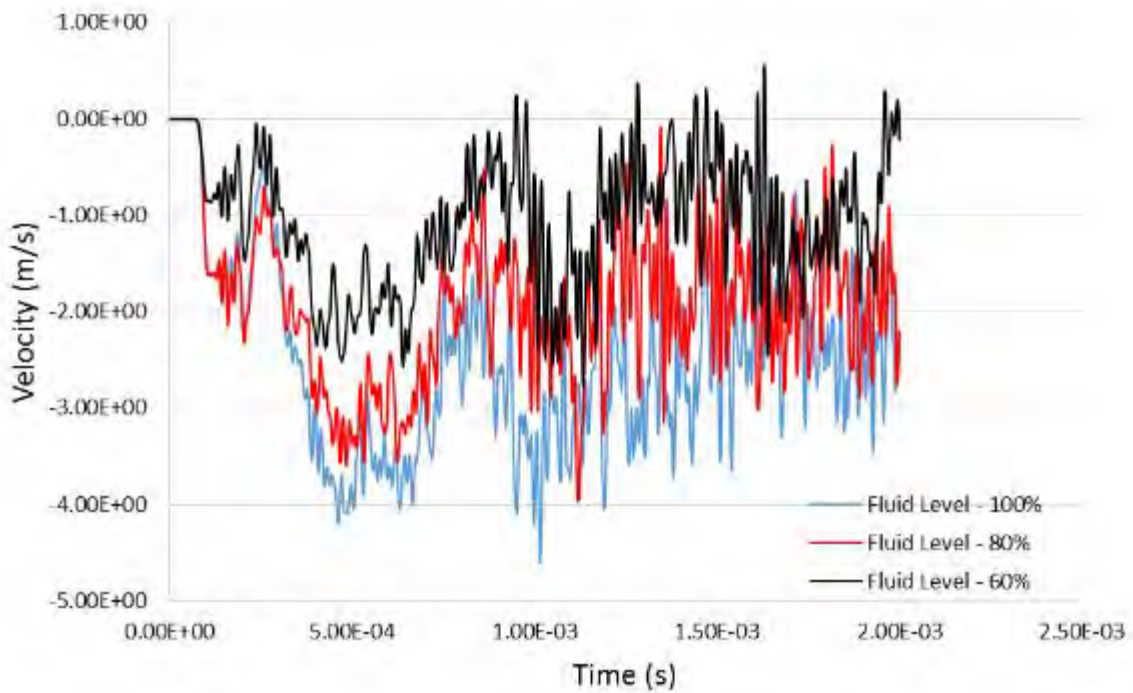


Figure 78. Left wall Z-Velocity for different fluid levels (Model 2).

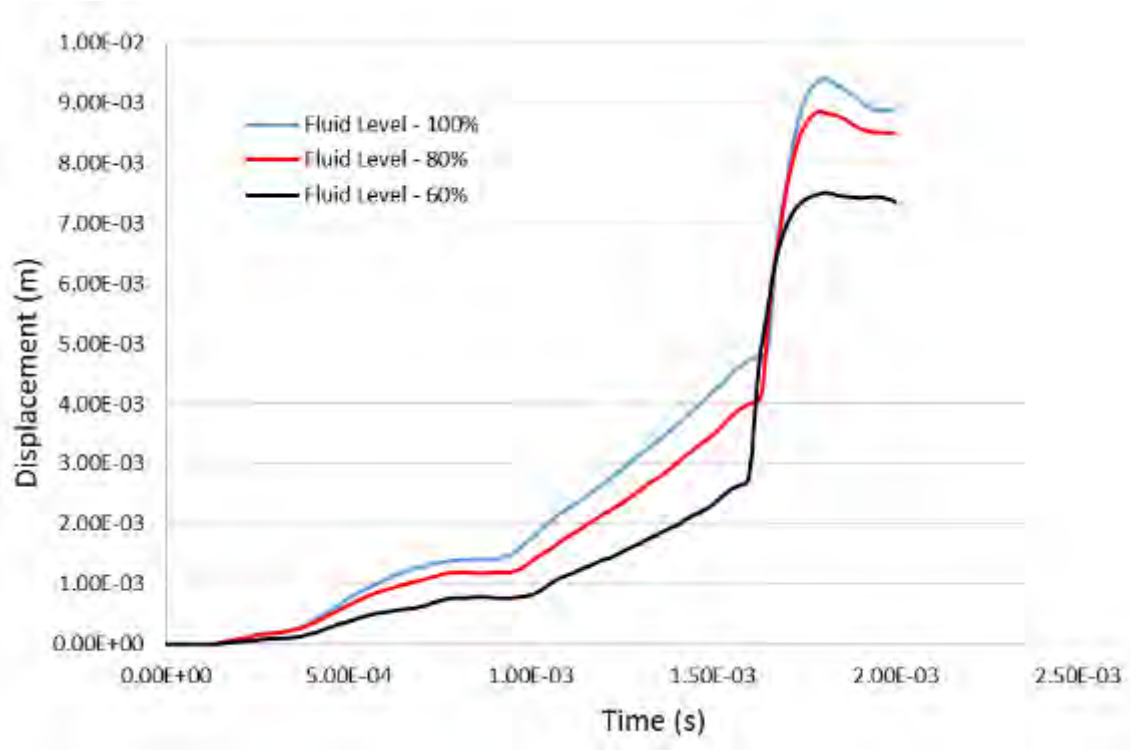


Figure 79. Exit wall resultant displacement for different fluid levels (Model 2).

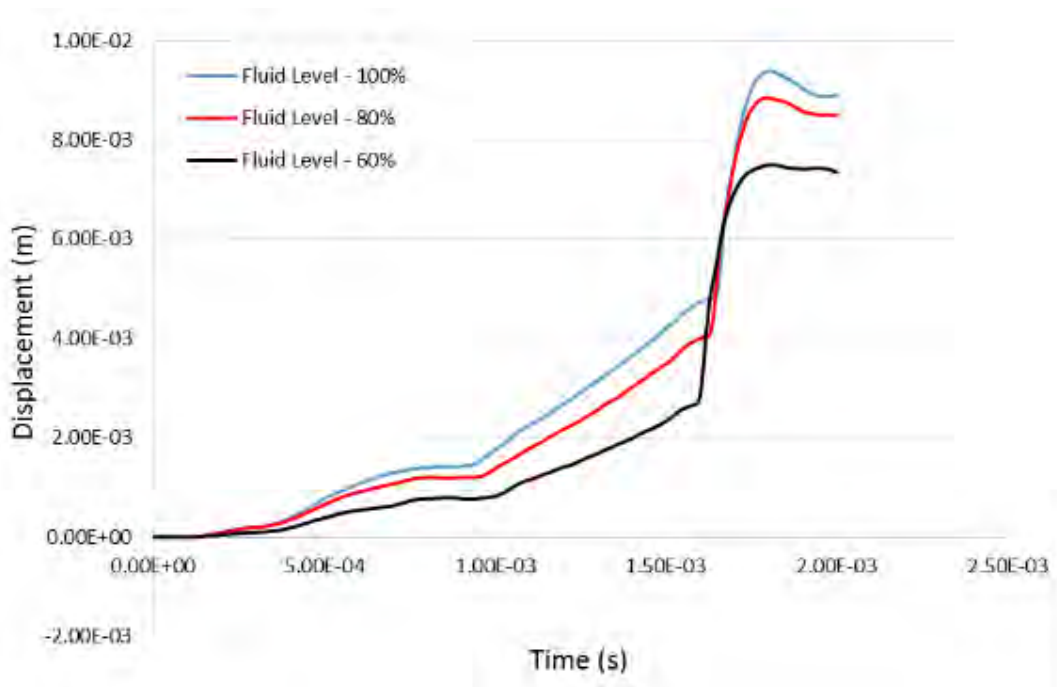


Figure 80. Exit wall X-Displacement for different fluid levels (Model 2).

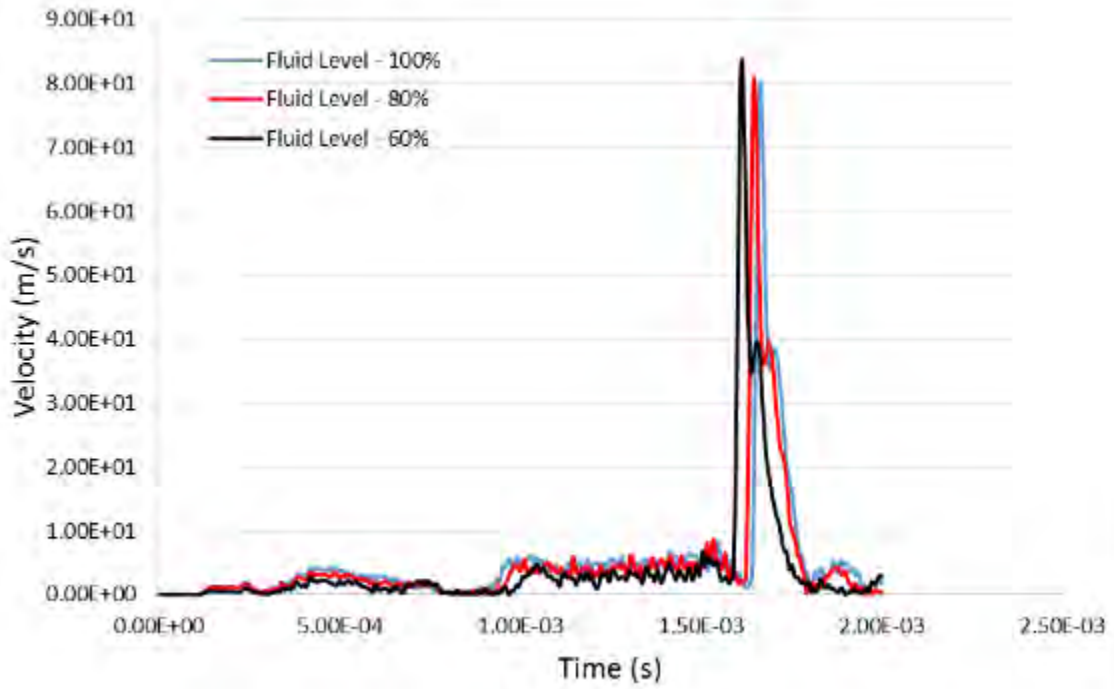


Figure 81. Exit wall X-Velocity for different fluid levels (Model 2).

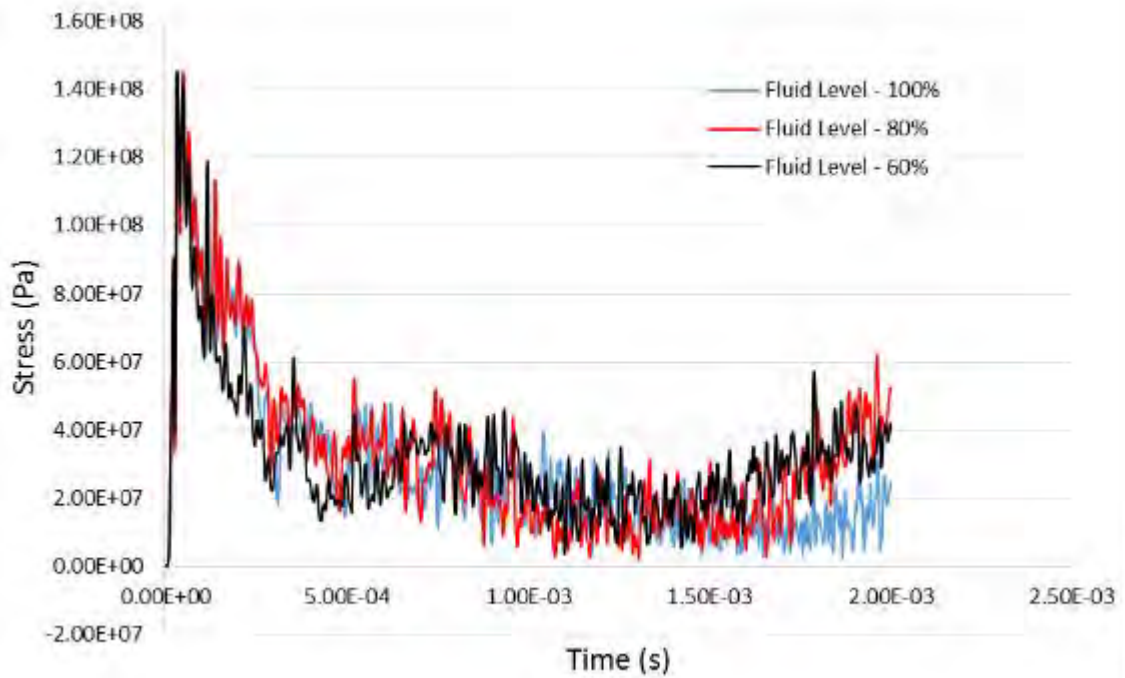


Figure 82. Entry wall effective stress for different fluid levels (Model 2).

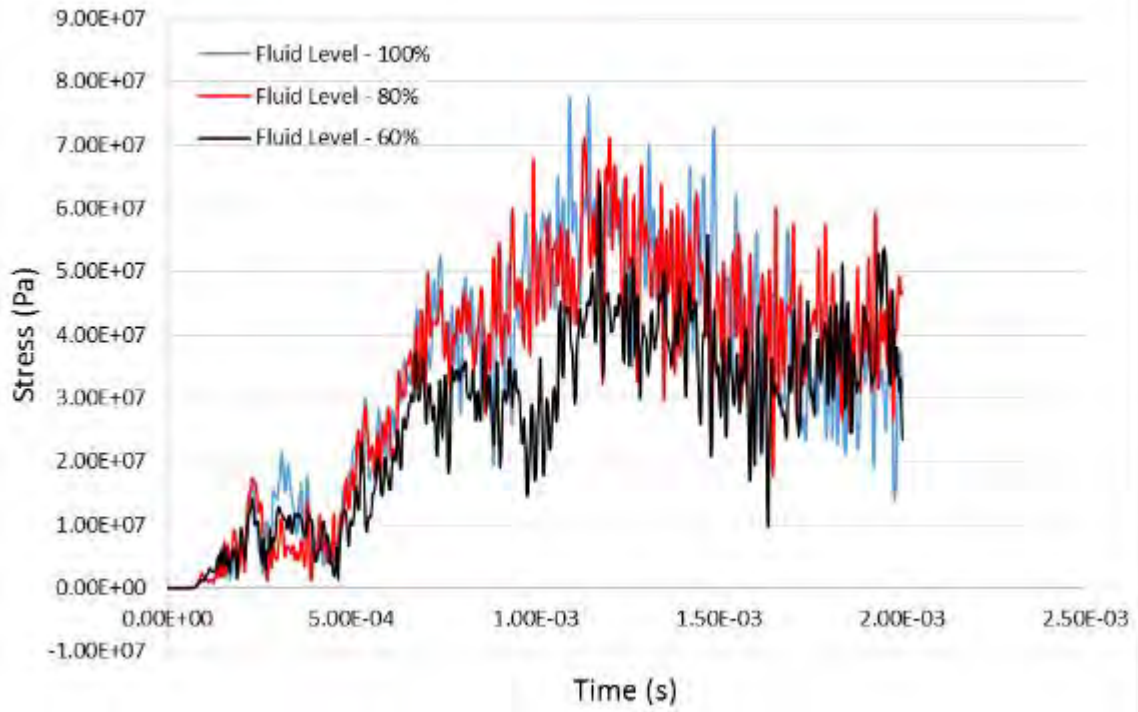


Figure 83. Left wall effective stress for different fluid levels (Model 2).

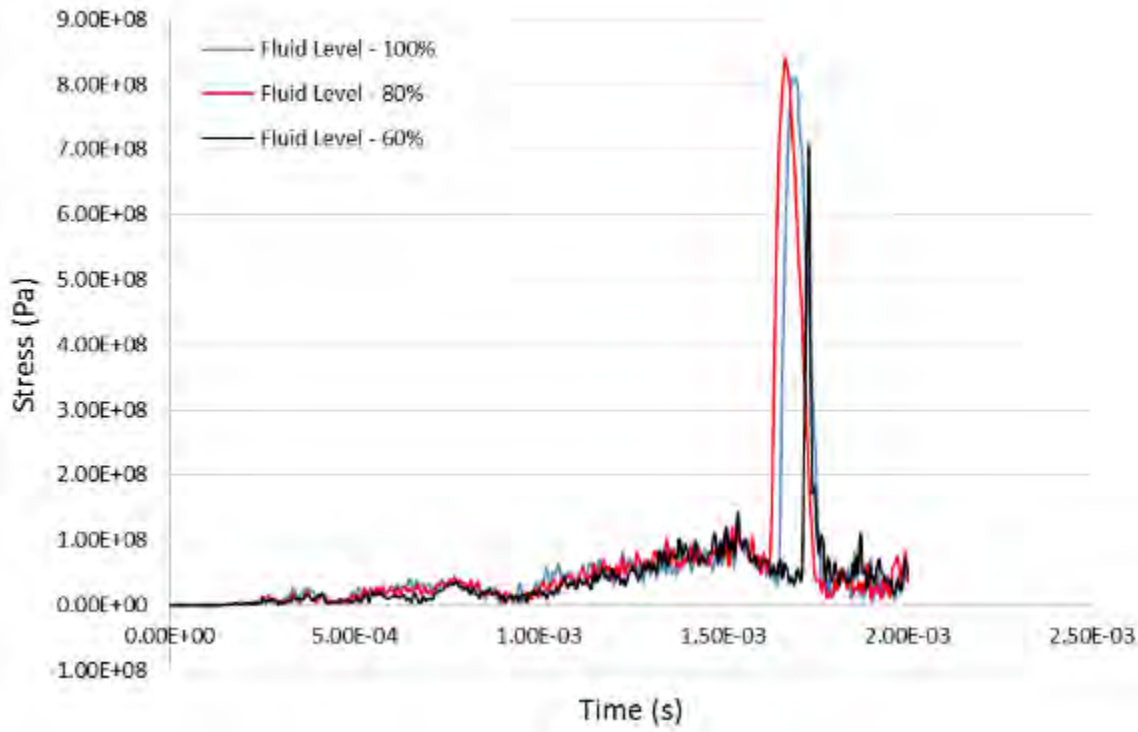


Figure 84. Exit wall effective stress for different fluid levels (Model 2).

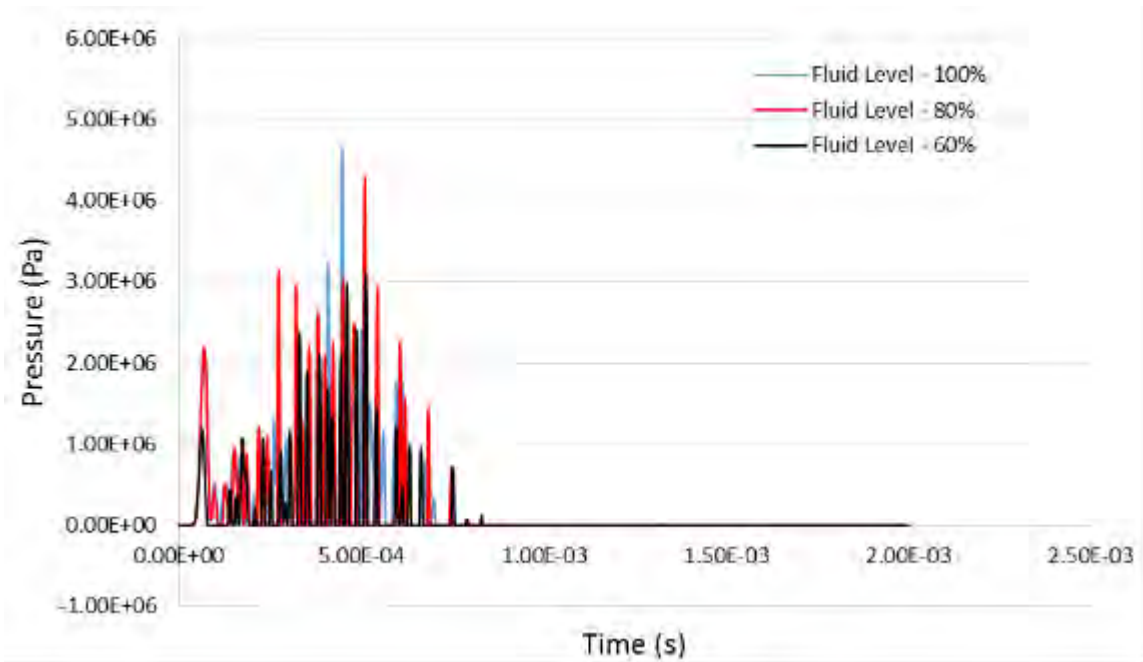


Figure 85. Drag phase pressure for different fluid levels (Model 2).

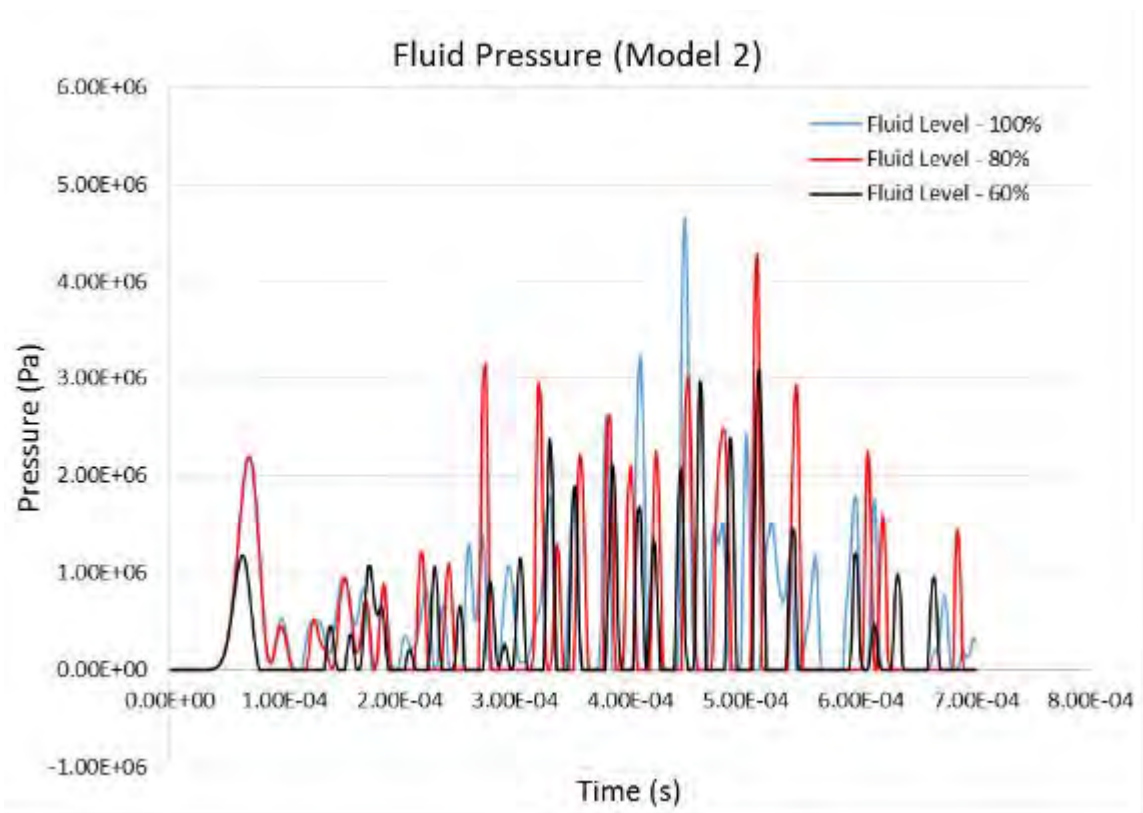
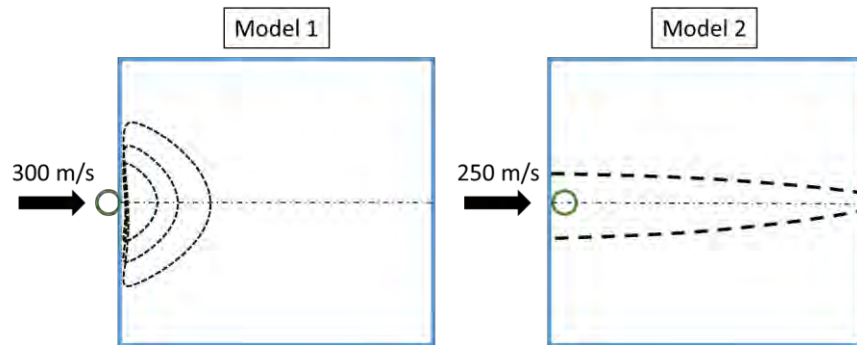


Figure 86. Drag phase pressure for different fluid levels (Model 2) - Enlarged.

APPENDIX B. GRAPHS FOR PROJECTILE MASS VARIATION



- Projectile mass investigated: 2g, 4g and 6g

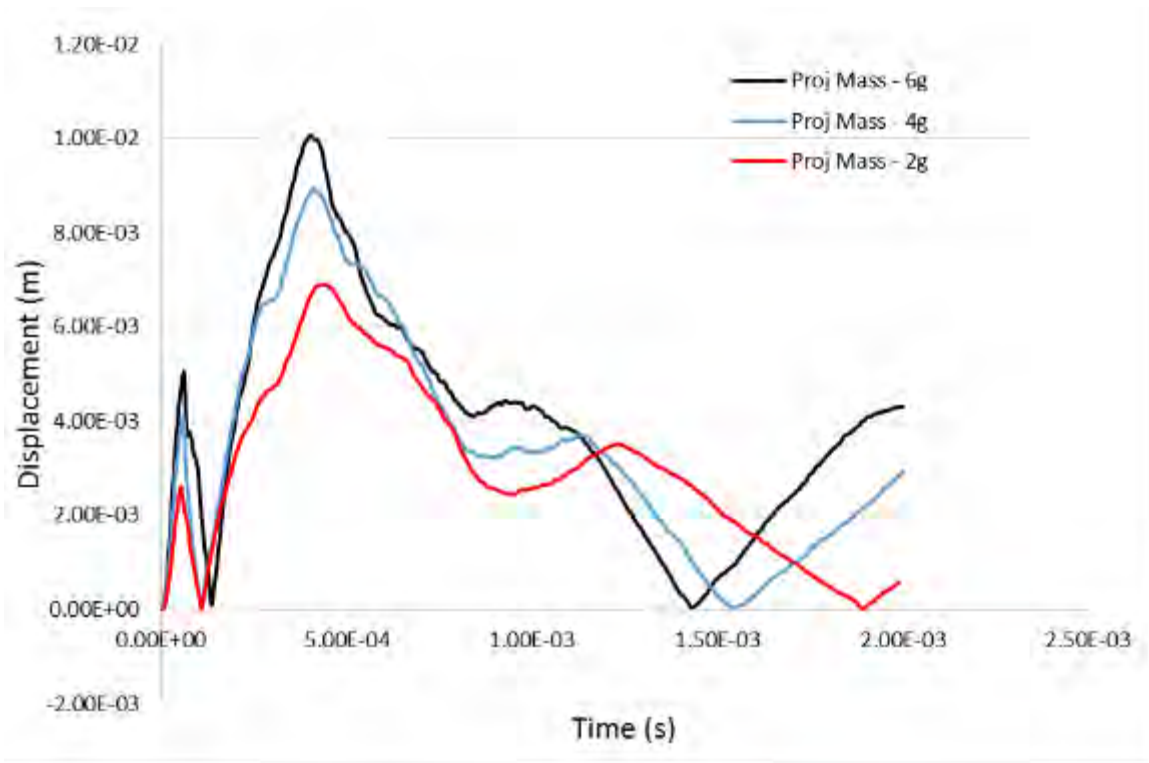


Figure 87. Entry wall resultant displacement for different projectile mass (Model 1).

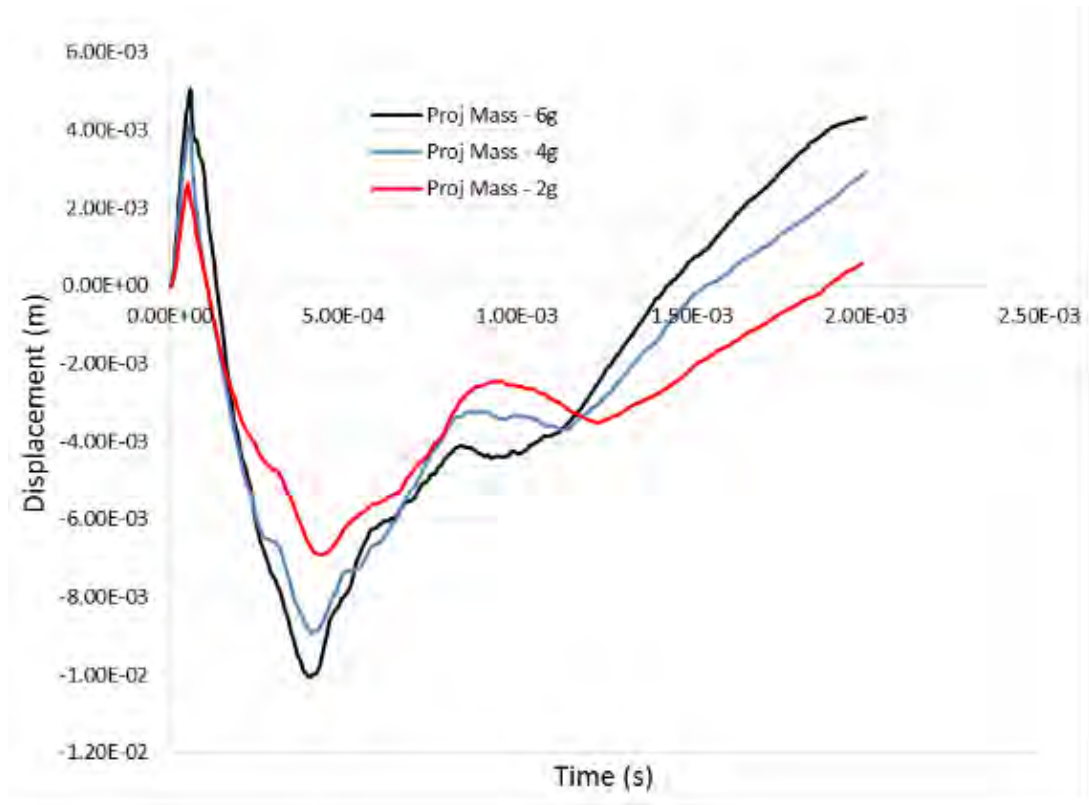


Figure 88. Entry wall X-Displacement for different projectile mass (Model 1).

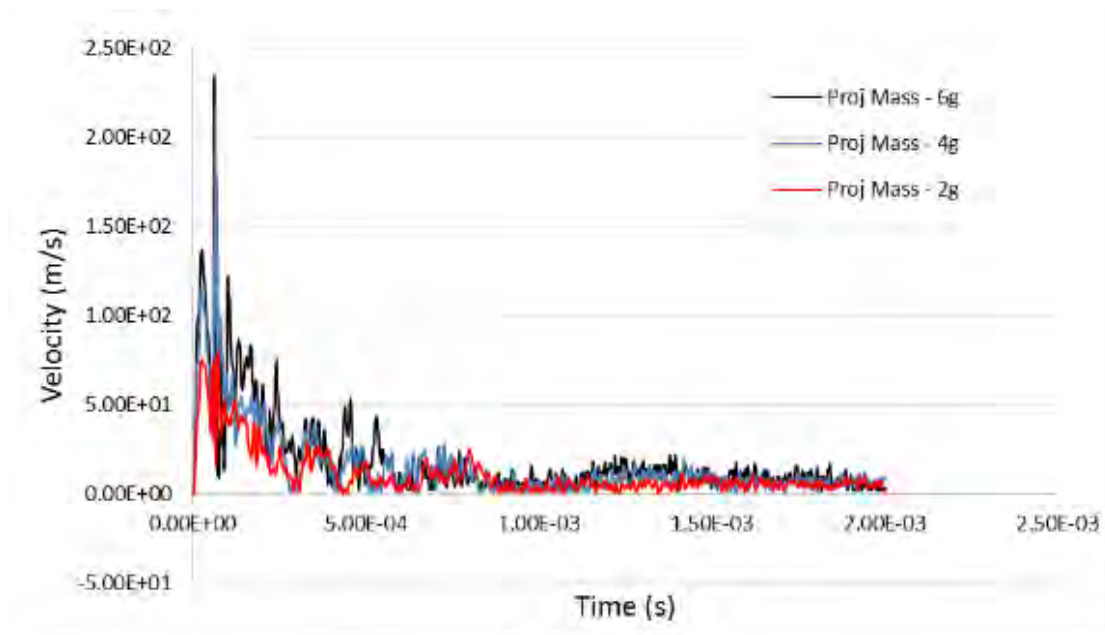


Figure 89. Entry wall resultant velocity for different projectile mass (Model 1).

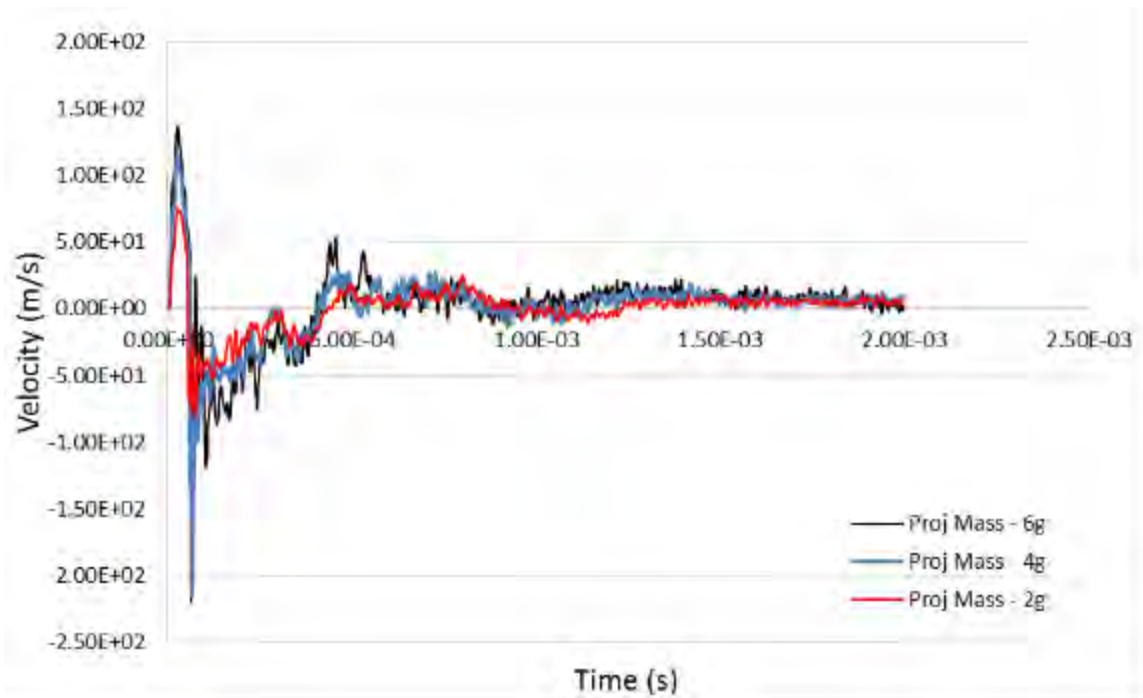


Figure 90. Entry wall X-Velocity for different projectile mass (Model 1).

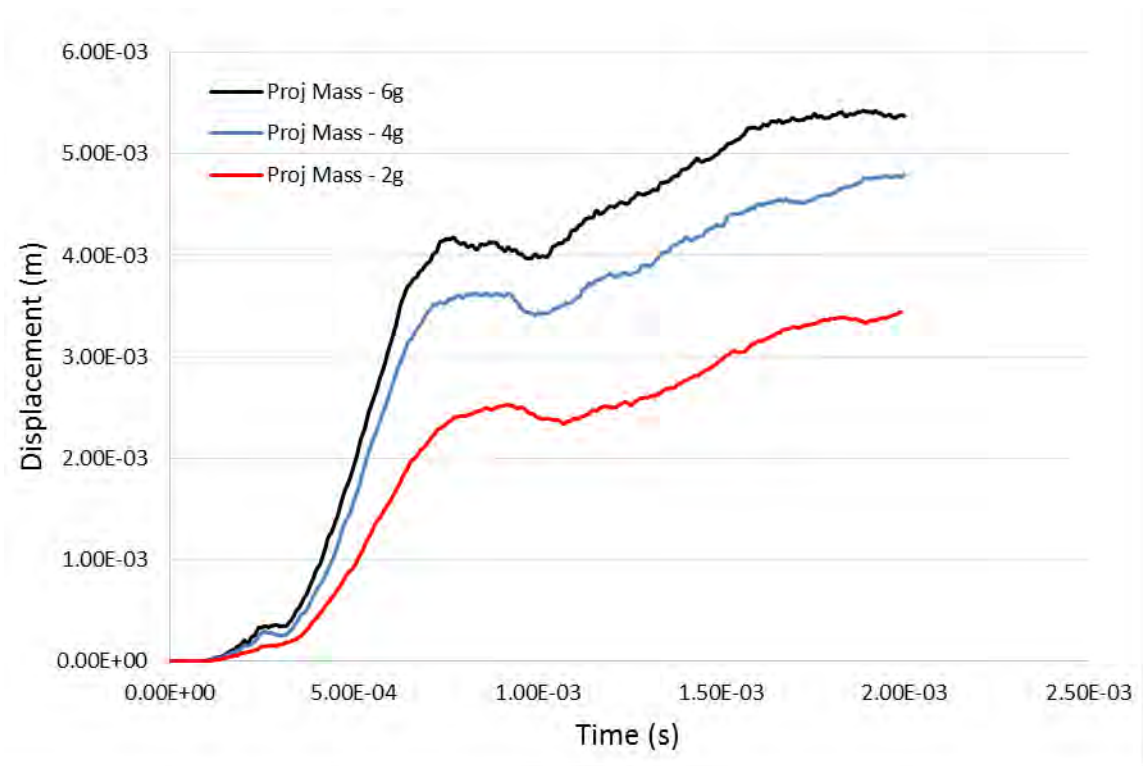


Figure 91. Left wall resultant displacement for different projectile mass (Model 1).

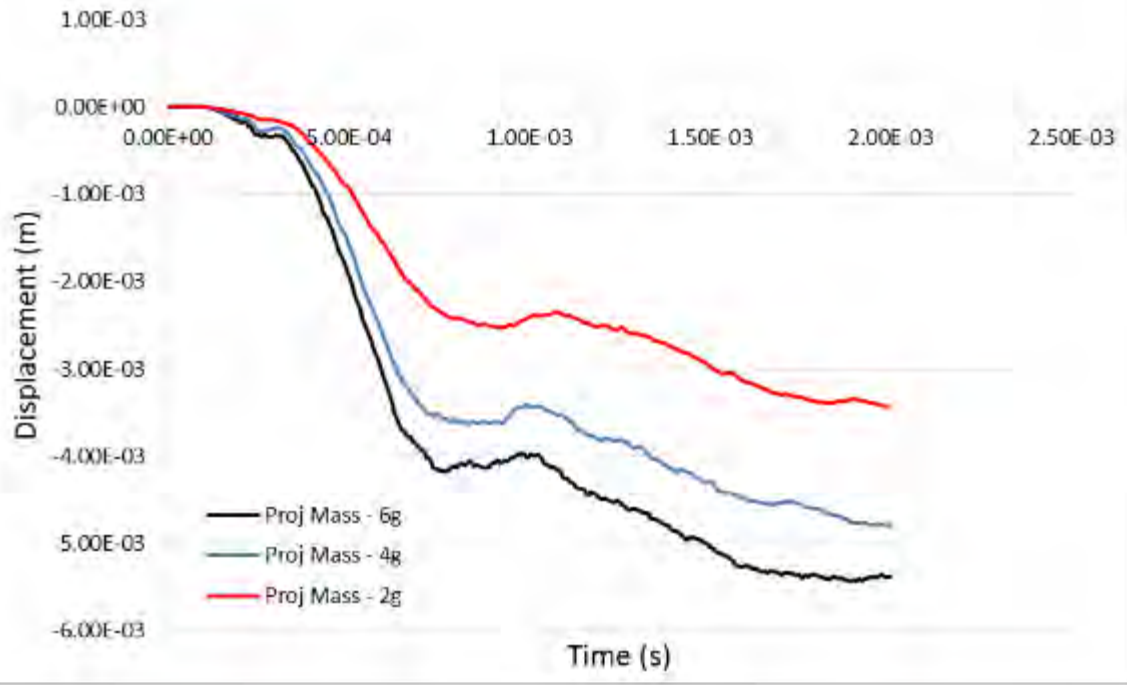


Figure 92. Left wall Z displacement for different projectile mass (Model 1).

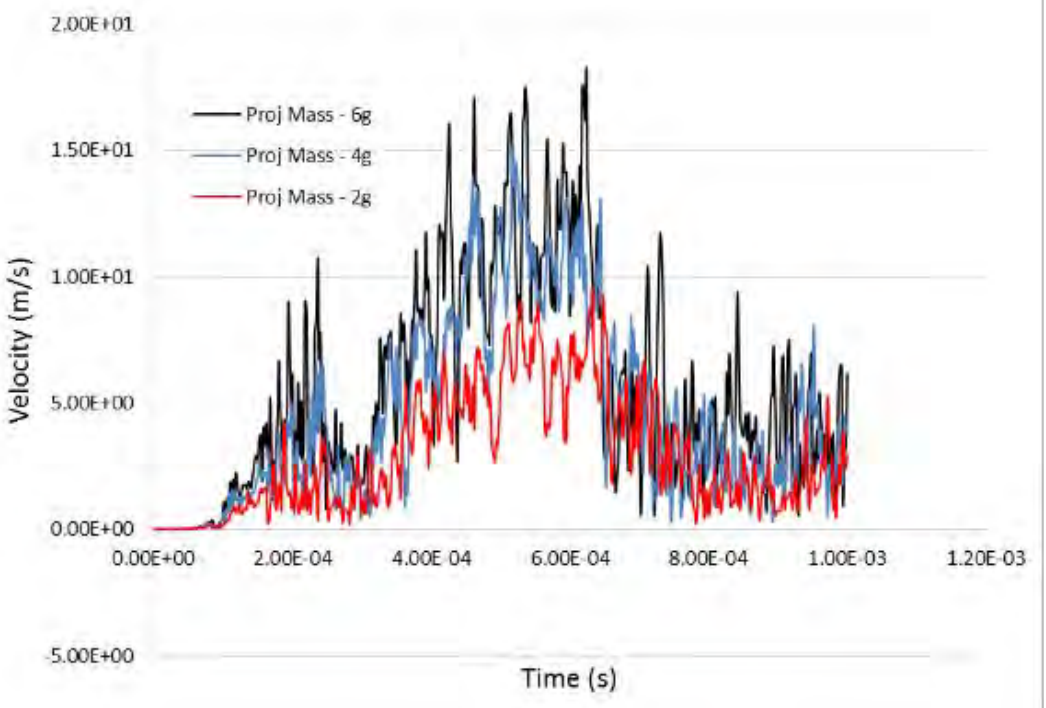


Figure 93. Left wall resultant velocity for different projectile mass (Model 1).

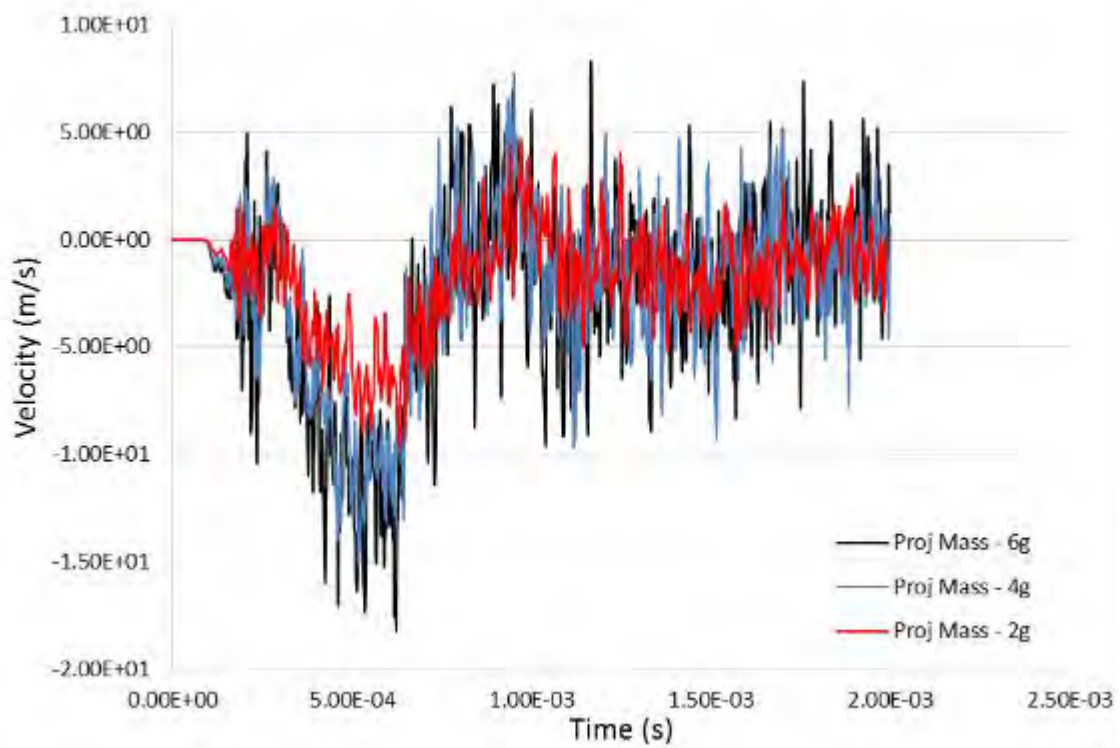


Figure 94. Left wall Z-Velocity for different projectile mass (Model 1).

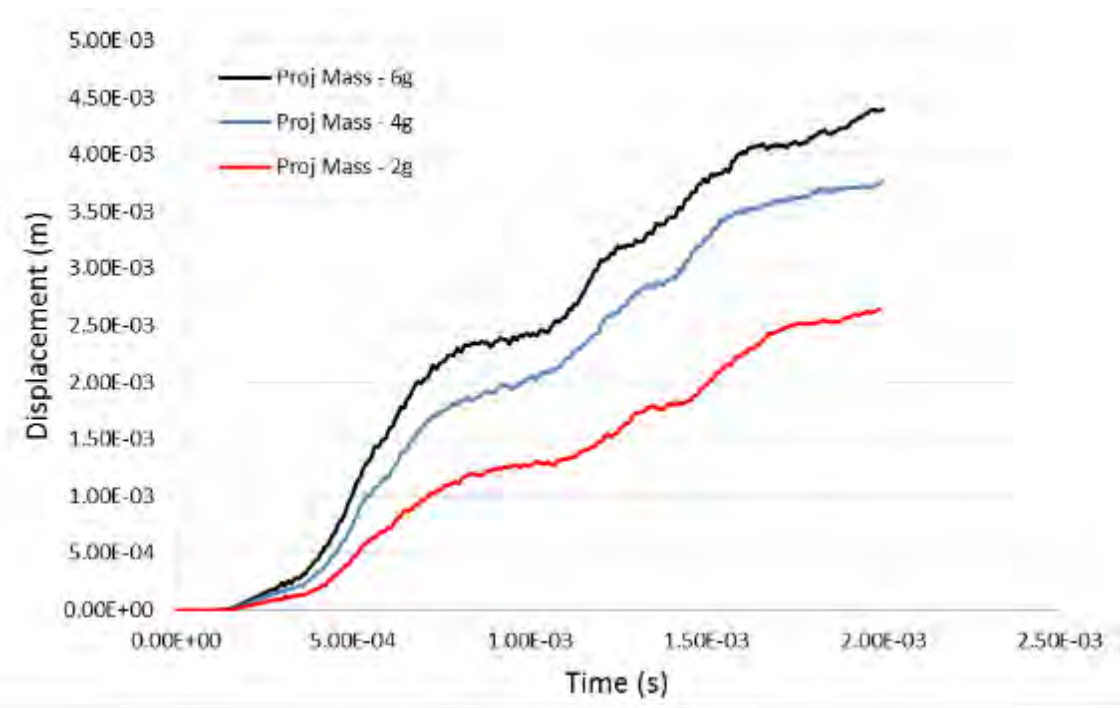


Figure 95. Exit wall resultant displacement for different projectile mass (Model 1).

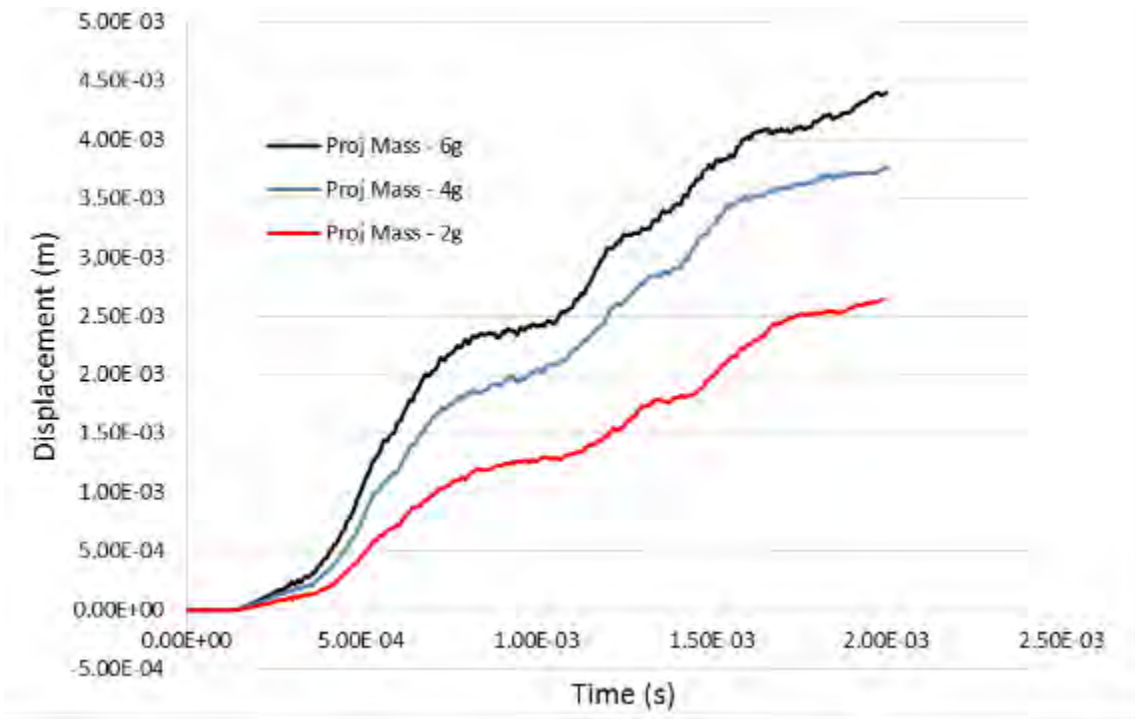


Figure 96. Exit wall X-Displacement for different projectile mass (Model 1).

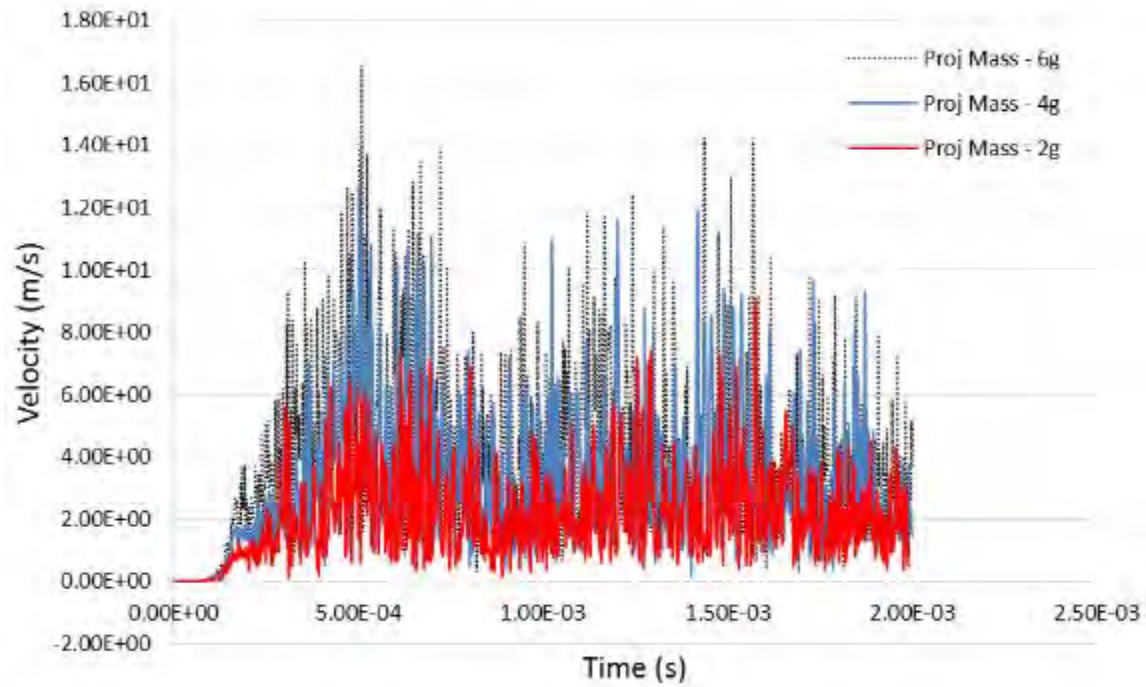


Figure 97. Exit wall resultant velocity for different projectile mass (Model 1).

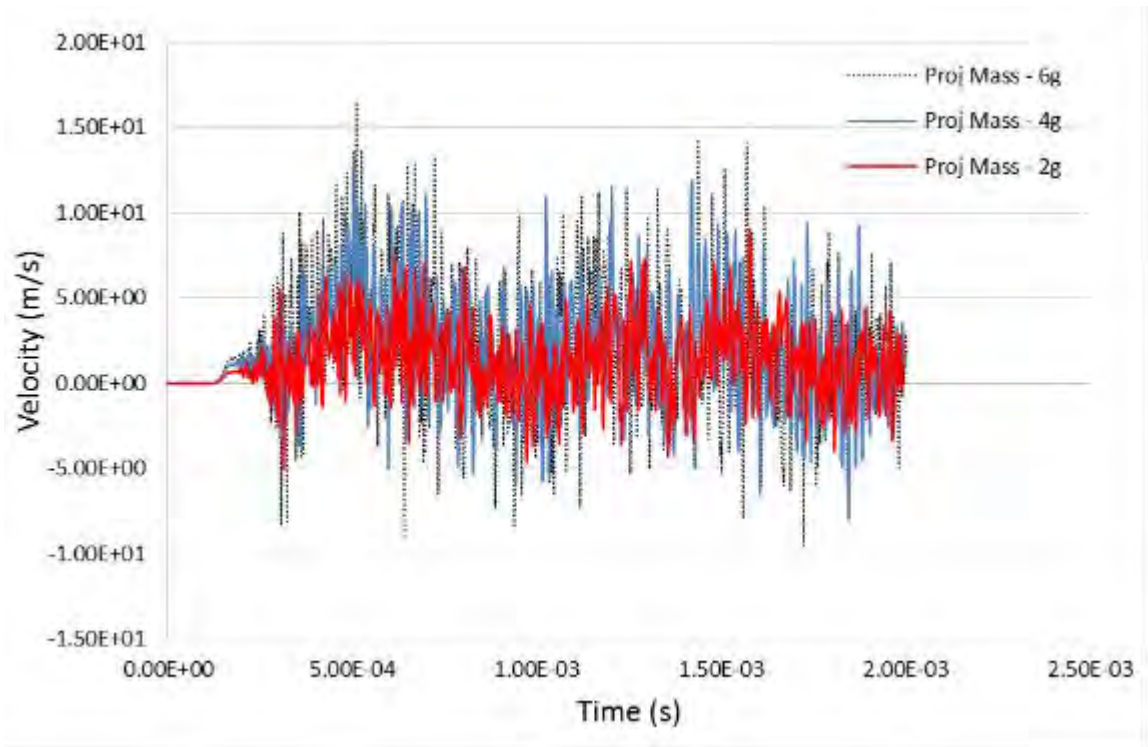


Figure 98. Exit wall X-Velocity for different projectile mass (Model 1).

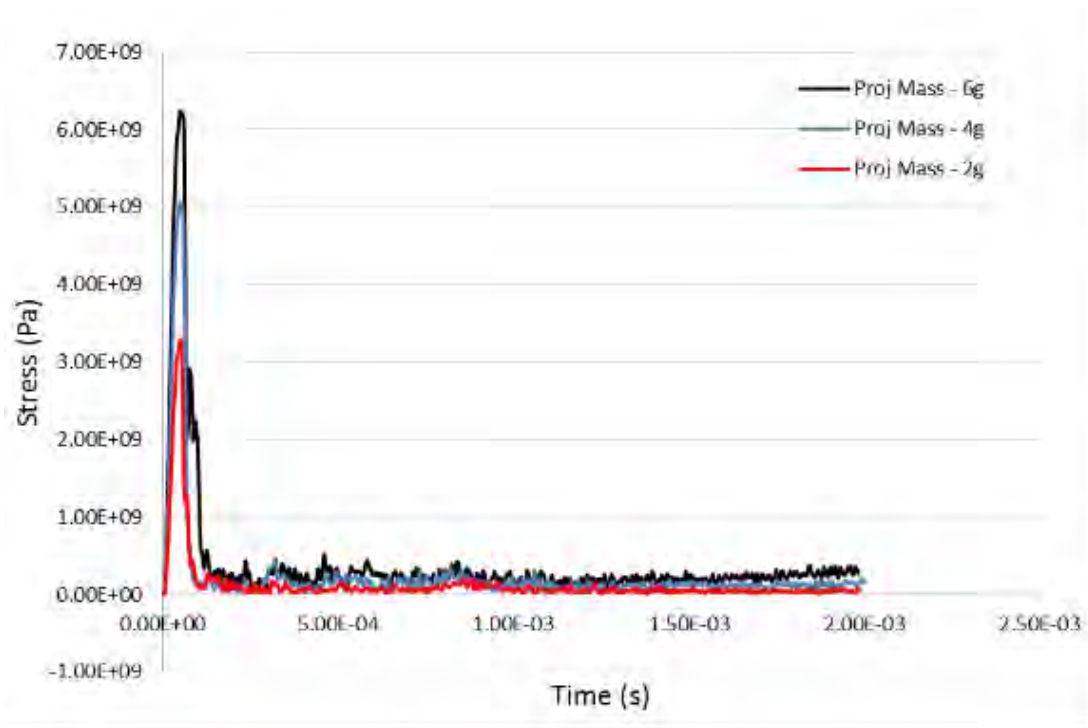


Figure 99. Entry wall effective stress for different projectile mass (Model 1).

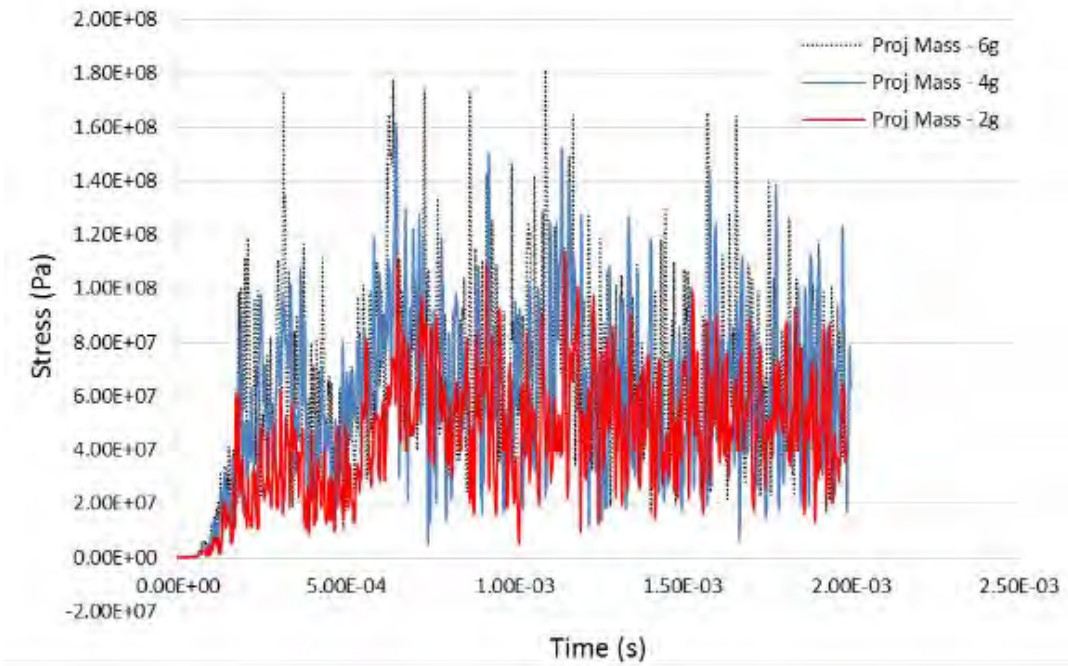


Figure 100. Left wall effective stress for different projectile mass (Model 1).

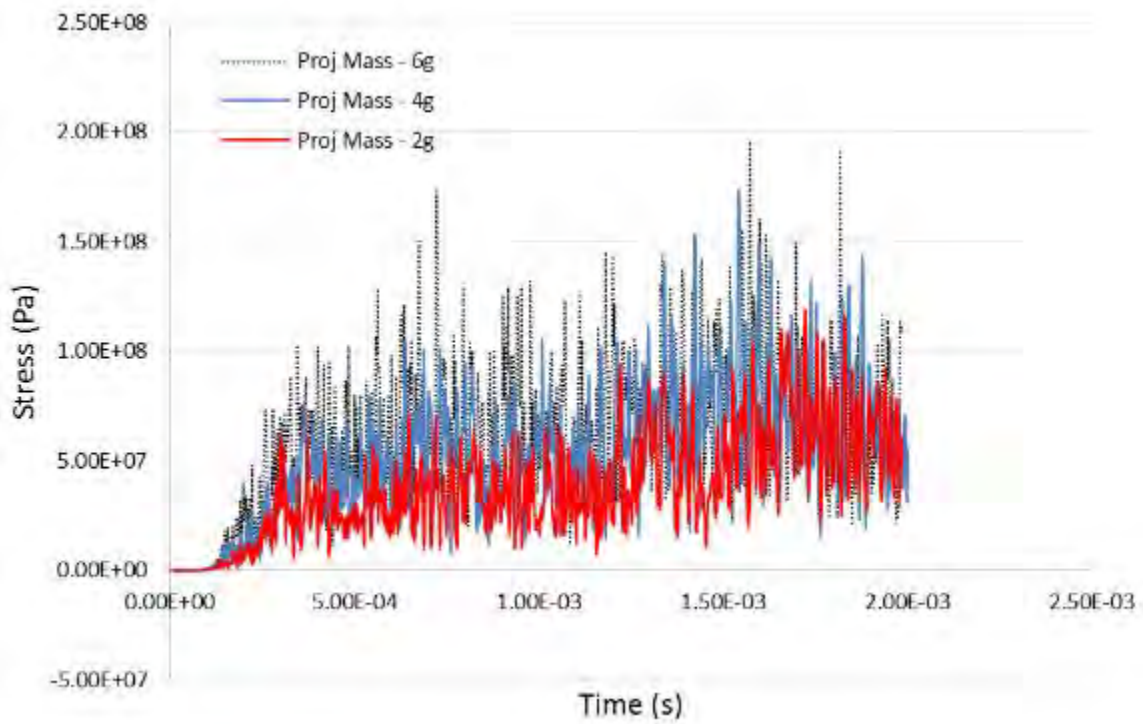


Figure 101. Exit wall effective stress for different projectile mass (Model 1).

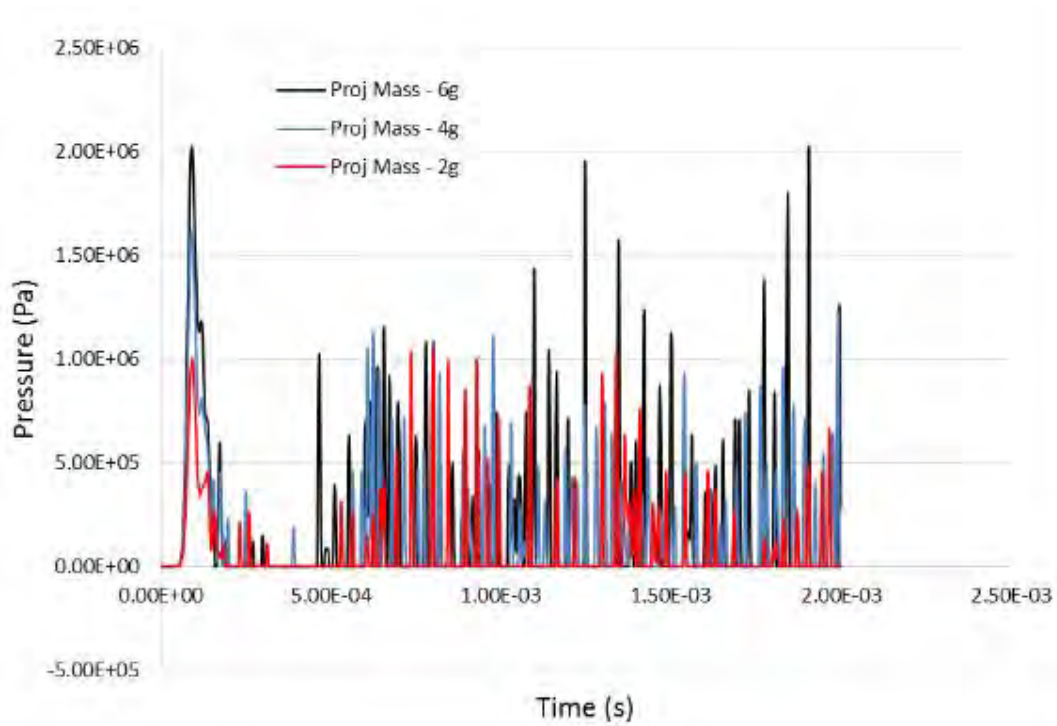


Figure 102. Fluid pressure for different projectile mass (Model 1).

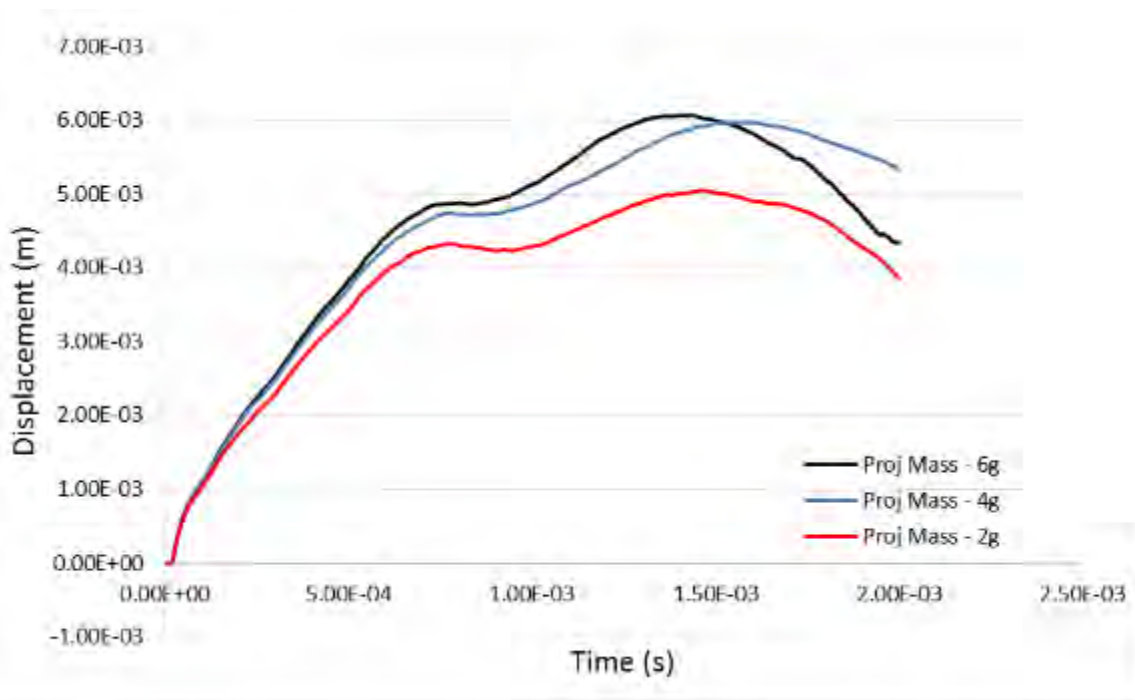


Figure 103. Entry wall resultant displacement for different projectile mass (Model 2).

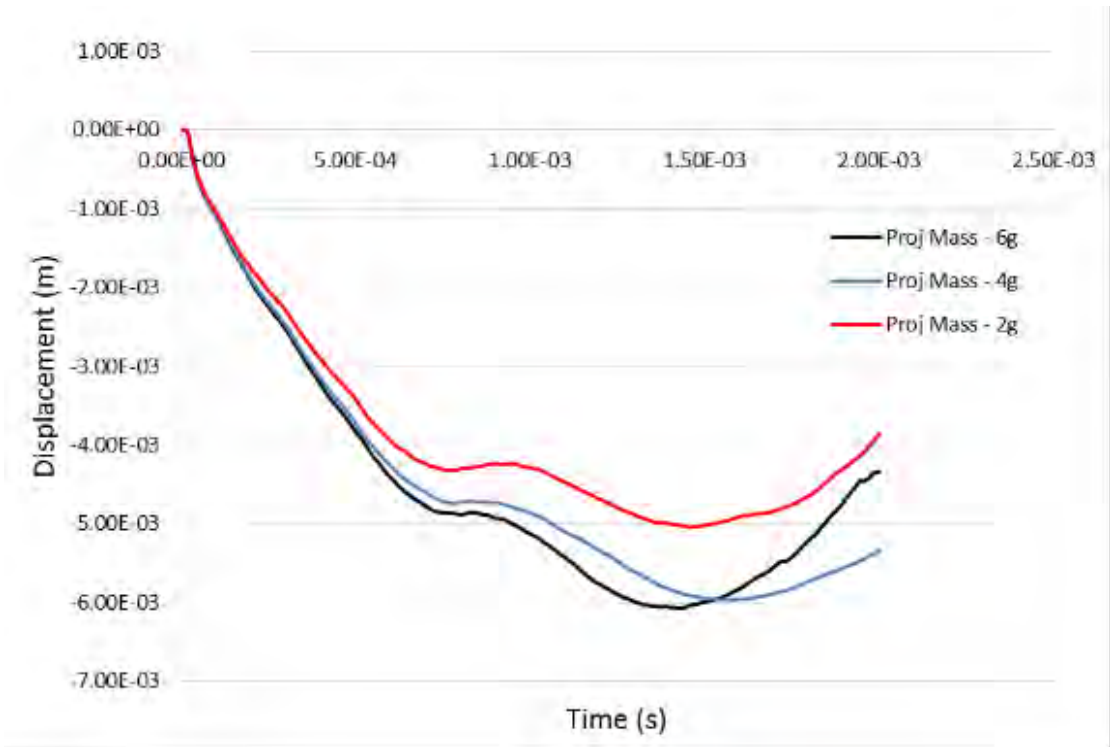


Figure 104. Entry wall X-Displacement for different projectile mass (Model 2).

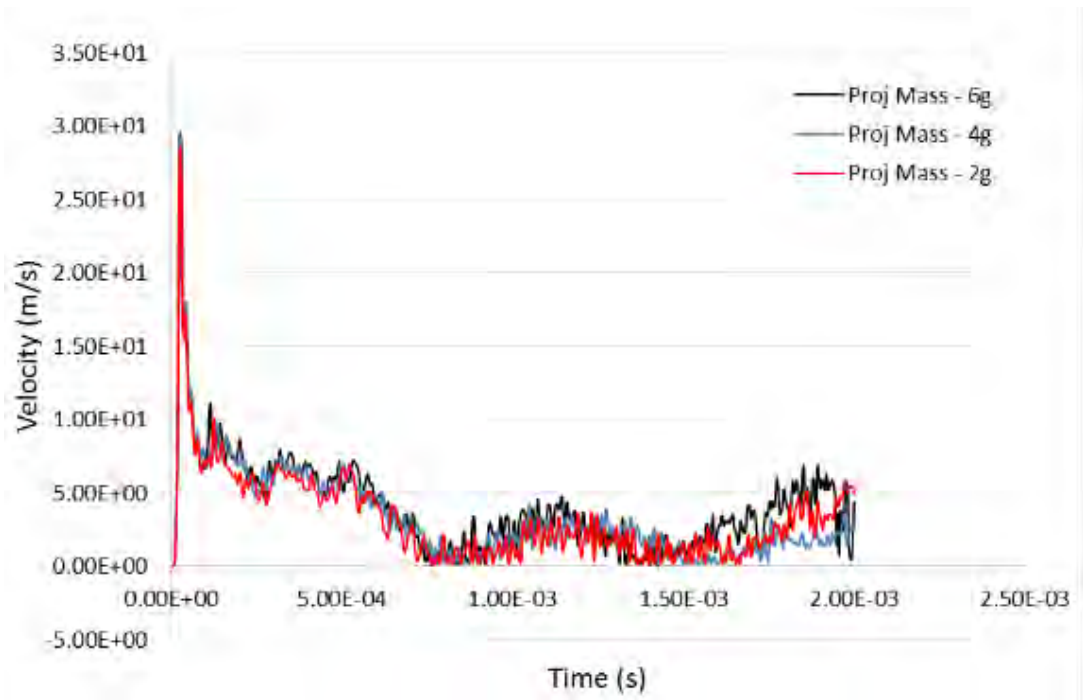


Figure 105. Entry wall resultant velocity for different projectile mass (Model 2).

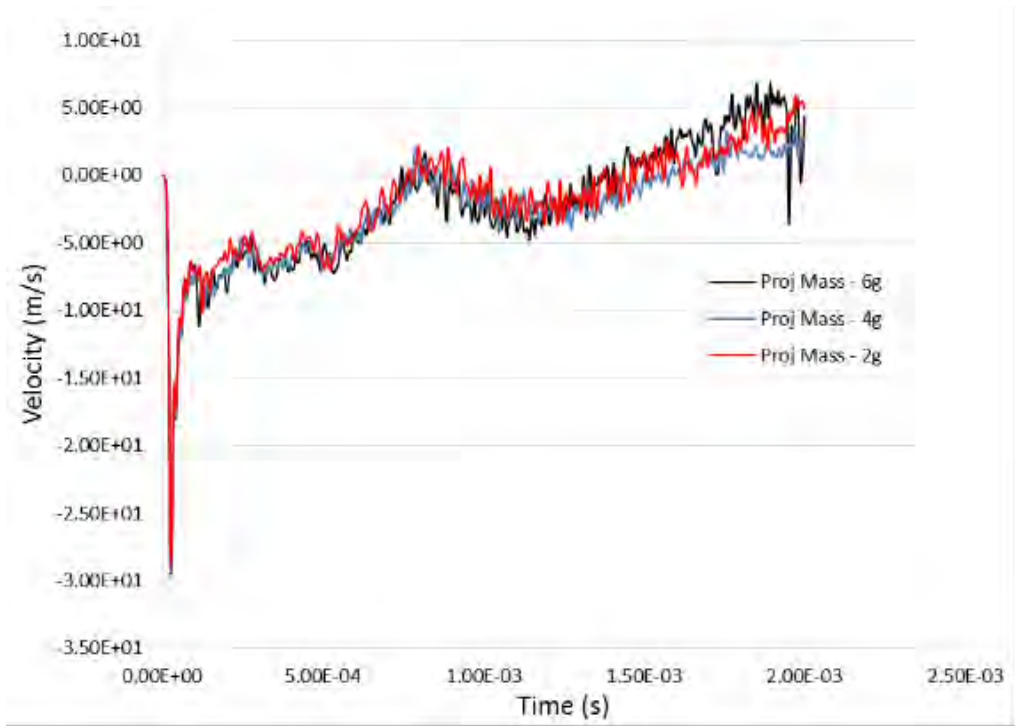


Figure 106. Entry wall X-Velocity for different projectile mass (Model 2).

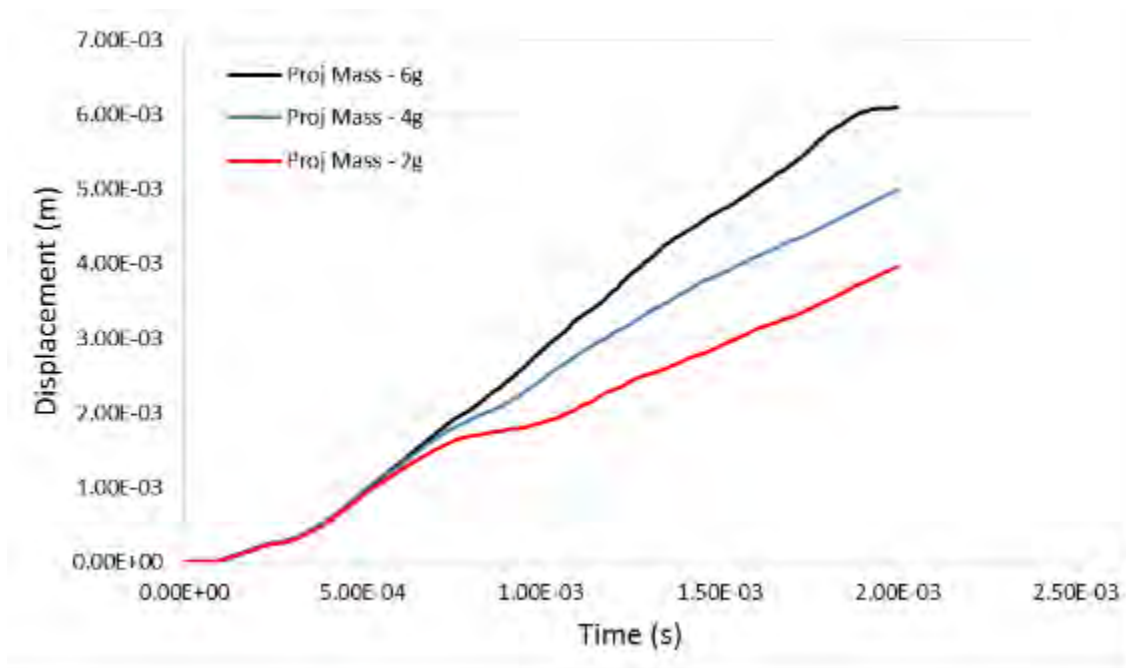


Figure 107. Left wall resultant displacement for different projectile mass (Model 2).

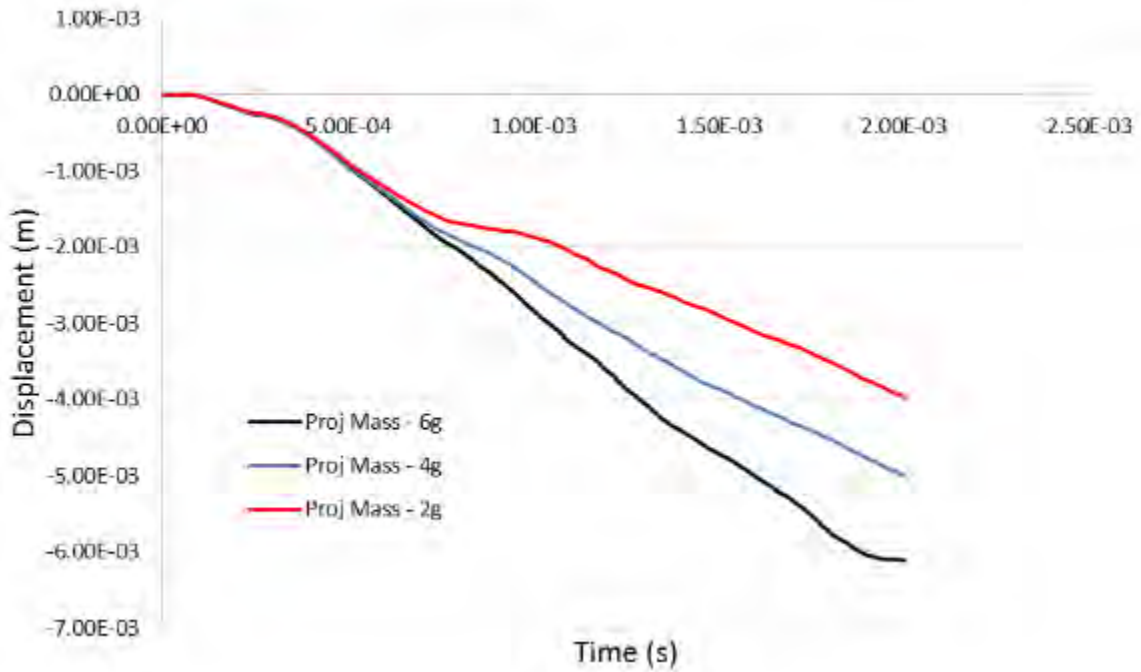


Figure 108. Left wall Z-Displacement for different projectile mass (Model 2).

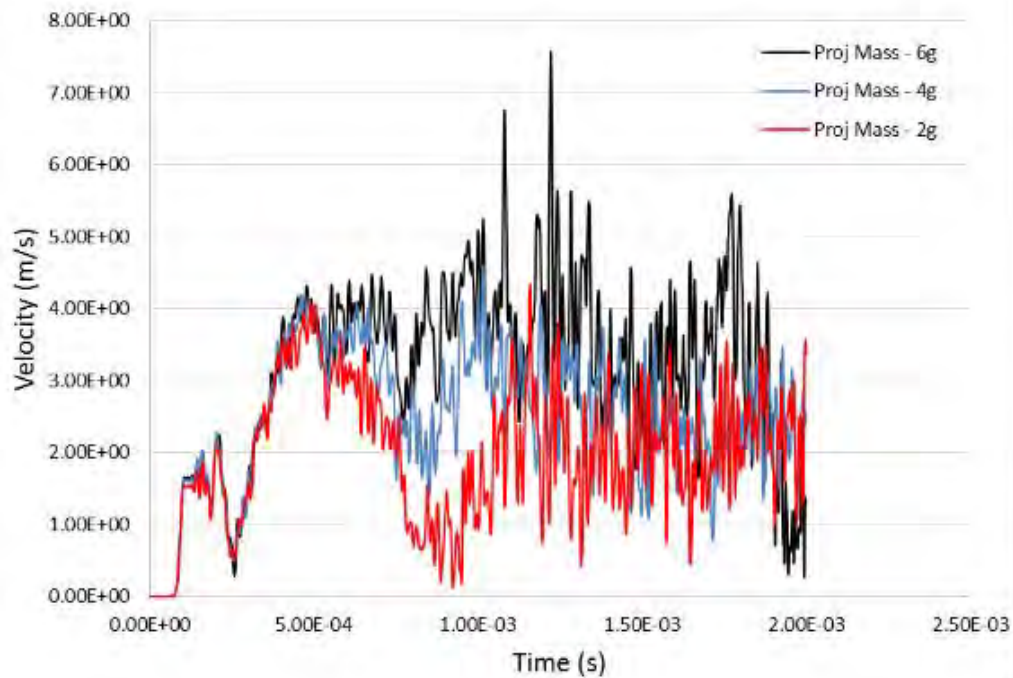


Figure 109. Left wall resultant velocity for different projectile mass (Model 2).

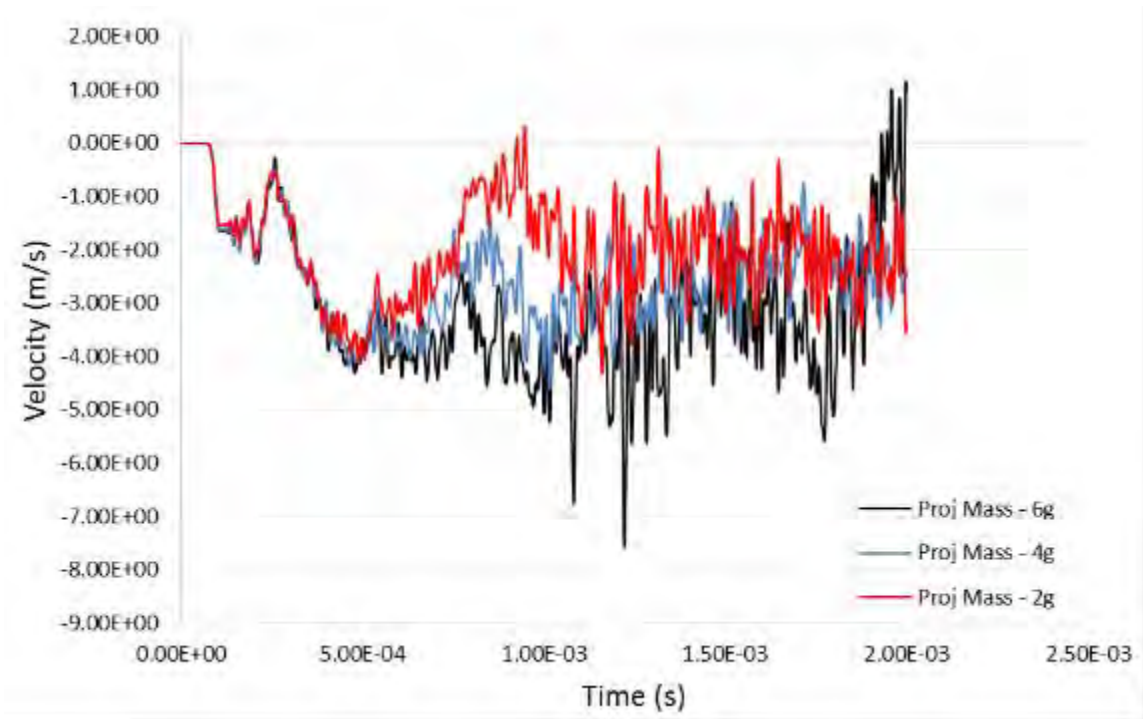


Figure 110. Left wall Z-Velocity for different projectile mass (Model 2).

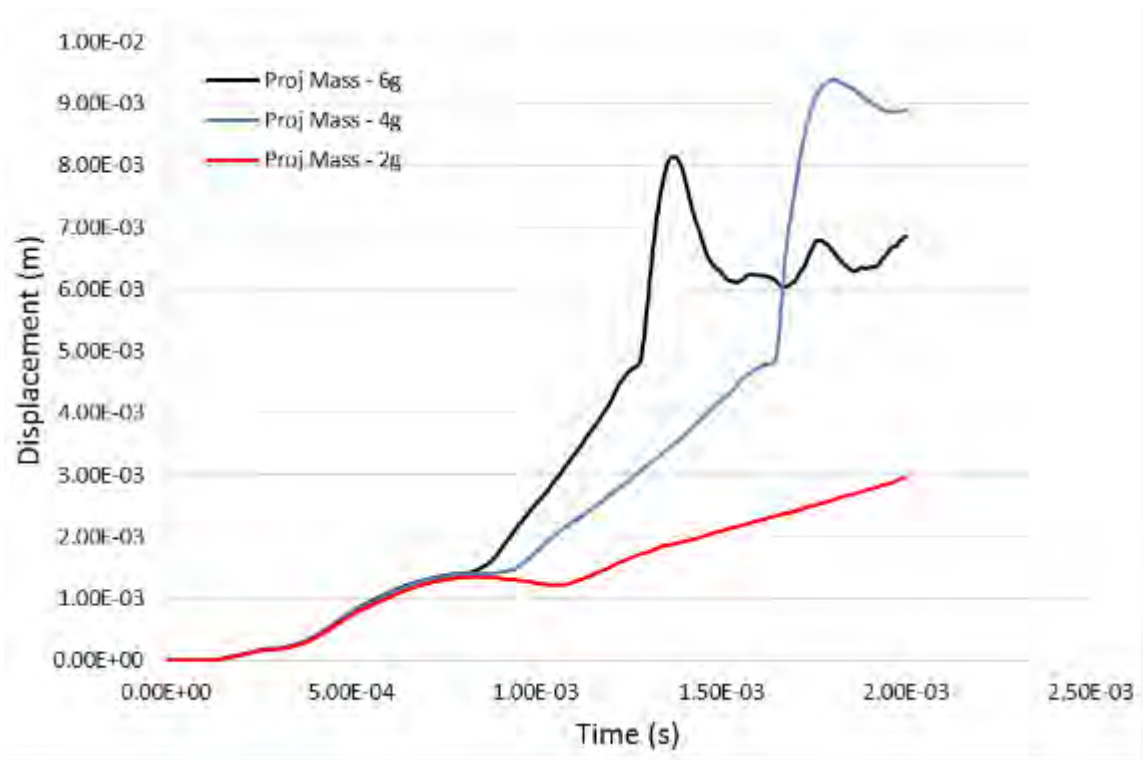


Figure 111. Exit wall resultant displacement for different projectile mass (Model 2).

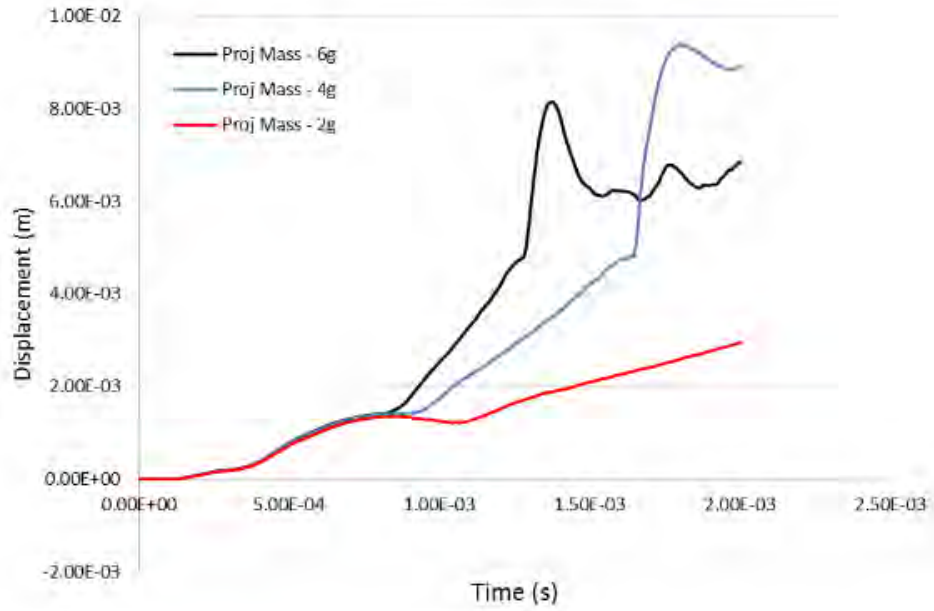


Figure 112. Exit wall X-Displacement for different projectile mass (Model 2).

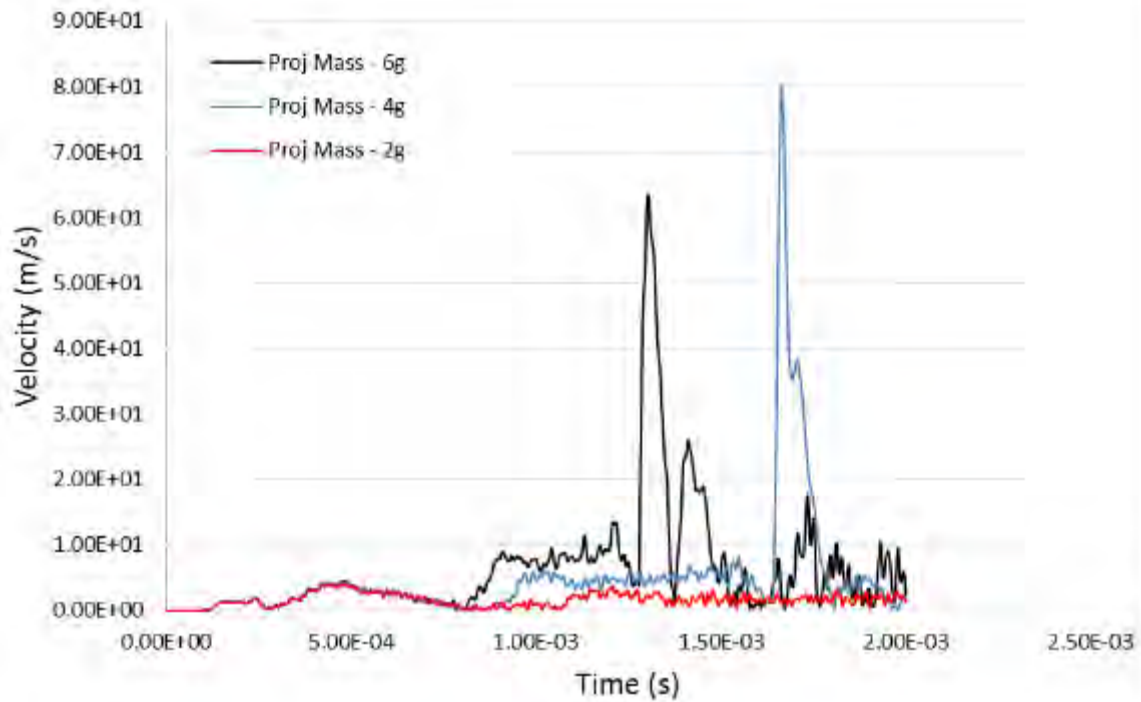


Figure 113. Exit wall resultant velocity for different projectile mass (Model 2).

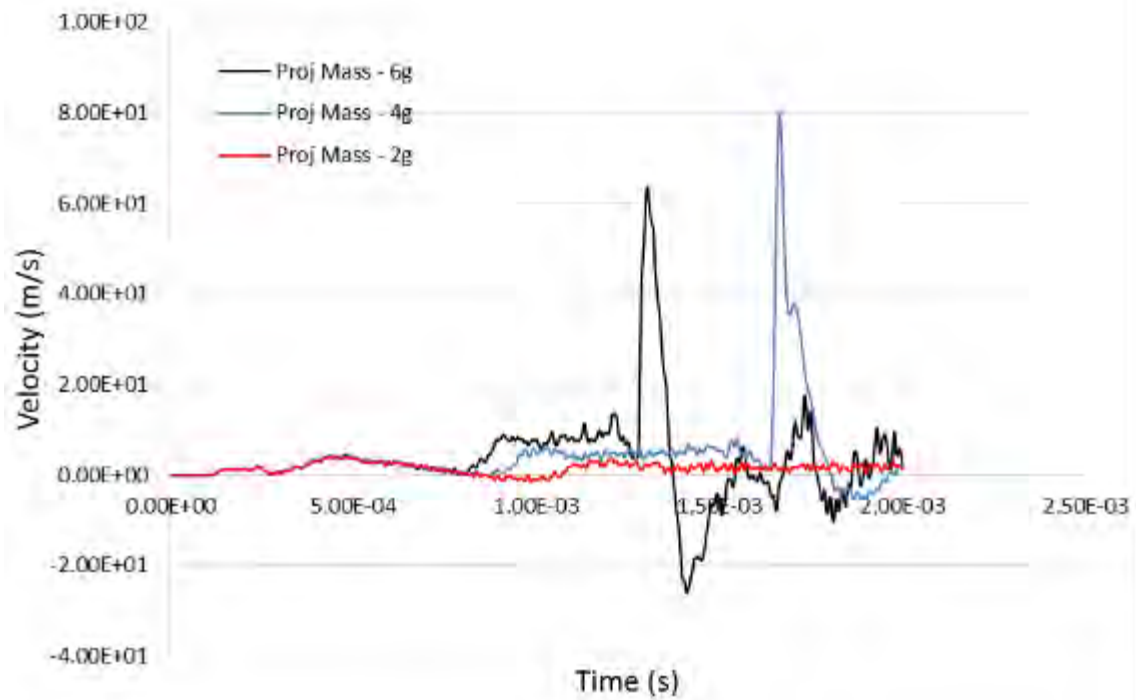


Figure 114. Exit wall X-Velocity for different projectile mass (Model 2).

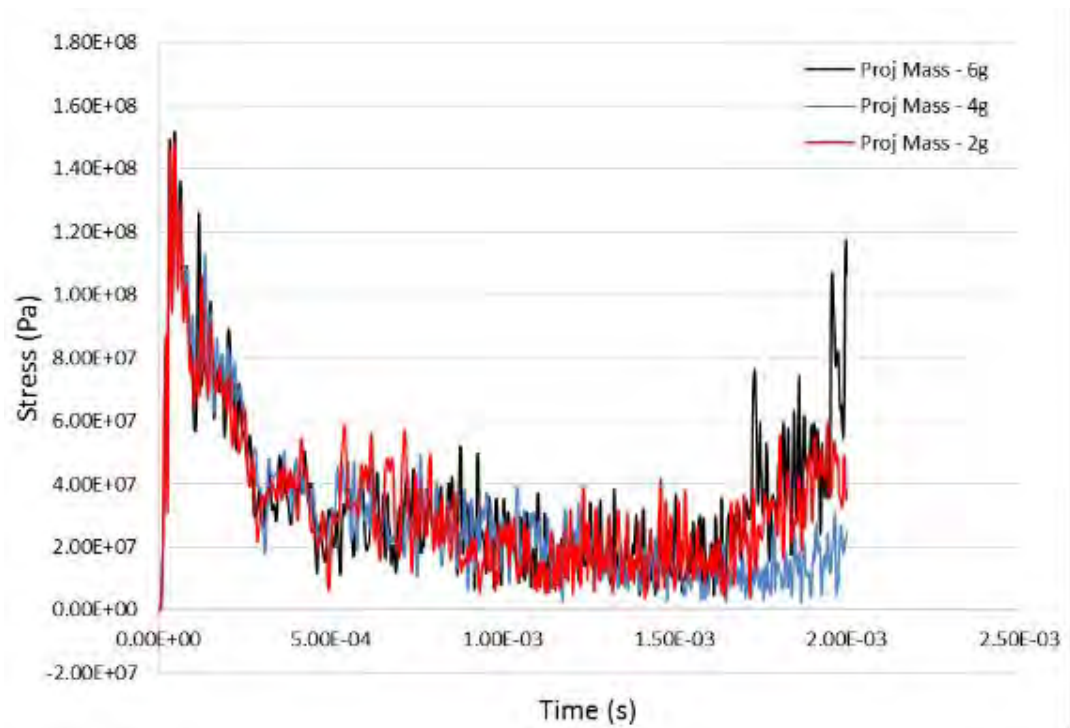


Figure 115. Entry wall effective stress for different projectile mass (Model 2).

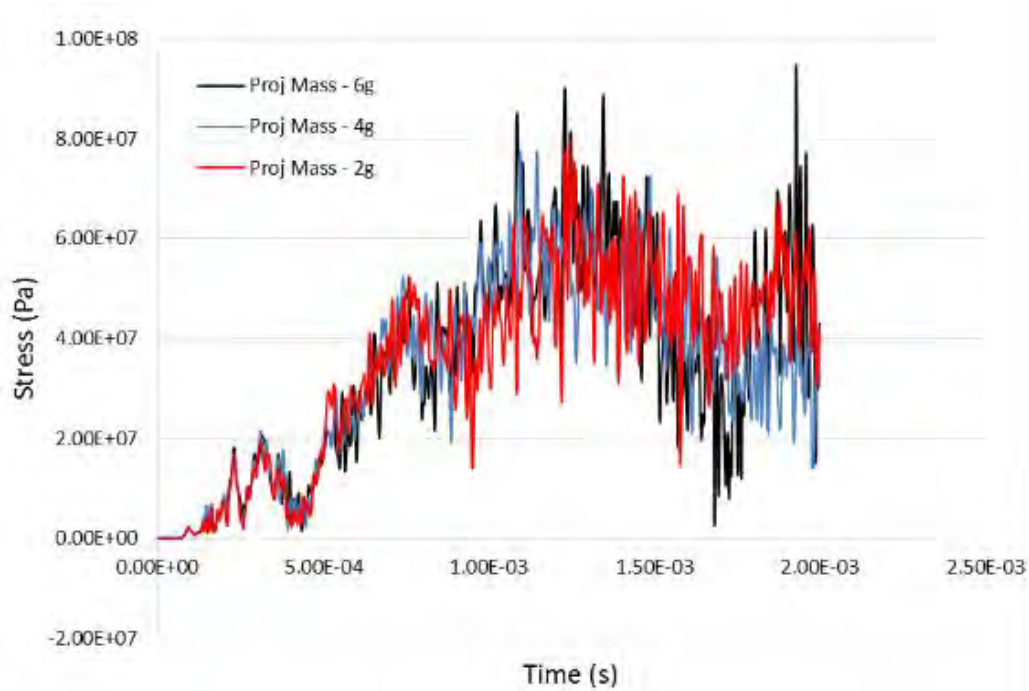


Figure 116. Left wall effective stress for different projectile mass (Model 2).

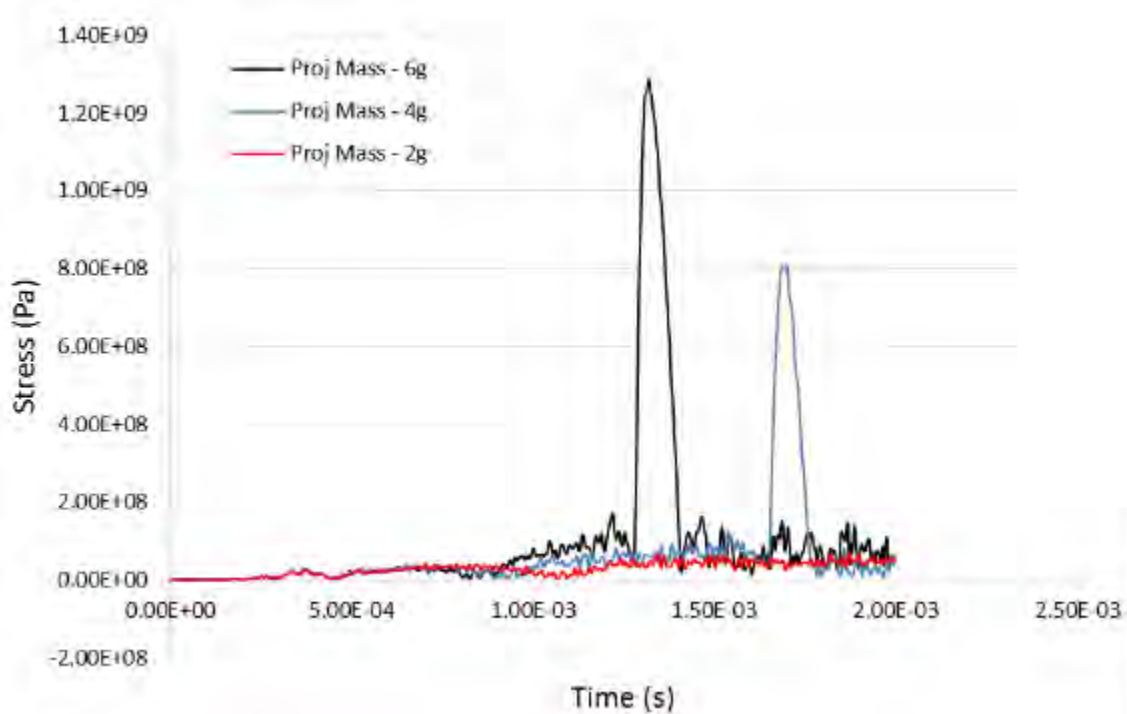


Figure 117. Exit wall effective stress for different projectile mass (Model 2).

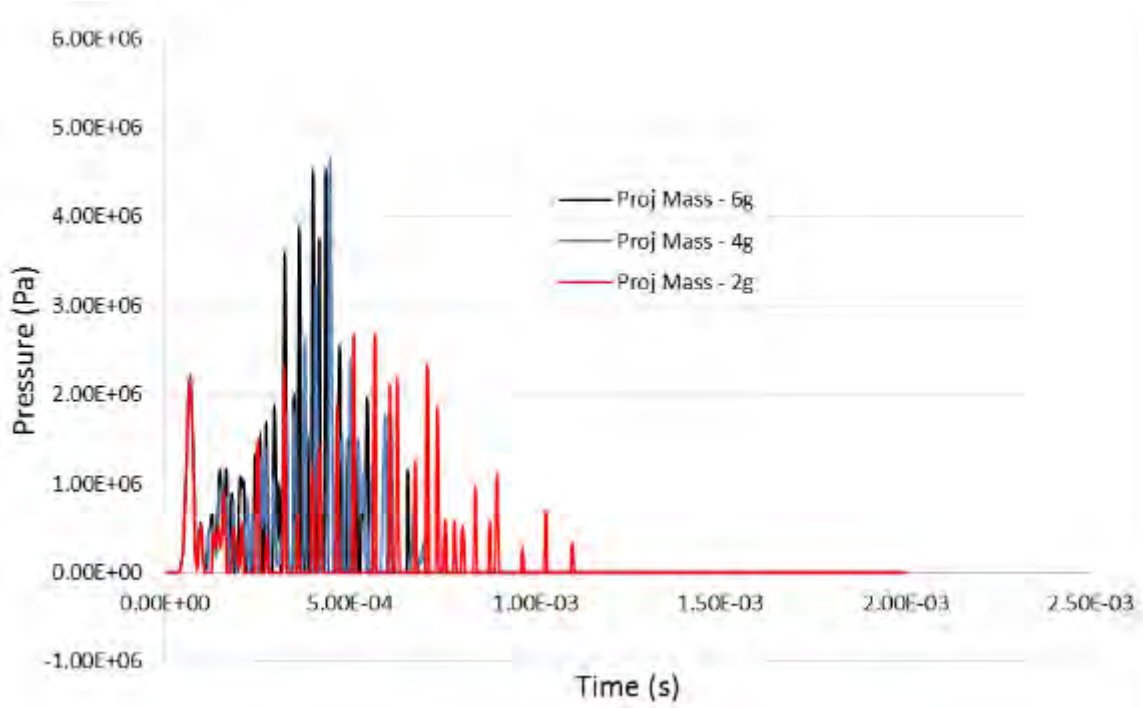


Figure 118. Drag phase pressure for different projectile mass (Model 2).

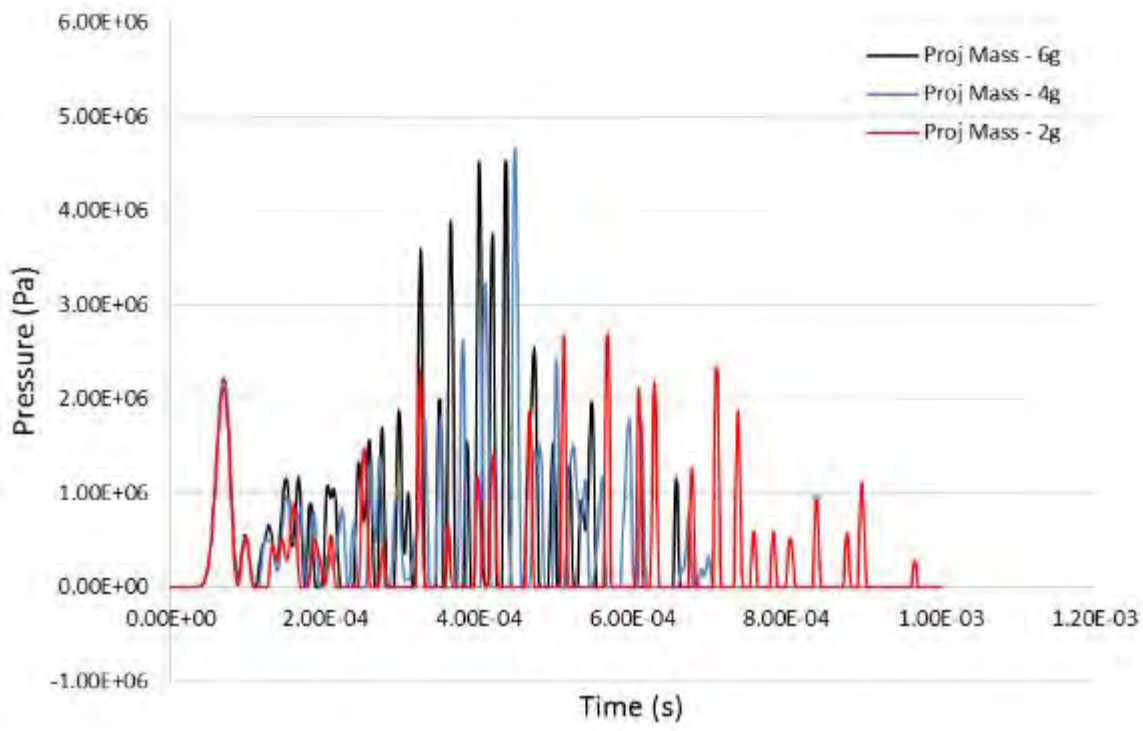
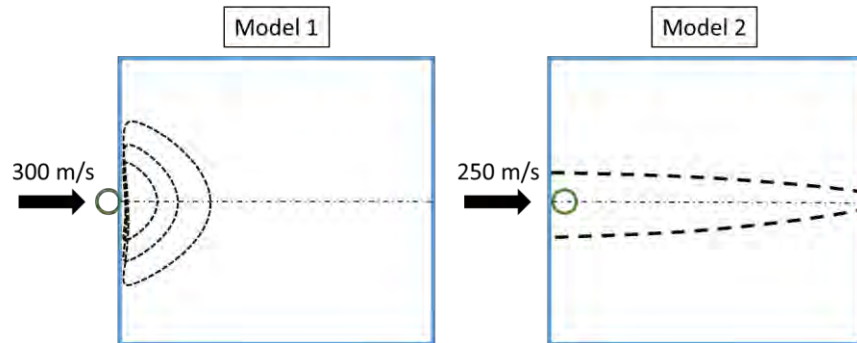


Figure 119. Drag phase pressure for different projectile mass (Model 2). –
Enlarged

THIS PAGE INTENTIONALLY LEFT BLANK

APPENDIX C. GRAPHS FOR PROJECTILE VELOCITY VARIATION



- Projectile velocities investigated: Model 1: 100m/s, 300m/s, 500m/s; Model 2: 100m/s, 250m/s, 500m/s.

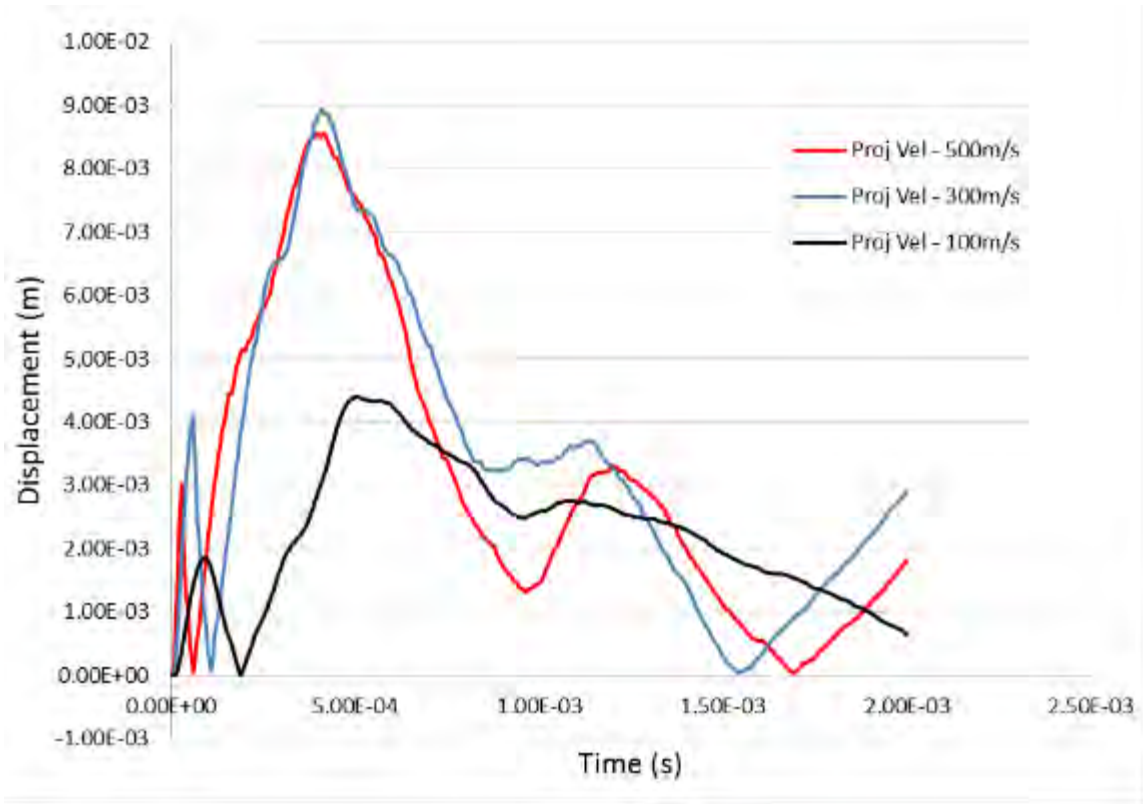


Figure 120. Exit wall resultant displacement for different projectile velocity (Model 1).

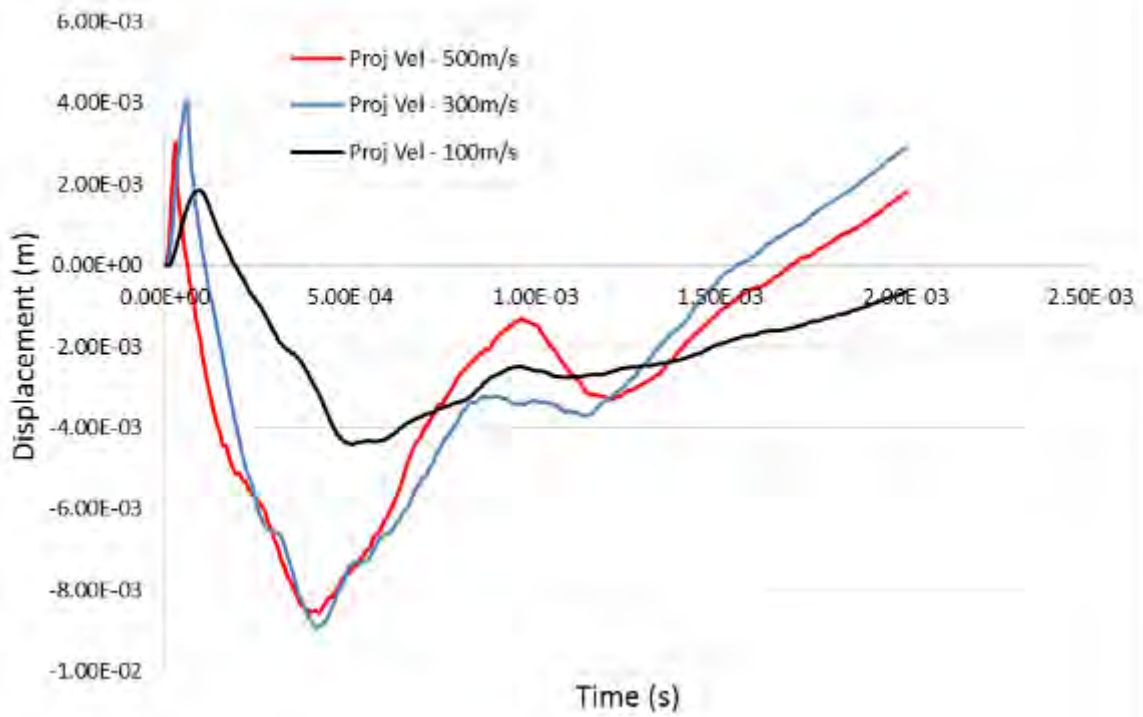


Figure 121. Exit wall X-Displacement for different projectile velocity (Model 1).

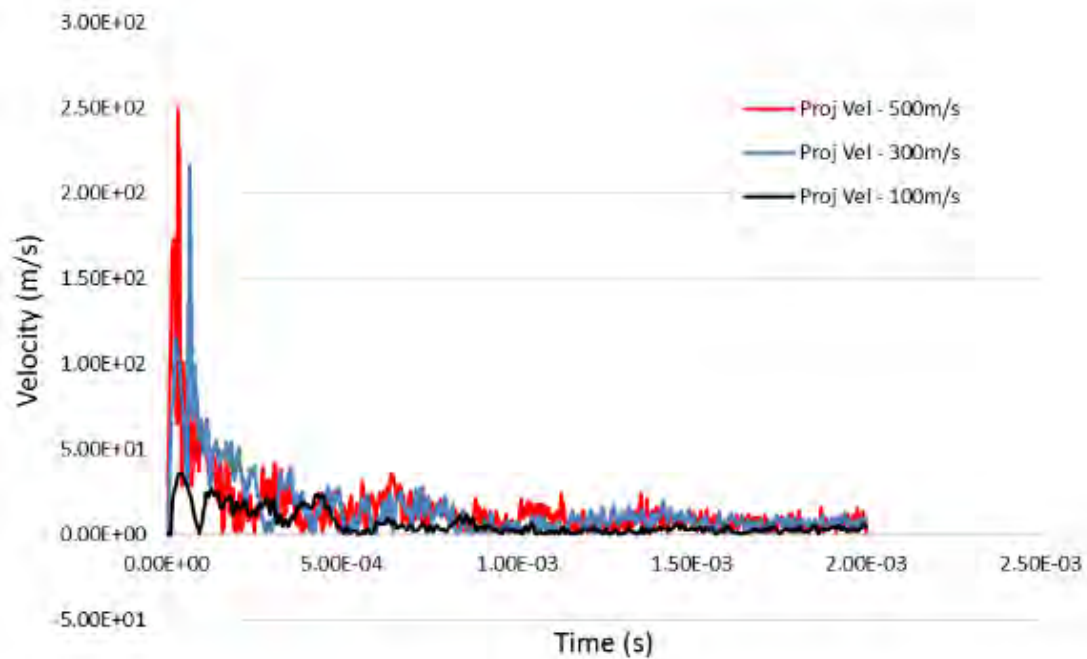


Figure 122. Exit wall resultant velocity for different projectile velocity (Model 1).

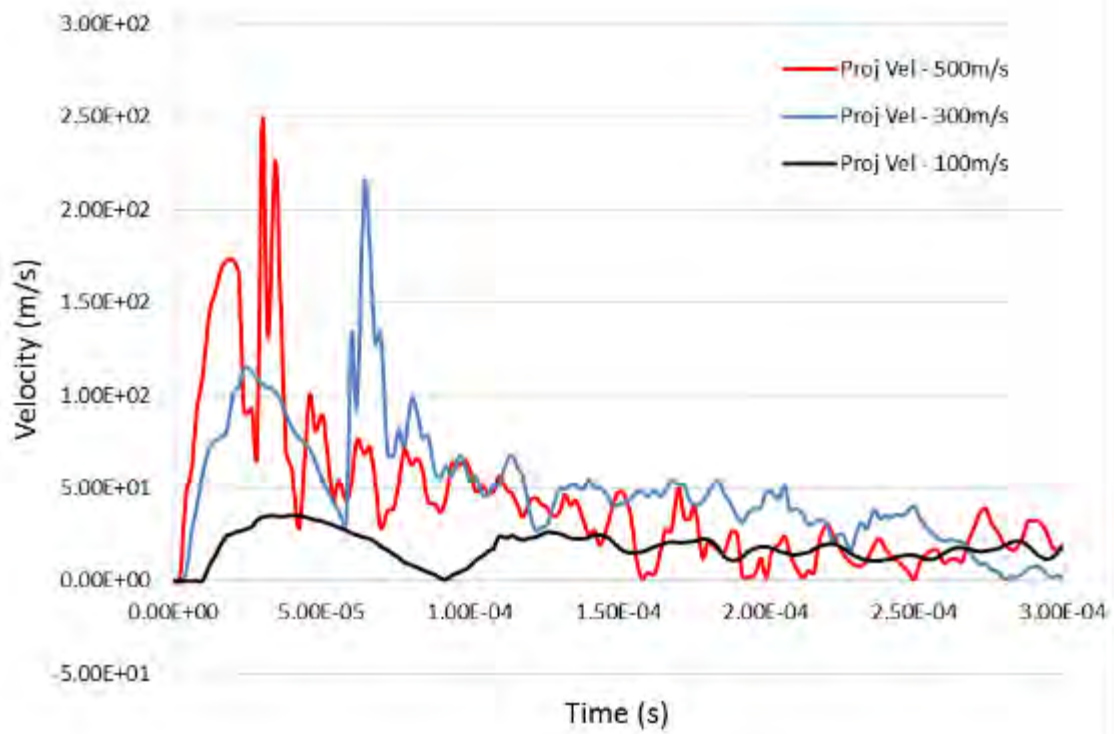


Figure 123. Exit wall resultant velocity for different projectile velocity (Model 1) – Enlarged.

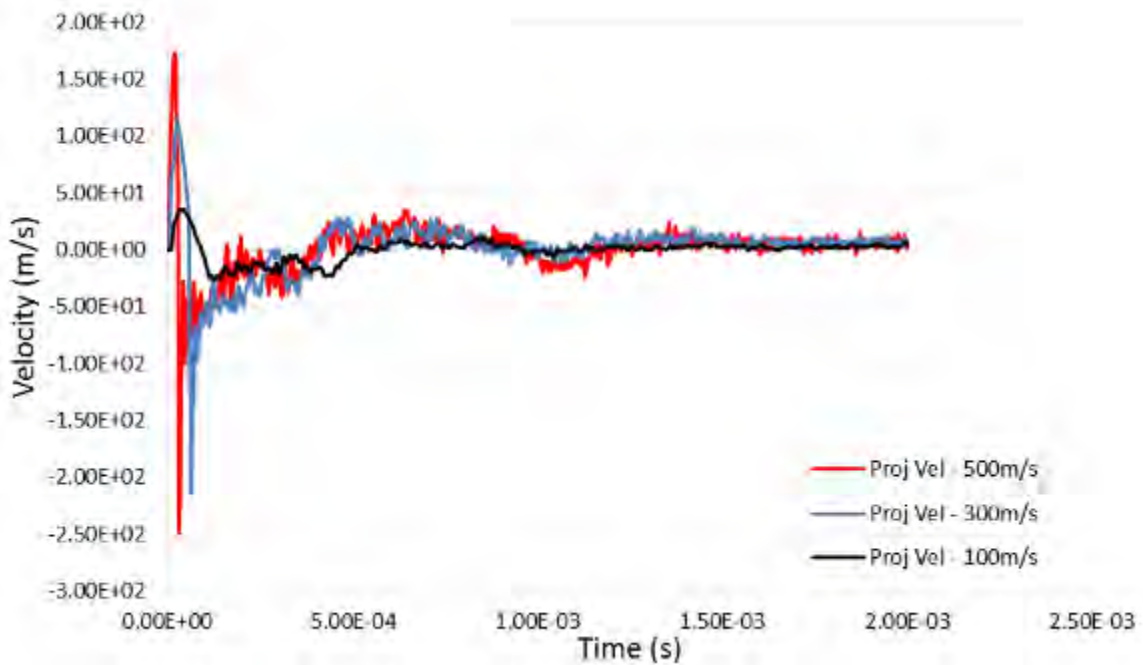


Figure 124. Exit wall X-Velocity for different projectile velocity (Model 1).

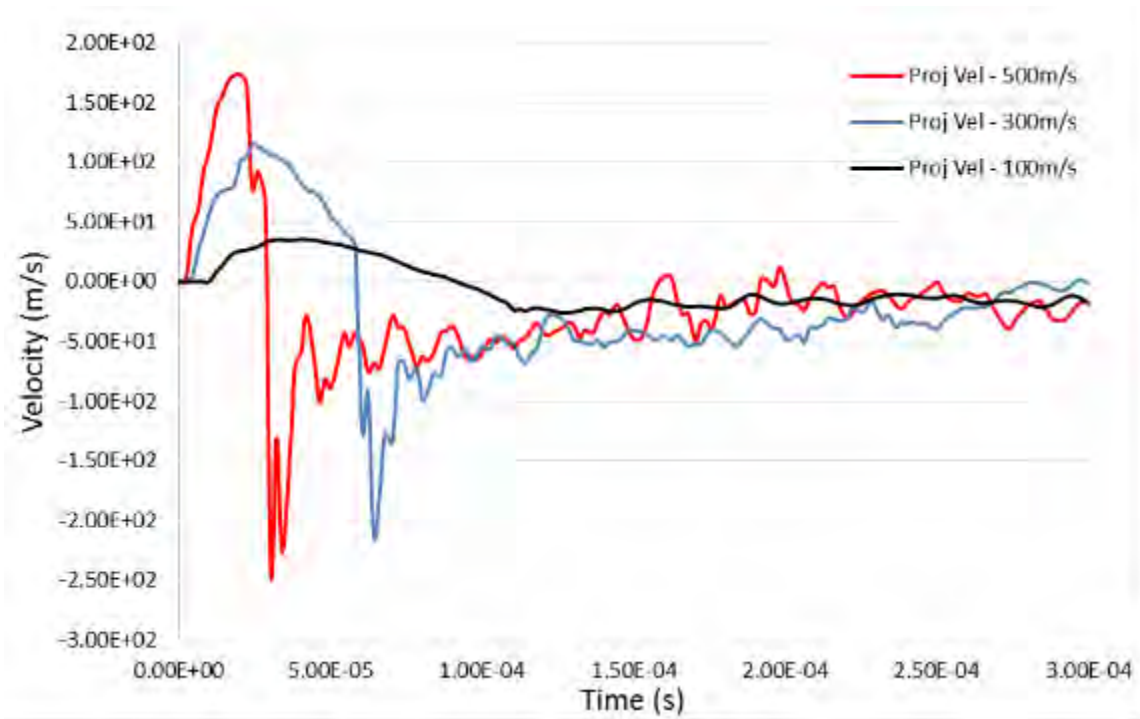


Figure 125. Exit wall X-Velocity for different projectile velocity (Model 1) – Enlarged.

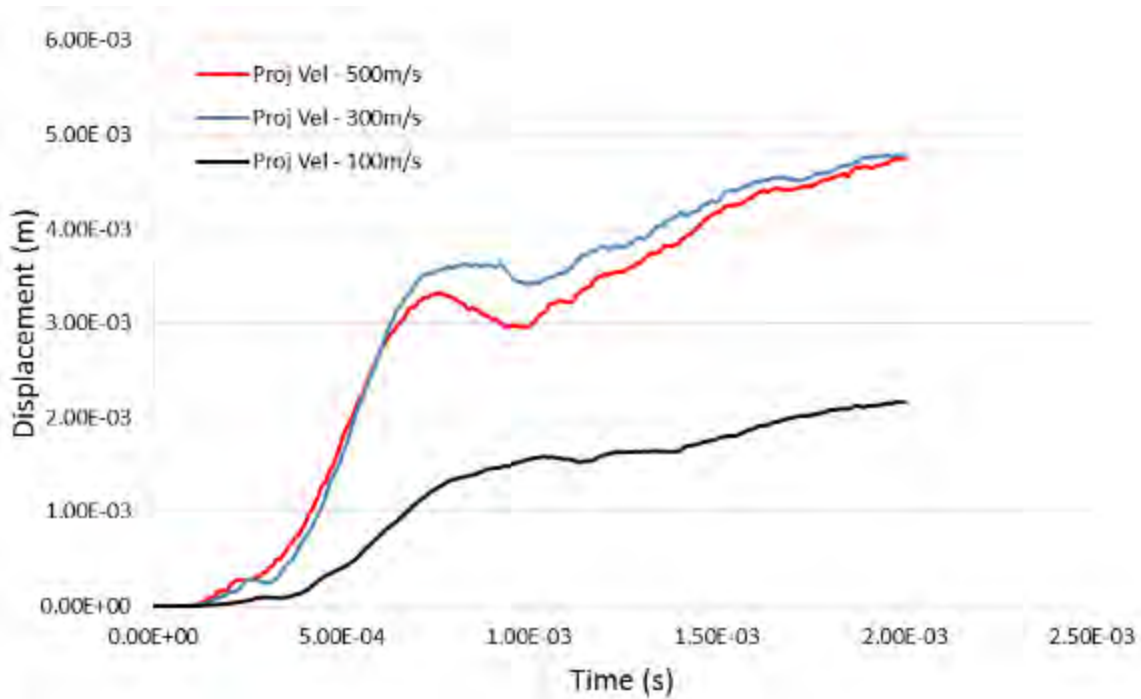


Figure 126. Left wall resultant displacement for different projectile velocity (Model 1).

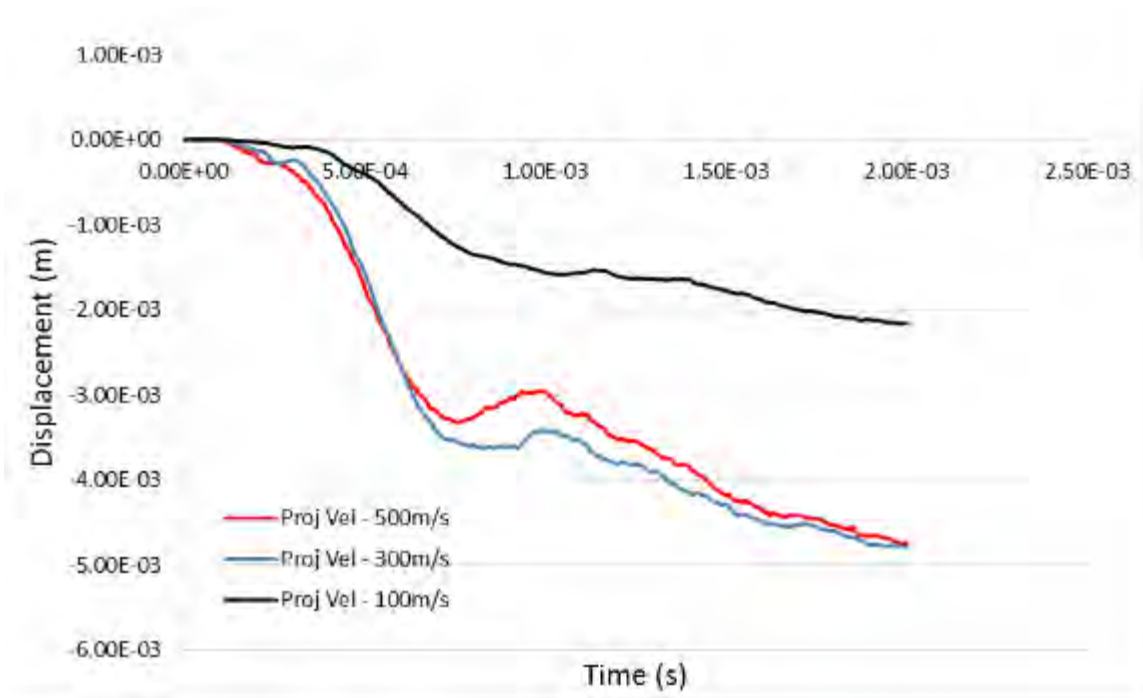


Figure 127. Left wall Z-Displacement for different projectile velocity (Model 1).

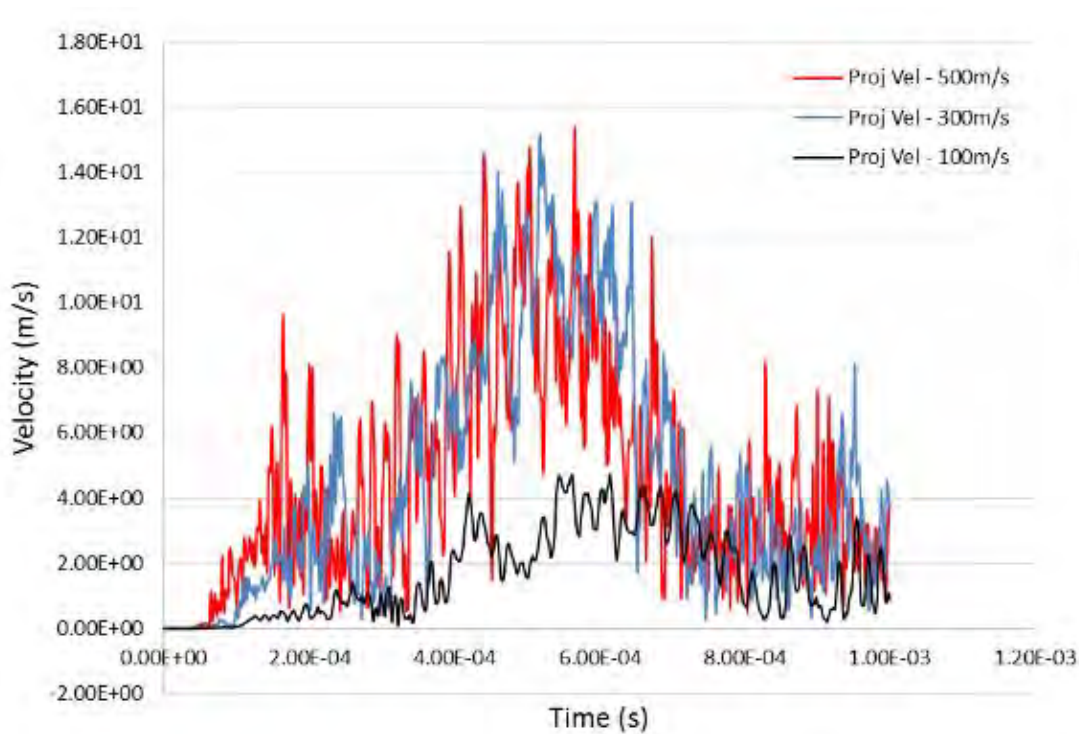


Figure 128. Left wall resultant velocity for different projectile velocity (Model 1).

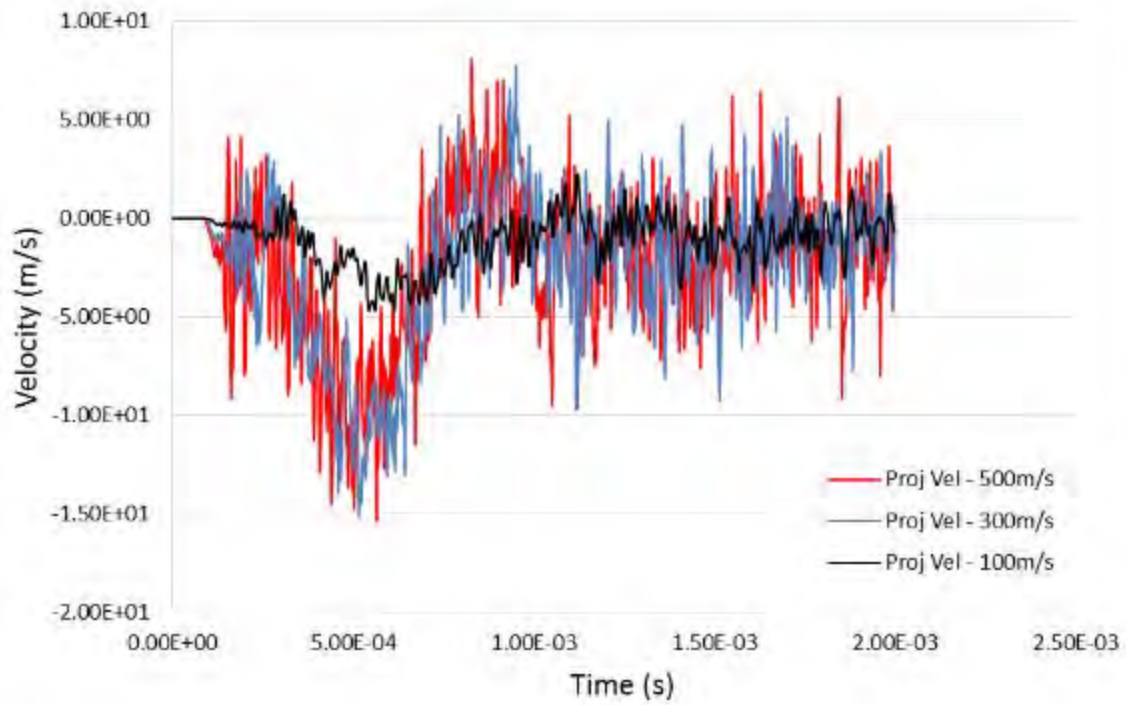


Figure 129. Left wall Z-Velocity for different projectile velocity (Model 1).

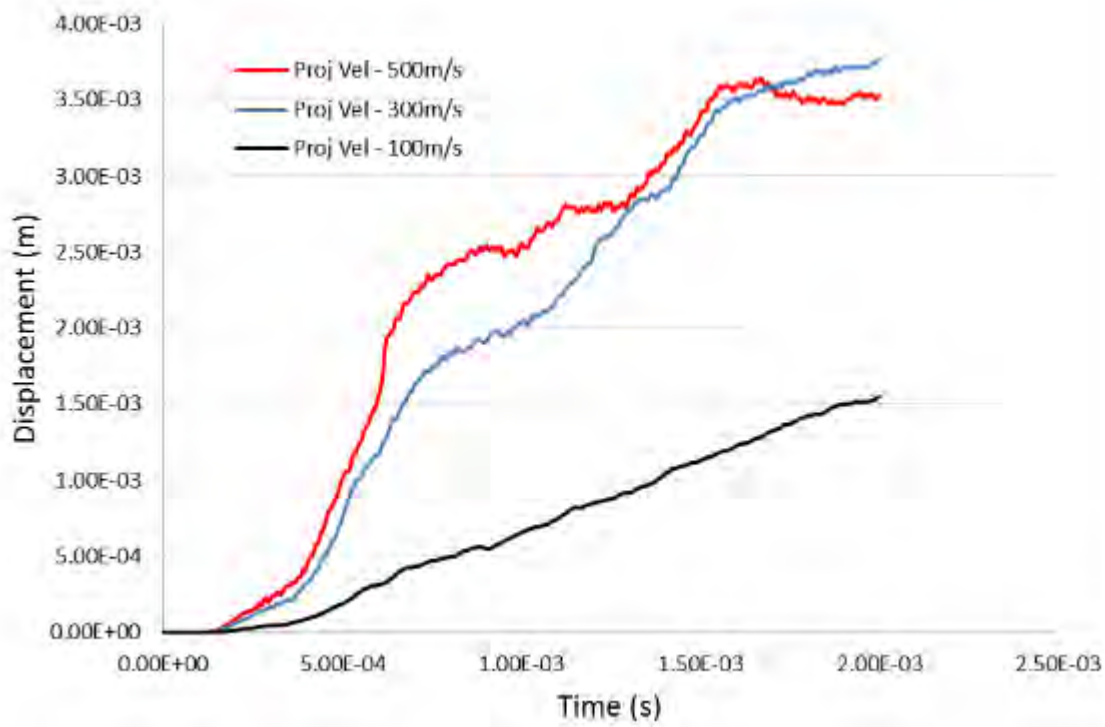


Figure 130. Exit wall resultant displacement for different projectile velocity (Model 1).

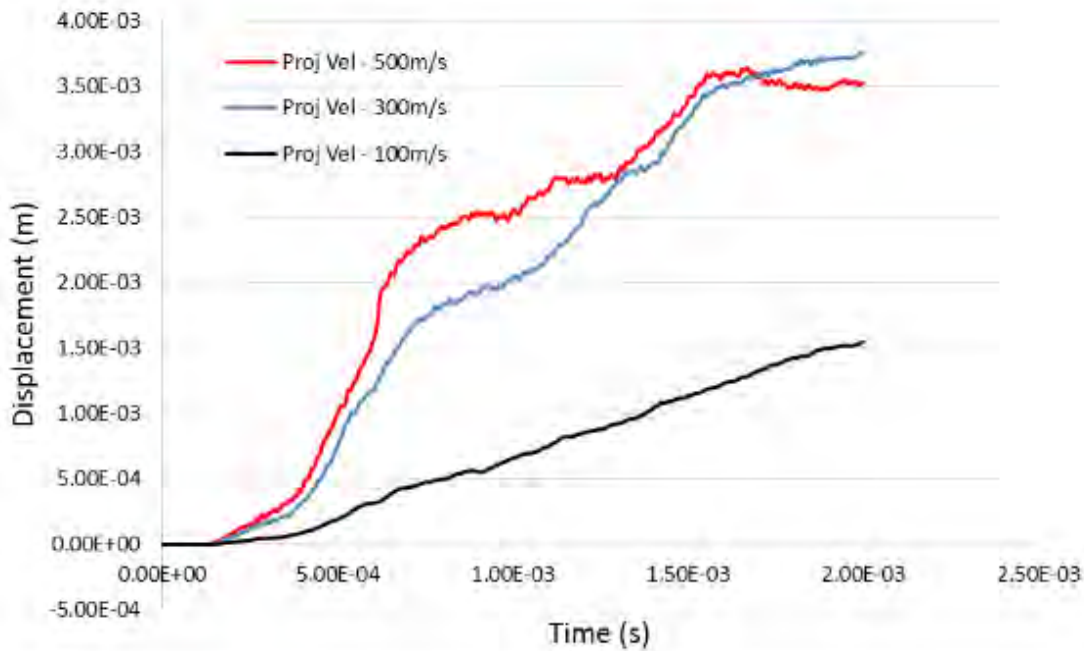


Figure 131. Exit wall X-Displacement for different projectile velocity (Model 1).

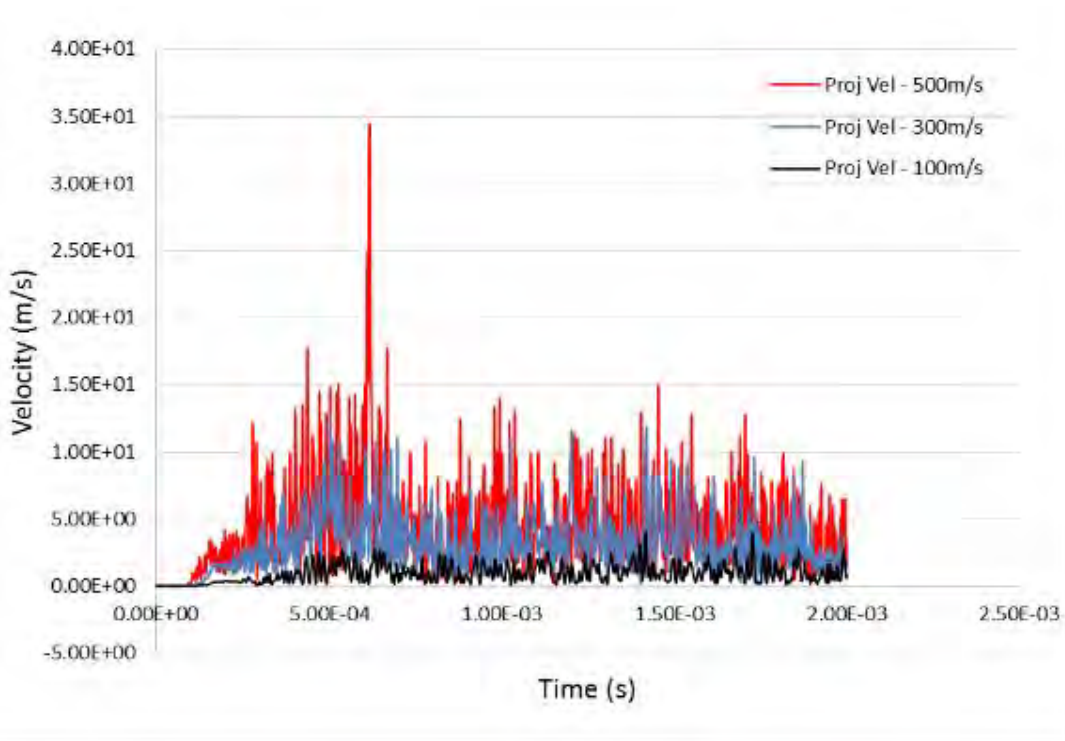


Figure 132. Exit wall resultant velocity for different projectile velocity (Model 1).

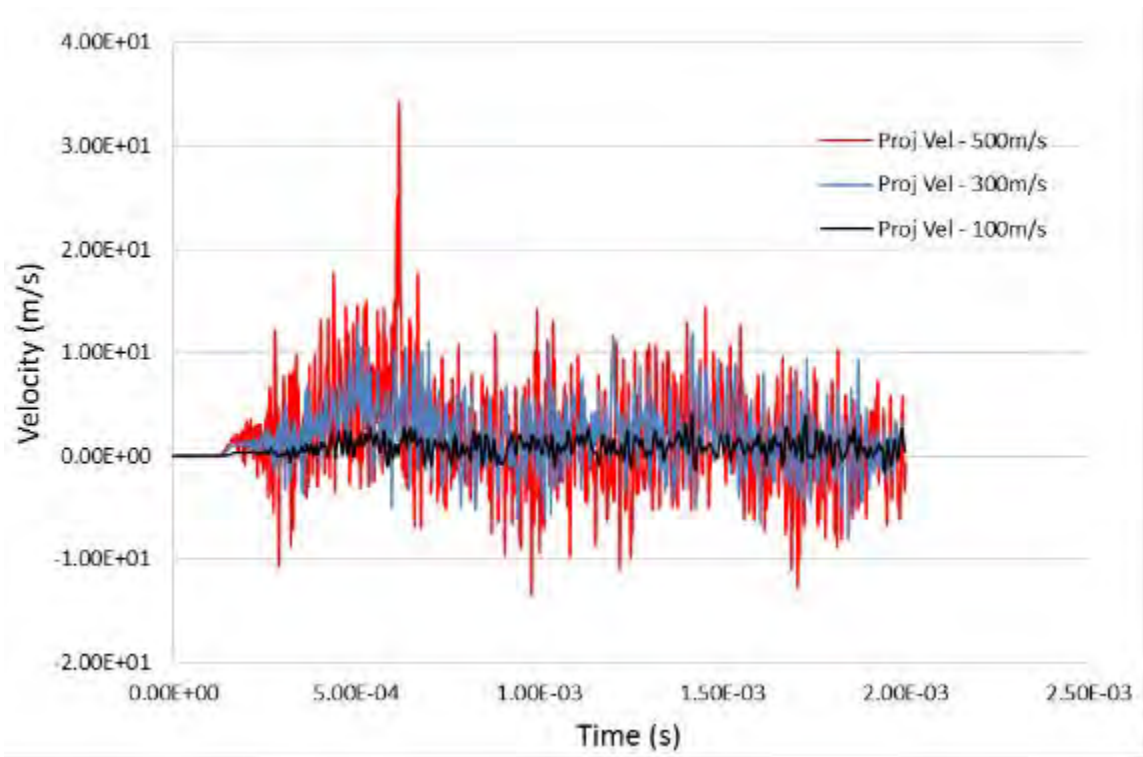


Figure 133. Exit wall X-Velocity for different projectile velocity (Model 1).

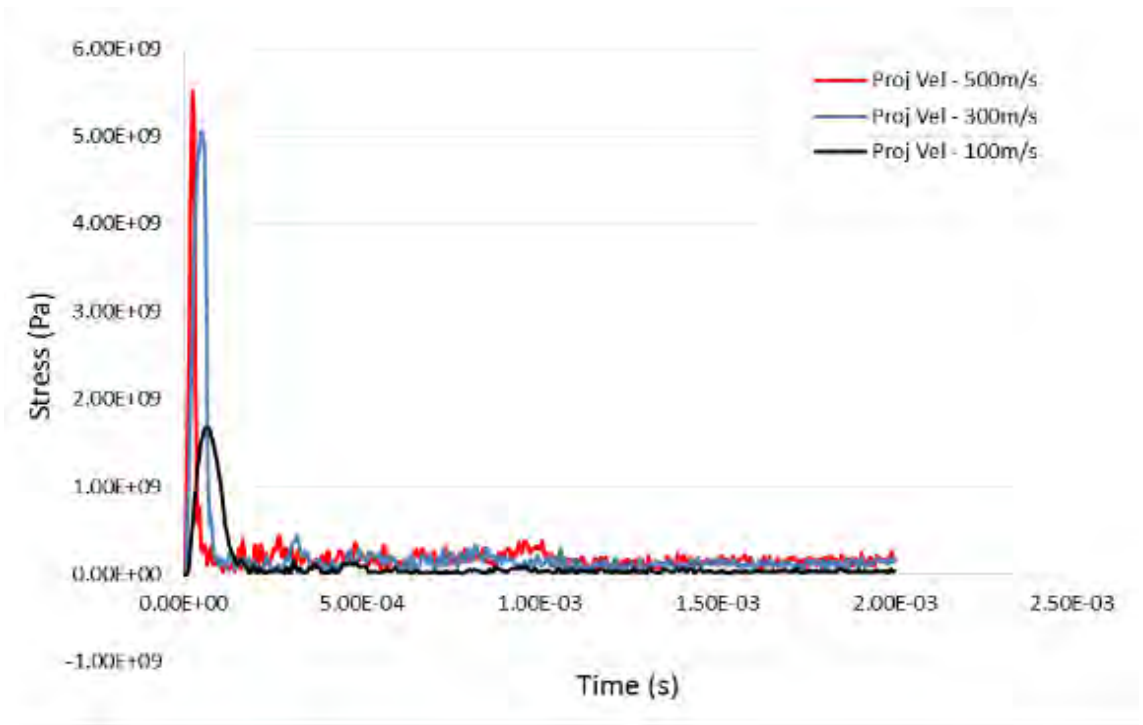


Figure 134. Entry wall effective stress for different projectile velocity (Model 1).

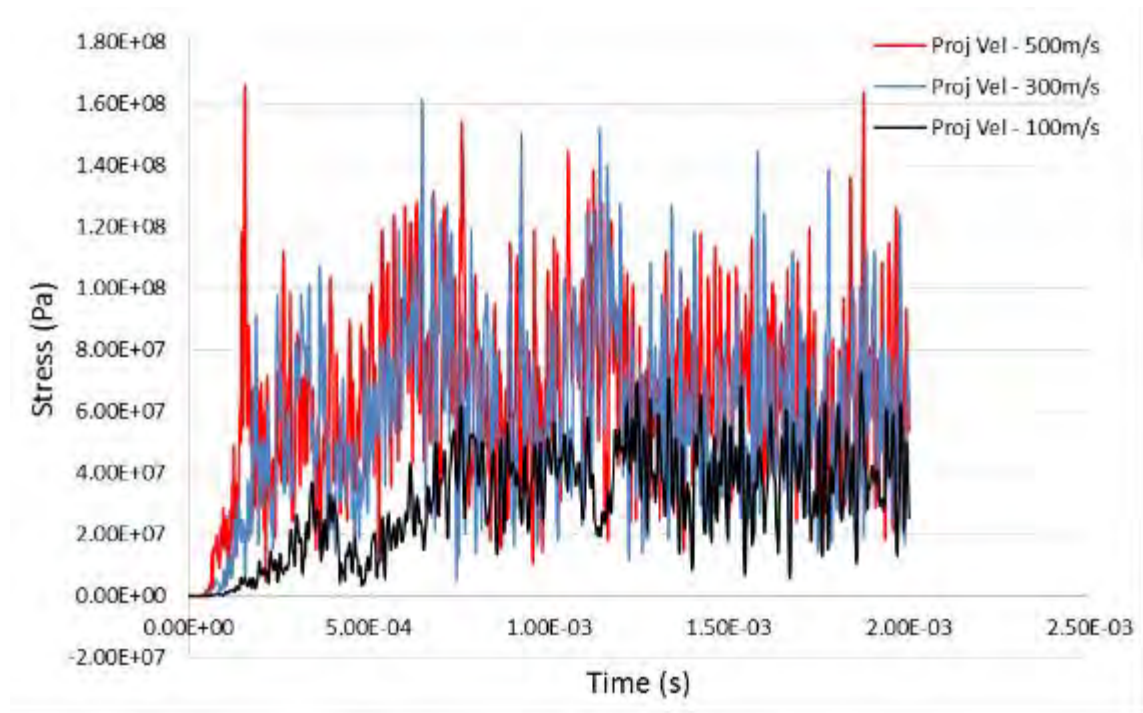


Figure 135. Left wall effective stress for different projectile velocity (Model 1).

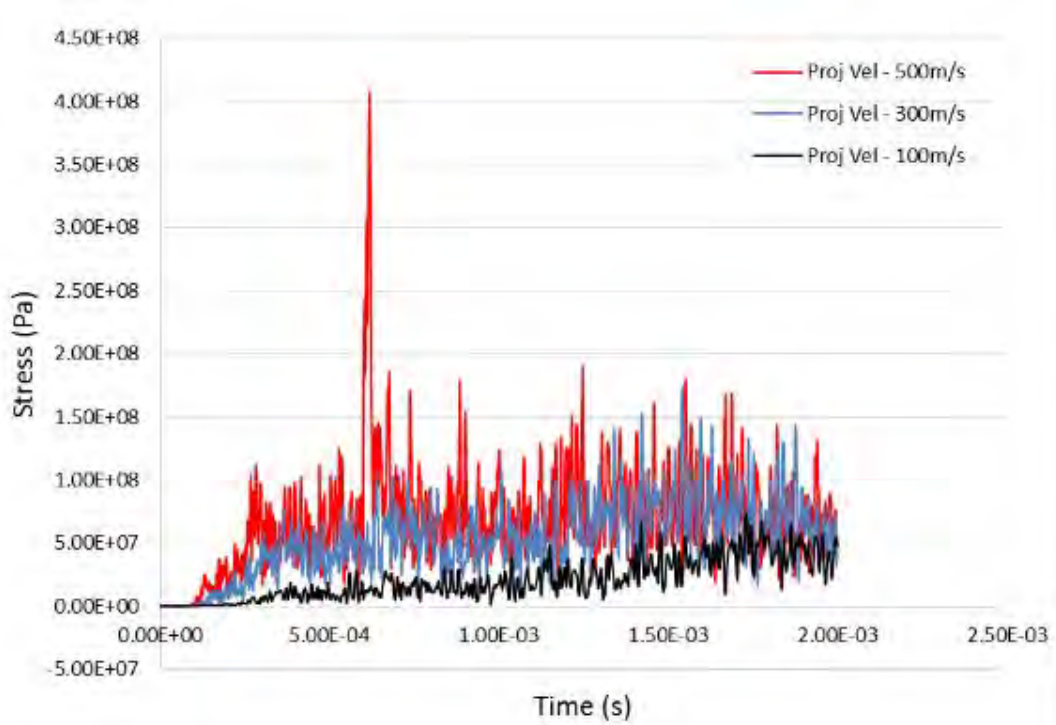


Figure 136. Exit wall effective stress for different projectile velocity (Model 1).

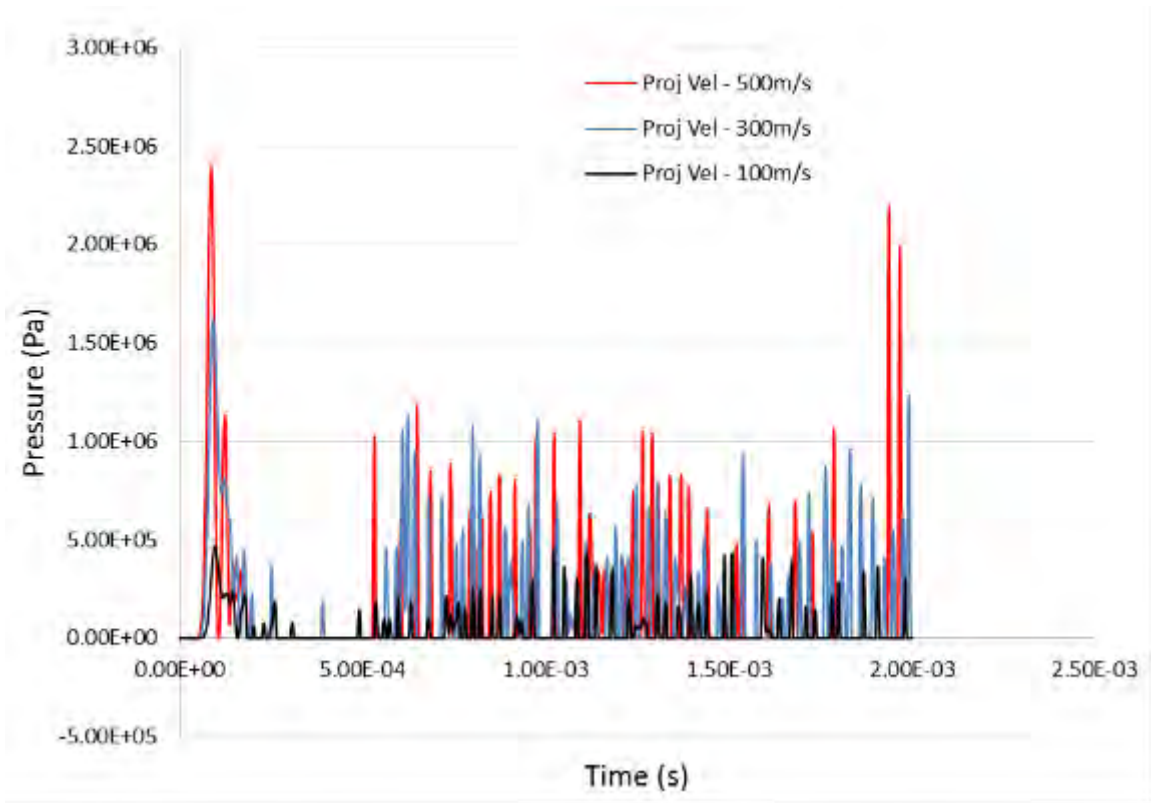


Figure 137. Fluid pressure for different projectile velocity (Model 1).

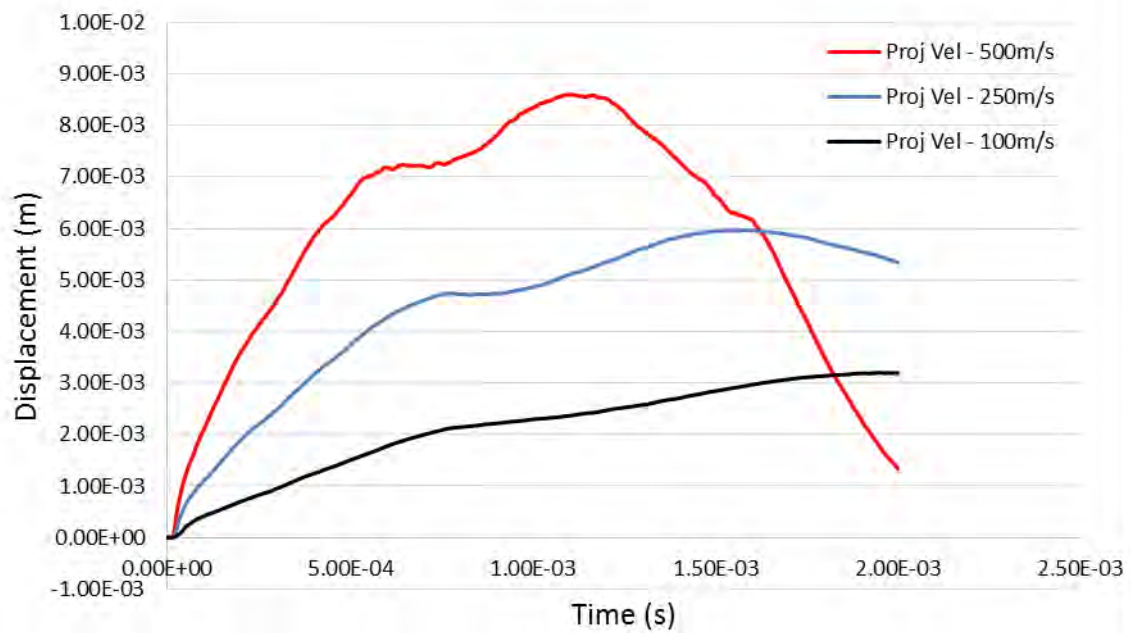


Figure 138. Entry wall resultant displacement for different projectile velocity (Model 2).

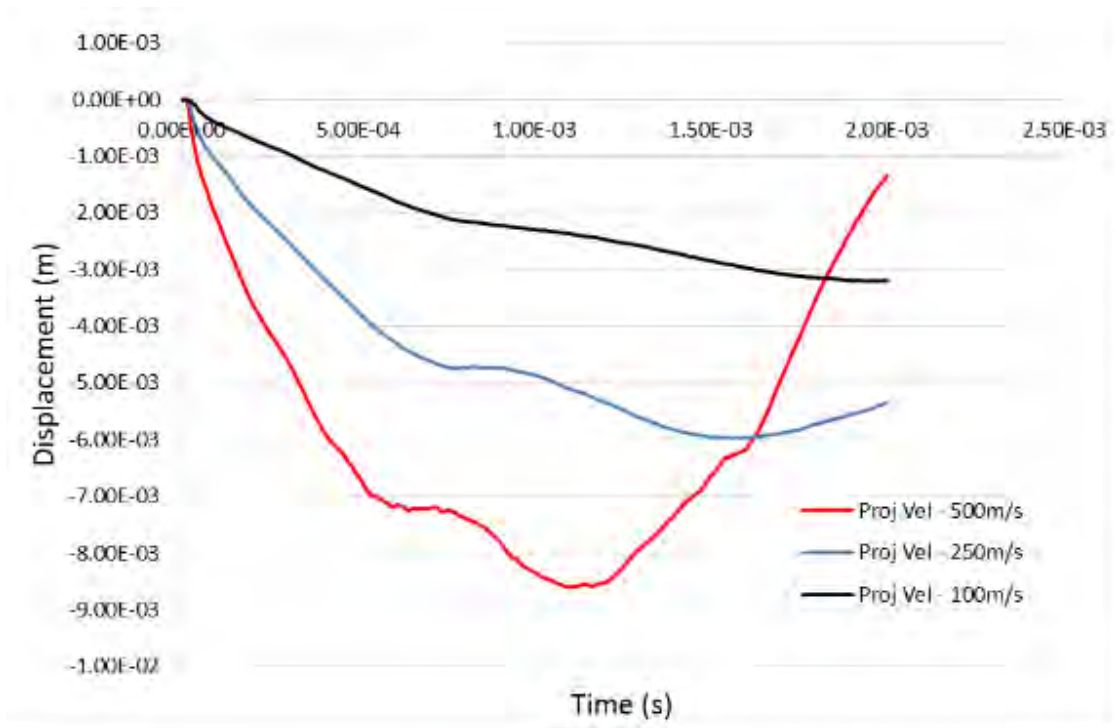


Figure 139. Entry wall X-Displacement for different projectile velocity (Model 2).

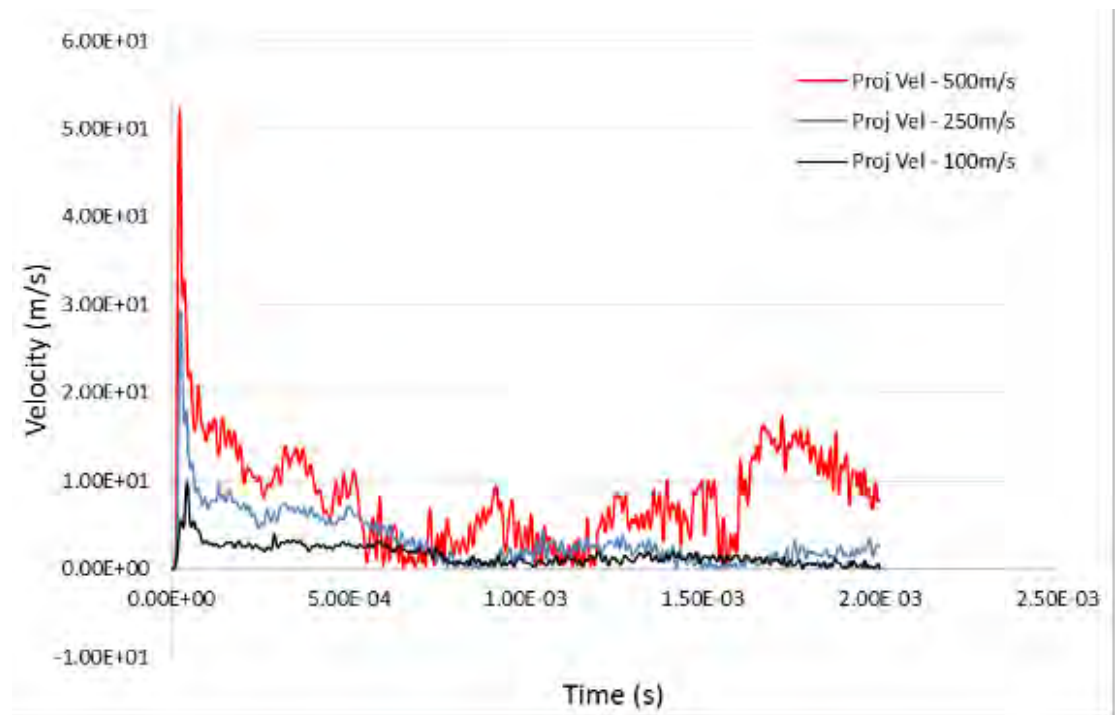


Figure 140. Entry wall resultant velocity for different projectile velocity (Model 2).

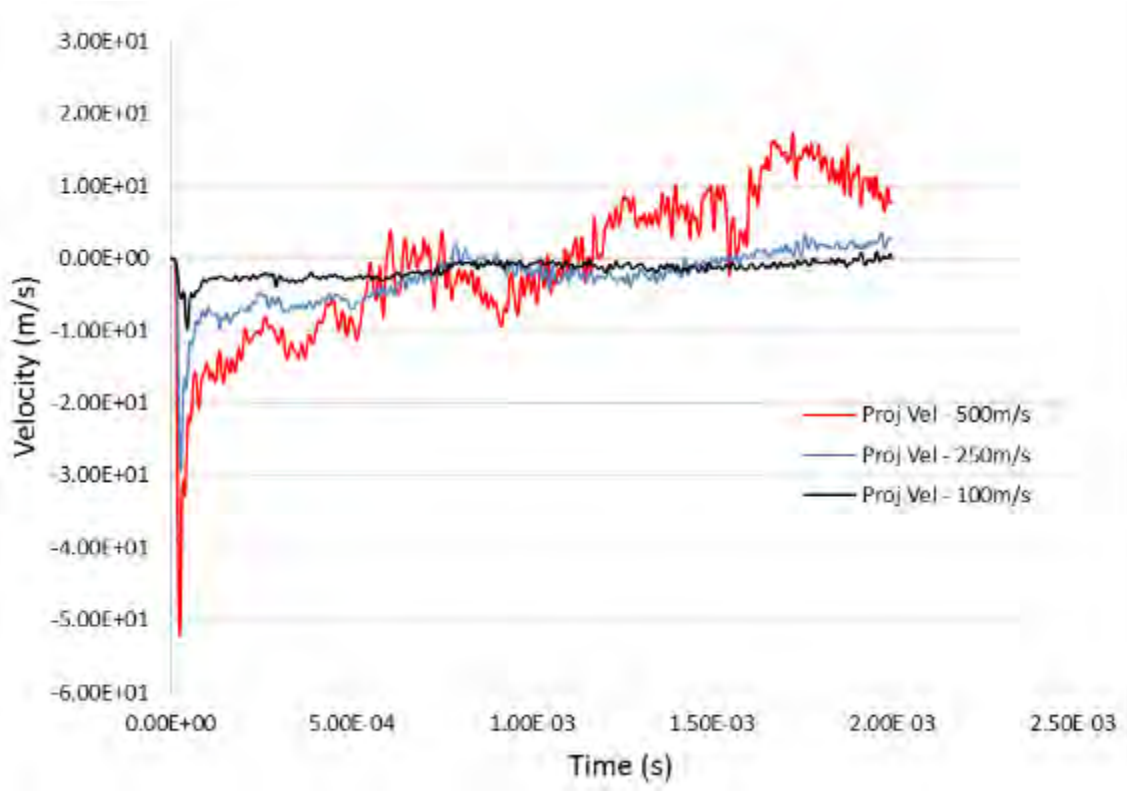


Figure 141. Entry wall X-Velocity for different projectile velocity (Model 2).

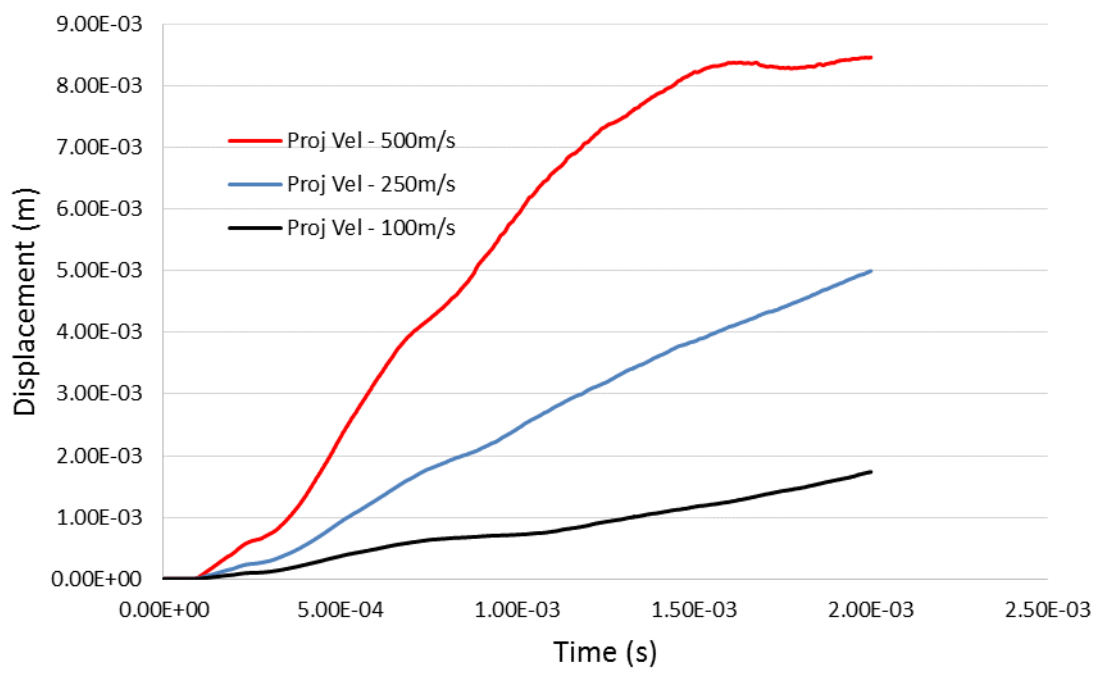


Figure 142. Left wall resultant displacement for different projectile velocity (Model 2).

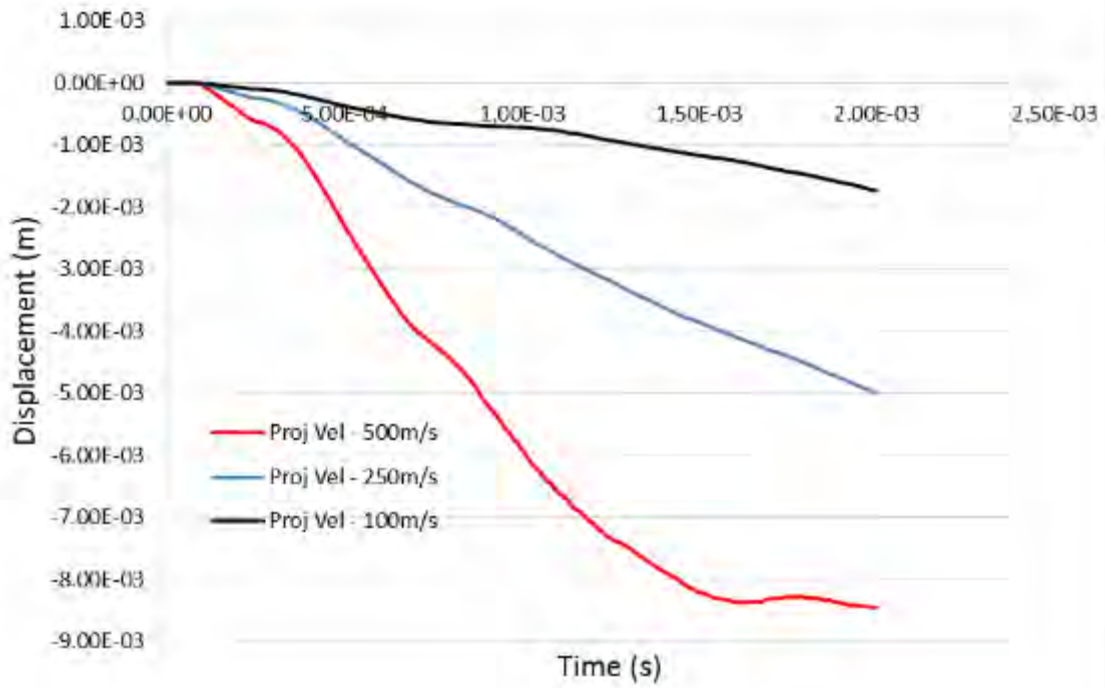


Figure 143. Left wall Z-Displacement for different projectile velocity (Model 2).

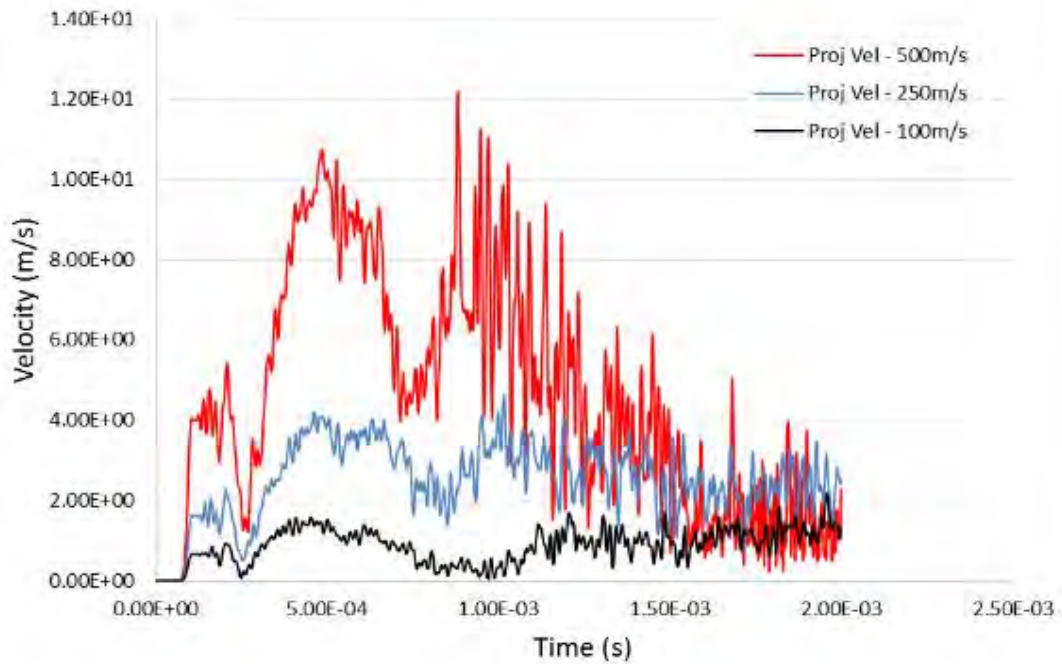


Figure 144. Left wall resultant velocity for different projectile velocity (Model 2).

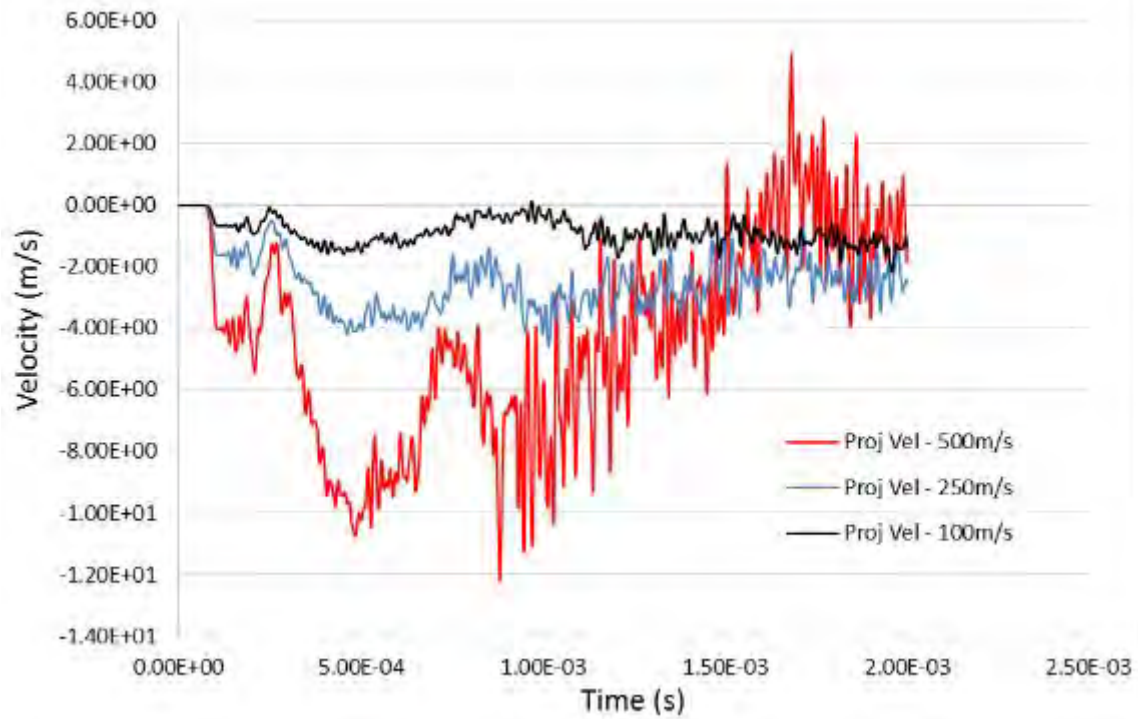


Figure 145. Left wall Z-Velocity for different projectile velocity (Model 2).

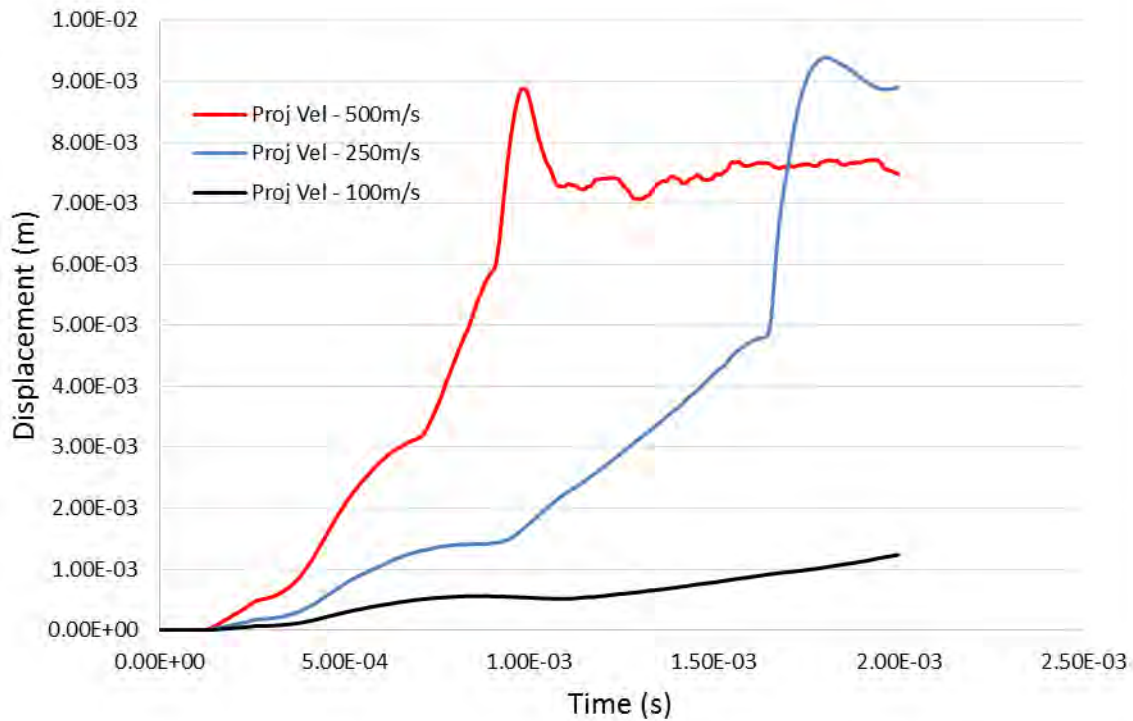


Figure 146. Exit wall resultant displacement for different projectile velocity (Model 2).

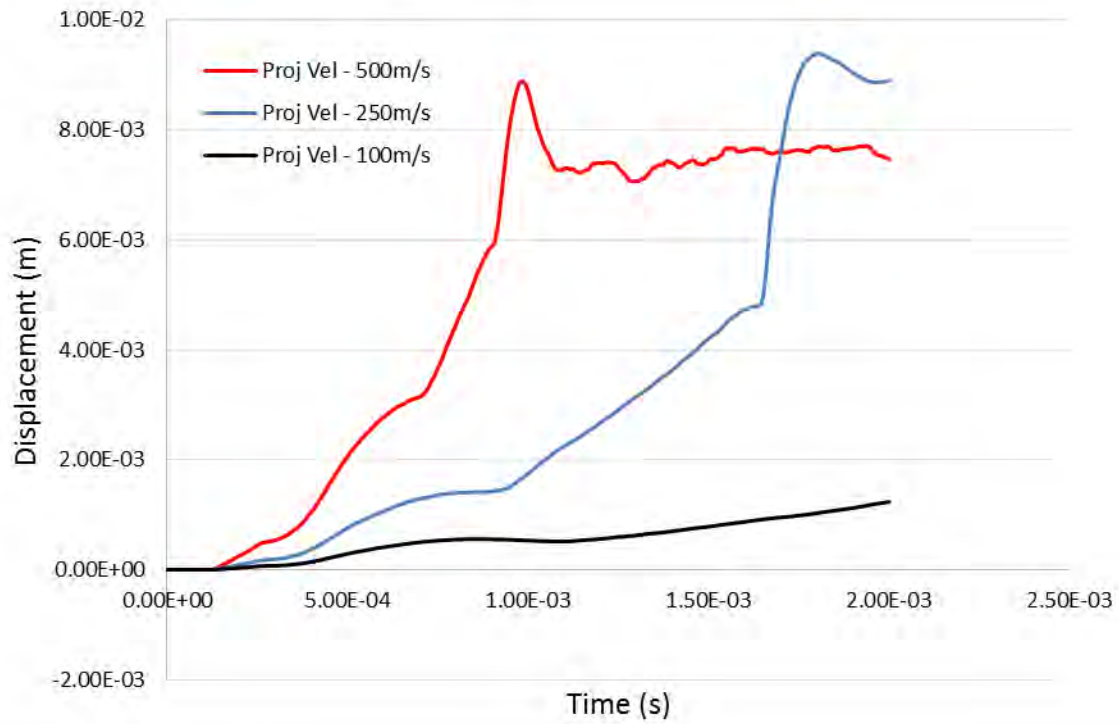


Figure 147. Exit wall X-Displacement for different projectile velocity (Model 2).

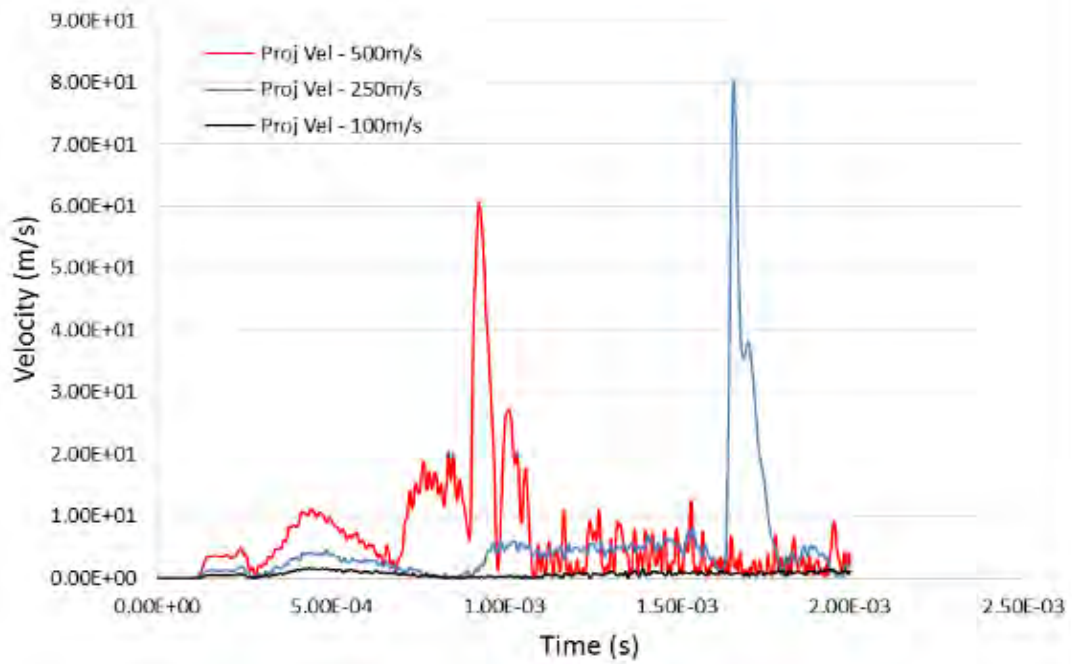


Figure 148. Exit wall resultant velocity for different projectile velocity (Model 2).

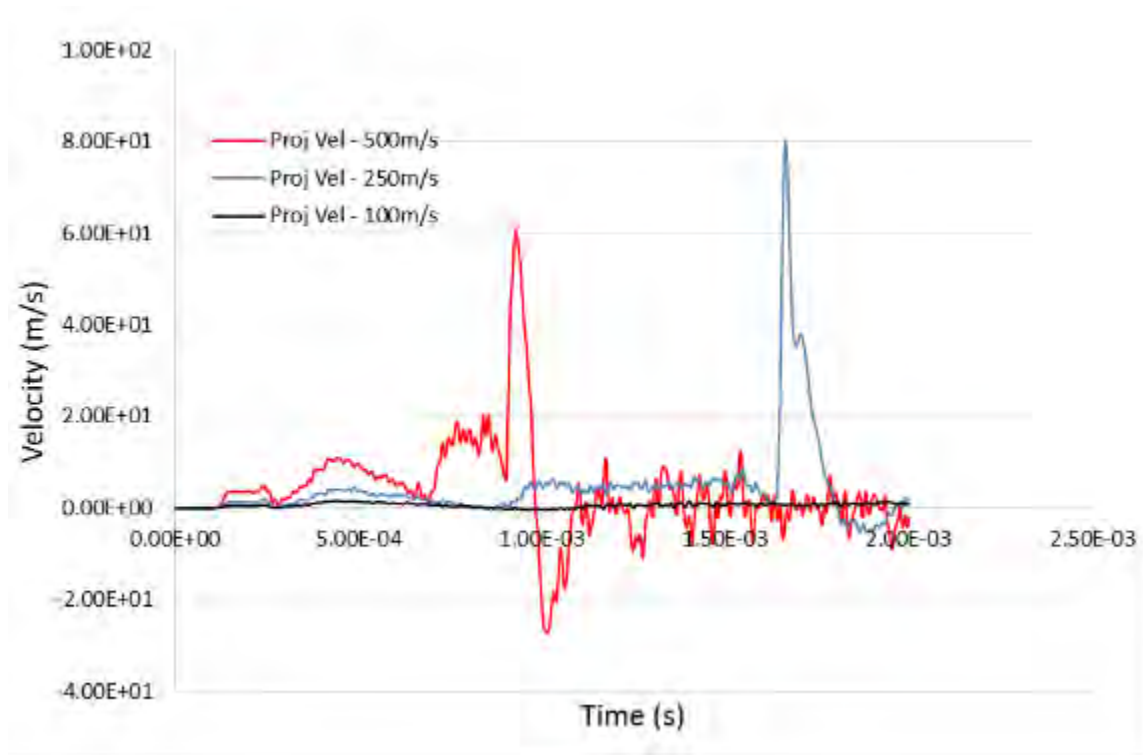


Figure 149. Exit wall X-Velocity for different projectile velocity (Model 2).

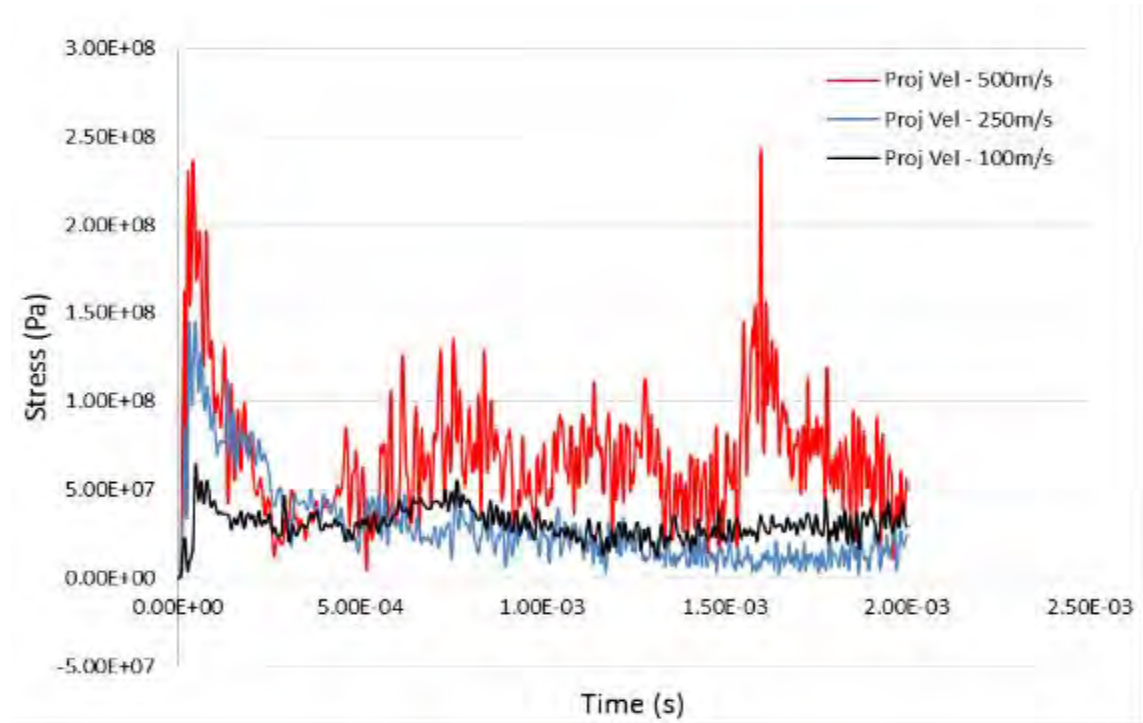


Figure 150. Entry wall effective stress for different projectile velocity (Model 2).

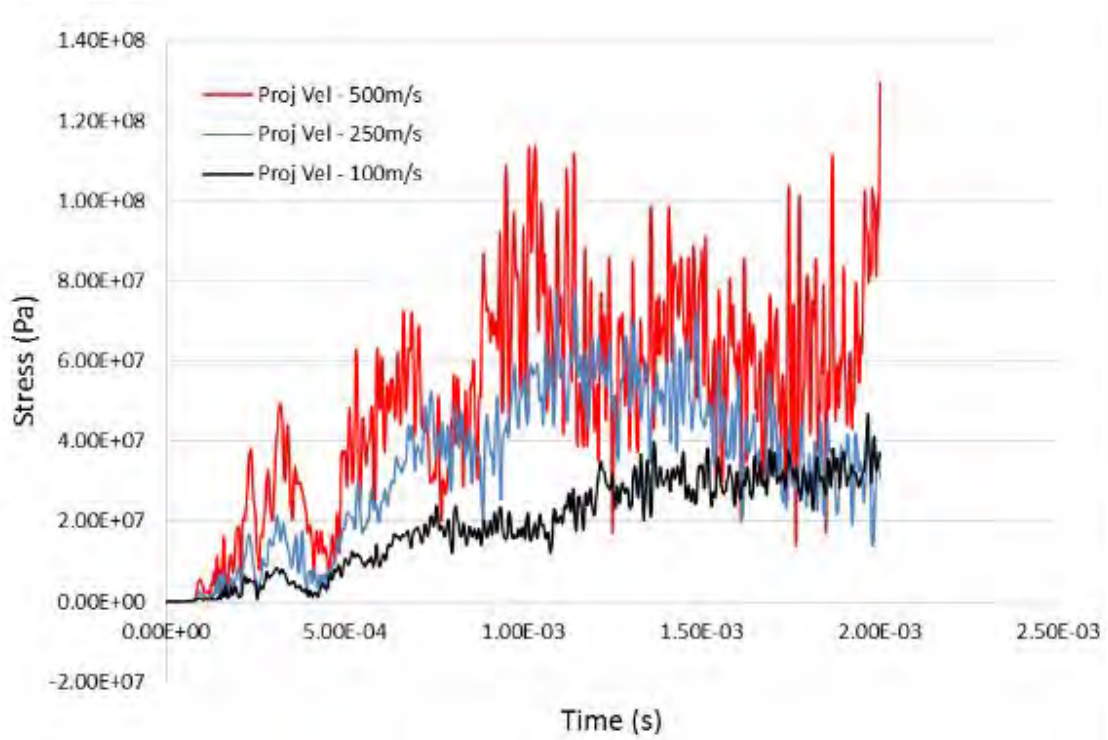


Figure 151. Left wall effective stress for different projectile velocity (Model 2).

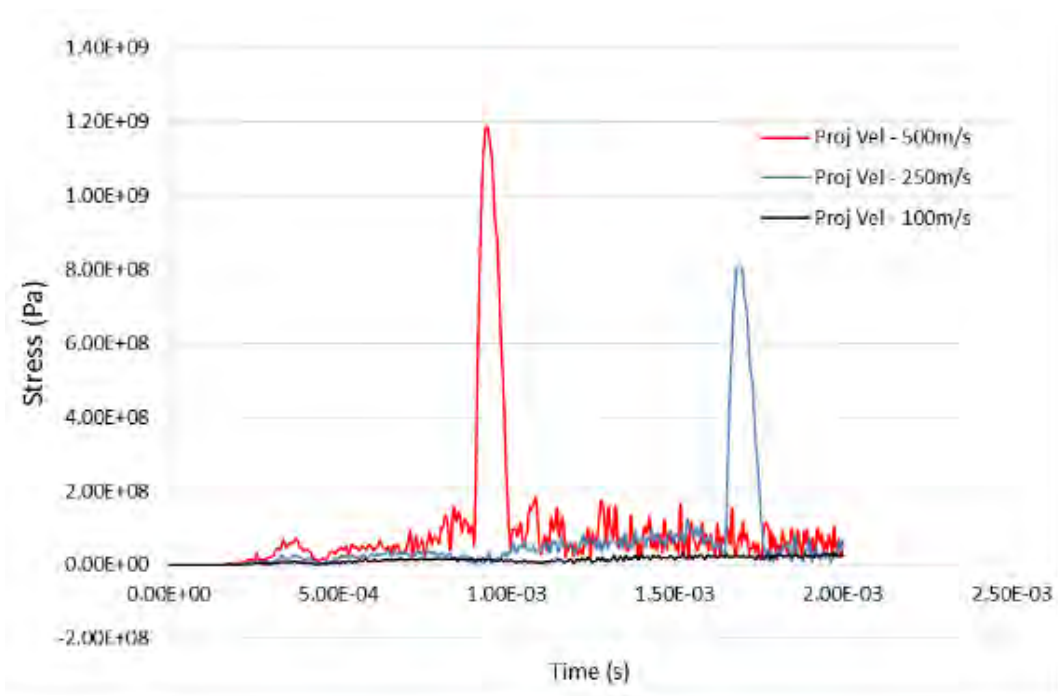


Figure 152. Exit wall effective stress for different projectile velocity (Model 2).

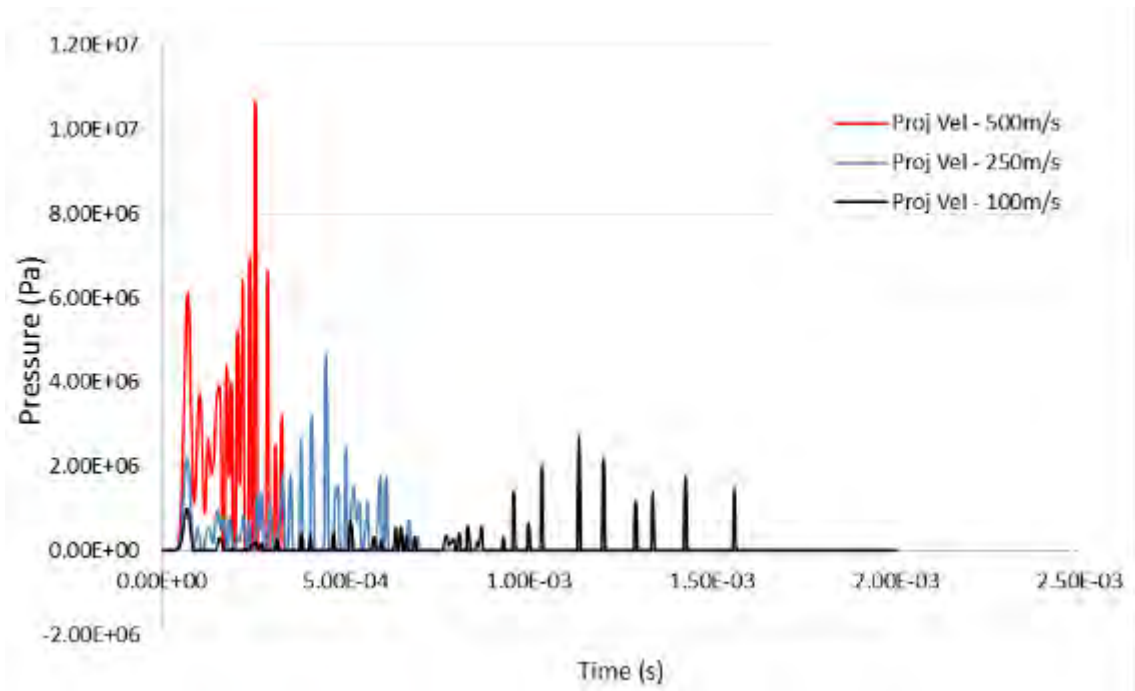


Figure 153. Drag phase pressure for different projectile velocity (Model 2).

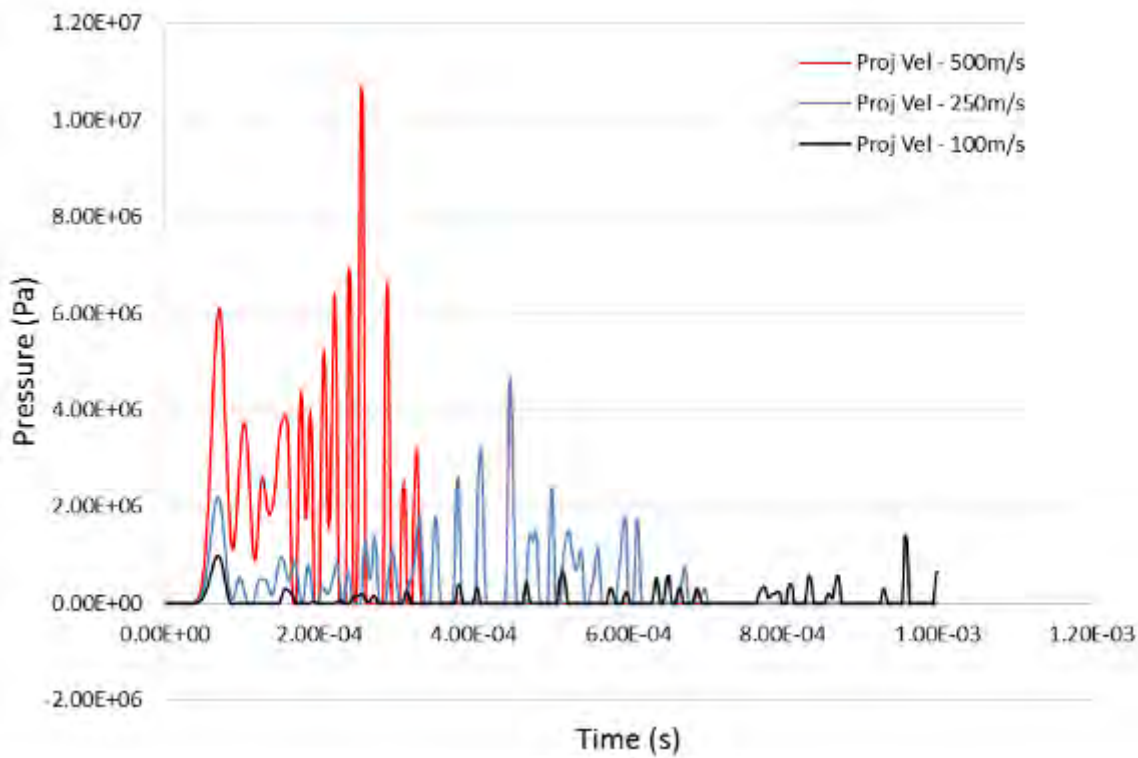


Figure 154. Drag phase pressure for different projectile velocity (Model 2) – Enlarged.

APPENDIX D. GRAPHS FOR TANK MATERIAL MODULUS VARIATION



Tank material modulus investigated: E=40GPa, E=70GPa and E=100GPa

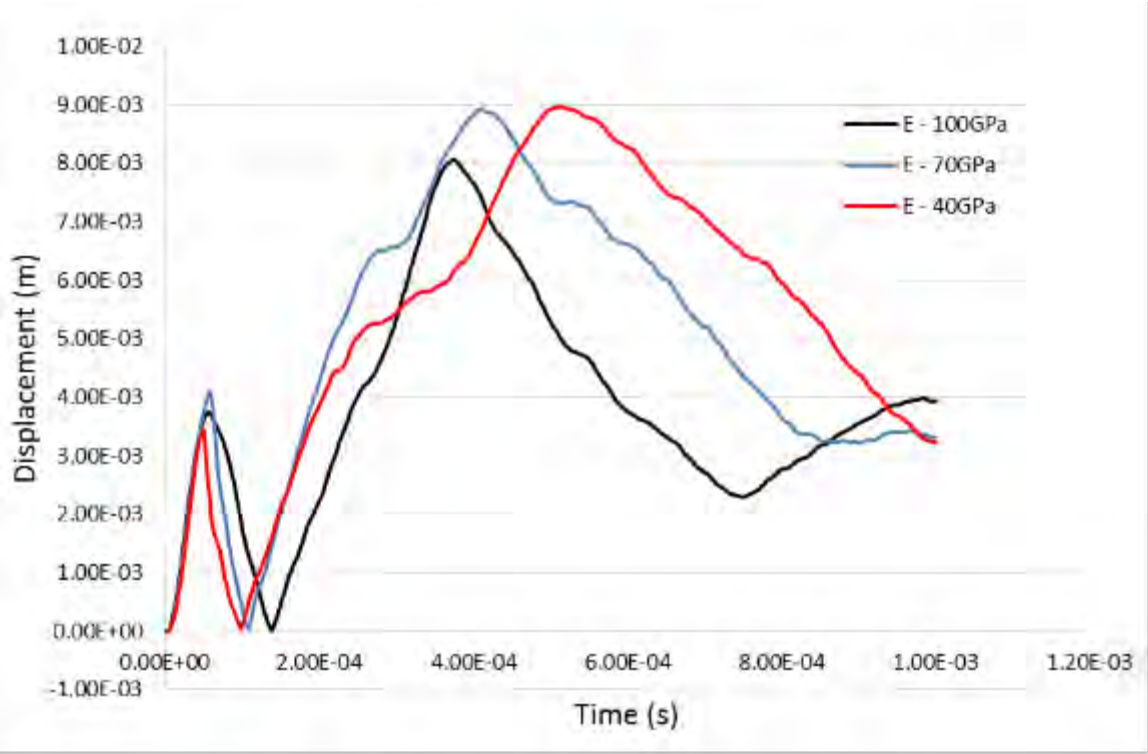


Figure 155. Entry wall resultant displacement for different material modulus (Model 1).

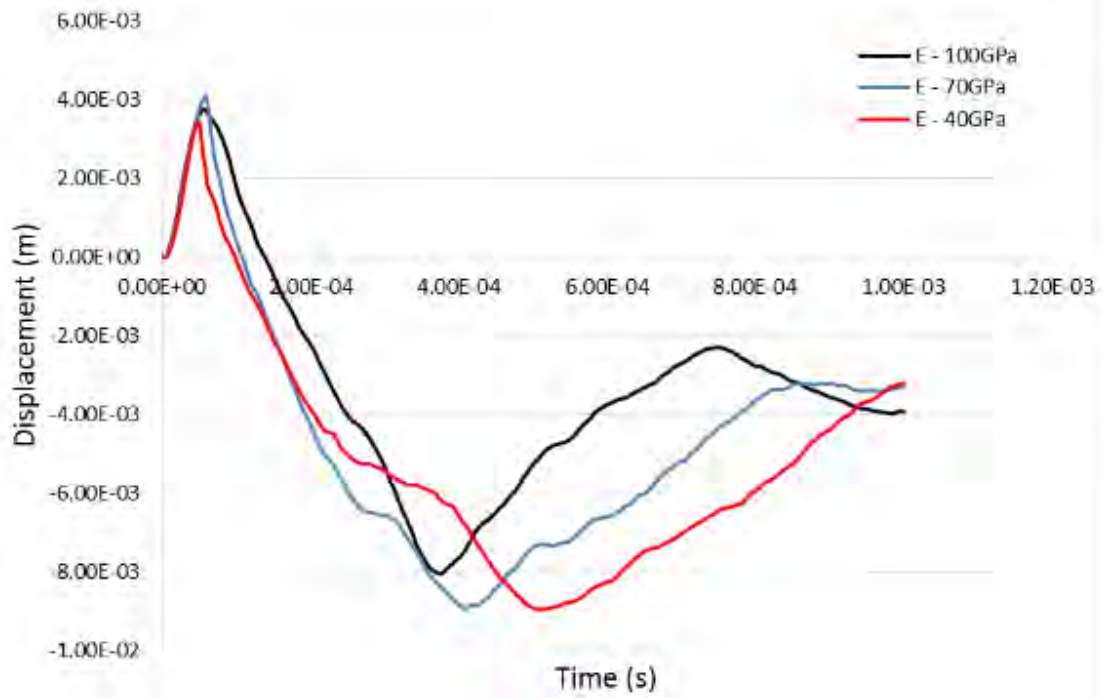


Figure 156. Entry wall X-Displacement for different material modulus (Model 1).

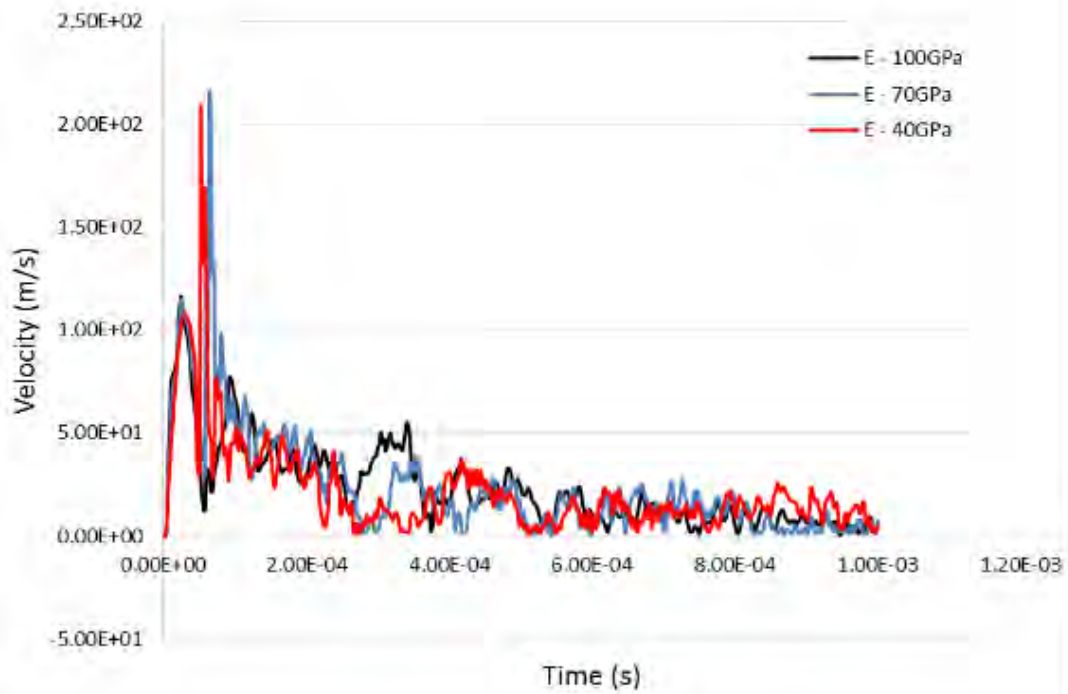


Figure 157. Entry wall resultant velocity for different material modulus (Model 1).

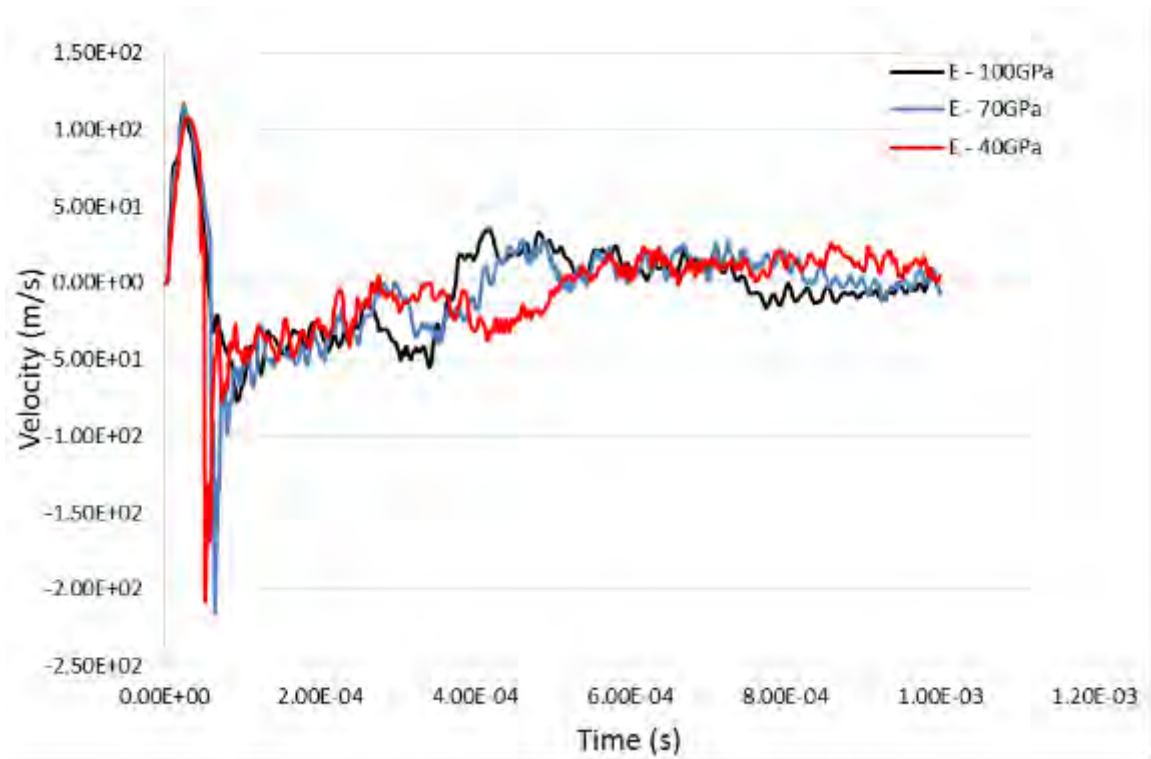


Figure 158. Entry wall X-Velocity for different material modulus (Model 1).

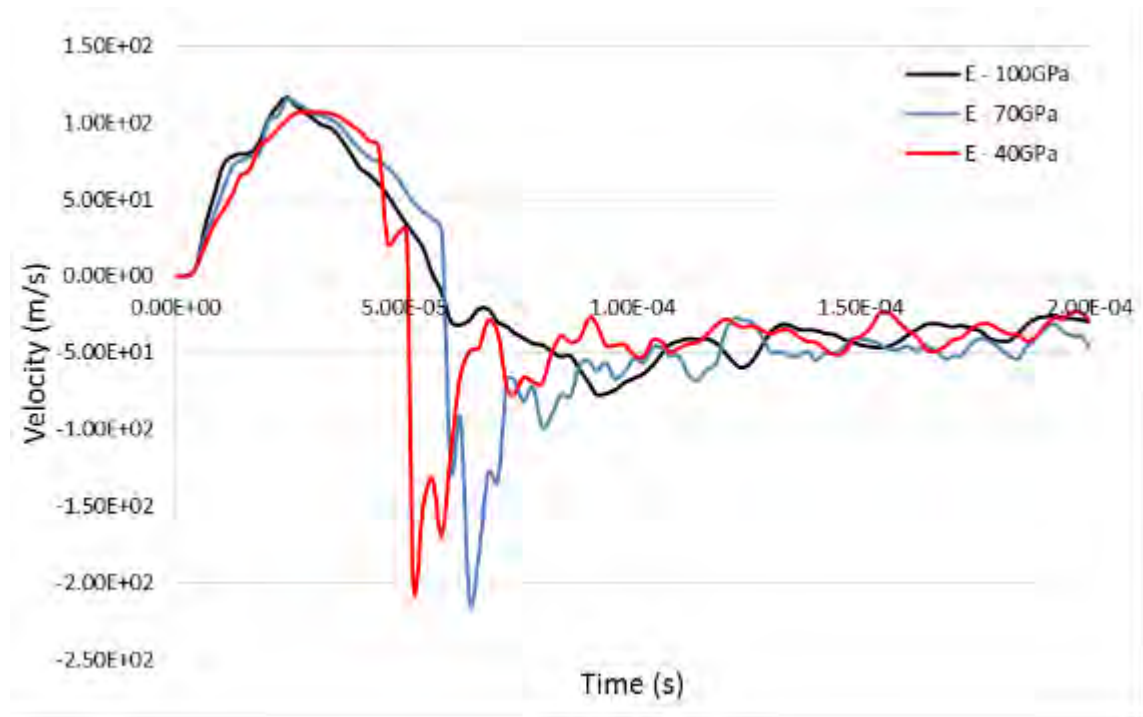


Figure 159. Entry wall X-Velocity for different material modulus (Model 1) – Enlarged.

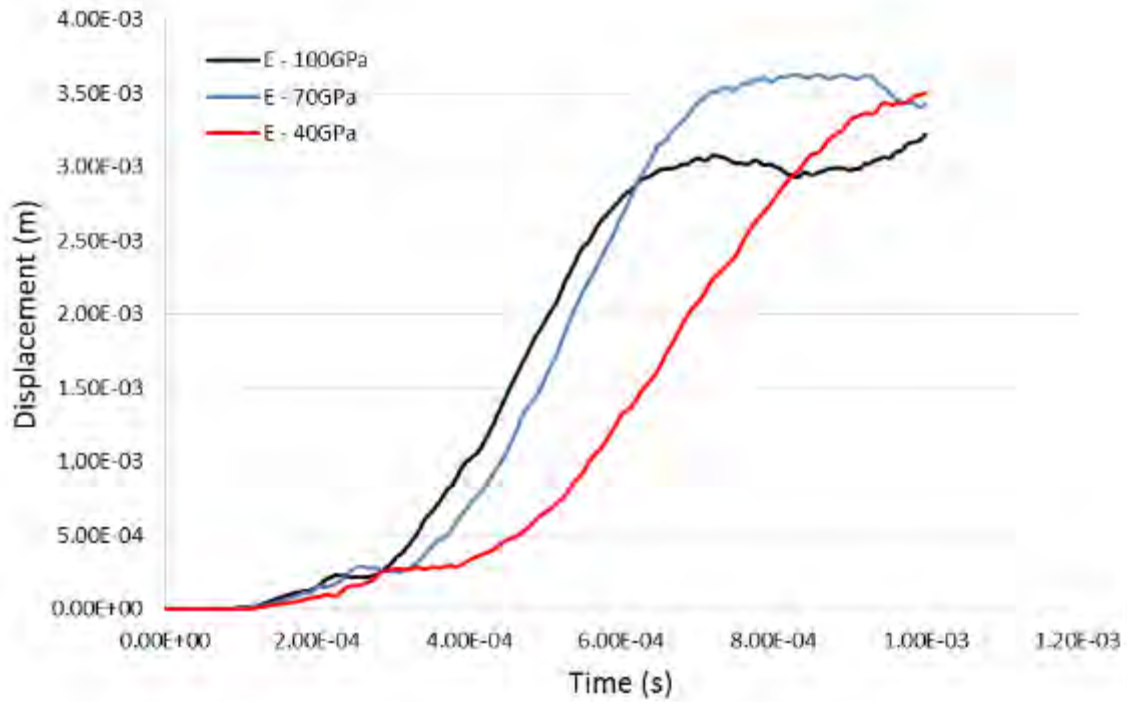


Figure 160. Left wall resultant displacement for different material modulus (Model 1).

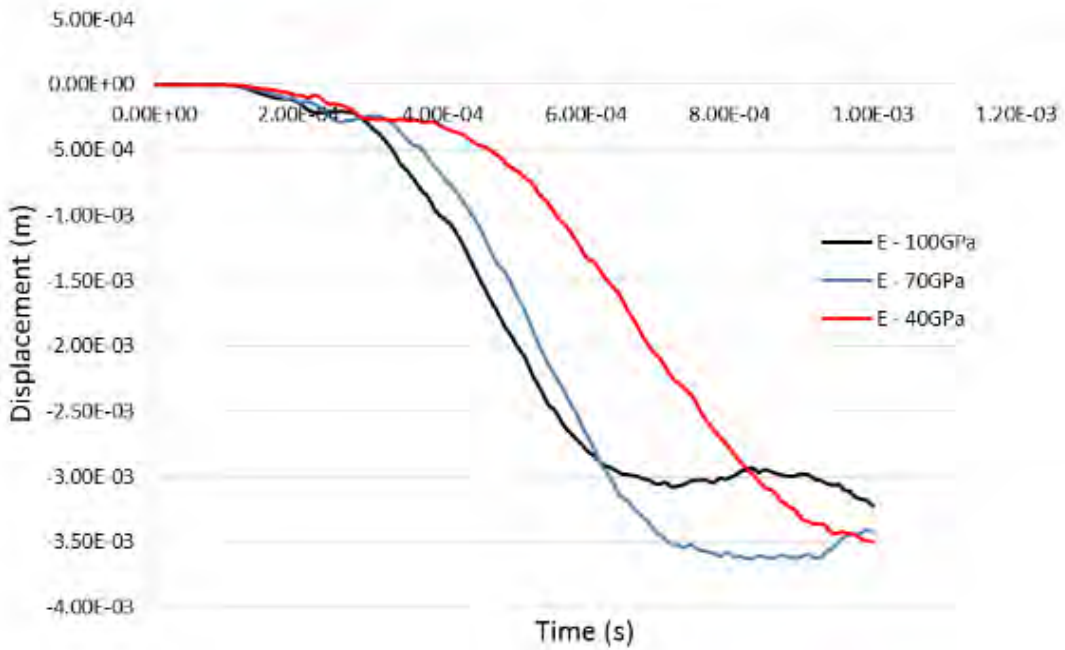


Figure 161. Left wall Z-Displacement for different material modulus (Model 1).

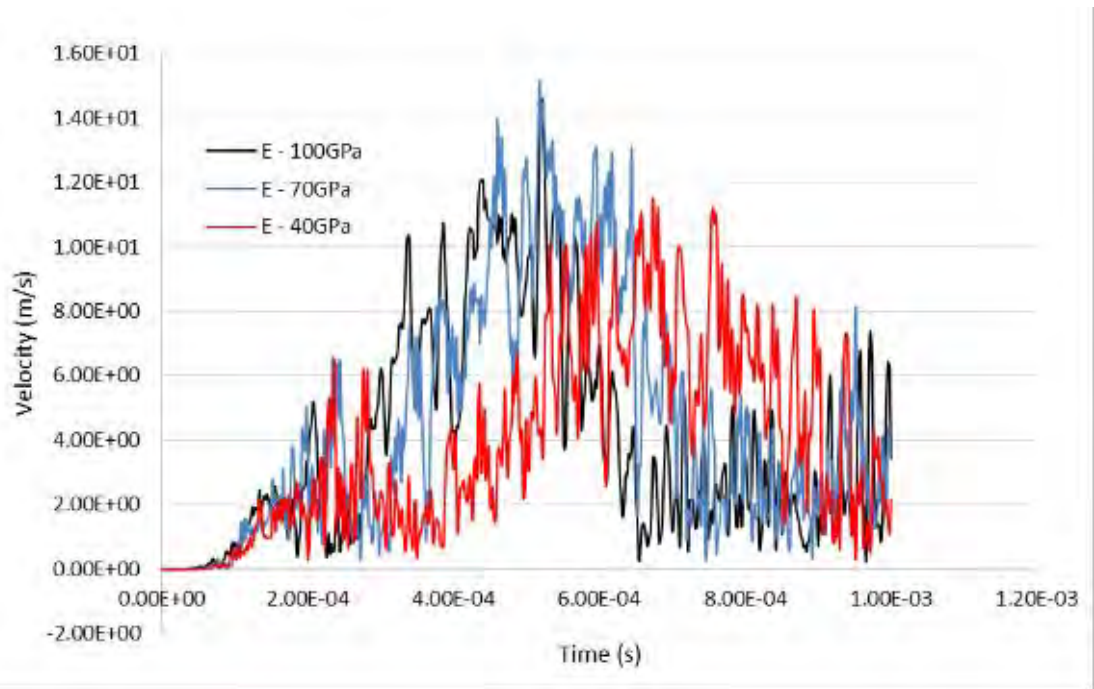


Figure 162. Left wall resultant velocity for different material modulus (Model 1).

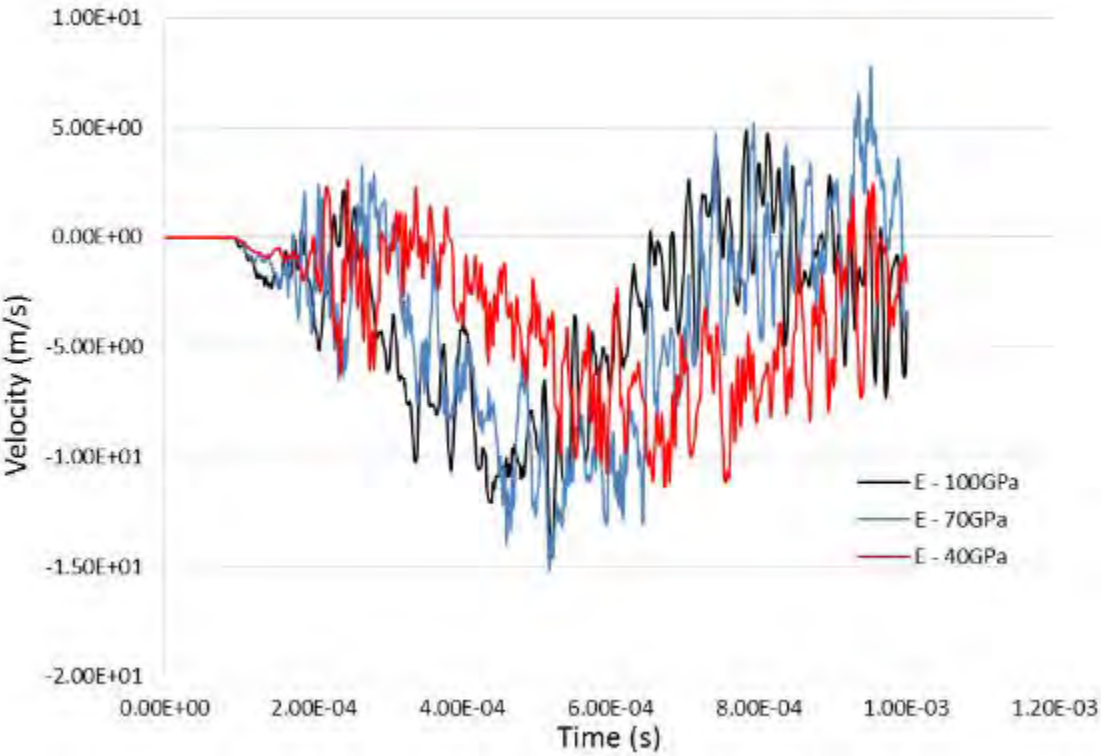


Figure 163. Left wall Z-Velocity for different material modulus (Model 1).

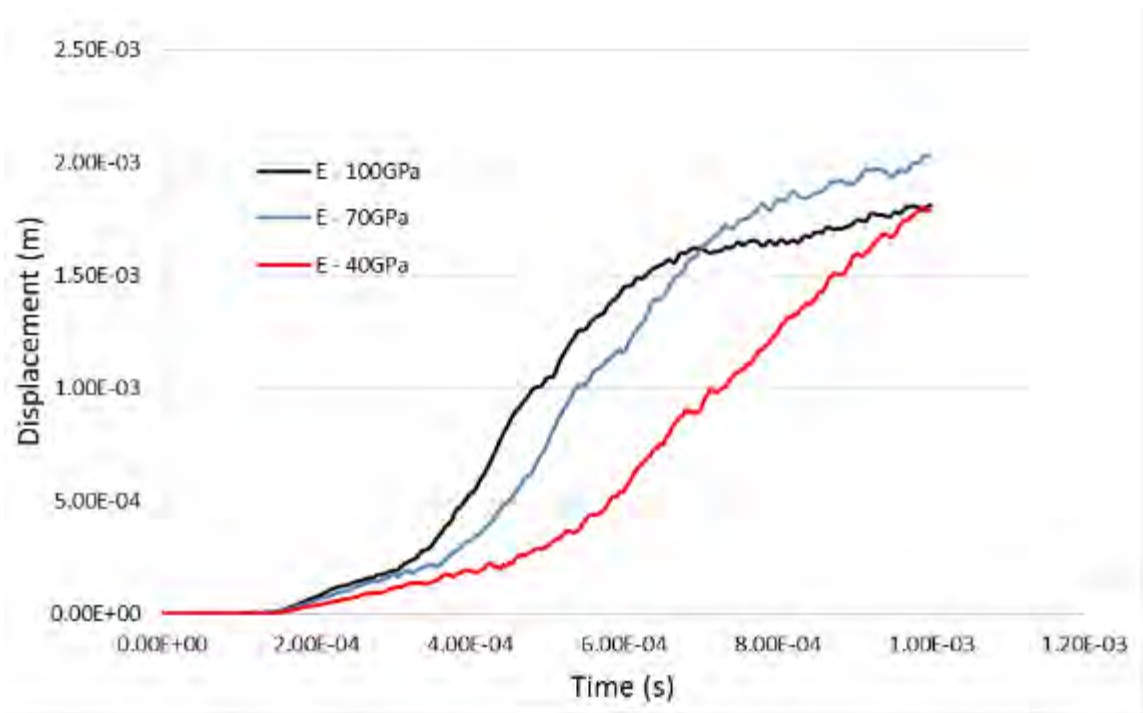


Figure 164. Exit wall resultant displacement for different material modulus (Model 1).

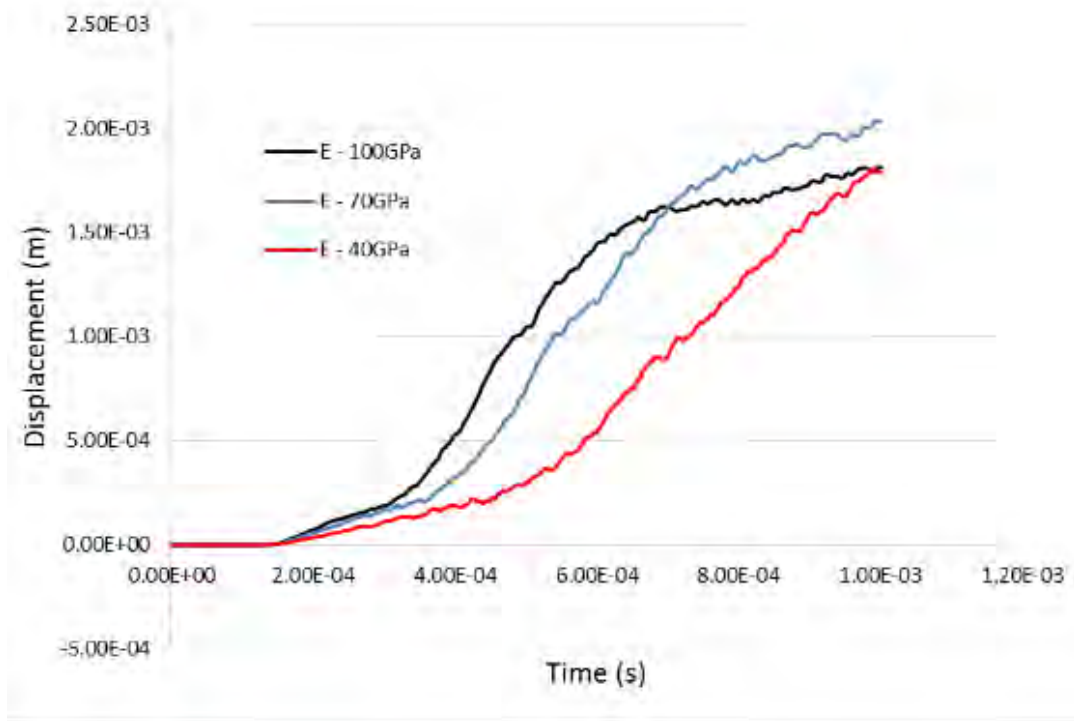


Figure 165. Exit wall X-Displacement for different material modulus (Model 1).

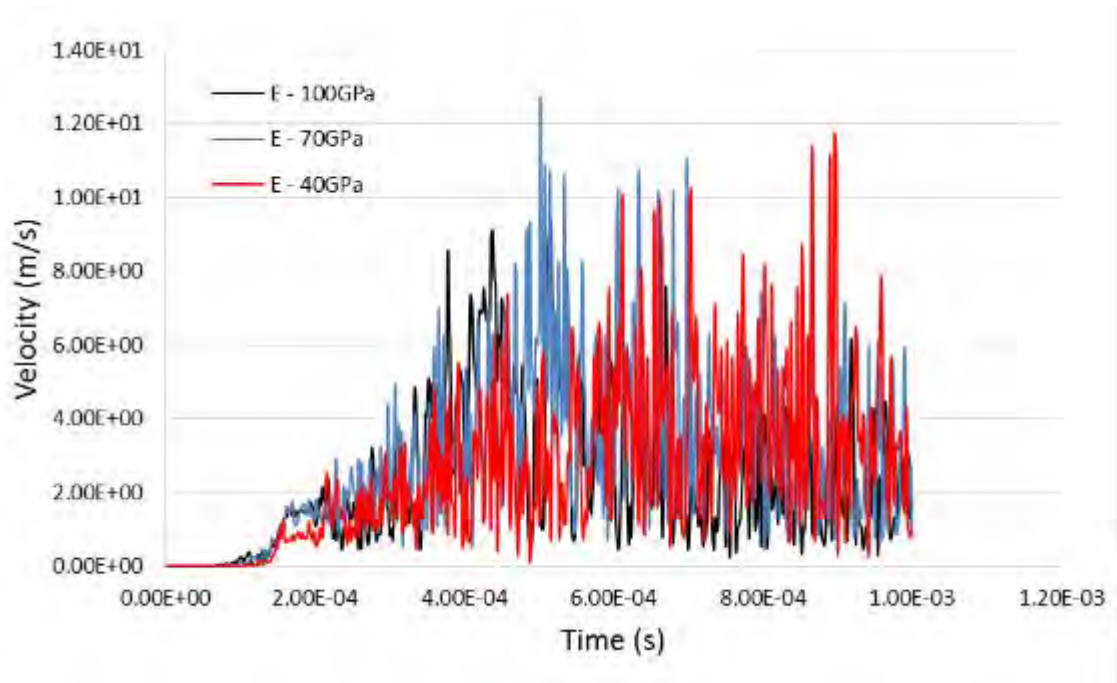


Figure 166. Exit wall resultant velocity for different material modulus (Model 1).

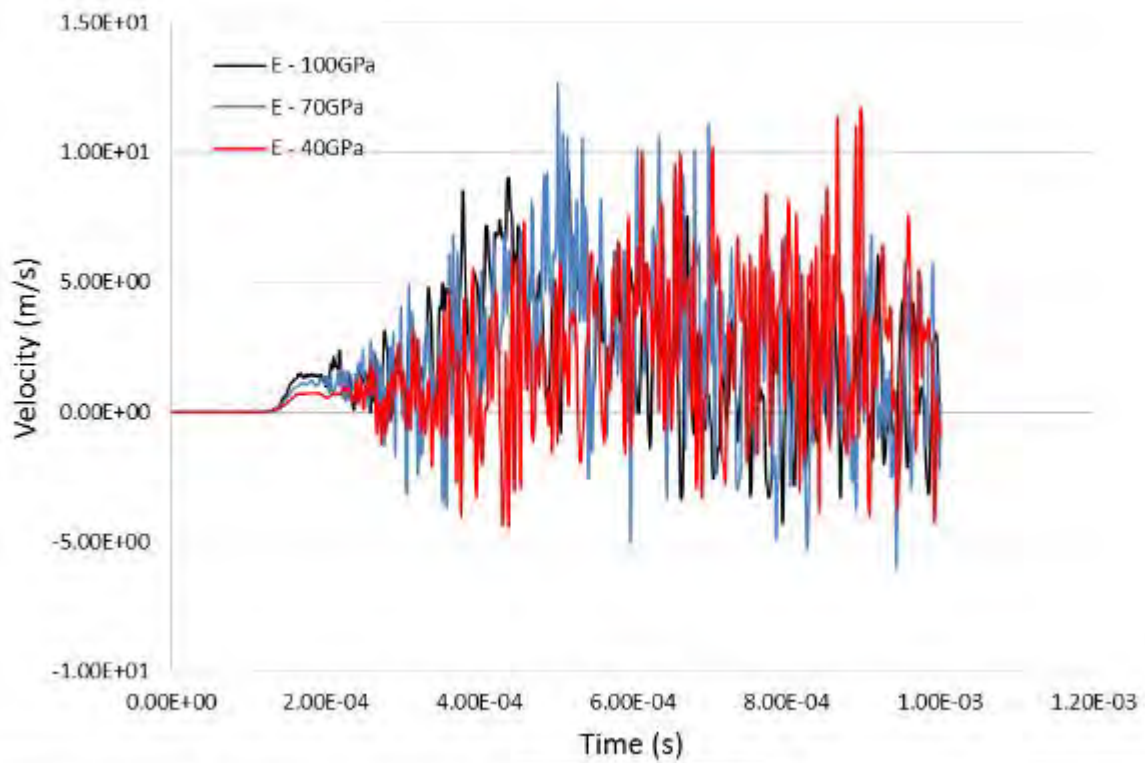


Figure 167. Exit wall X-Velocity for different material modulus (Model 1).

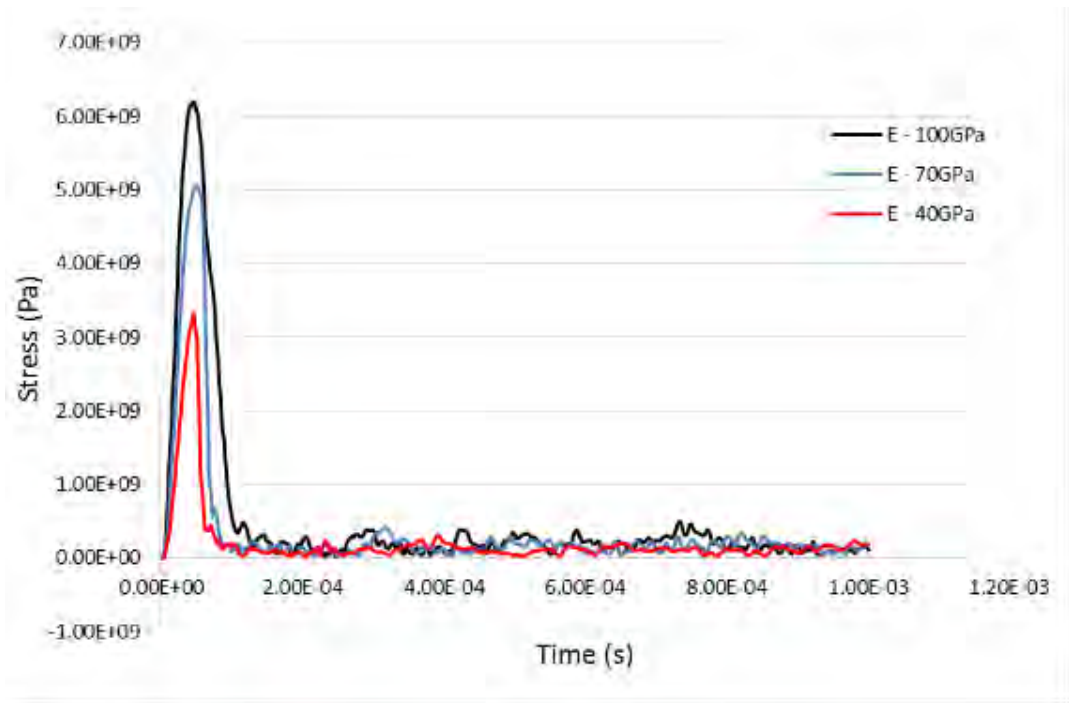


Figure 168. Entry wall effective stress for different material modulus (Model 1).

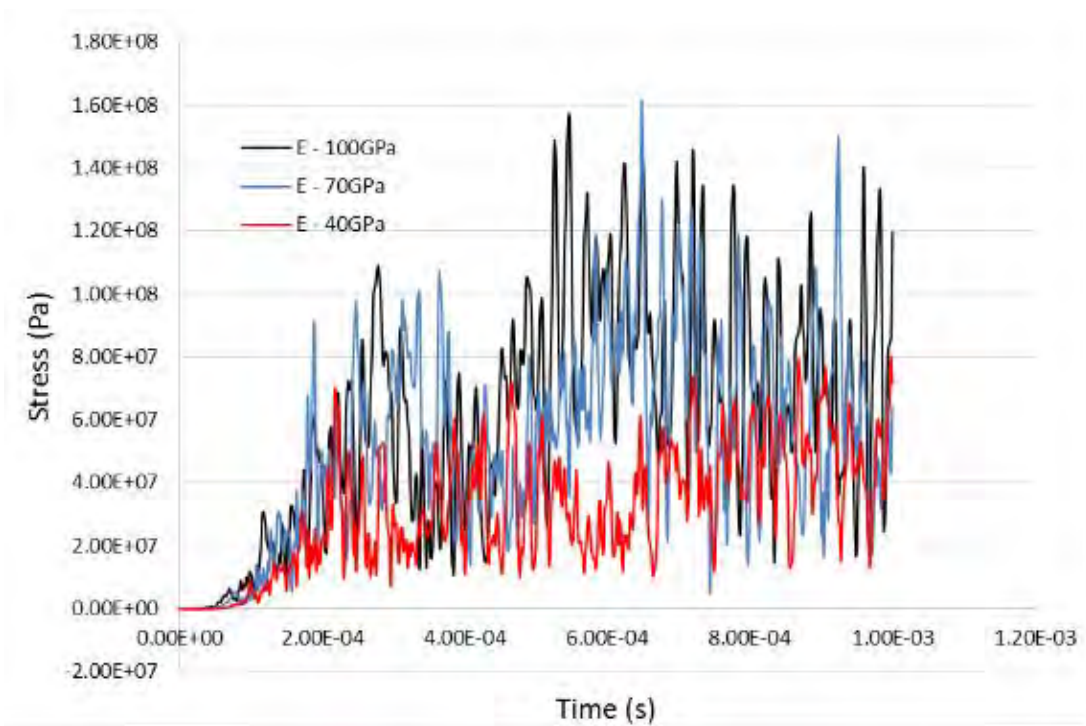


Figure 169. Left wall effective stress for different material modulus (Model 1).

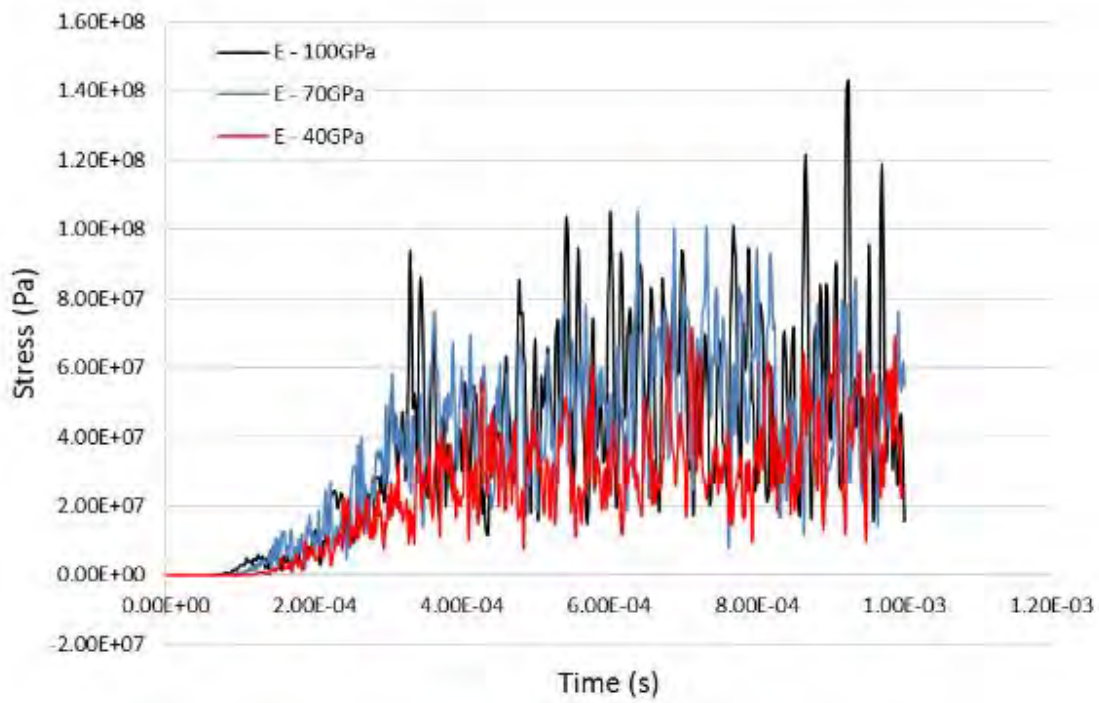


Figure 170. Exit wall effective stress for different material modulus (Model 1).

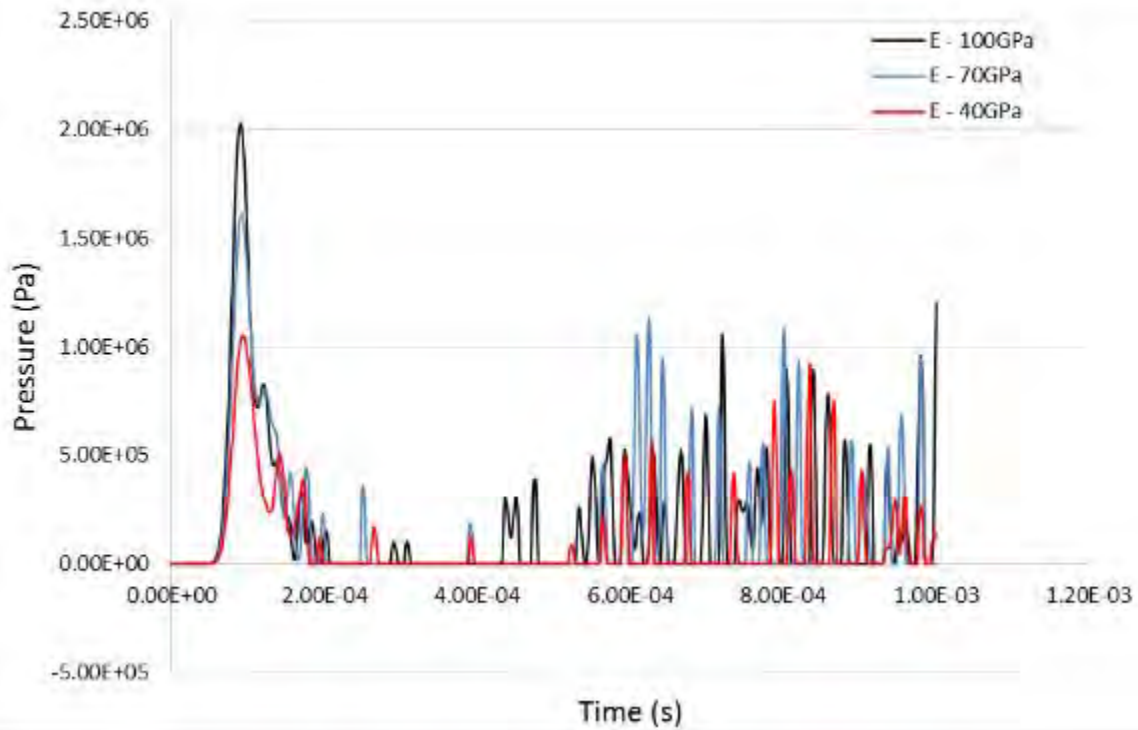


Figure 171. Fluid pressure for different material modulus (Model 1).

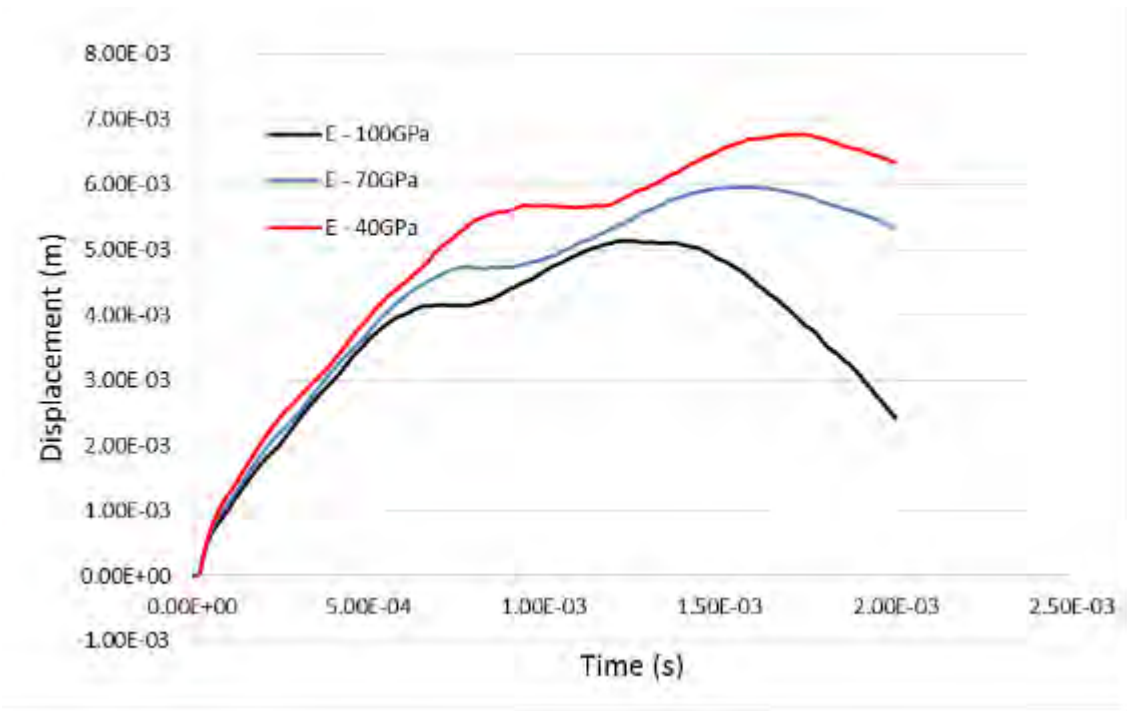


Figure 172. Entry wall resultant displacement for different material modulus (Model 2).

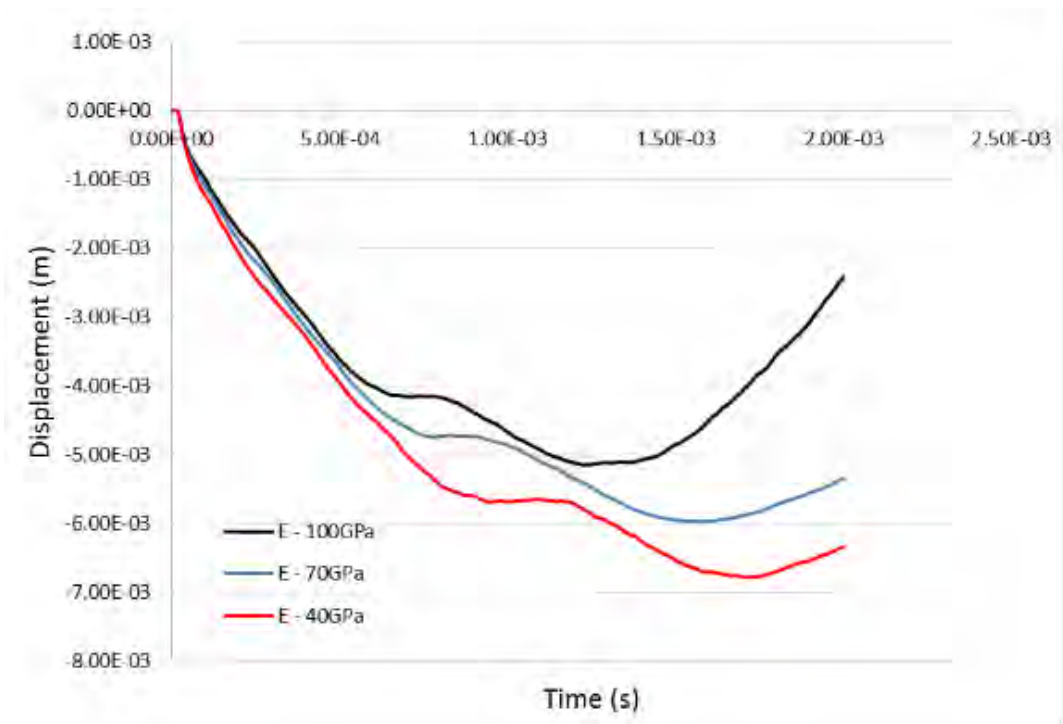


Figure 173. Entry wall X-Displacement for different material modulus (Model 2).

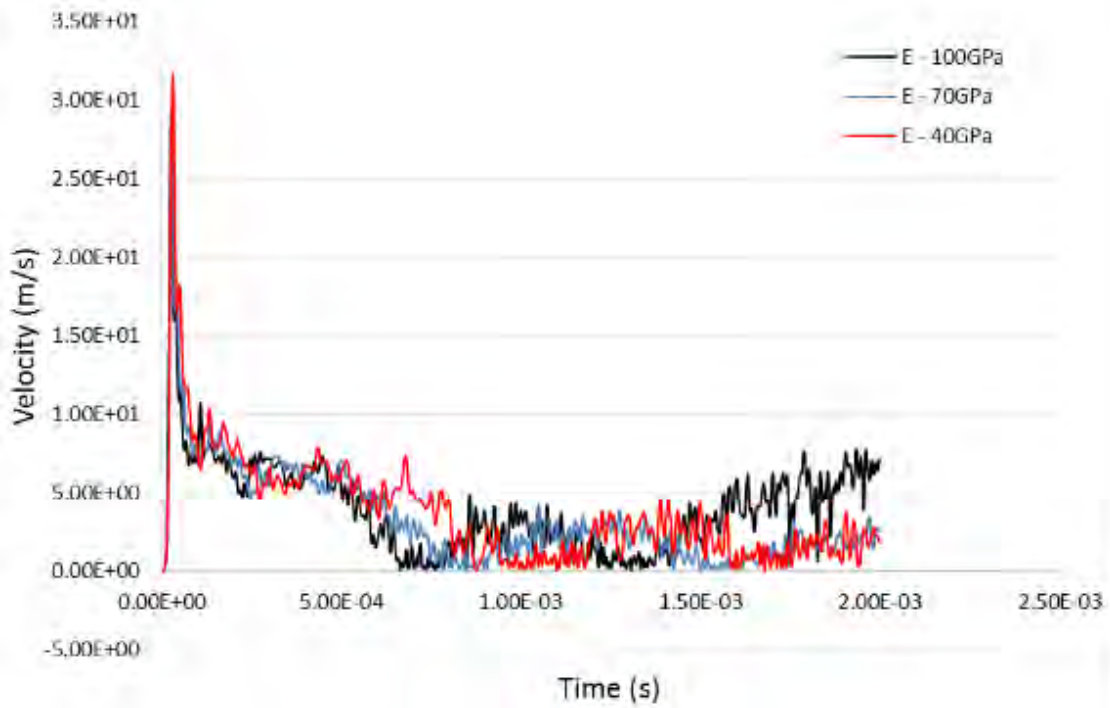


Figure 174. Entry wall resultant velocity for different material modulus (Model 2).

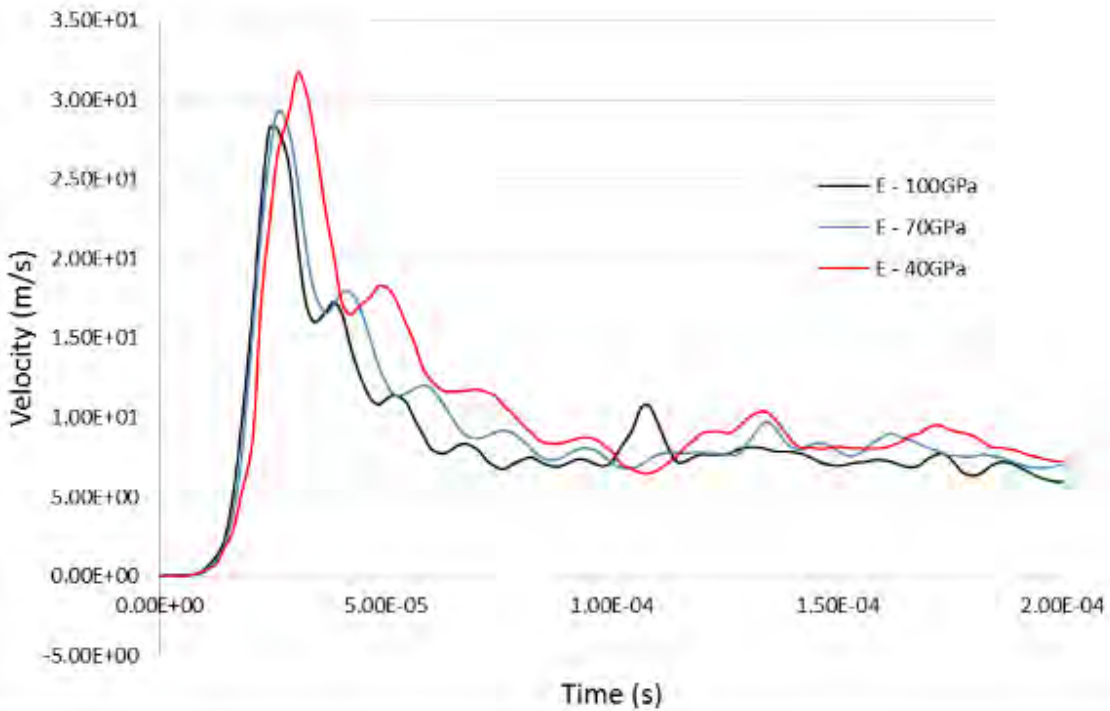


Figure 175. Entry wall resultant velocity for different material modulus (Model 2) – Enlarged.

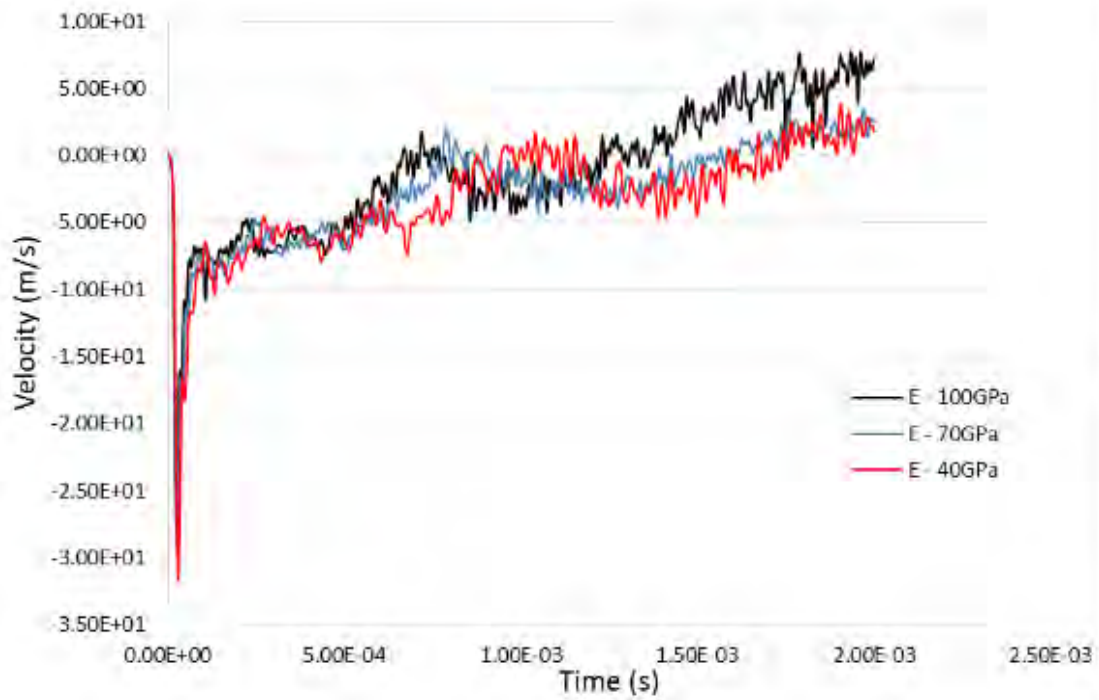


Figure 176. Entry wall X-Velocity for different material modulus (Model 2).

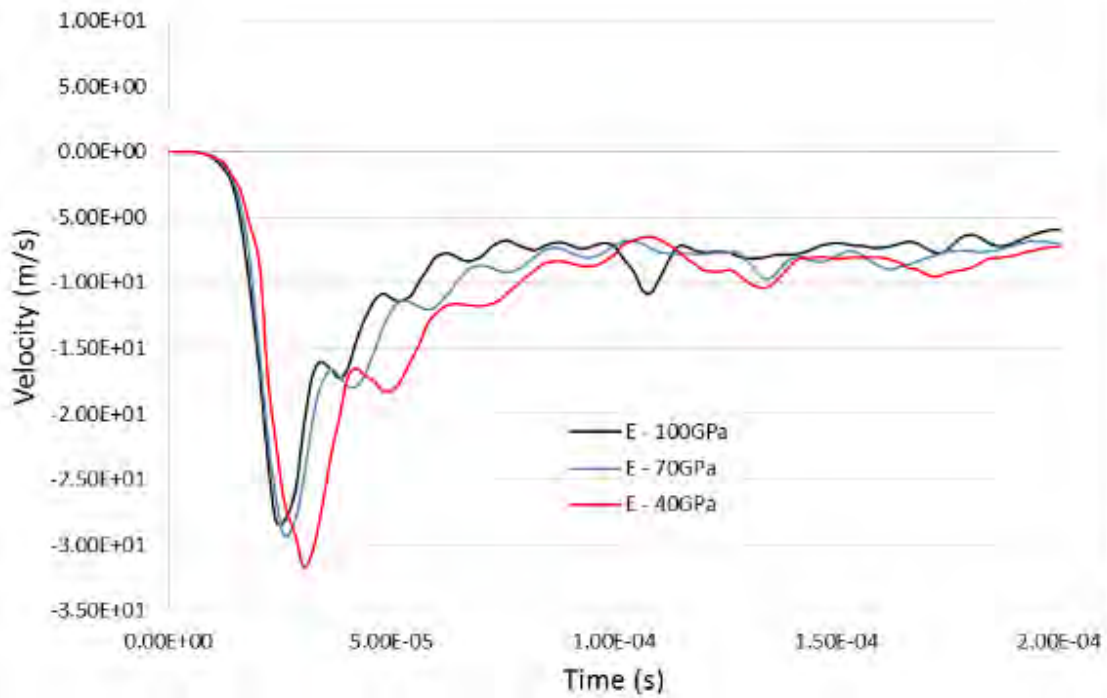


Figure 177. Entry wall X-Velocity for different material modulus (Model 2) – Enlarged.

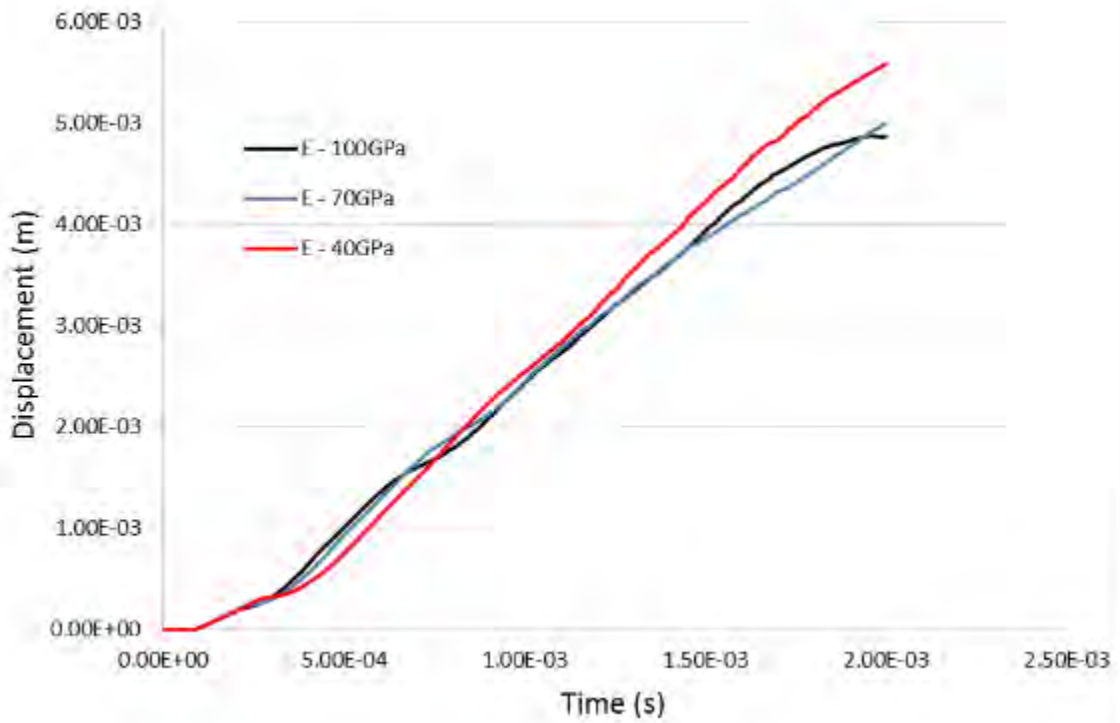


Figure 178. Left wall resultant displacement for different material modulus (Model 2).

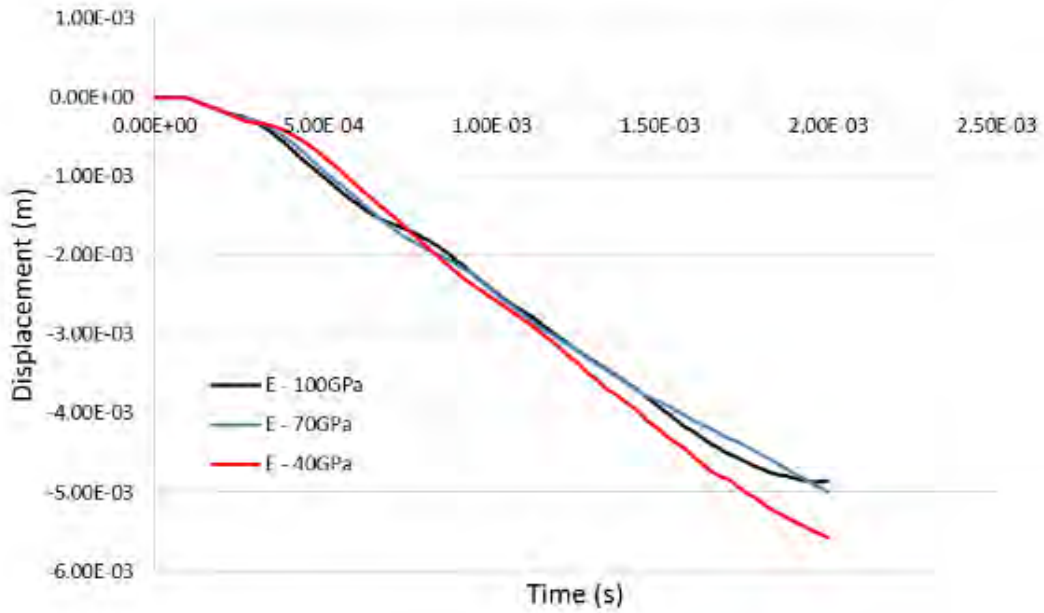


Figure 179. Left wall Z-Displacement for different material modulus (Model 2).

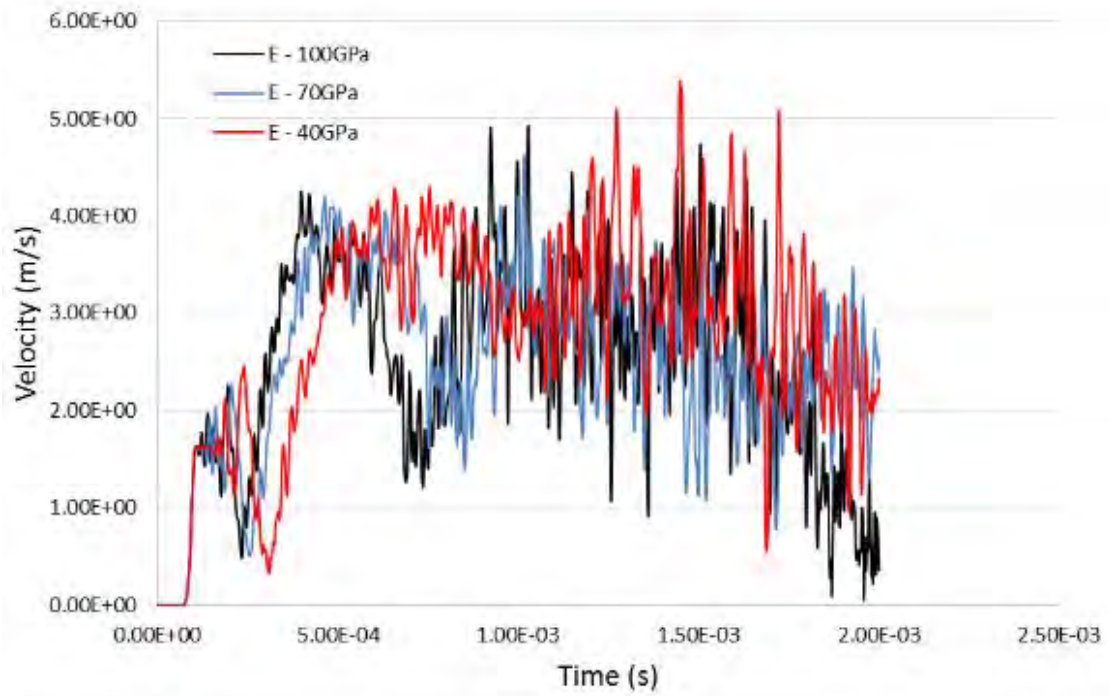


Figure 180. Left wall resultant velocity for different material modulus (Model 2).

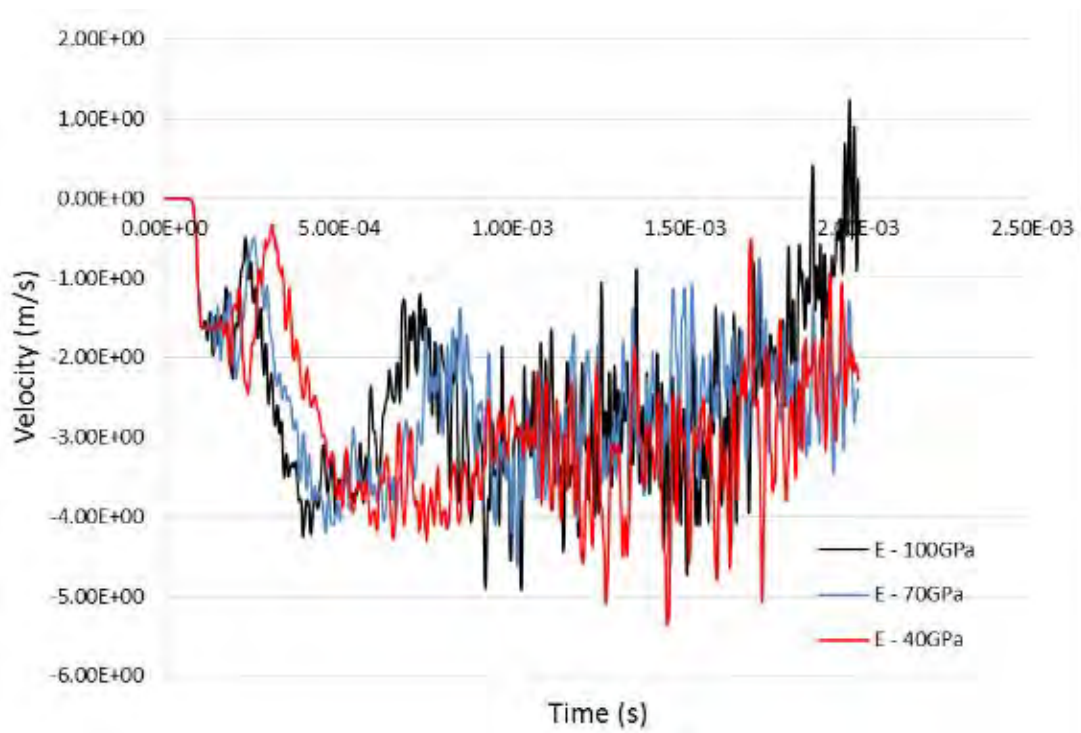


Figure 181. Left wall Z-Velocity for different material modulus (Model 2).

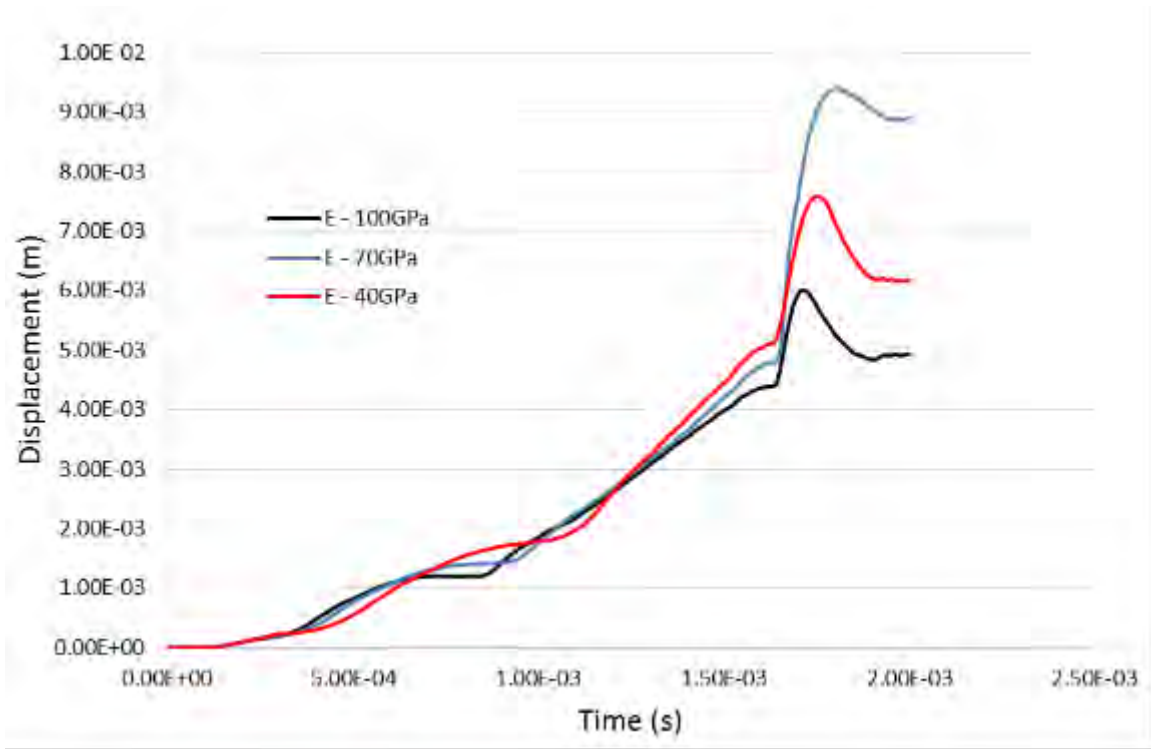


Figure 182. Exit wall resultant displacement for different material modulus (Model 2).

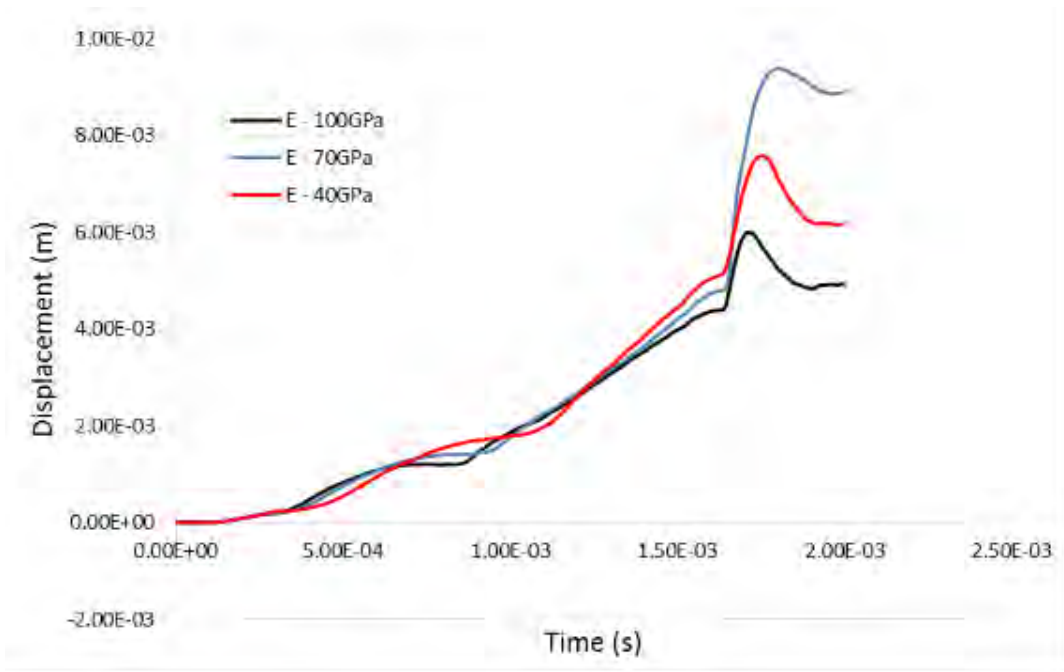


Figure 183. Exit wall X-Displacement for different material modulus (Model 2).

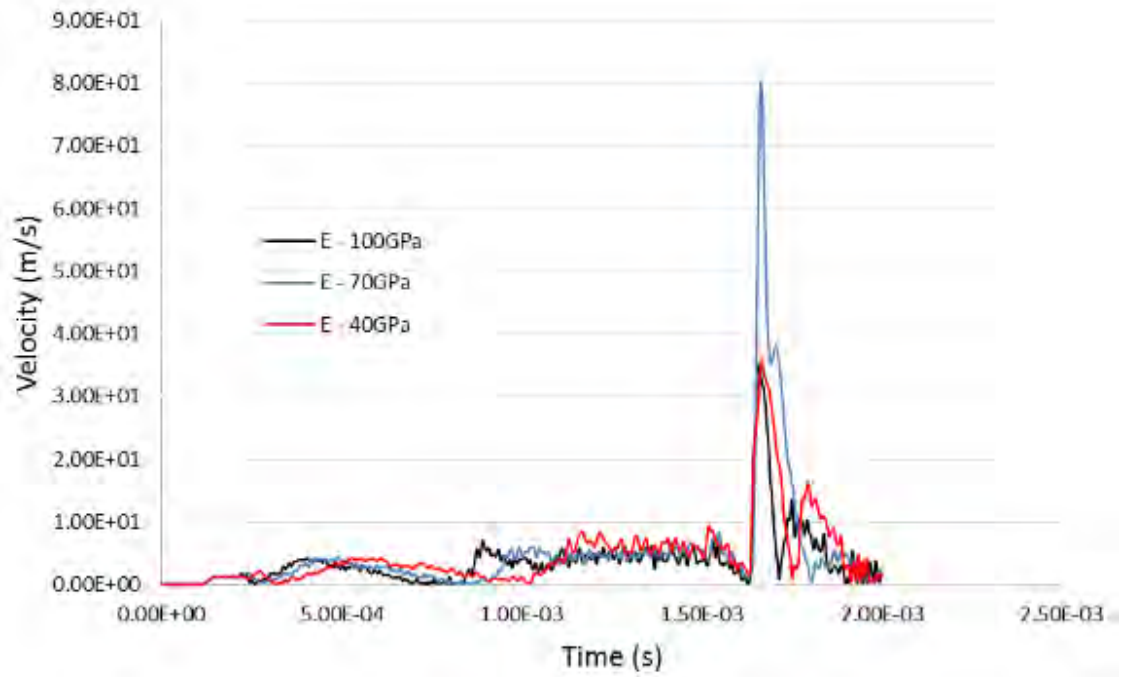


Figure 184. Exit wall resultant velocity for different material modulus (Model 2).

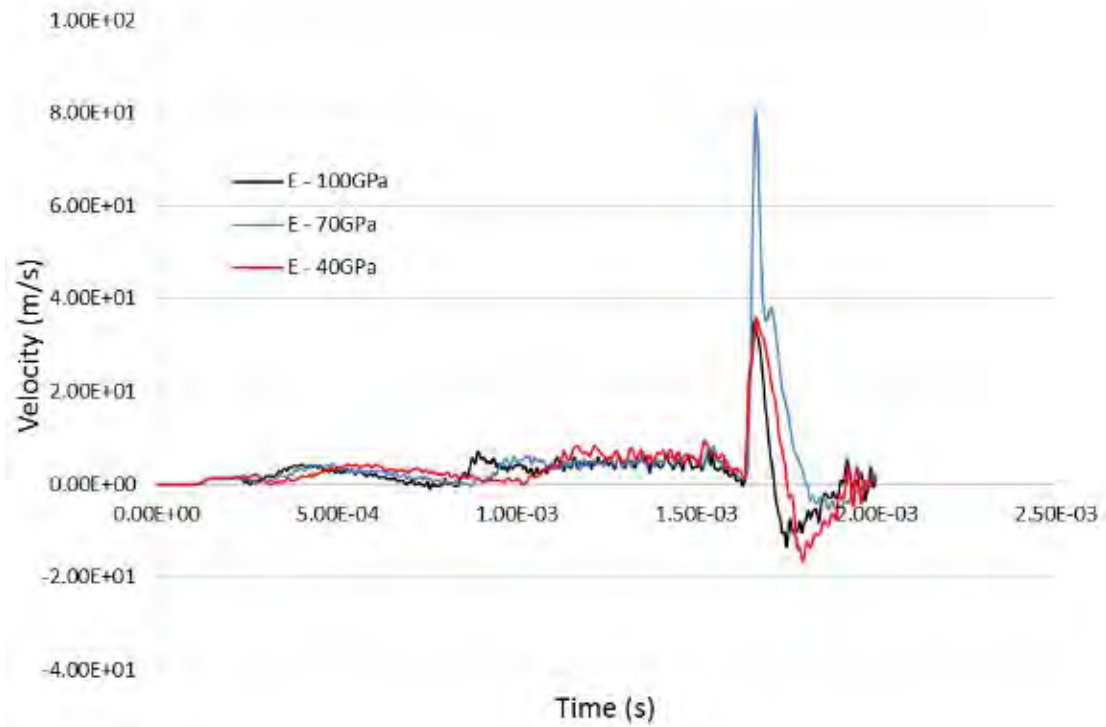


Figure 185. Exit wall X-Velocity for different material modulus (Model 2).

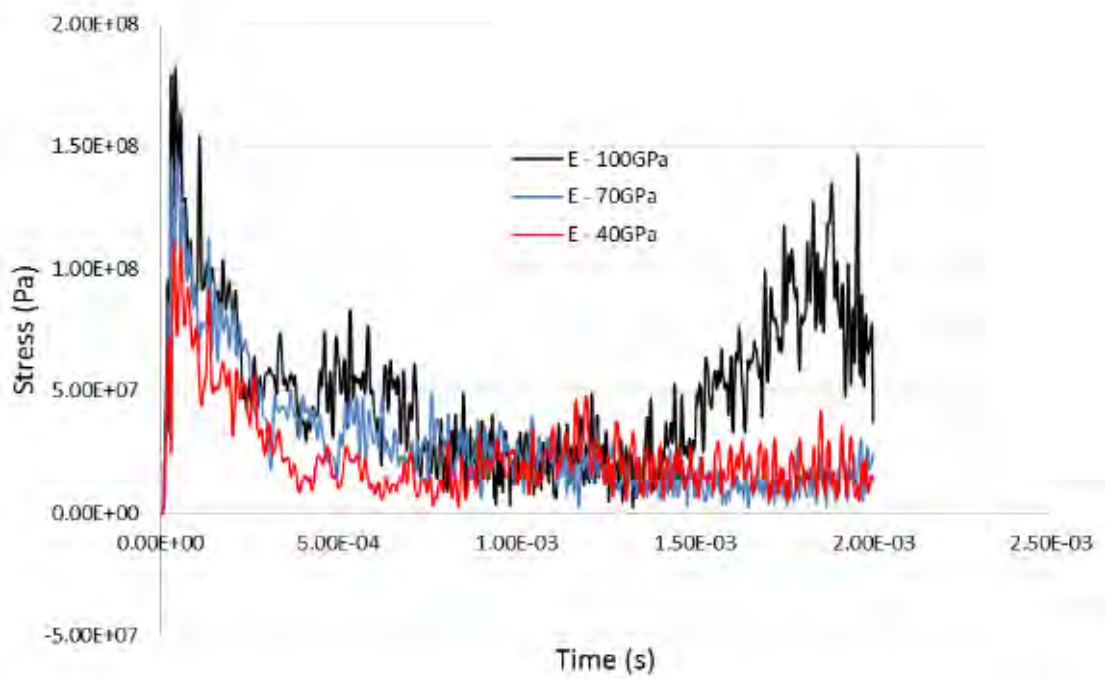


Figure 186. Entry wall effective stress for different material modulus (Model 2).

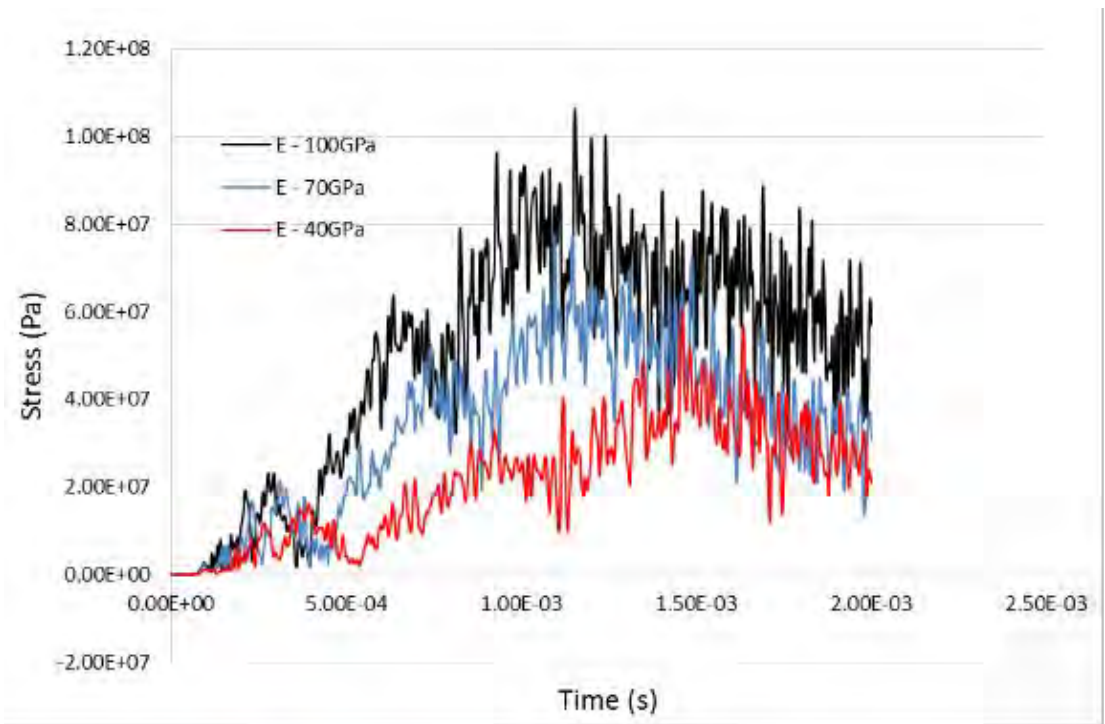


Figure 187. Left wall effective stress for different material modulus (Model 2).

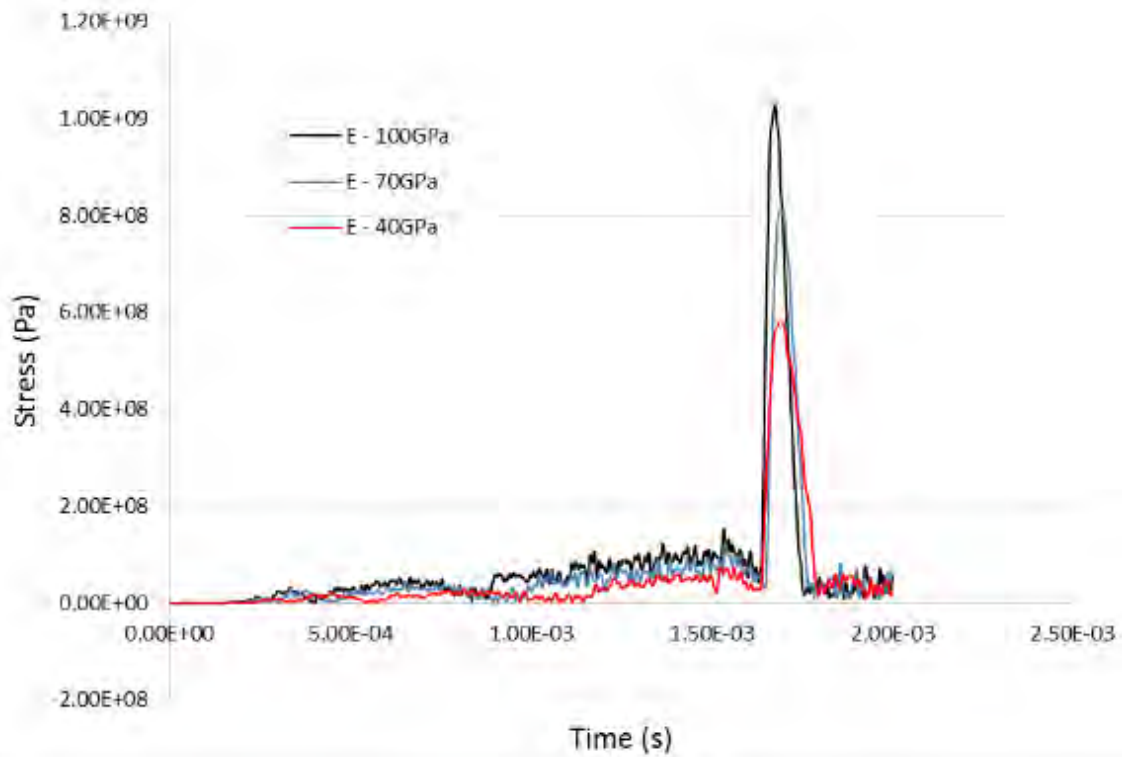


Figure 188. Exit wall effective stress for different material modulus (Model 2).

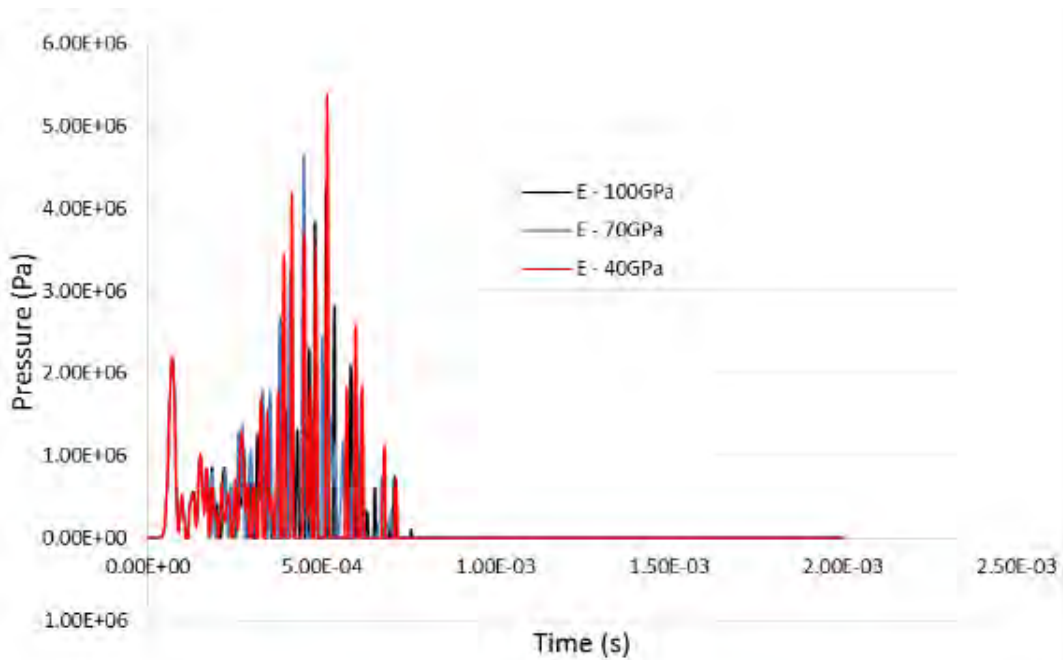


Figure 189. Drag phase pressure for different material modulus (Model 2).

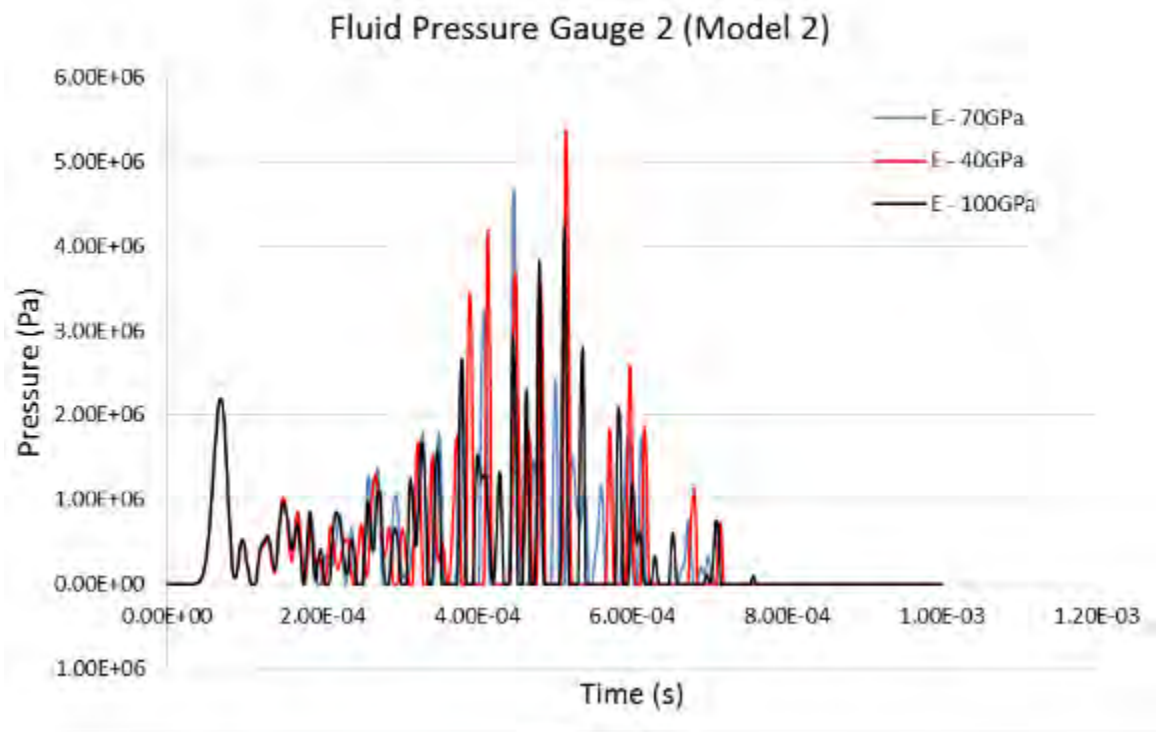
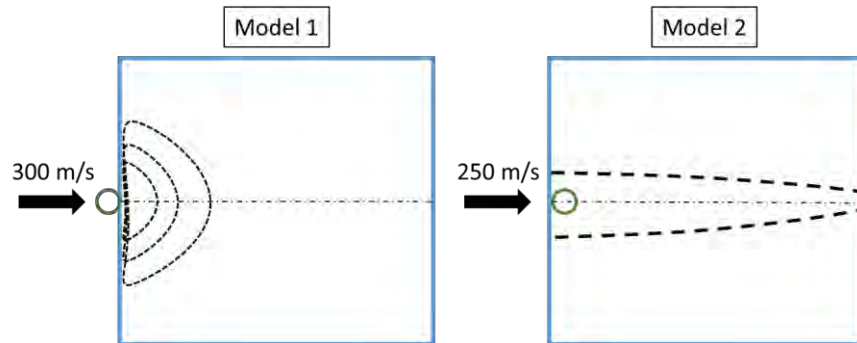


Figure 190. Drag phase pressure for different material modulus (Model 2) - Enlarged.

THIS PAGE INTENTIONALLY LEFT BLANK

APPENDIX E. GRAPHS FOR TANK MATERIAL DENSITY VARIATION



Tank material density investigated: 1500kg/m^3 , 2700kg/m^3 and 4500kg/m^3

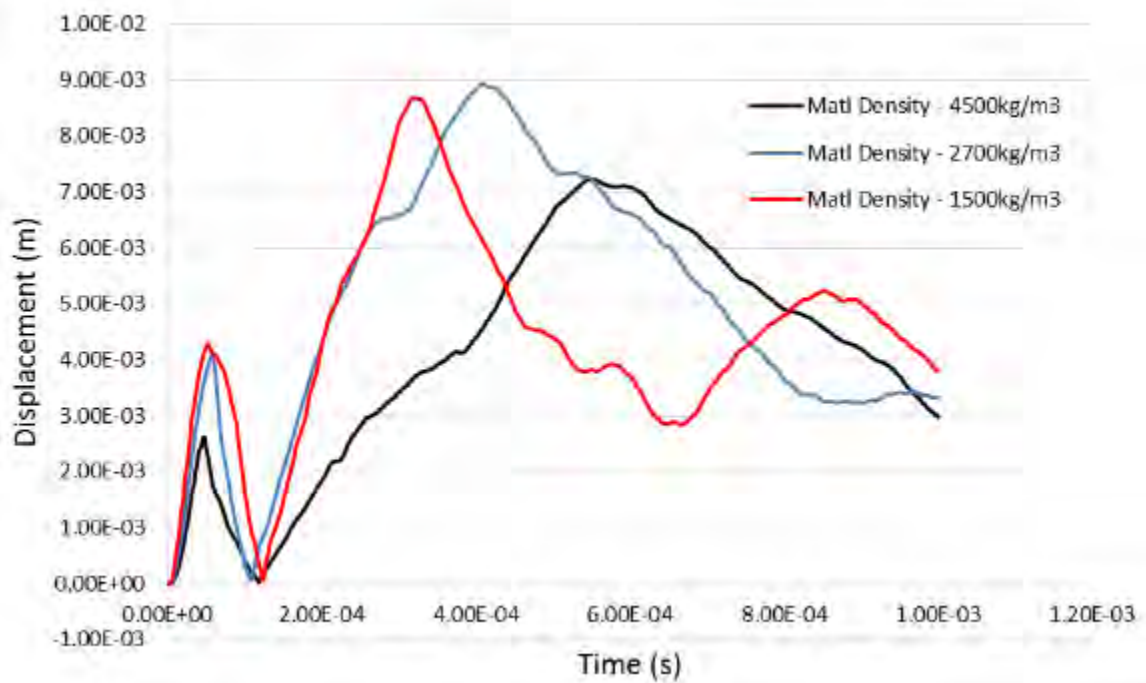


Figure 191. Entry wall resultant displacement for different material density (Model 1).

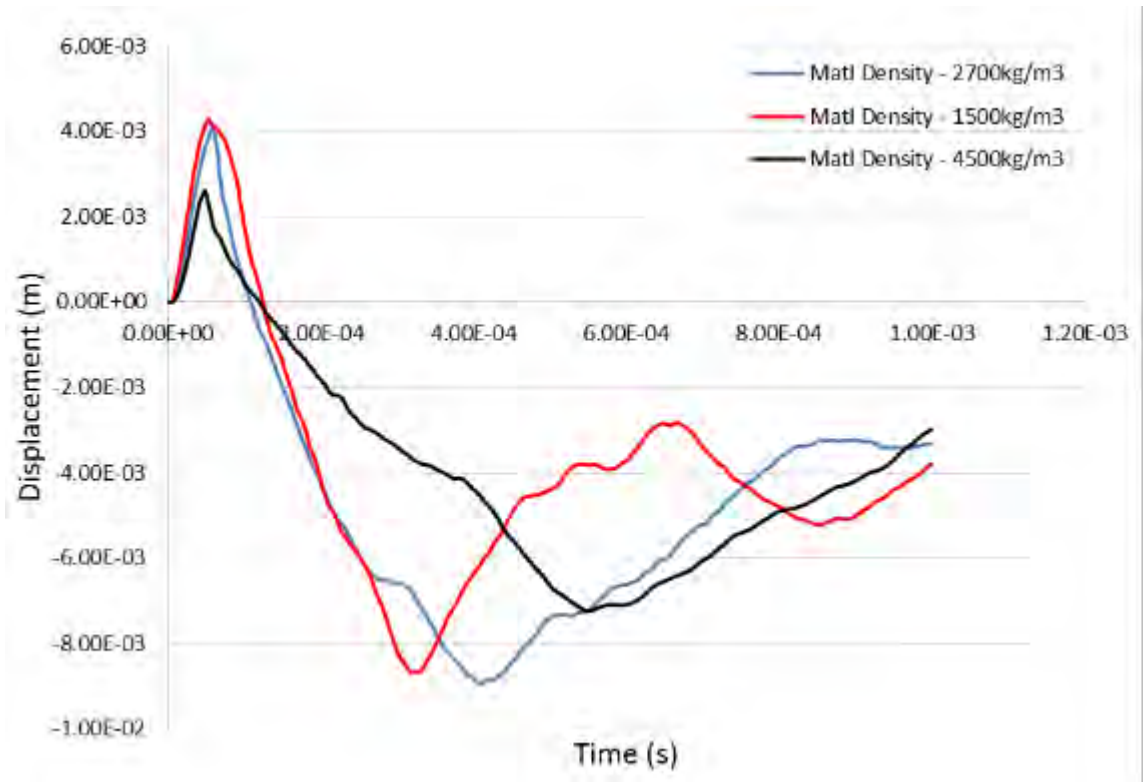


Figure 192. Entry wall X-Displacement for different material density (Model 1).

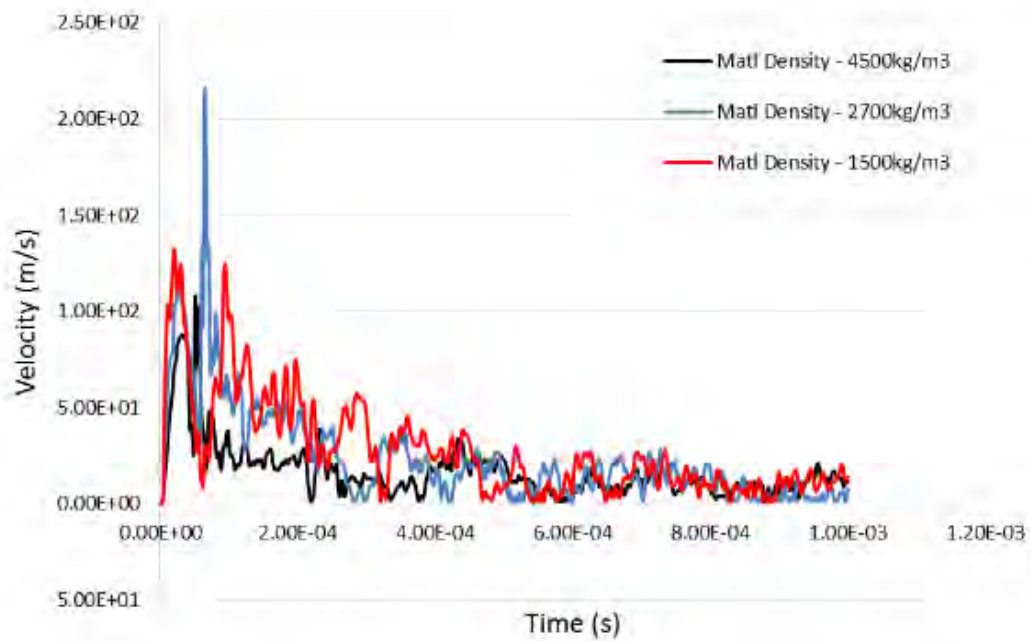


Figure 193. Entry wall resultant velocity for different material density (Model 1).

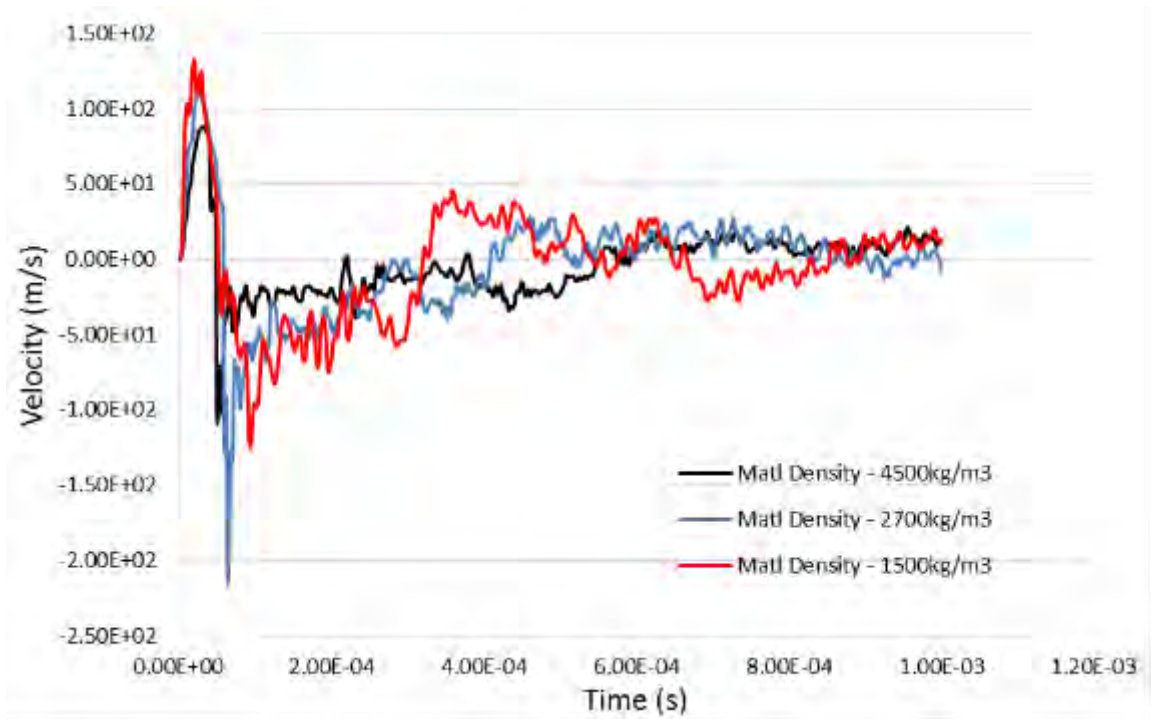


Figure 194. Entry wall X-Velocity for different material density (Model 1).

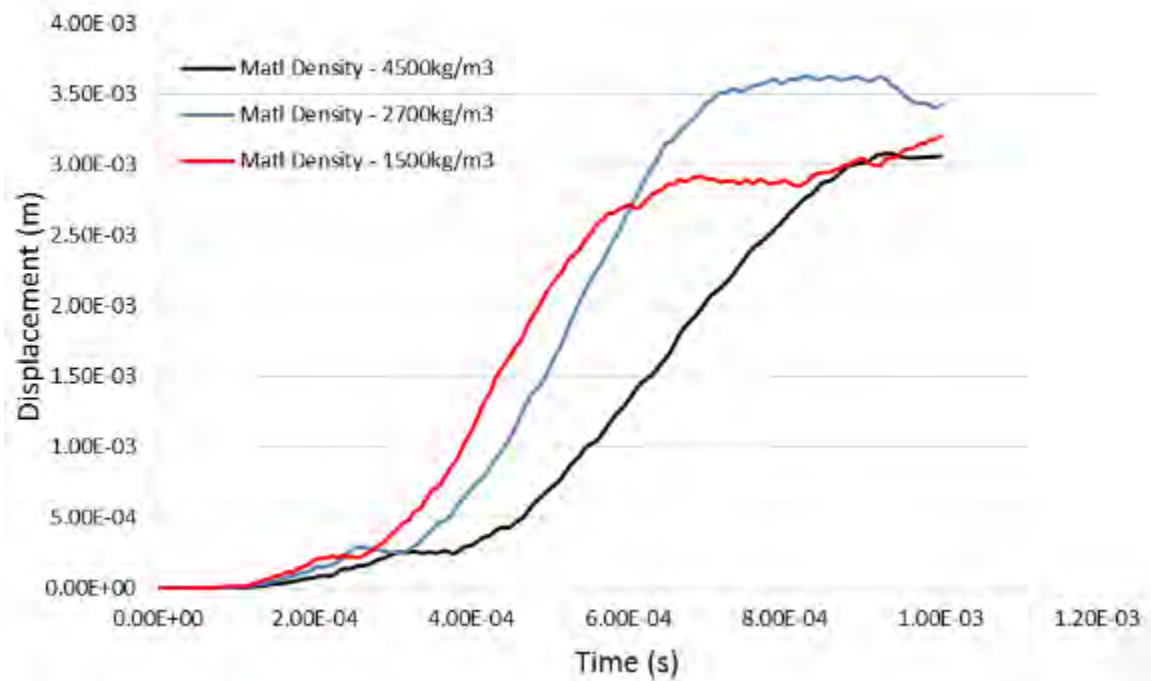


Figure 195. Left wall resultant displacement for different material density (Model 1).

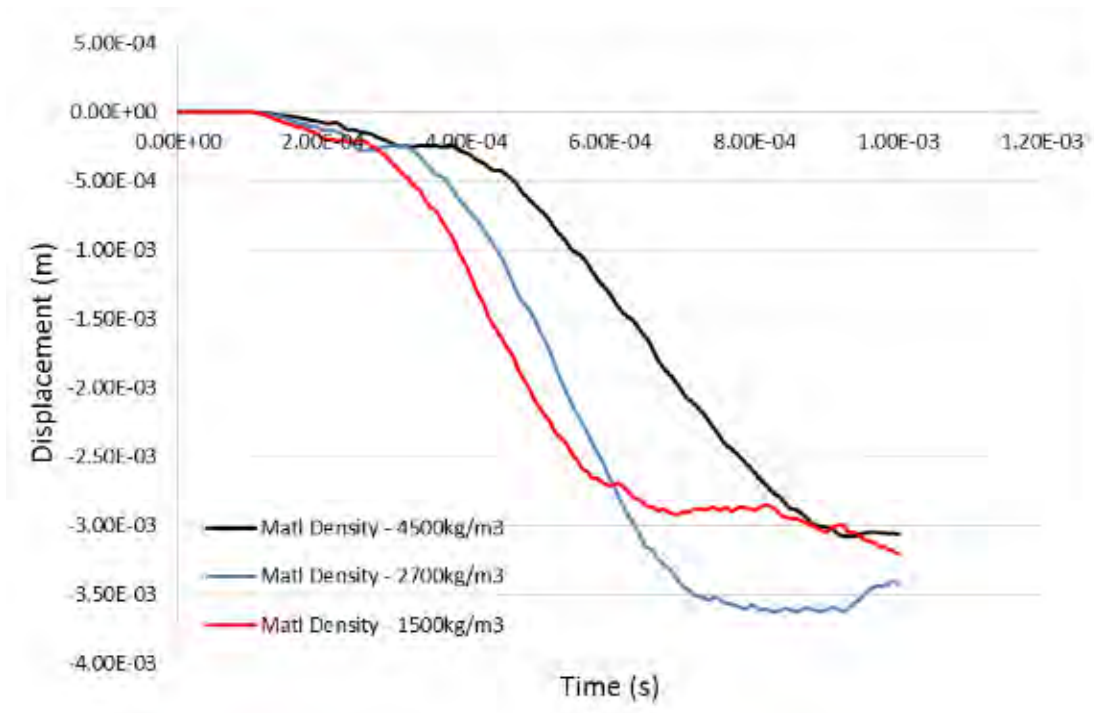


Figure 196. Left wall Z-Displacement for different material density (Model 1).

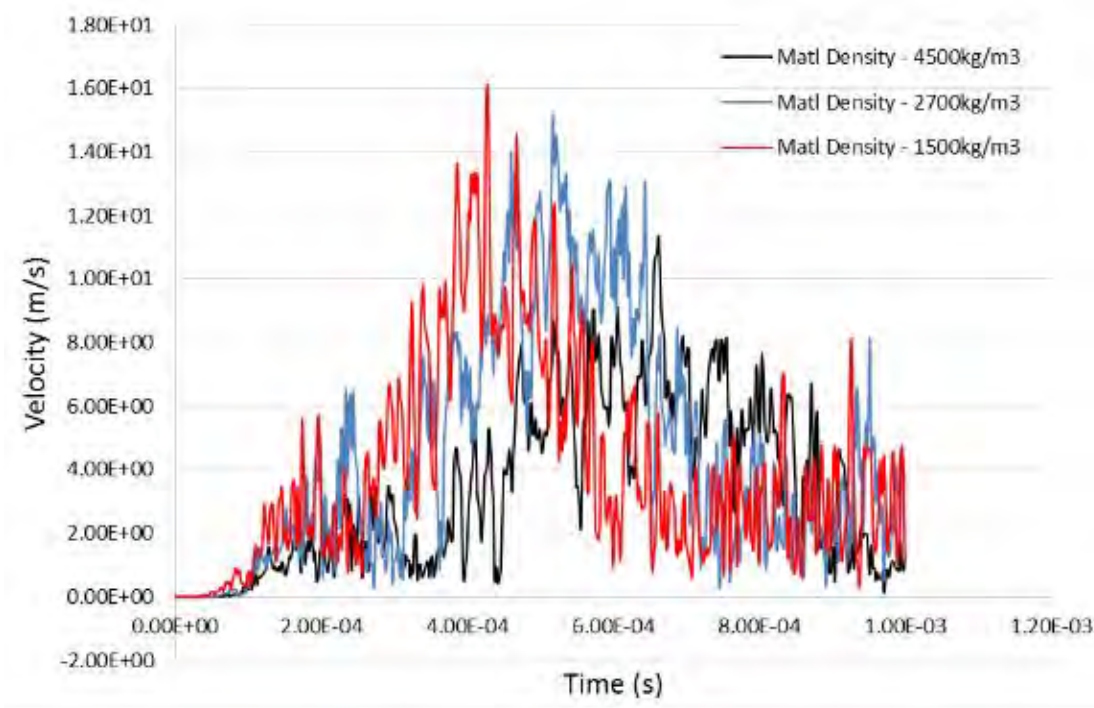


Figure 197. Left wall resultant velocity for different material density (Model 1).

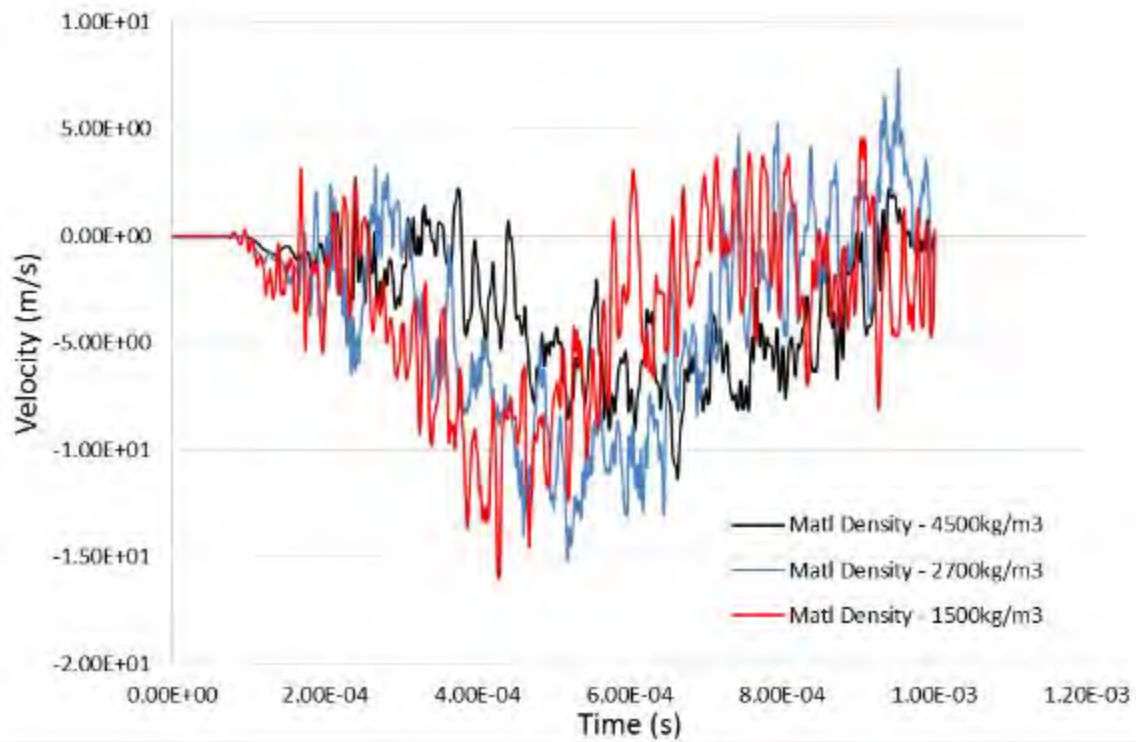


Figure 198. Left wall Z-Velocity for different material density (Model 1).

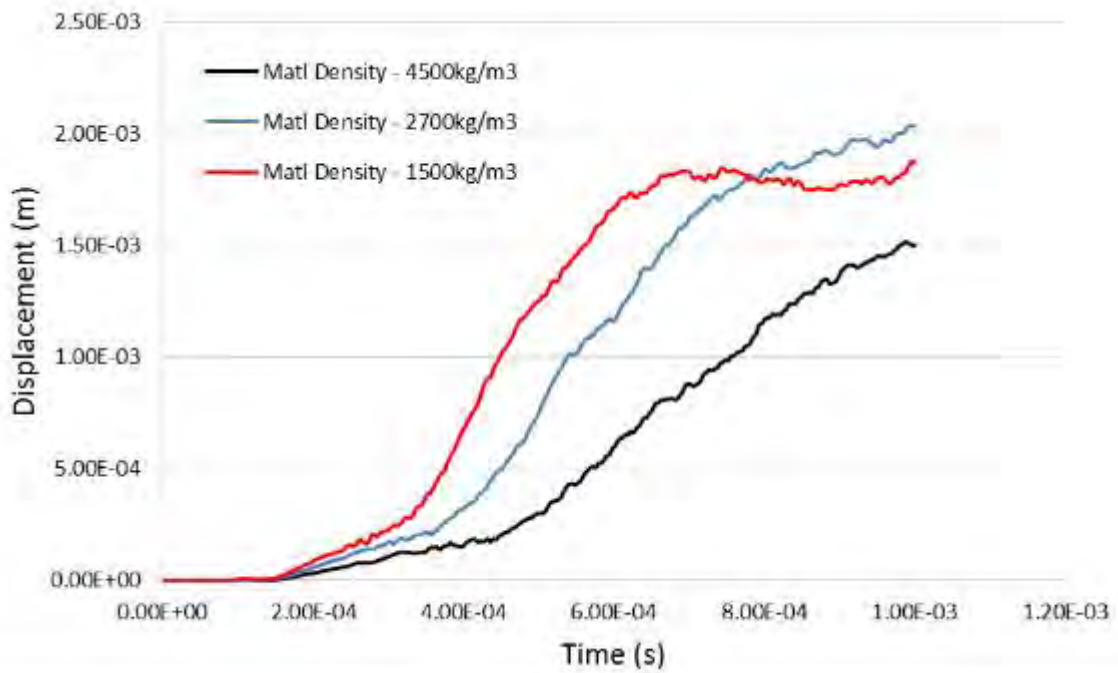


Figure 199. Exit wall resultant displacement for different material density (Model 1).

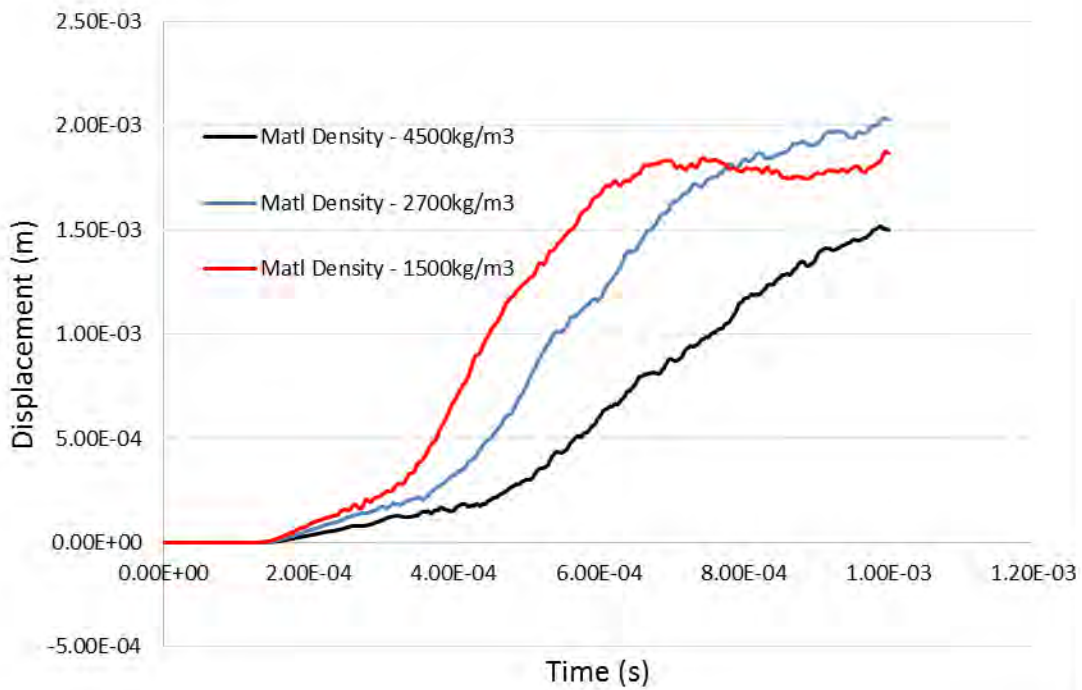


Figure 200. Exit wall X-Displacement for different material density (Model 1).

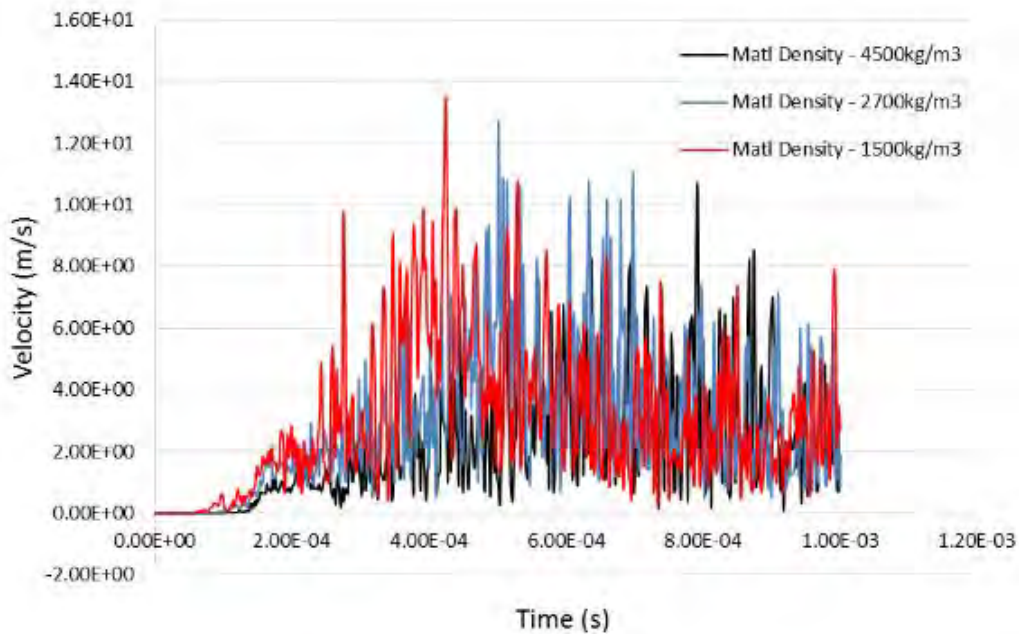


Figure 201. Exit wall resultant velocity for different material density (Model 1).

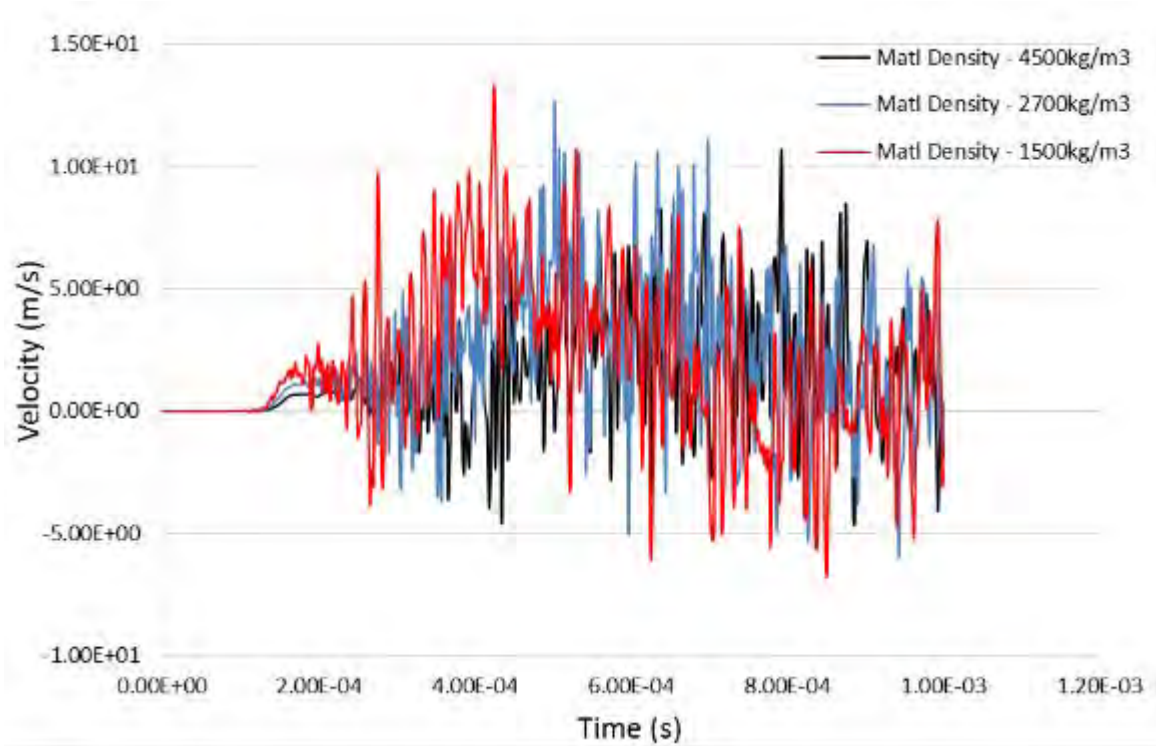


Figure 202. Exit wall X-Velocity for different material density (Model 1).

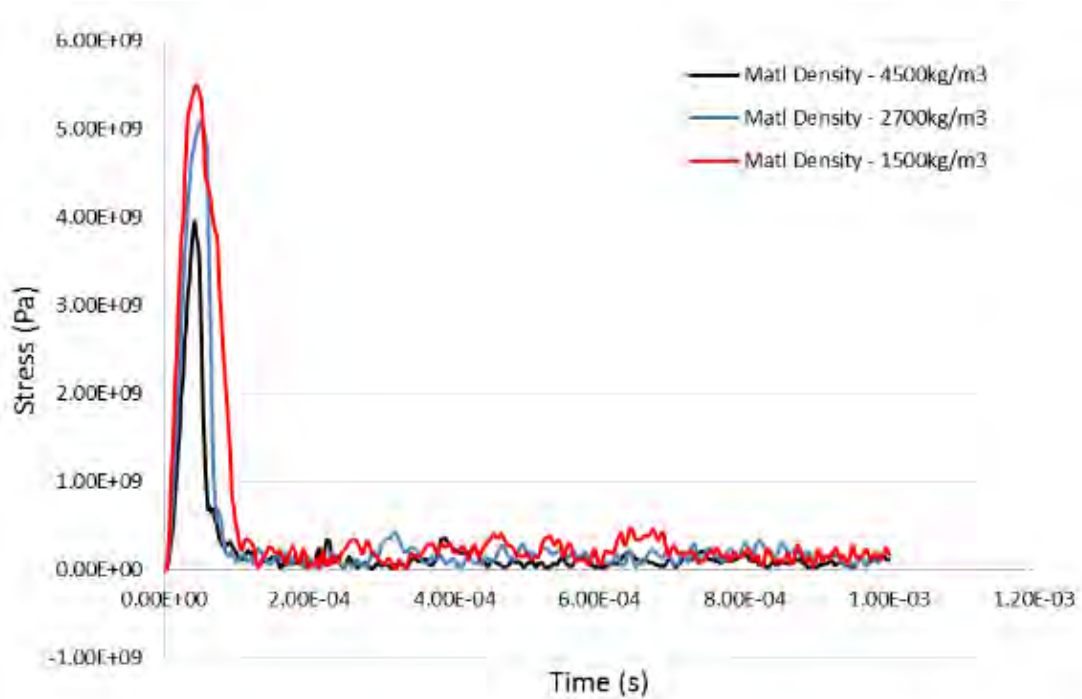


Figure 203. Entry wall effective stress for different material density (Model 1).

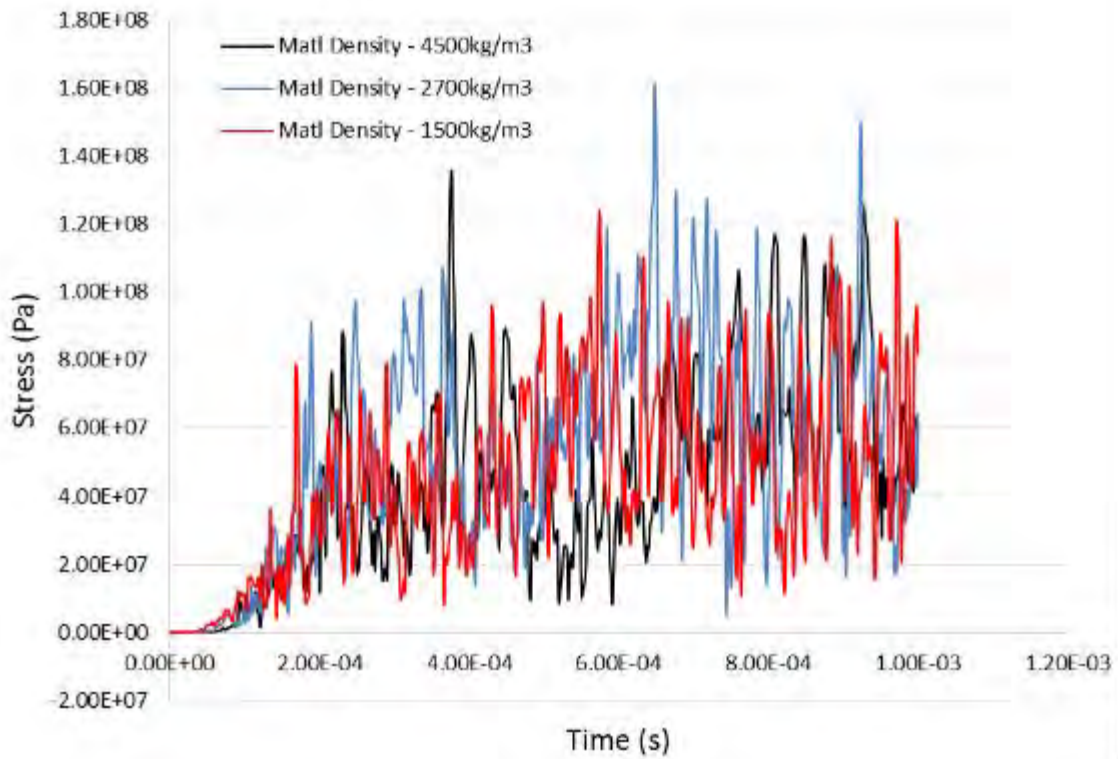


Figure 204. Left wall effective stress for different material density (Model 1).

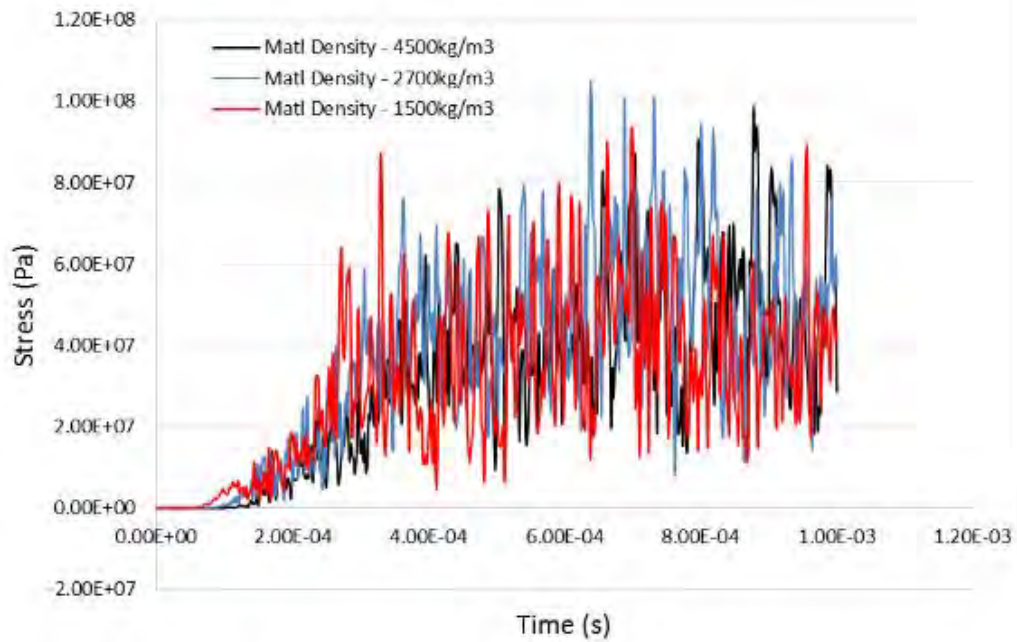


Figure 205. Exit wall effective stress for different material density (Model 1).

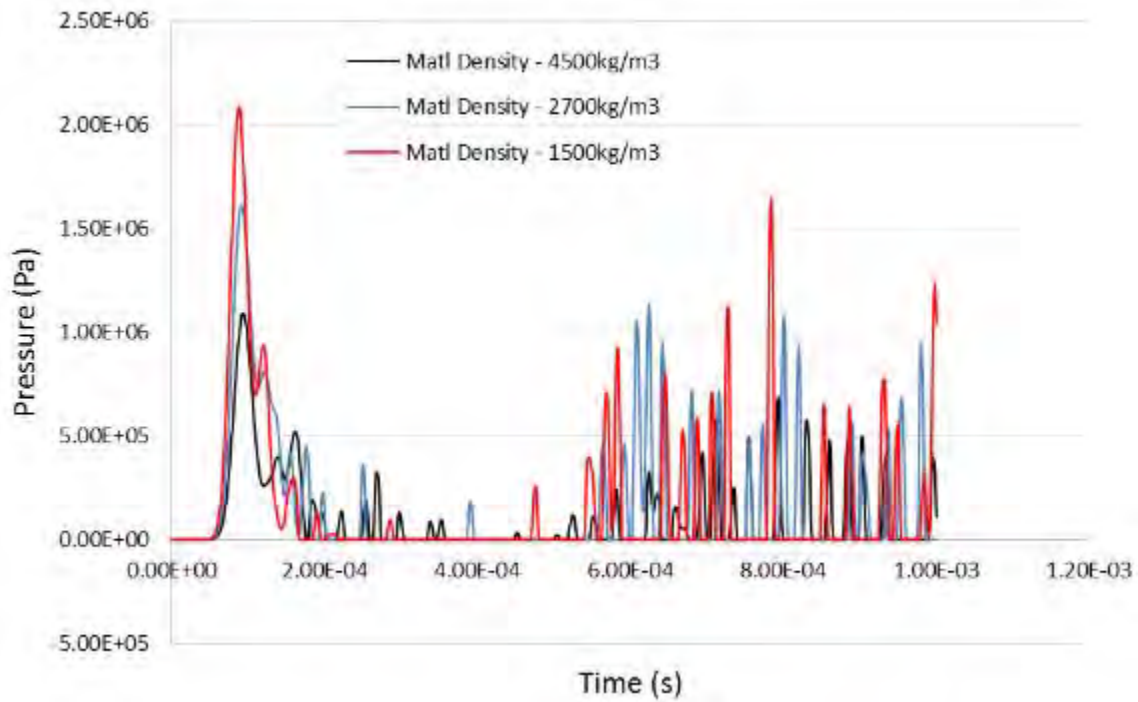


Figure 206. Fluid pressure for different material density (Model 1).

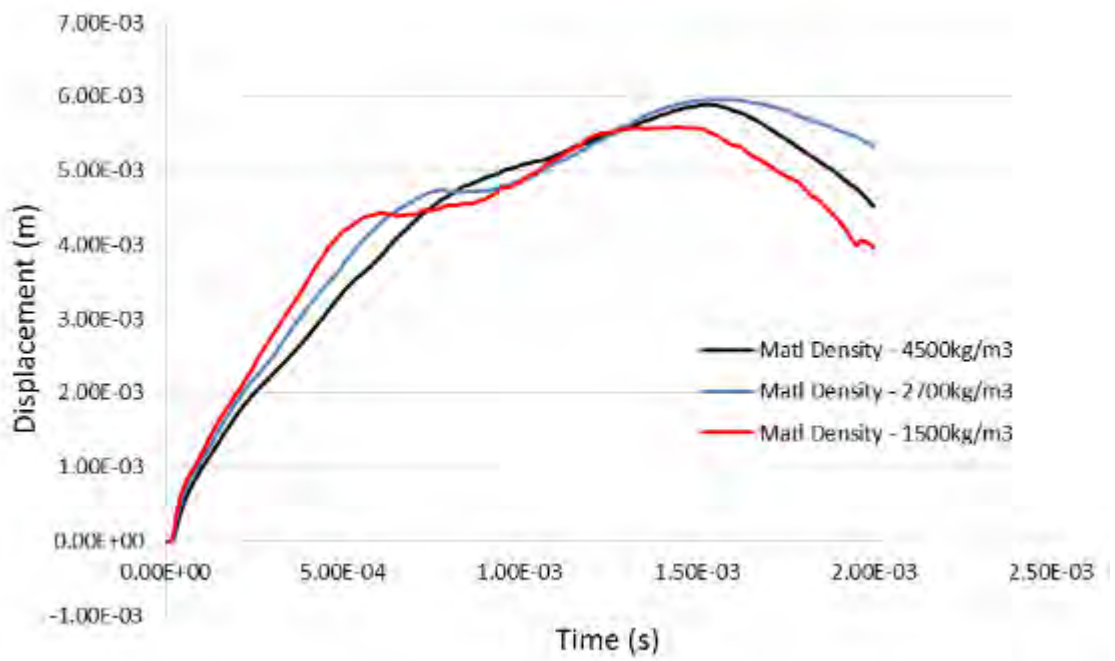


Figure 207. Entry wall resultant displacement for different material density (Model 2).

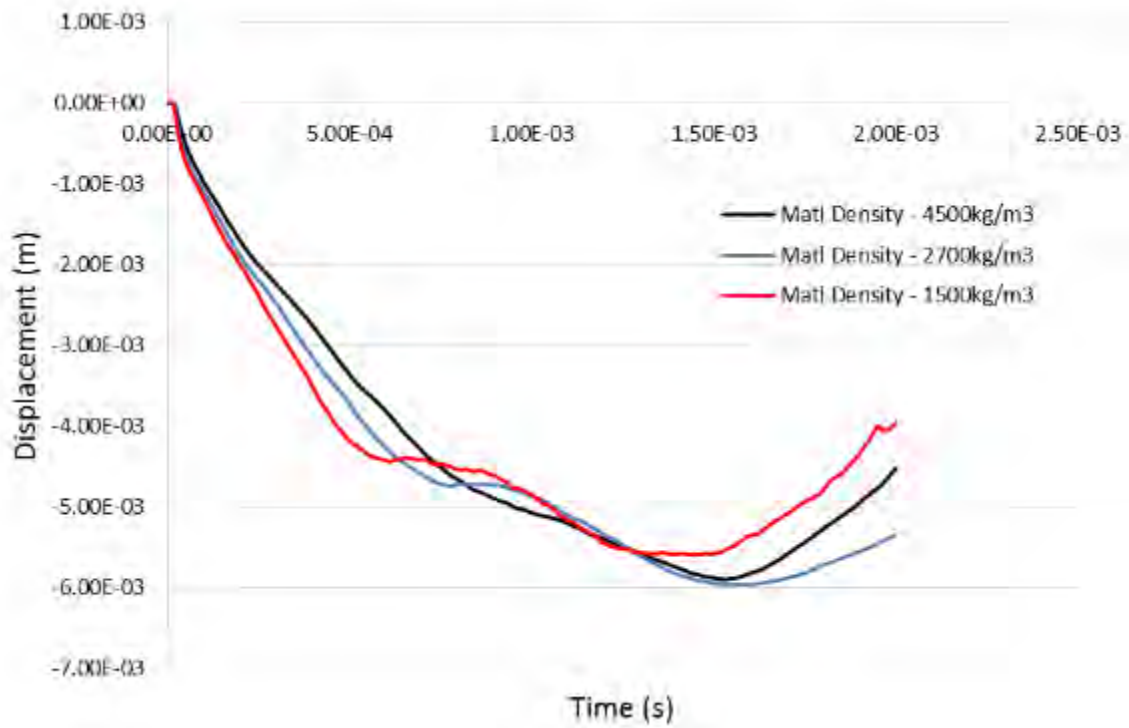


Figure 208. Entry wall X-Displacement for different material density (Model 2).

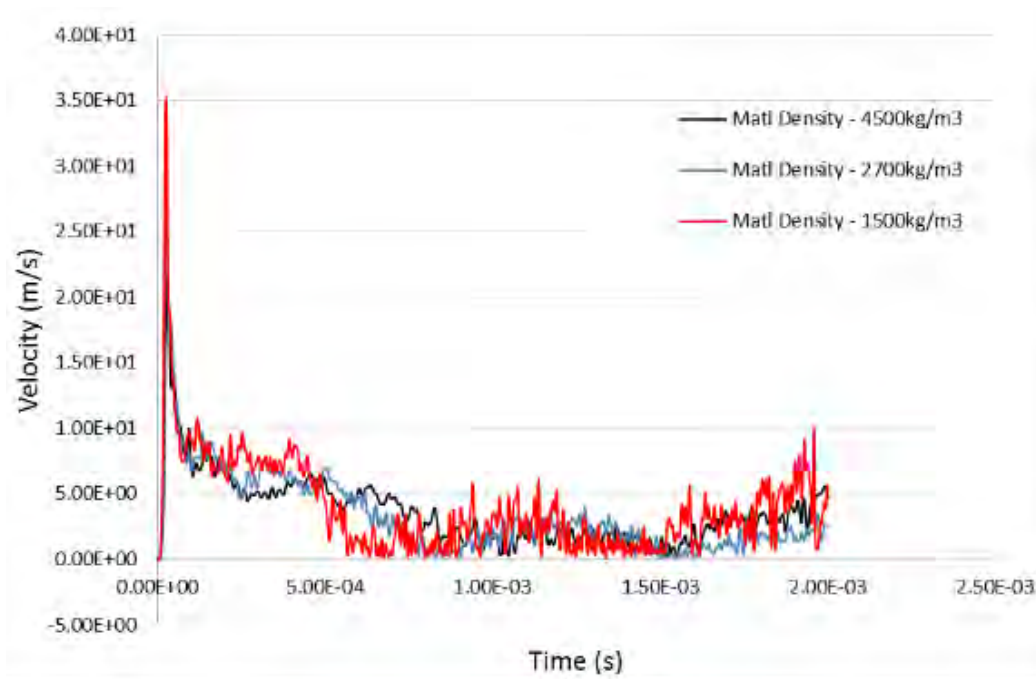


Figure 209. Entry wall resultant velocity for different material density (Model 2).

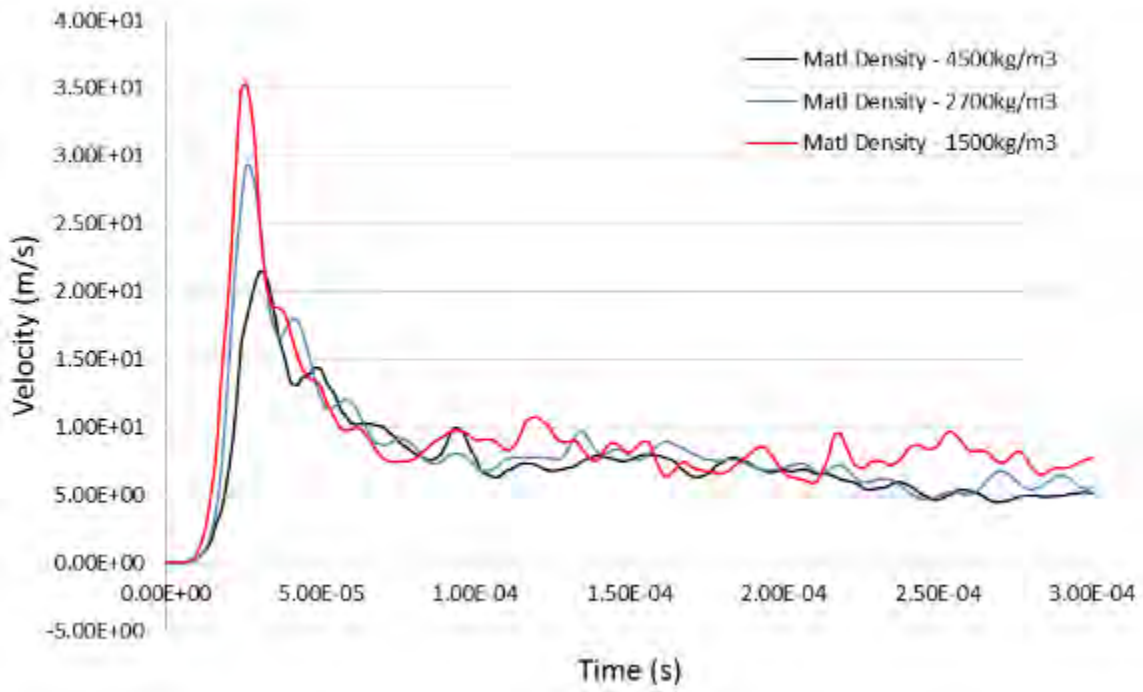


Figure 210. Entry wall resultant velocity for different material density (Model 2) – Enlarged.

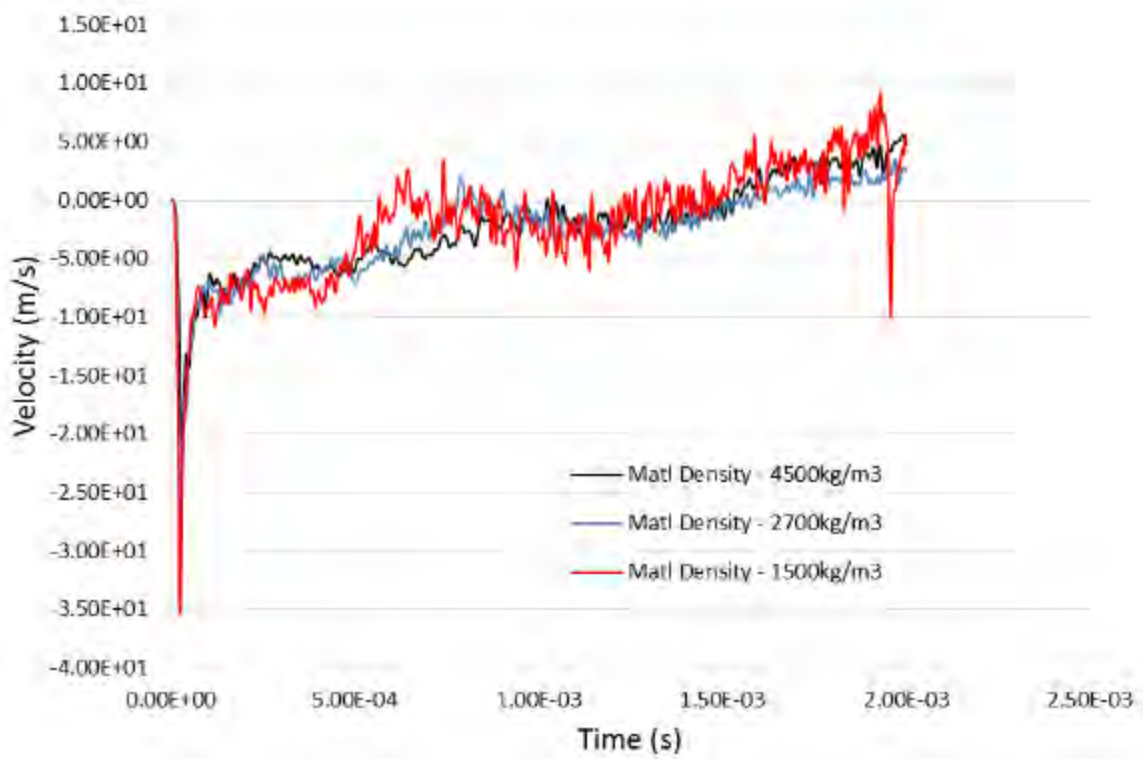


Figure 211. Entry wall X-Velocity for different material density (Model 2).

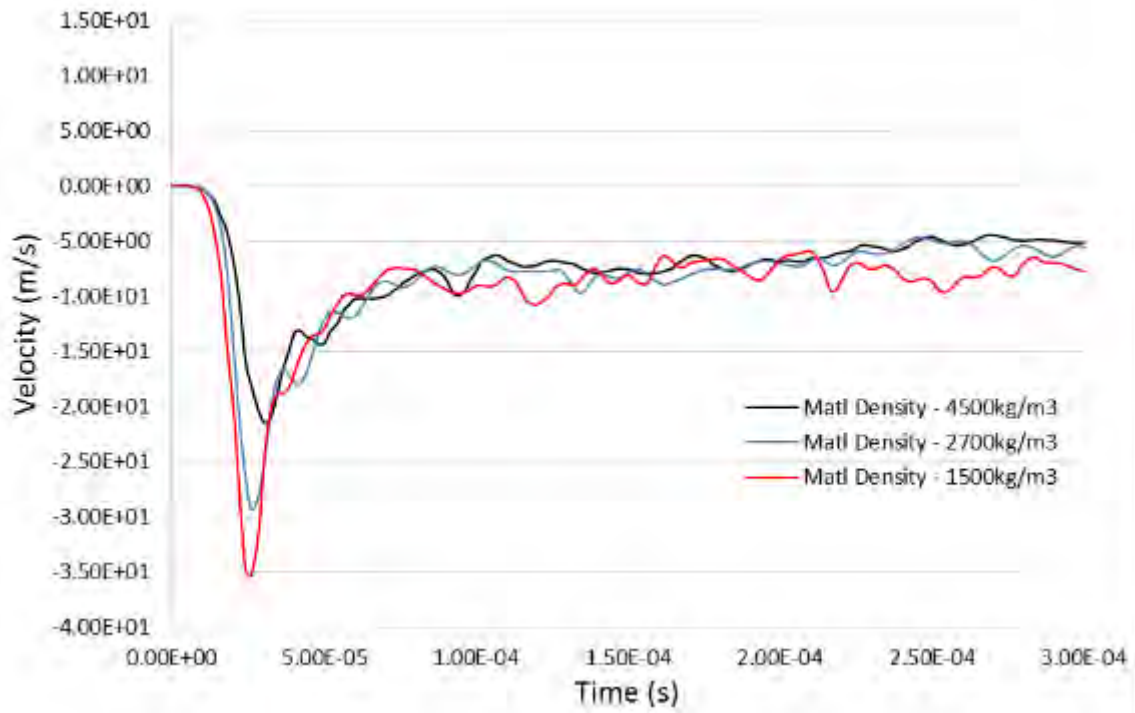


Figure 212. Entry wall X-Velocity for different material density (Model 2) – Enlarged.

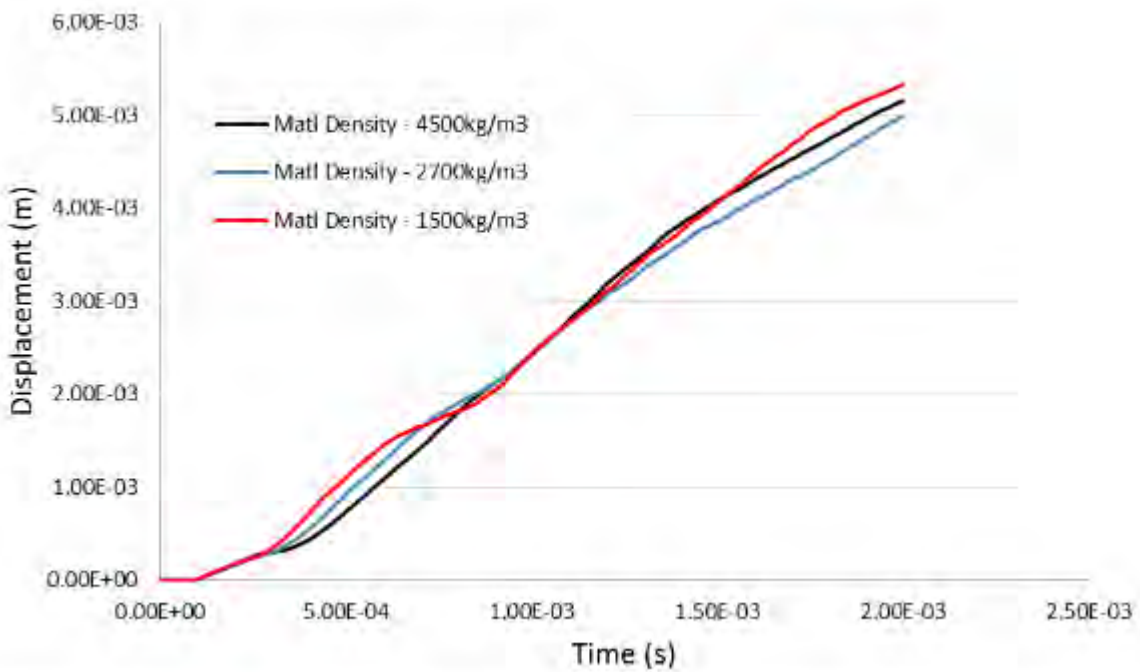


Figure 213. Left wall resultant displacement for different material density (Model 2).

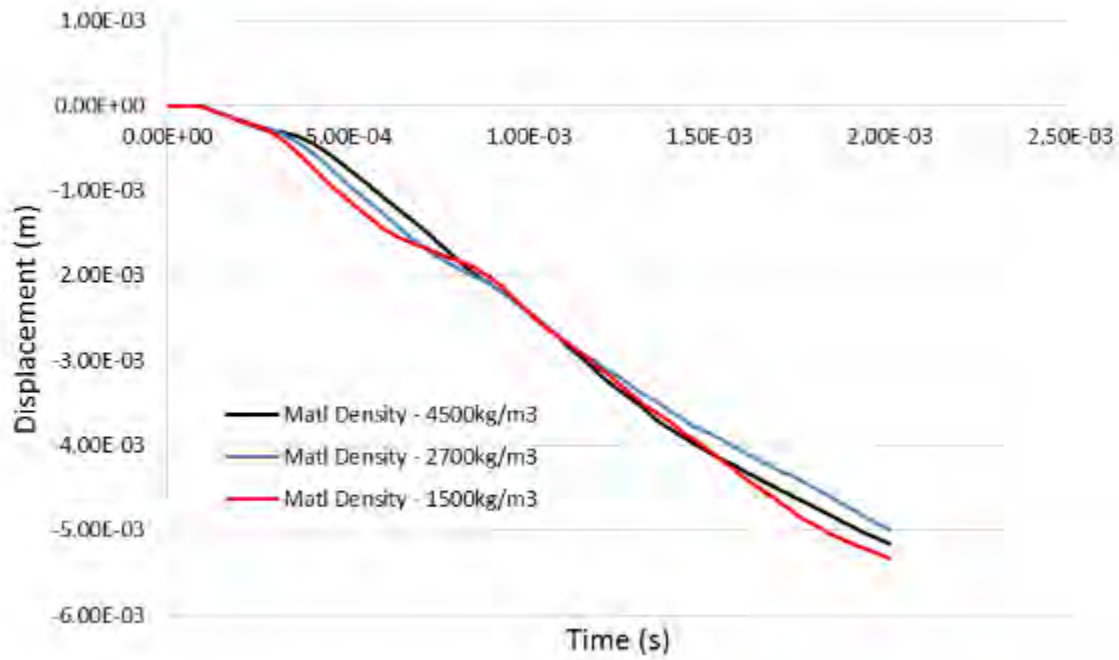


Figure 214. Left wall Z-Displacement for different material density (Model 2).

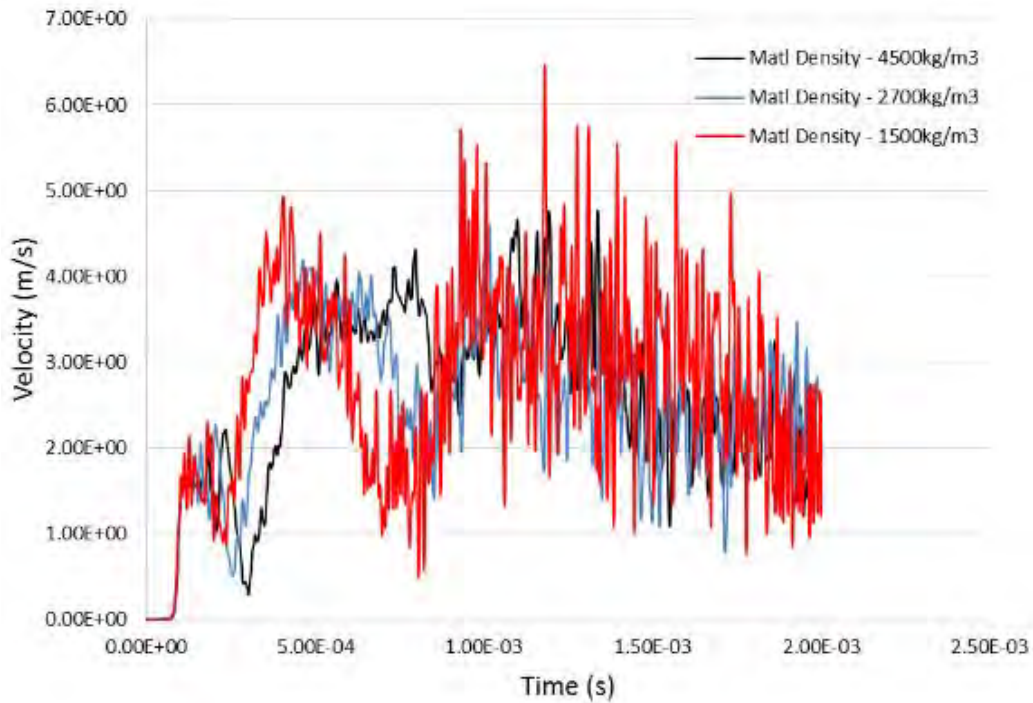


Figure 215. Left wall resultant velocity for different material density (Model 2).

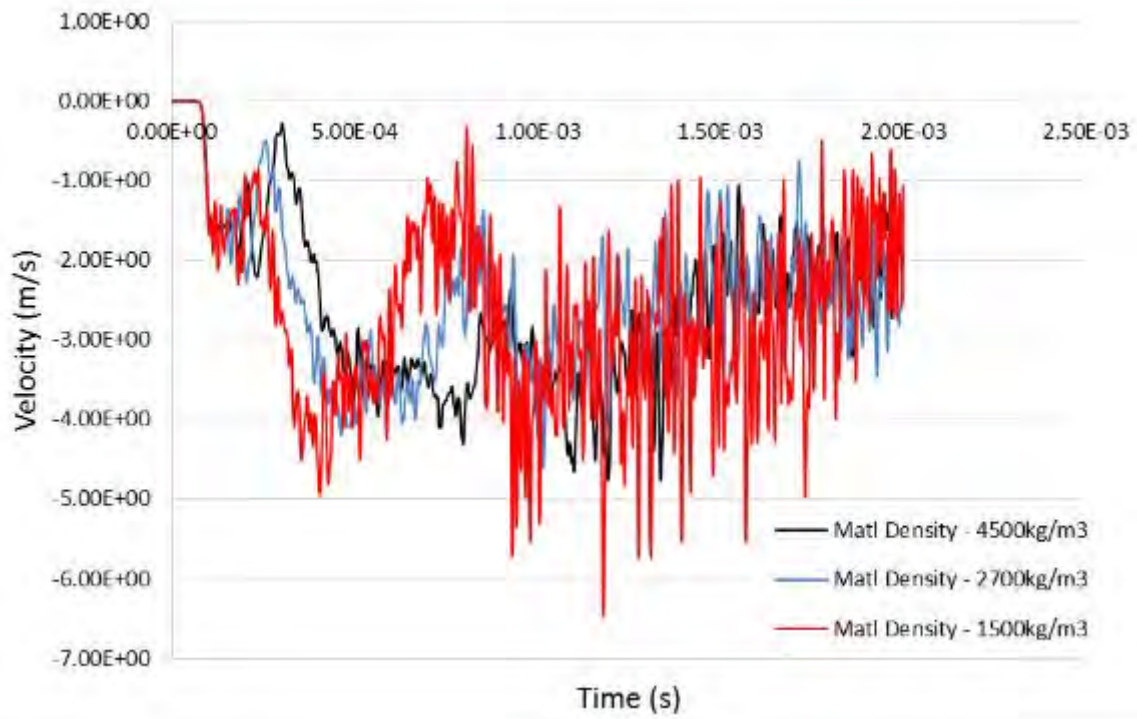


Figure 216. Left wall Z-Velocity for different material density (Model 2).

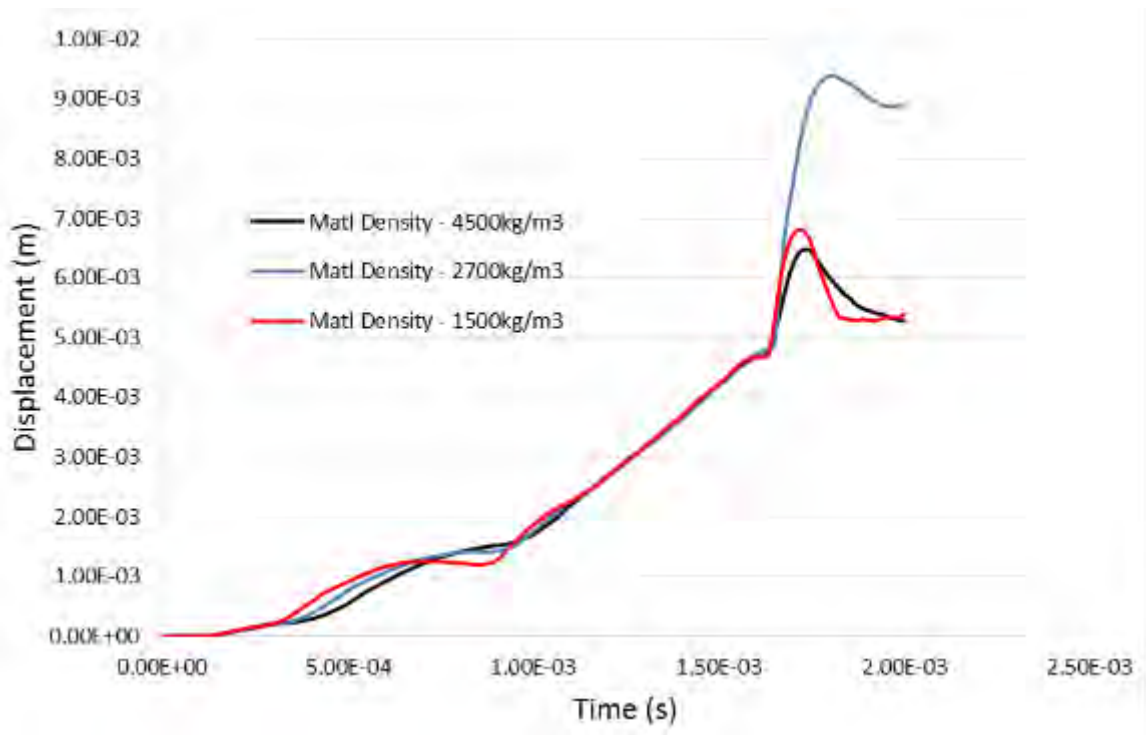


Figure 217. Exit wall resultant displacement for different material density (Model 2).

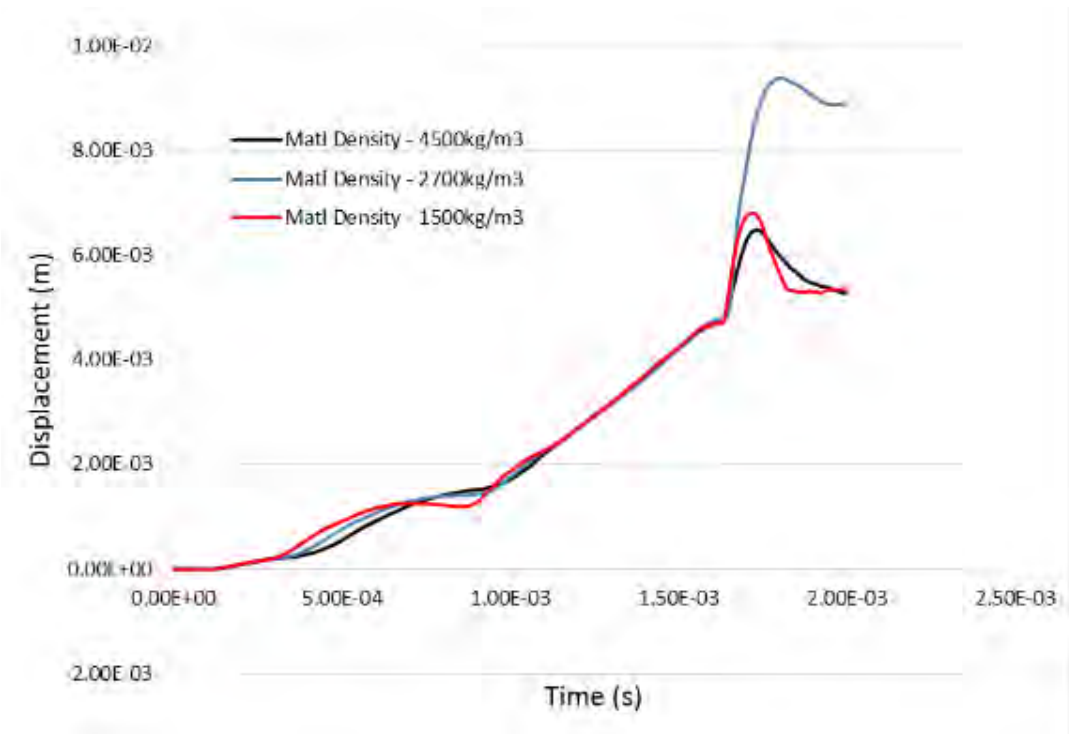


Figure 218. Exit wall X-Displacement for different material density (Model 2).

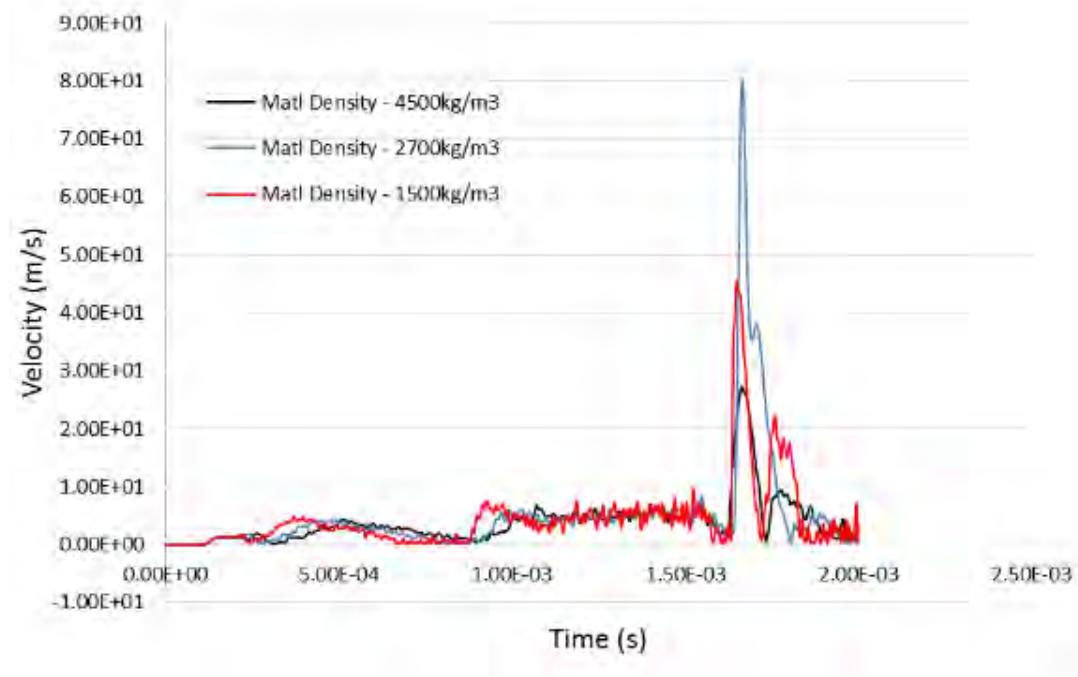


Figure 219. Exit wall resultant velocity for different material density (Model 2).

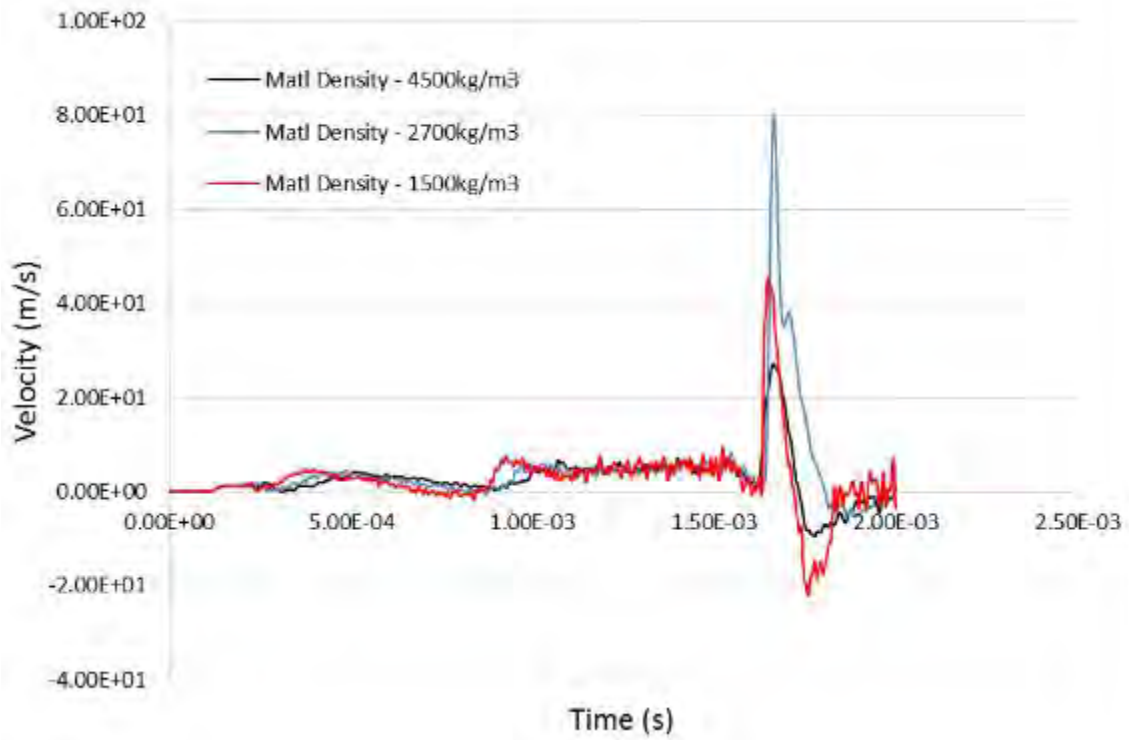


Figure 220. Exit wall X-Velocity for different material density (Model 2).

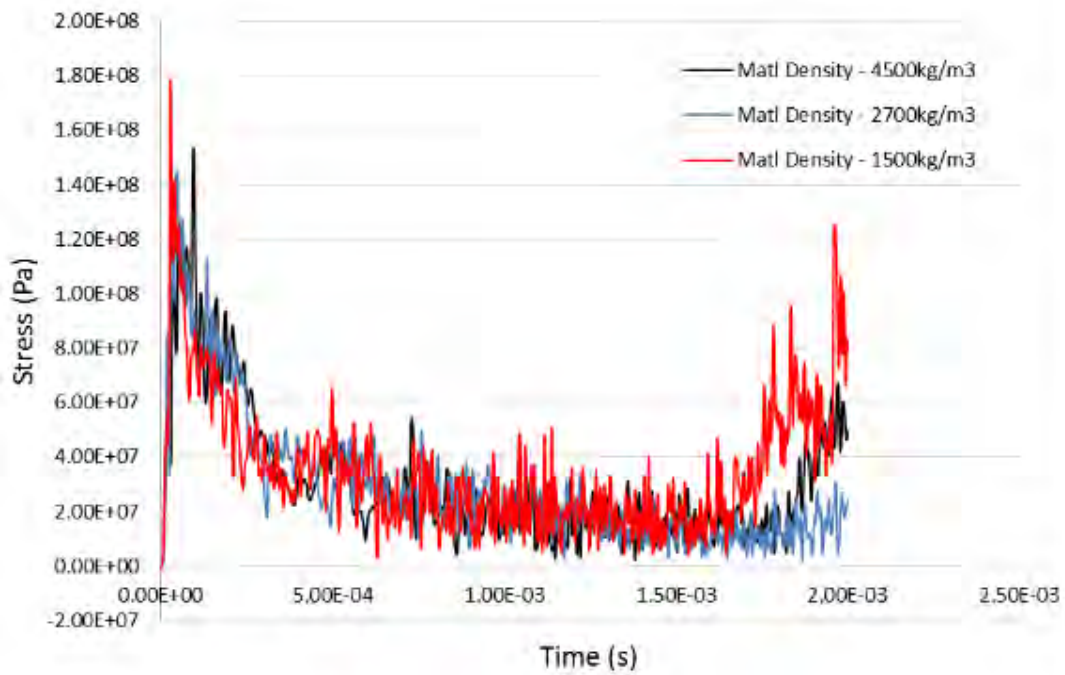


Figure 221. Entry wall effective stress for different material density (Model 2).

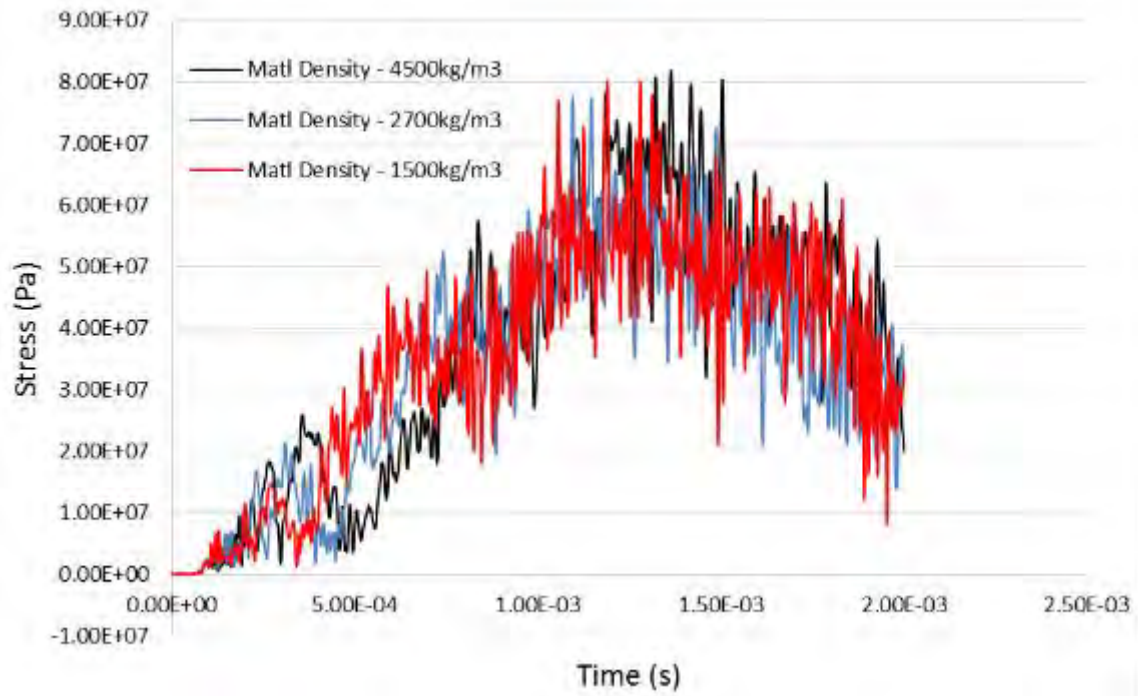


Figure 222. Left wall effective stress for different material density (Model 2).

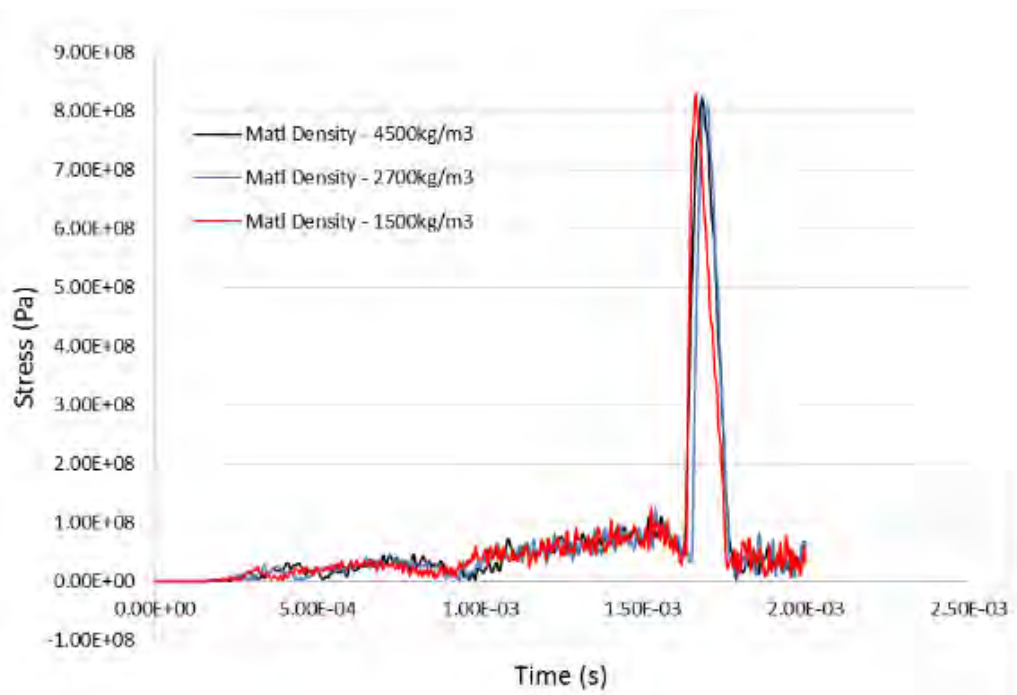


Figure 223. Exit wall effective stress for different material density (Model 2).

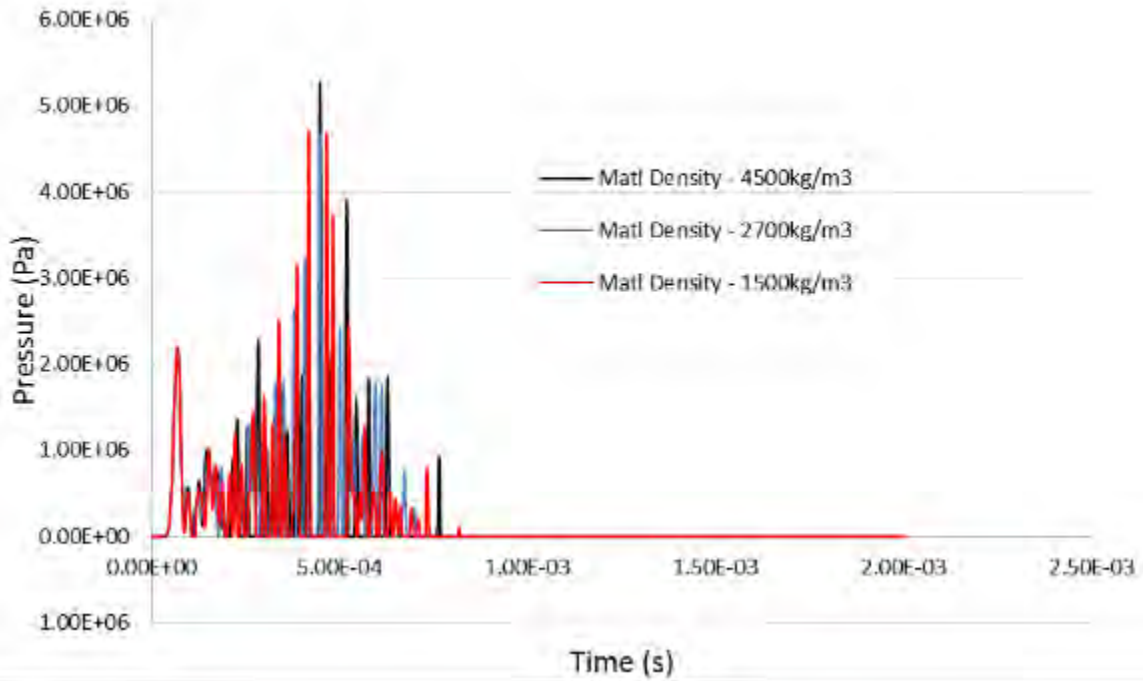


Figure 224. Drag phase pressure for different material density (Model 2).

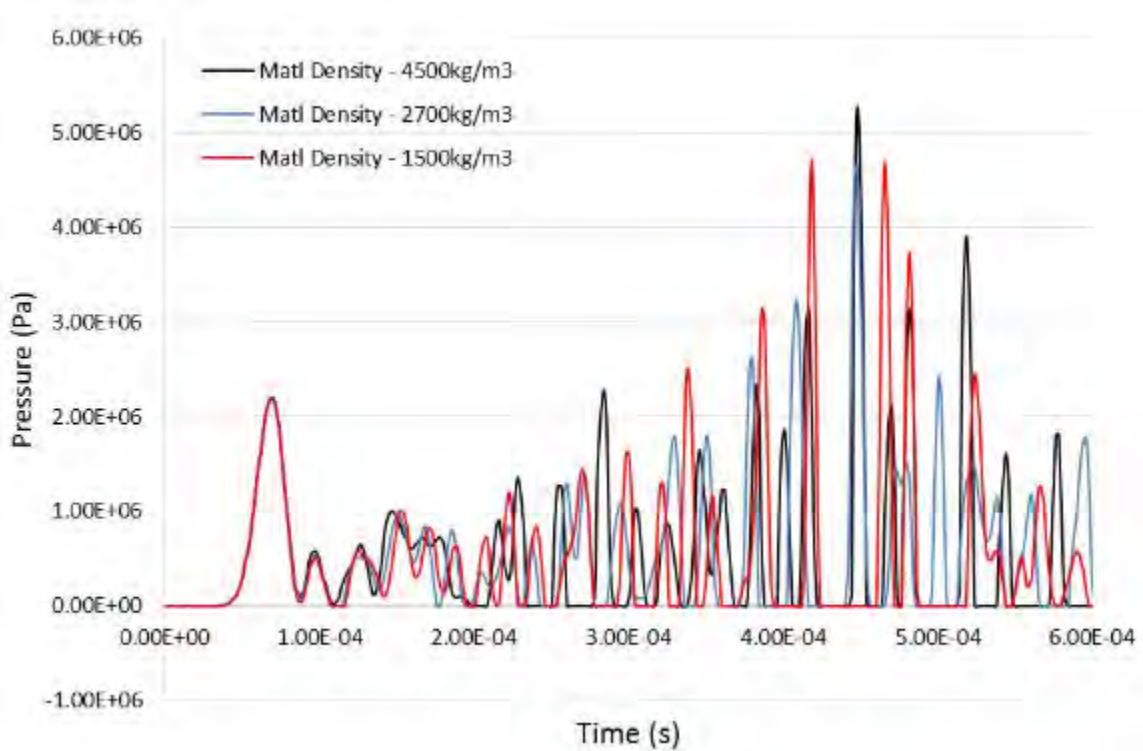
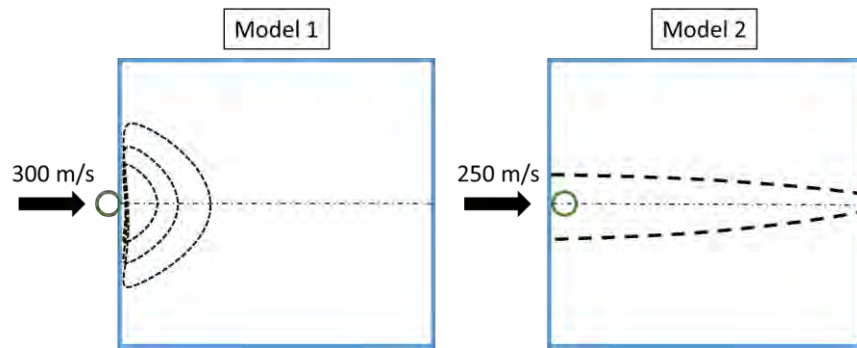


Figure 225. Drag phase pressure for different material density (Model 2) - Enlarged.

APPENDIX F. GRAPHS FOR FLUID DENSITY VARIATION



Fluid density investigated: 800kg/m^3 , 1000kg/m^3 and 1200kg/m^3

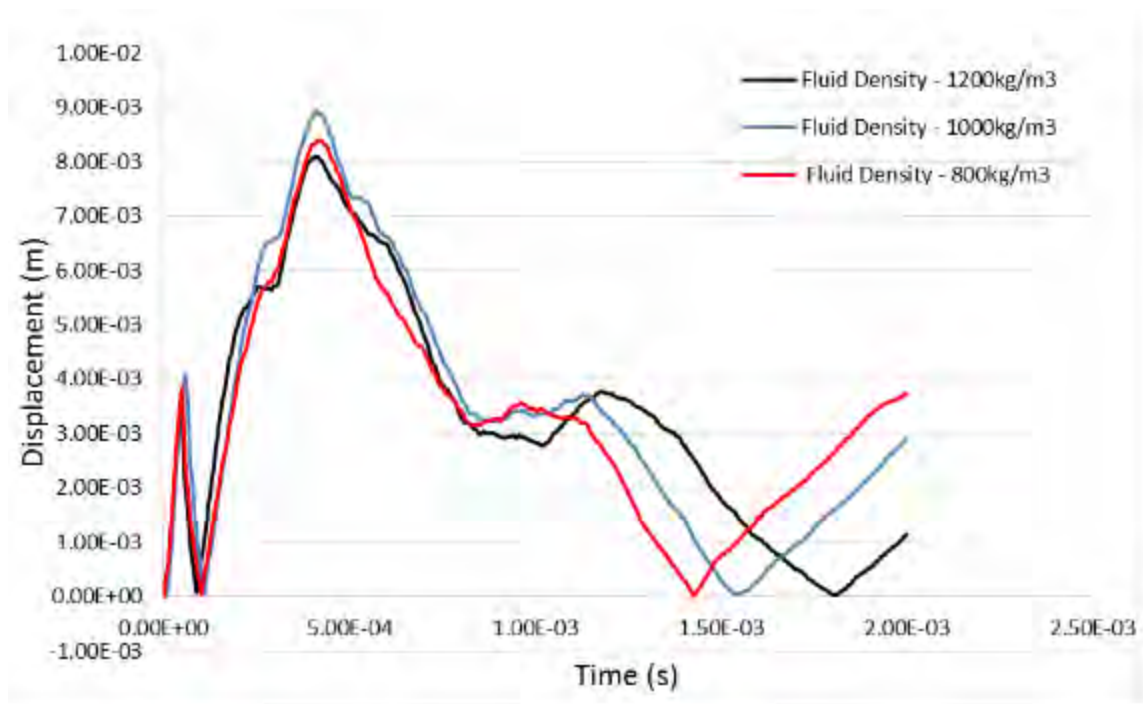


Figure 226. Entry wall resultant displacement for different fluid density (Model 1).

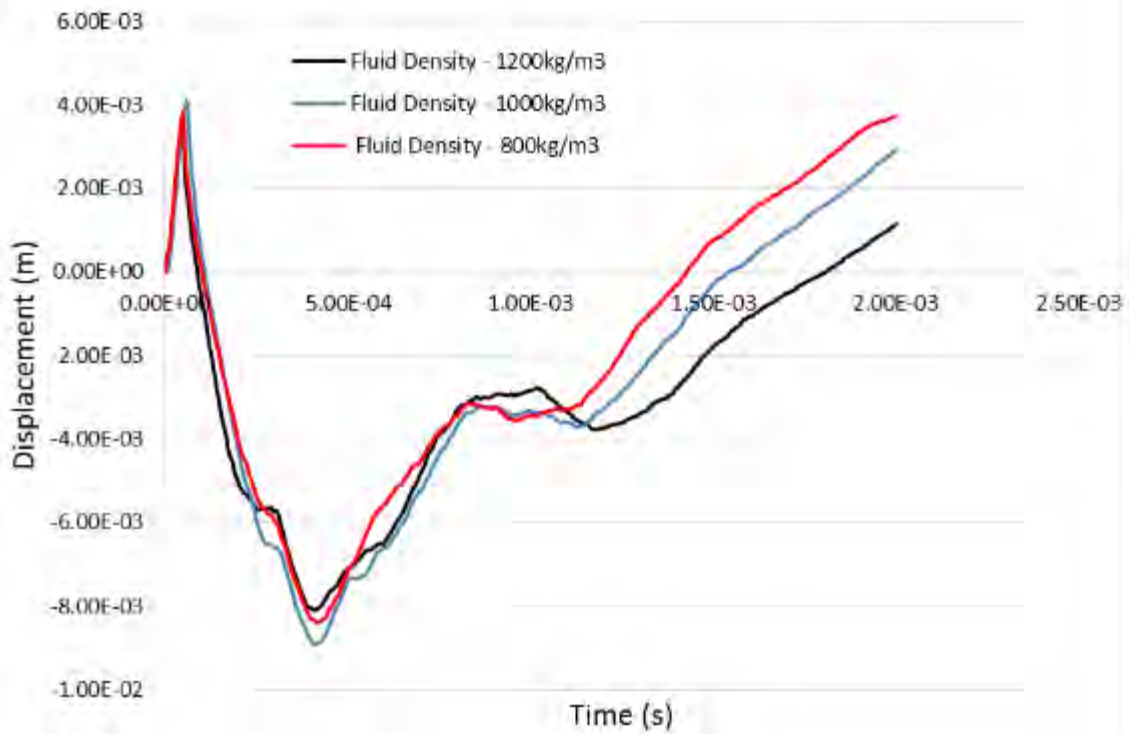


Figure 227. Entry wall X-Displacement for different fluid density (Model 1).

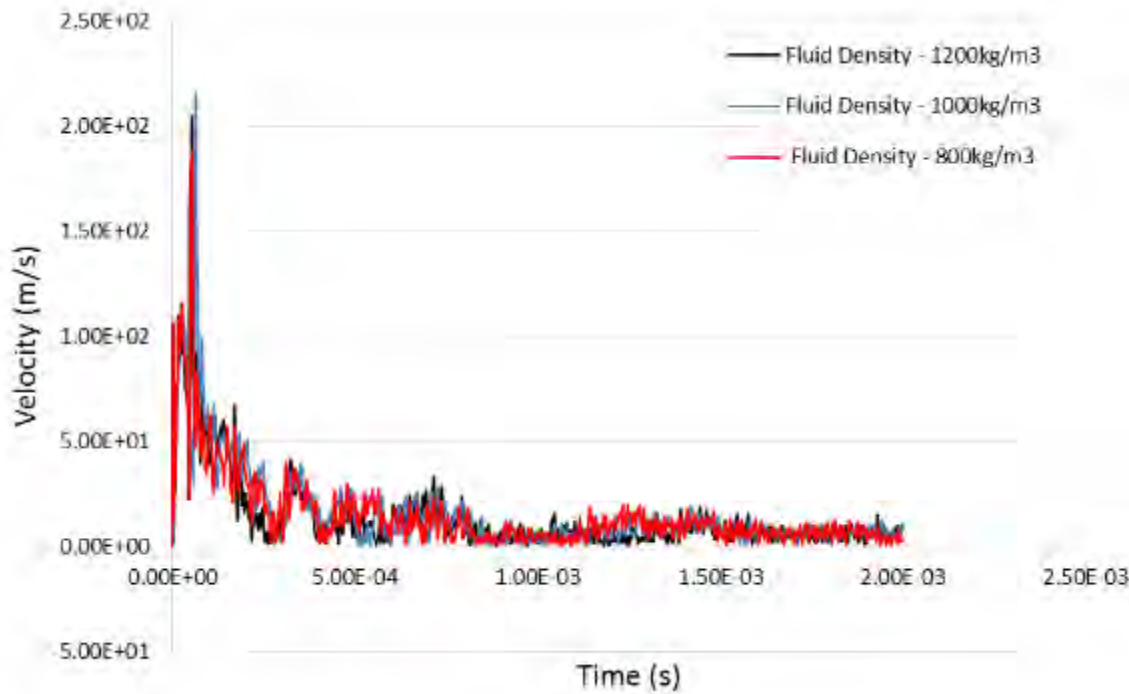


Figure 228. Entry wall resultant velocity for different fluid density (Model 1).

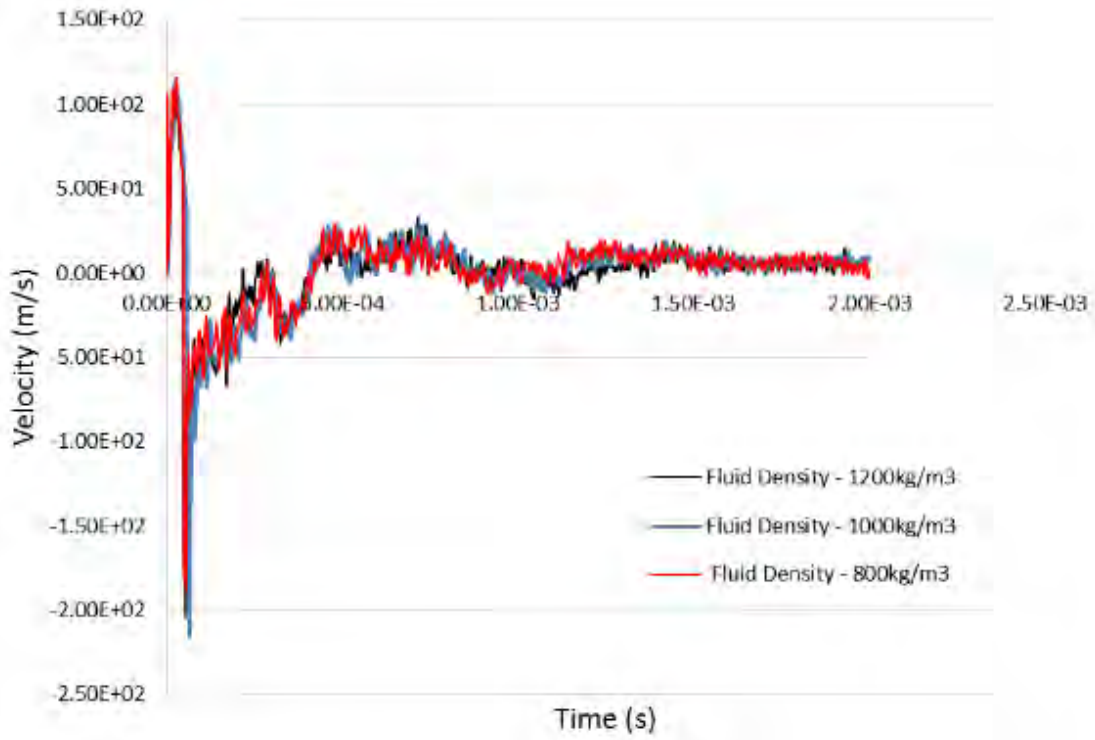


Figure 229. Entry wall X-Velocity for different fluid density (Model 1).

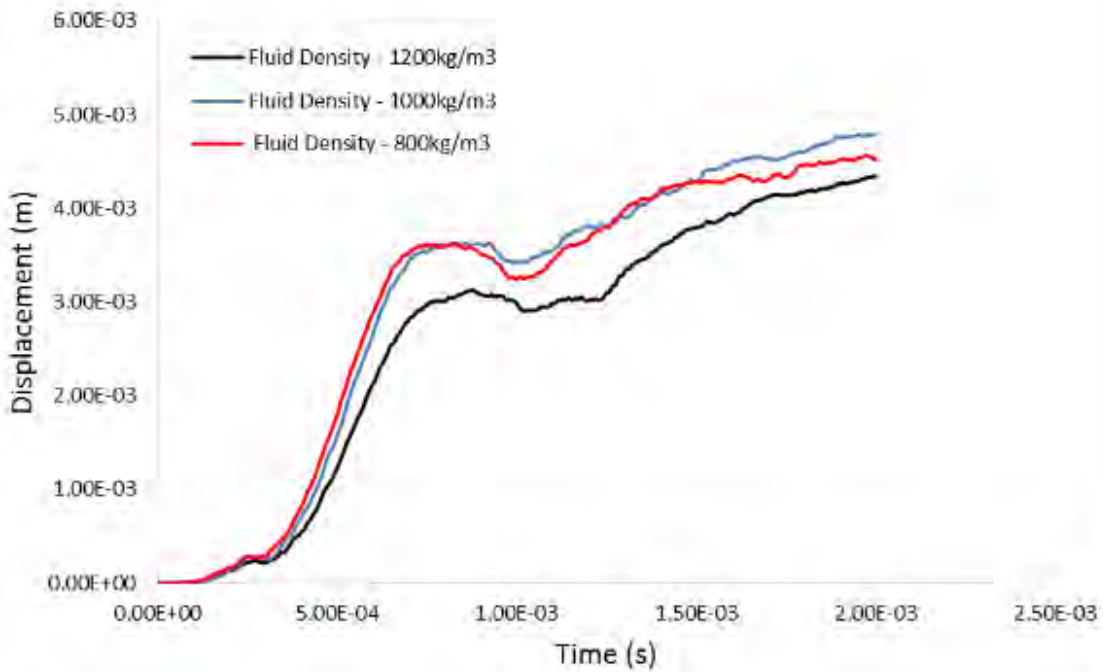


Figure 230. Left wall resultant displacement for different fluid density (Model 1).

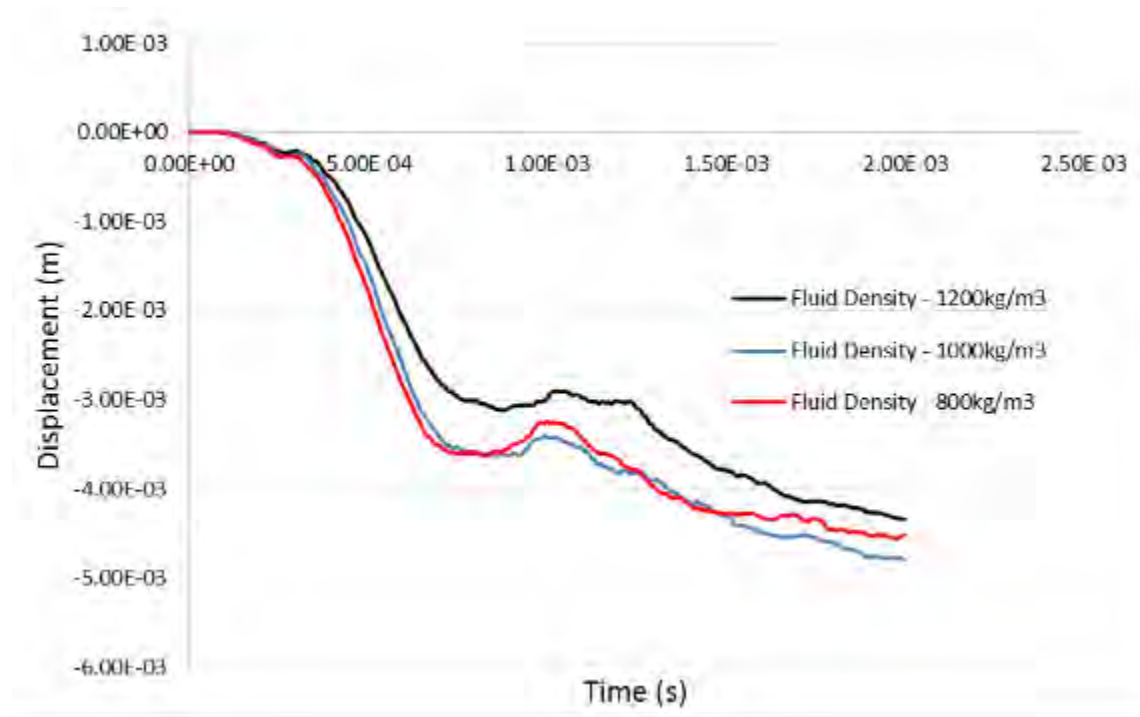


Figure 231. Left wall Z-Displacement for different fluid density (Model 1).

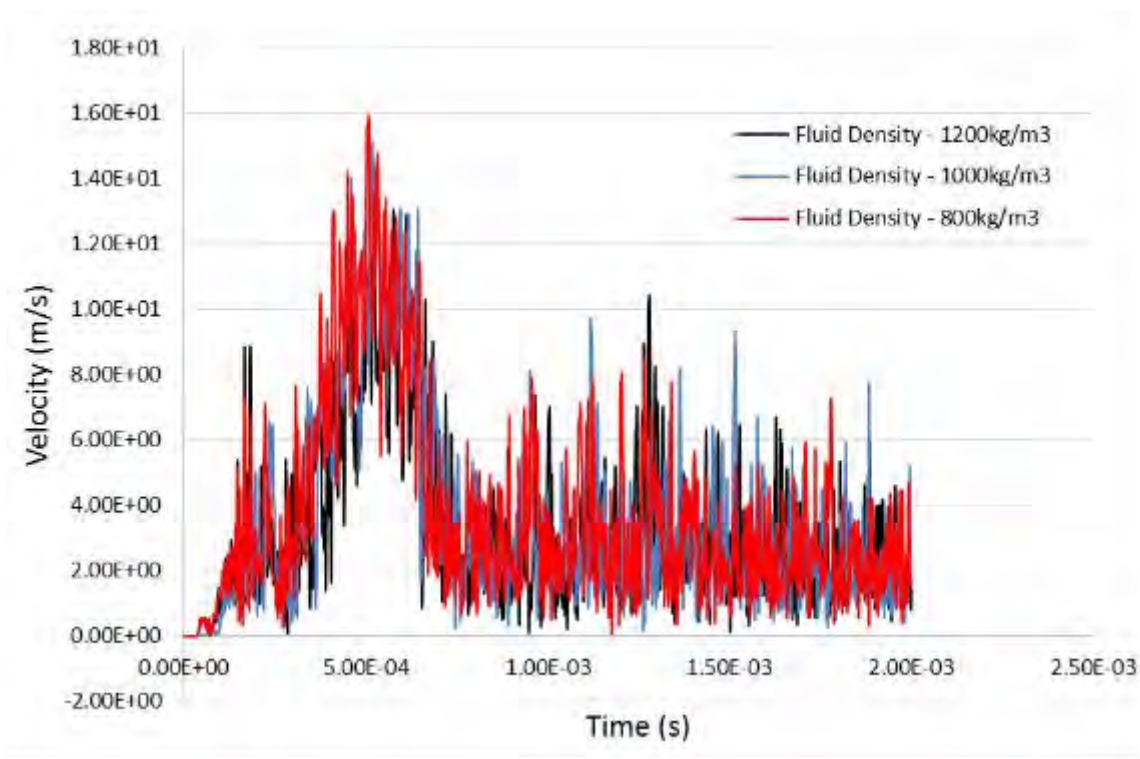


Figure 232. Left wall resultant velocity for different fluid density (Model 1).

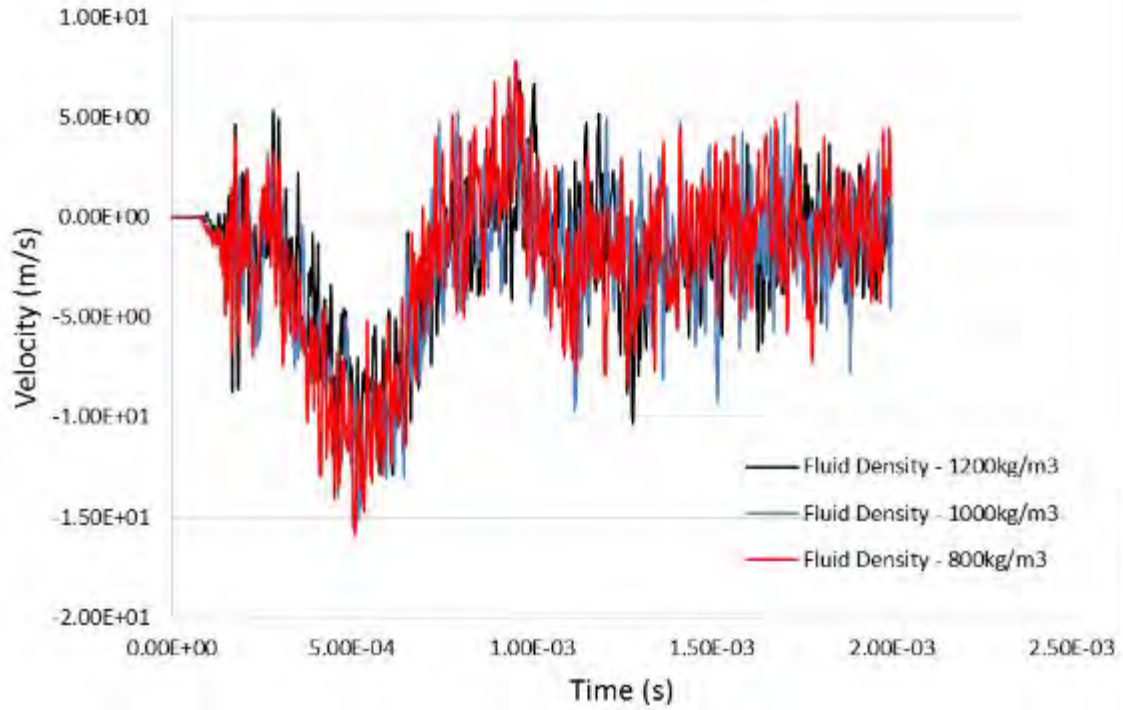


Figure 233. Left wall Z-Velocity for different fluid density (Model 1).

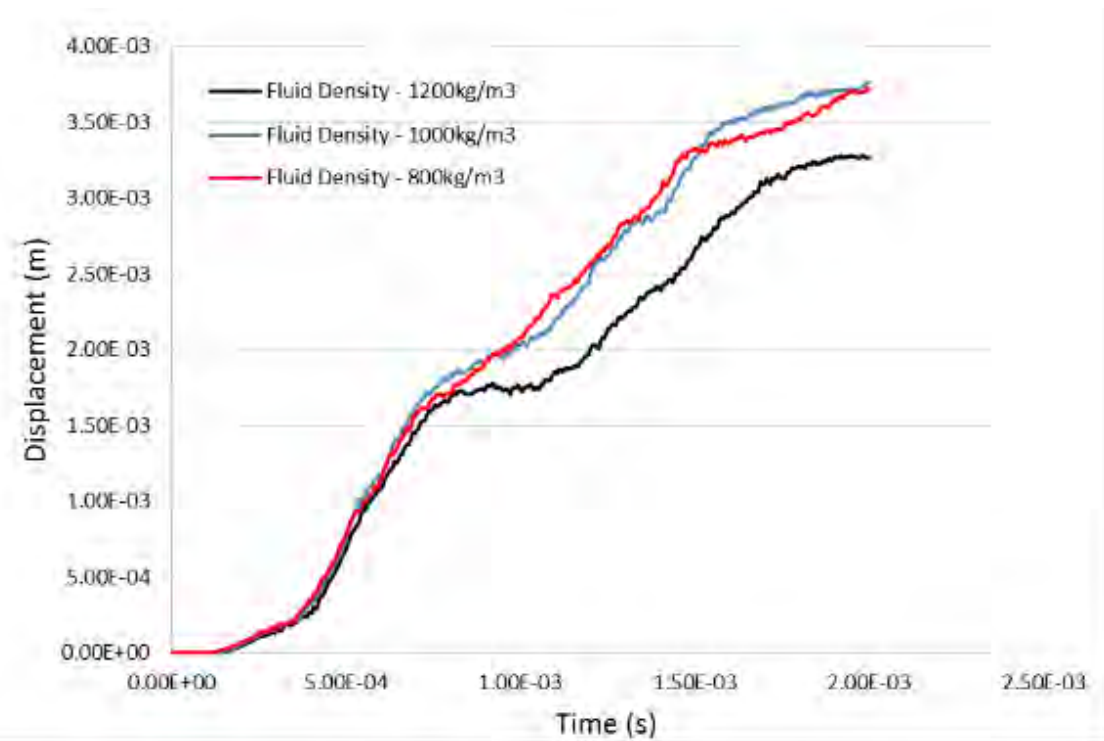


Figure 234. Exit wall resultant displacement for different fluid density (Model 1).

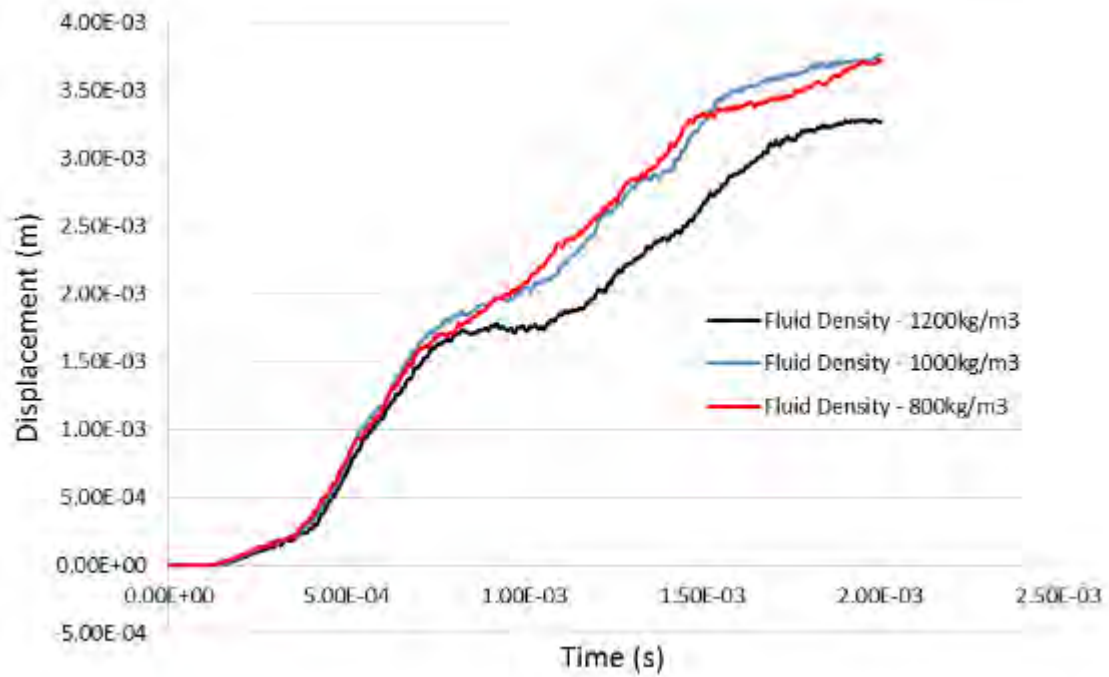


Figure 235. Exit wall X-Displacement for different fluid density (Model 1).

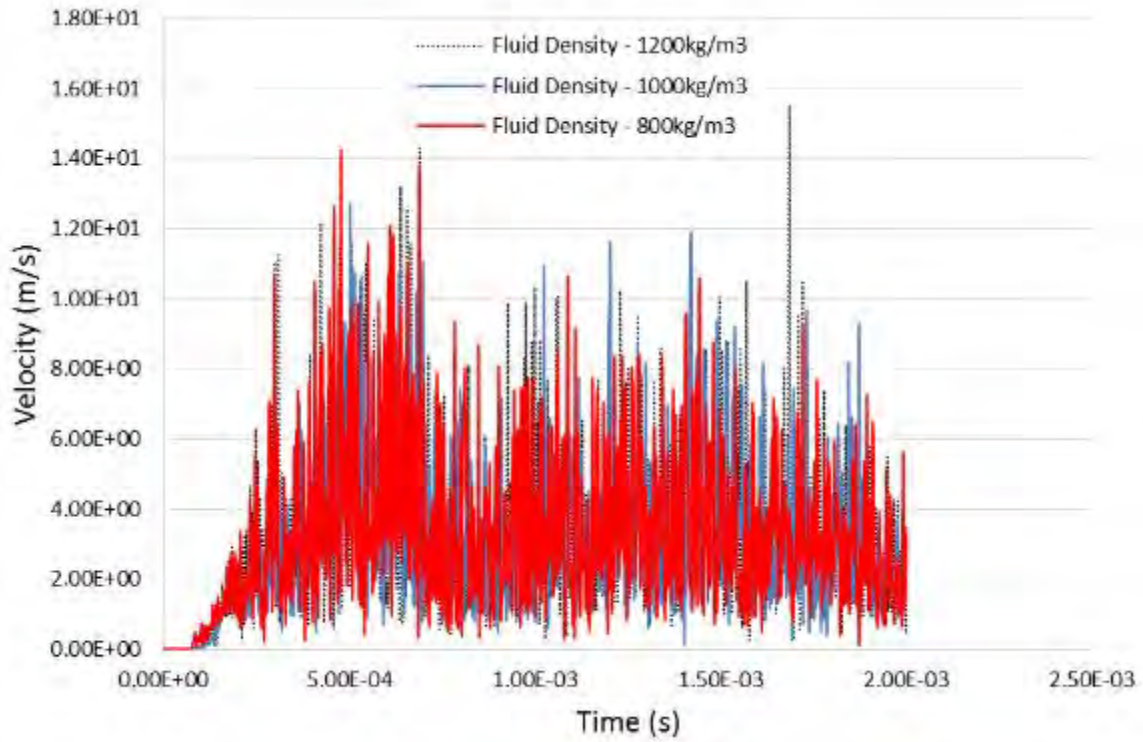


Figure 236. Exit wall resultant velocity for different fluid density (Model 1).

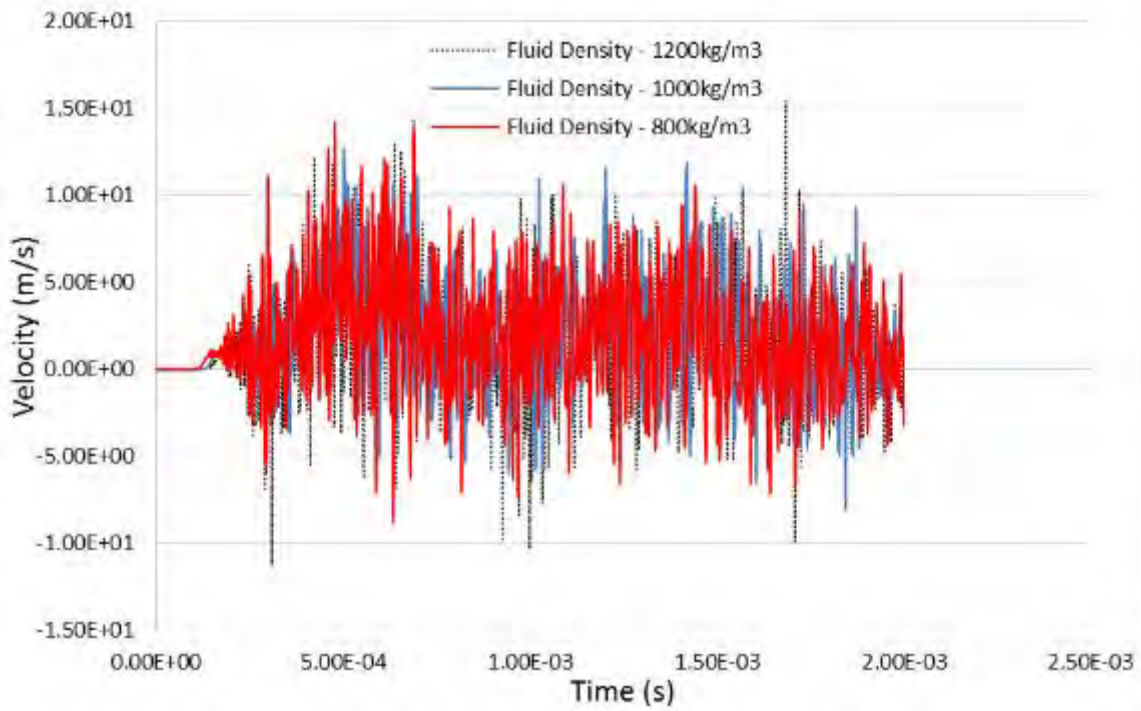


Figure 237. Exit wall X-Velocity for different fluid density (Model 1).

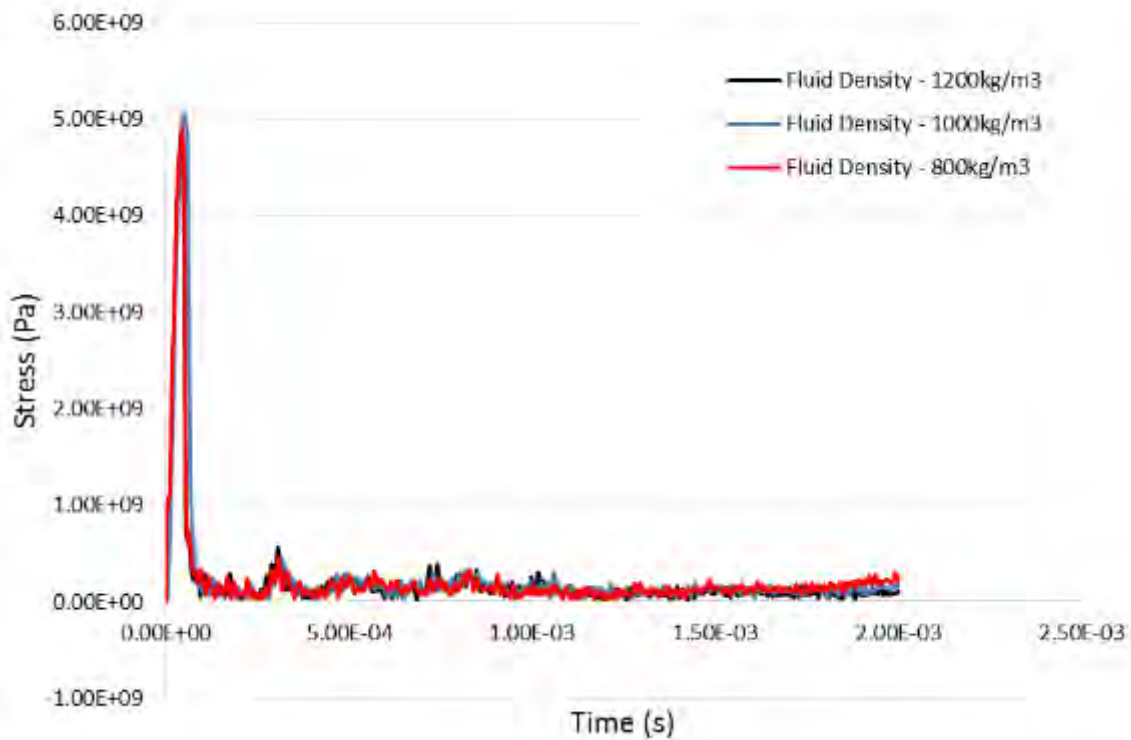


Figure 238. Entry wall effective stress for different fluid density (Model 1).

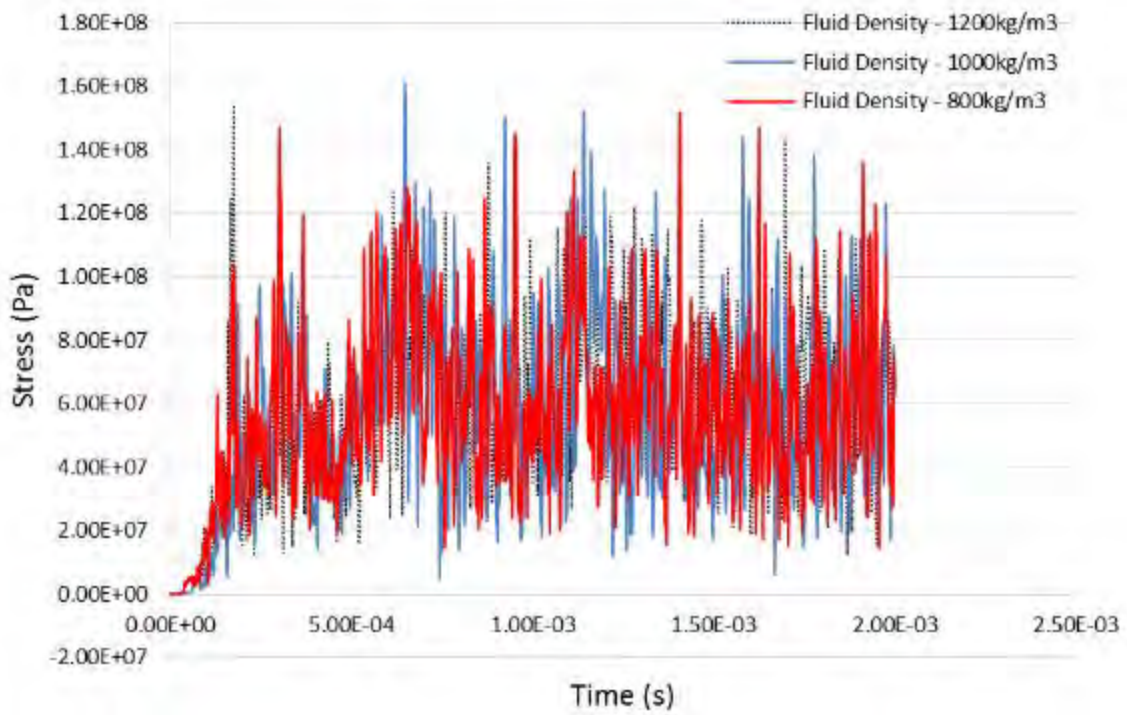


Figure 239. Left wall effective stress for different fluid density (Model 1).

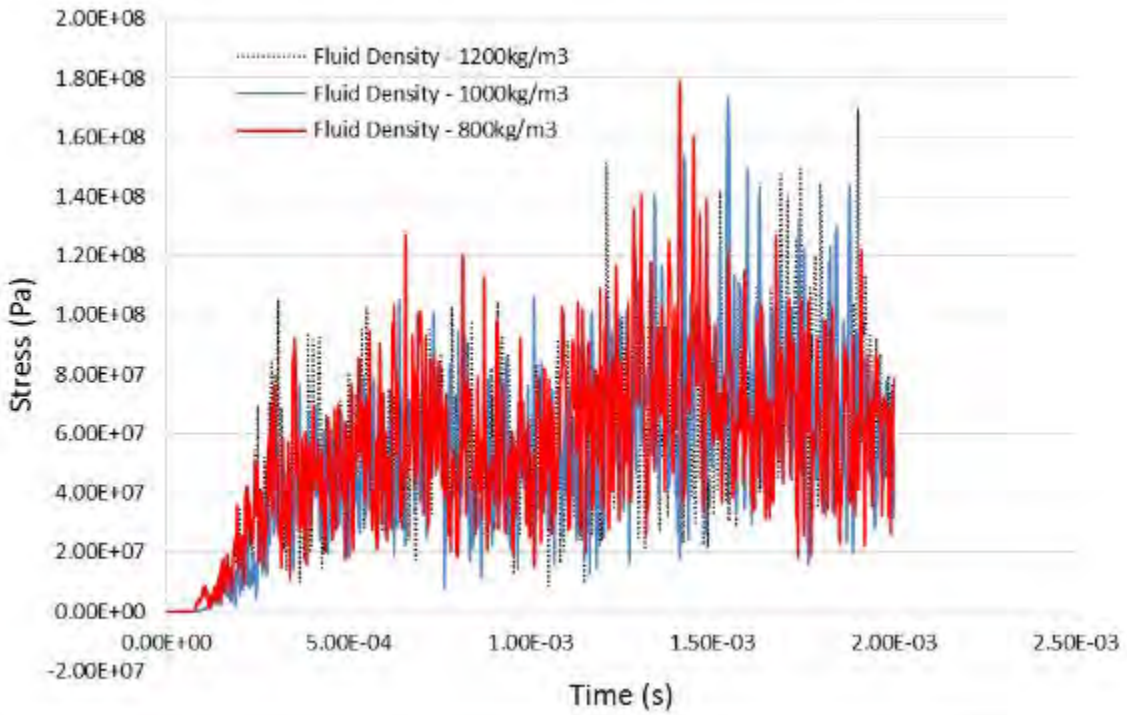


Figure 240. Exit wall effective stress for different fluid density (Model 1).

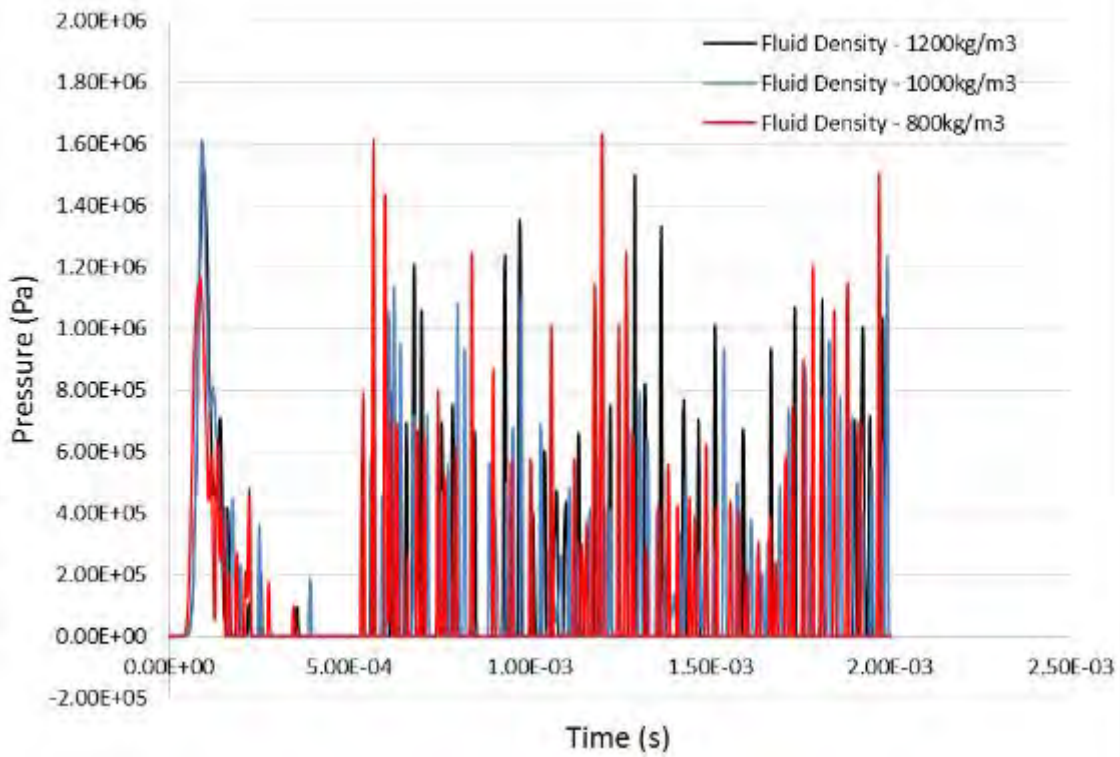


Figure 241. Fluid pressure for different fluid density (Model 1).

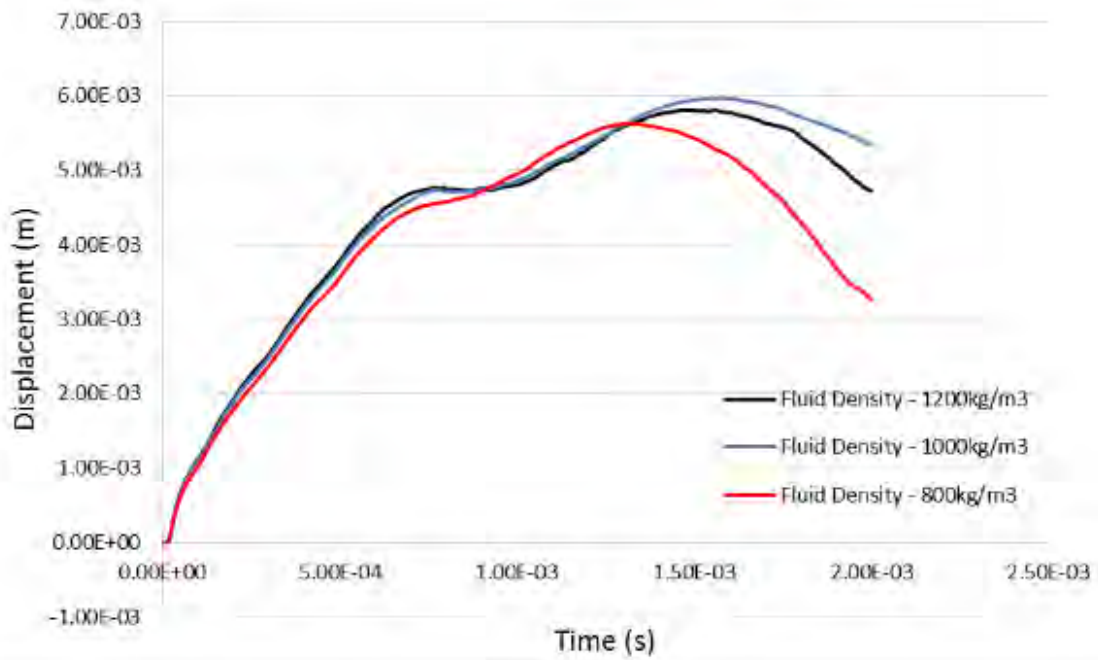


Figure 242. Entry wall resultant displacement for different fluid density (Model 2).

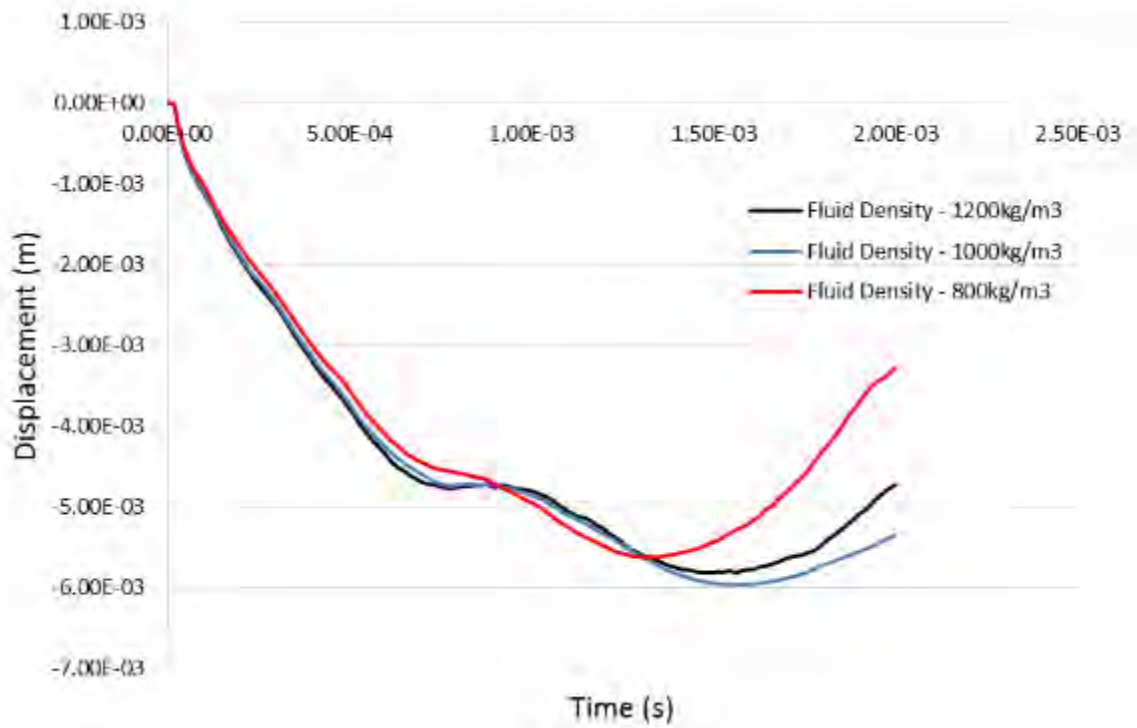


Figure 243. Entry wall X-Displacement for different fluid density (Model 2).

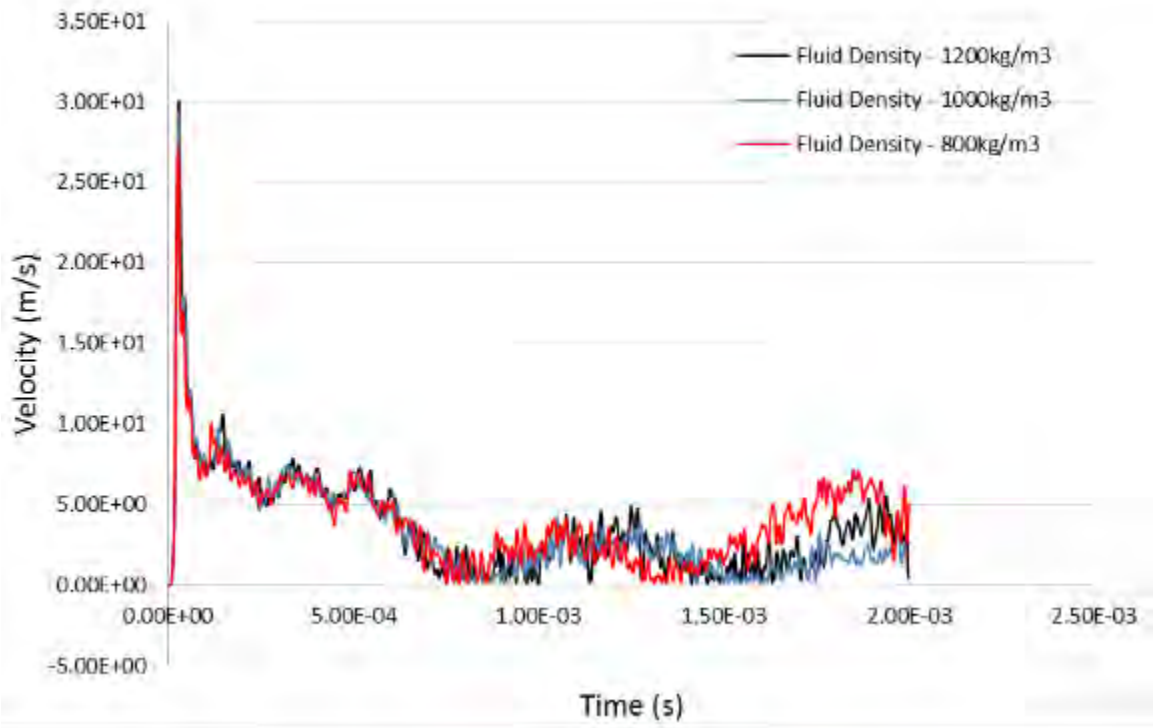


Figure 244. Entry wall resultant velocity for different fluid density (Model 2).

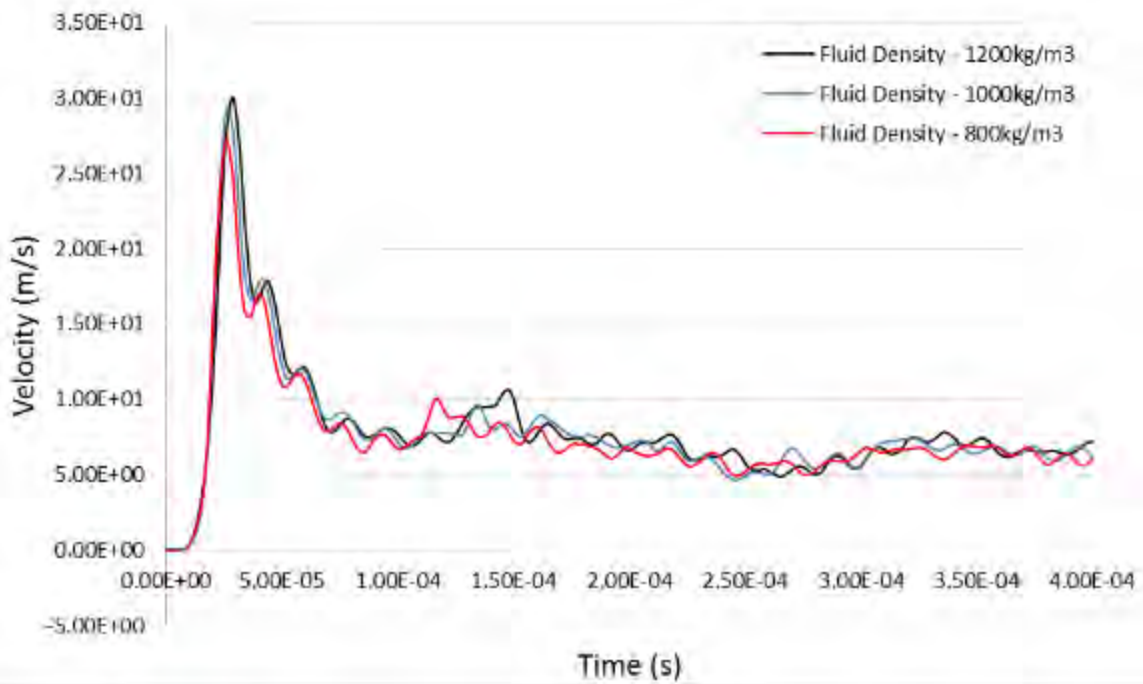


Figure 245. Entry wall resultant velocity for different fluid density (Model 2) – Enlarged.

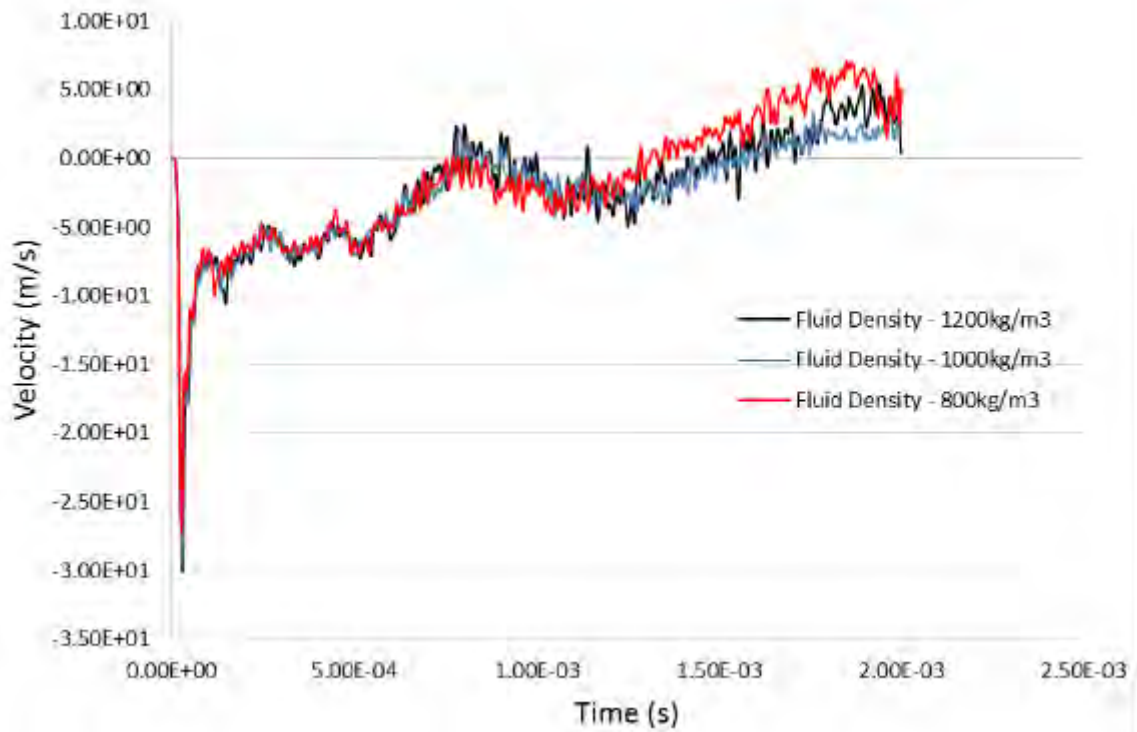


Figure 246. Entry wall X-Velocity for different fluid density (Model 2).

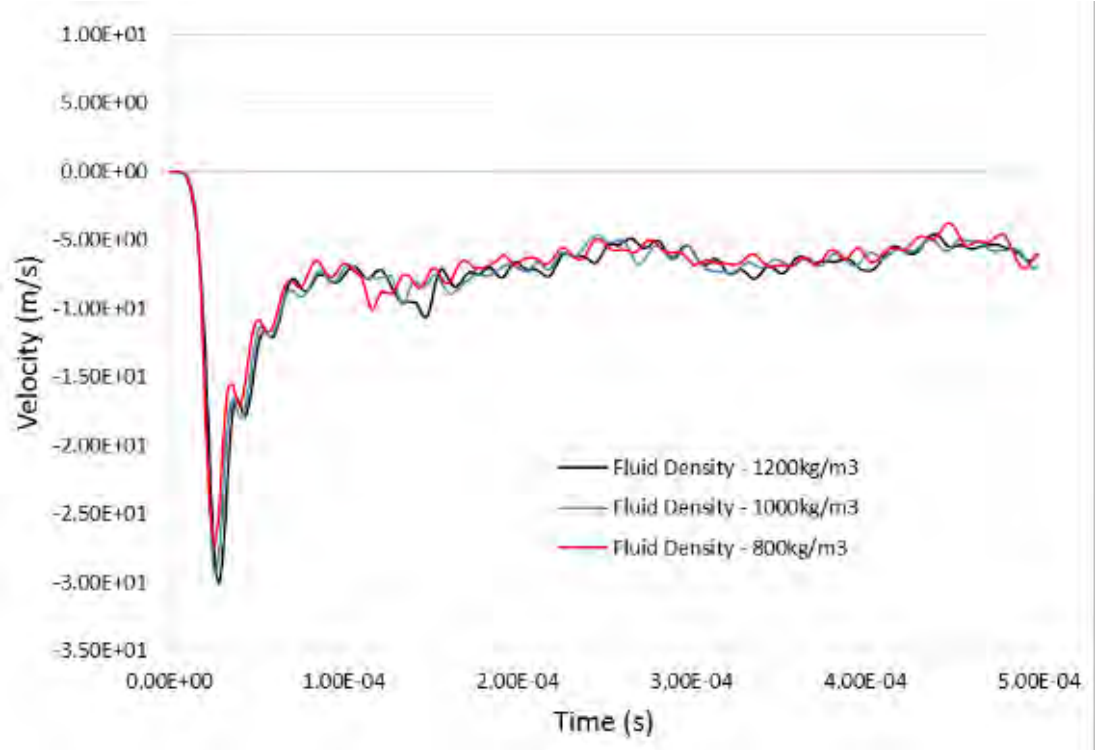


Figure 247. Entry wall X-Velocity for different fluid density (Model 2) – Enlarged.

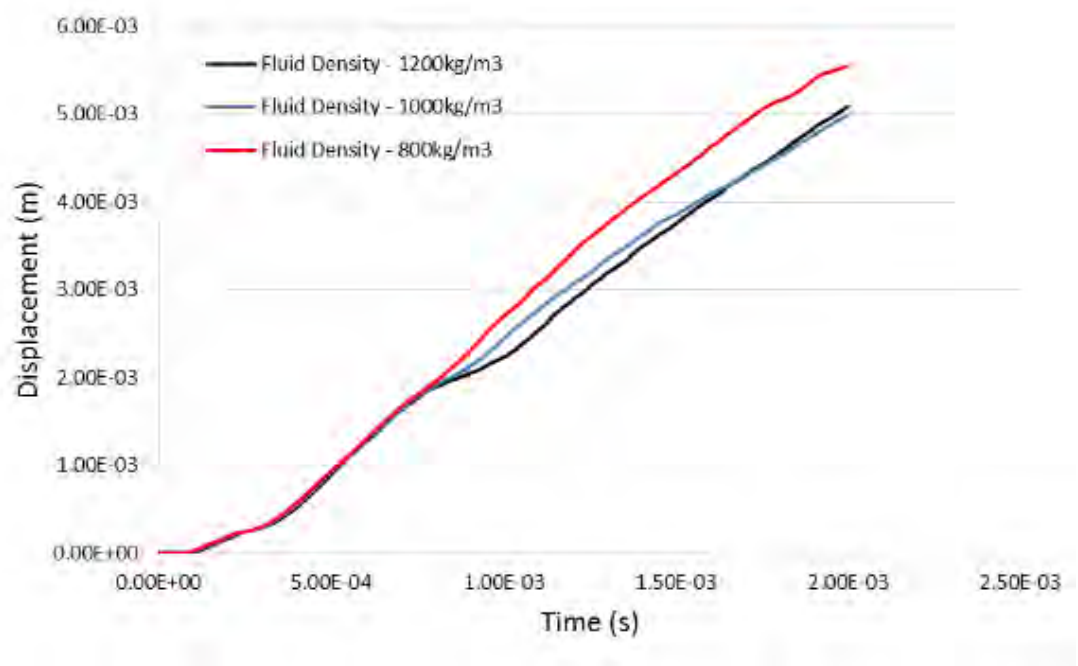


Figure 248. Left wall resultant displacement for different fluid density (Model 2).

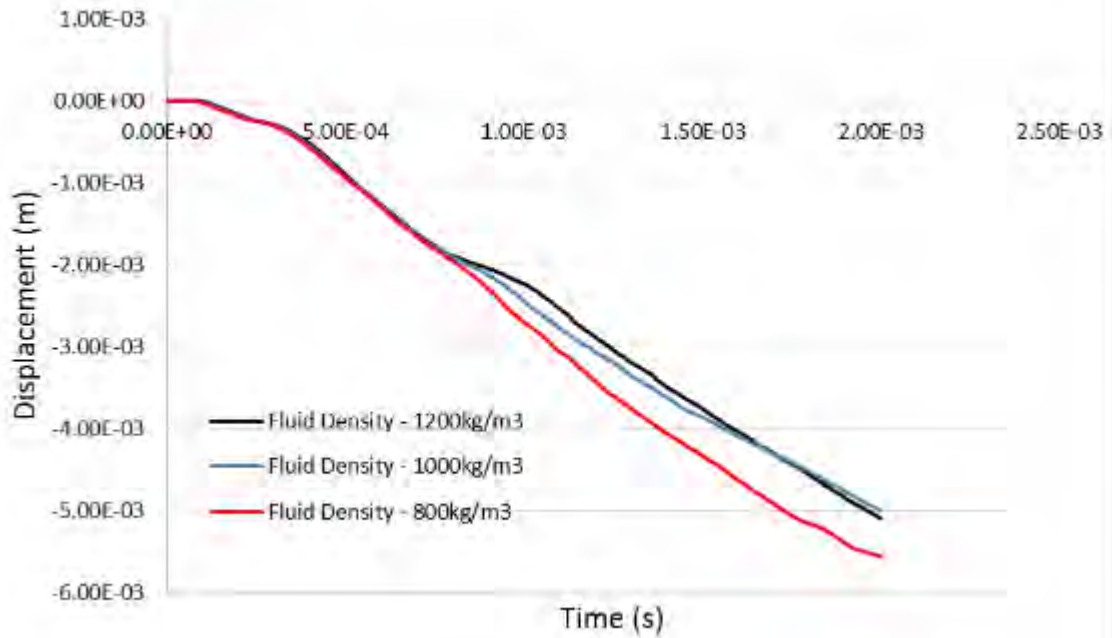


Figure 249. Left wall Z-Displacement for different fluid density (Model 2).

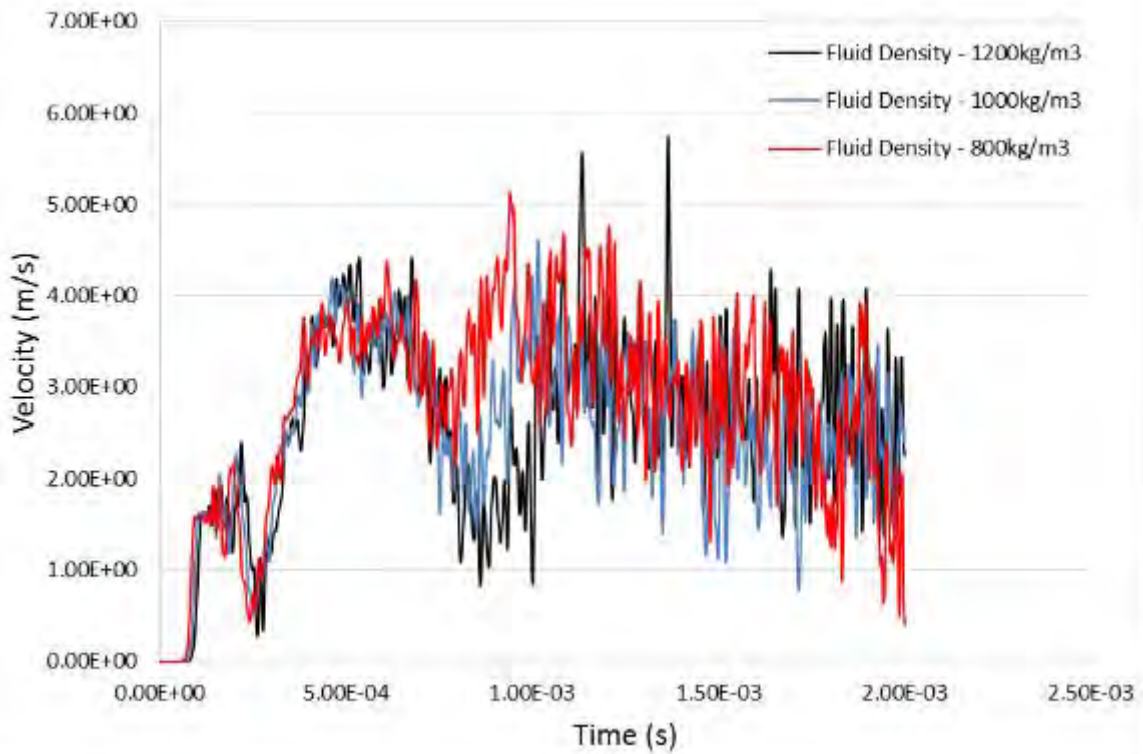


Figure 250. Left wall resultant velocity for different fluid density (Model 2).

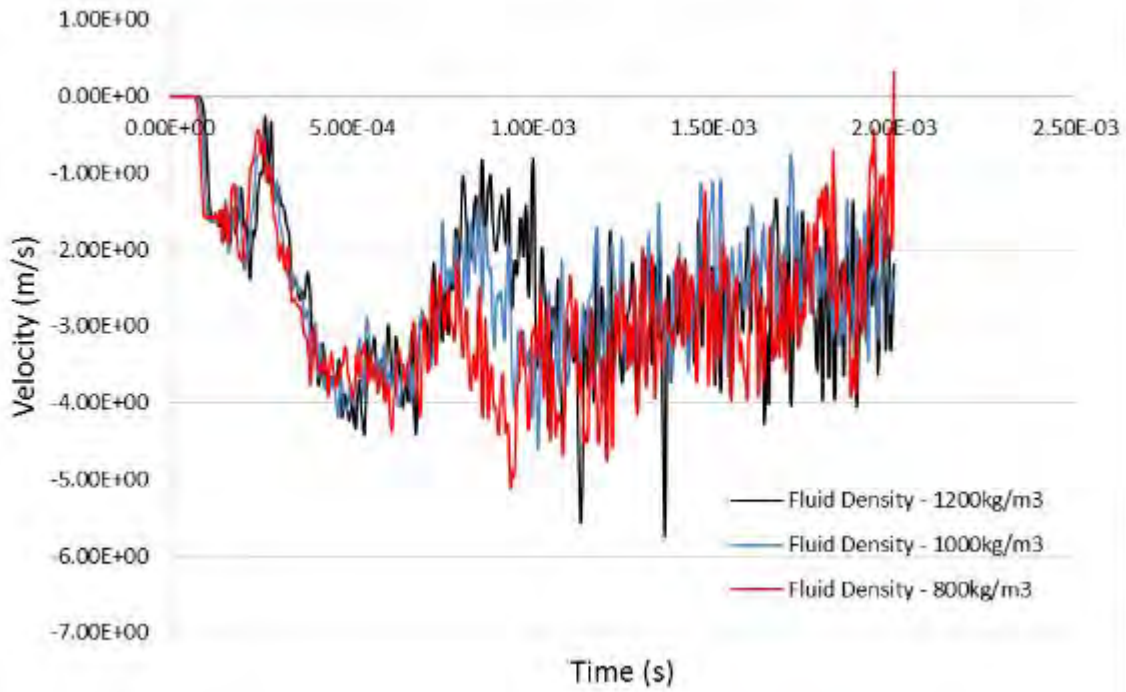


Figure 251. Left wall Z-Velocity for different fluid density (Model 2).

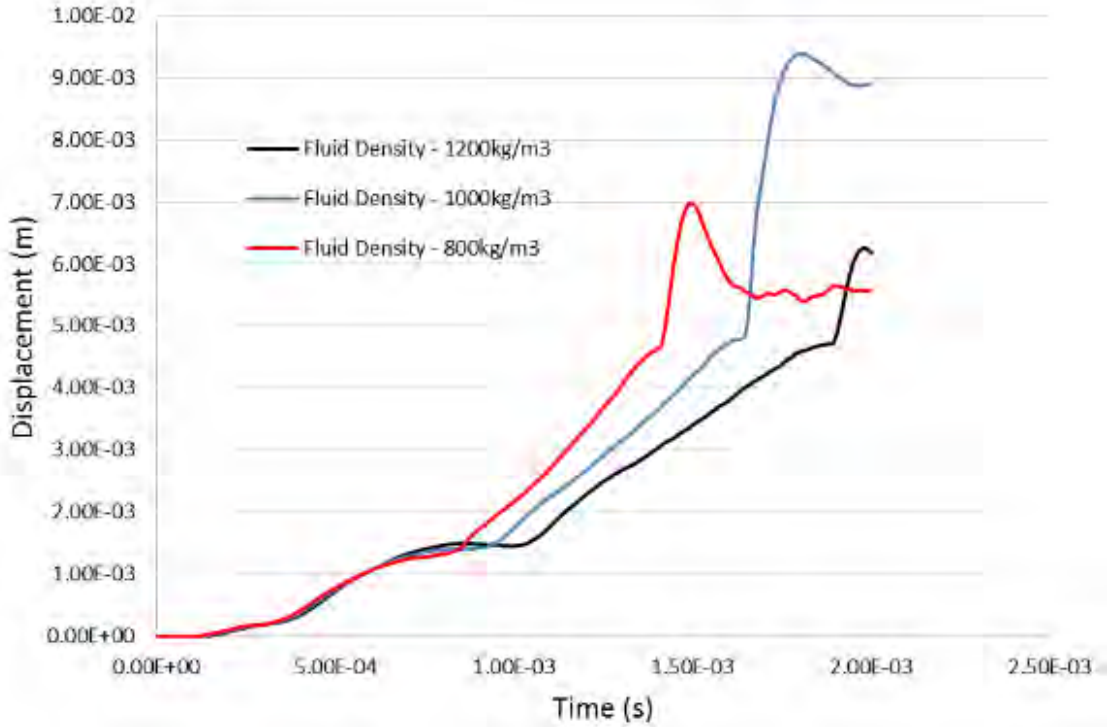


Figure 252. Exit wall resultant displacement for different fluid density (Model 2).

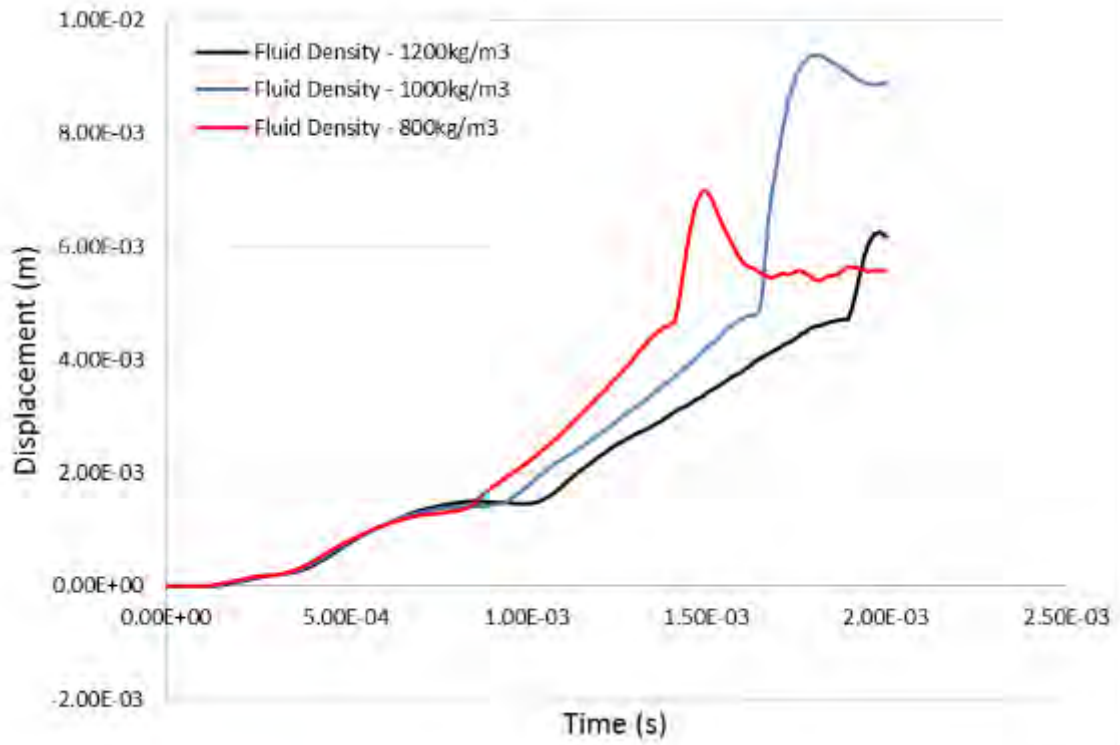


Figure 253. Exit wall X-Displacement for different fluid density (Model 2).

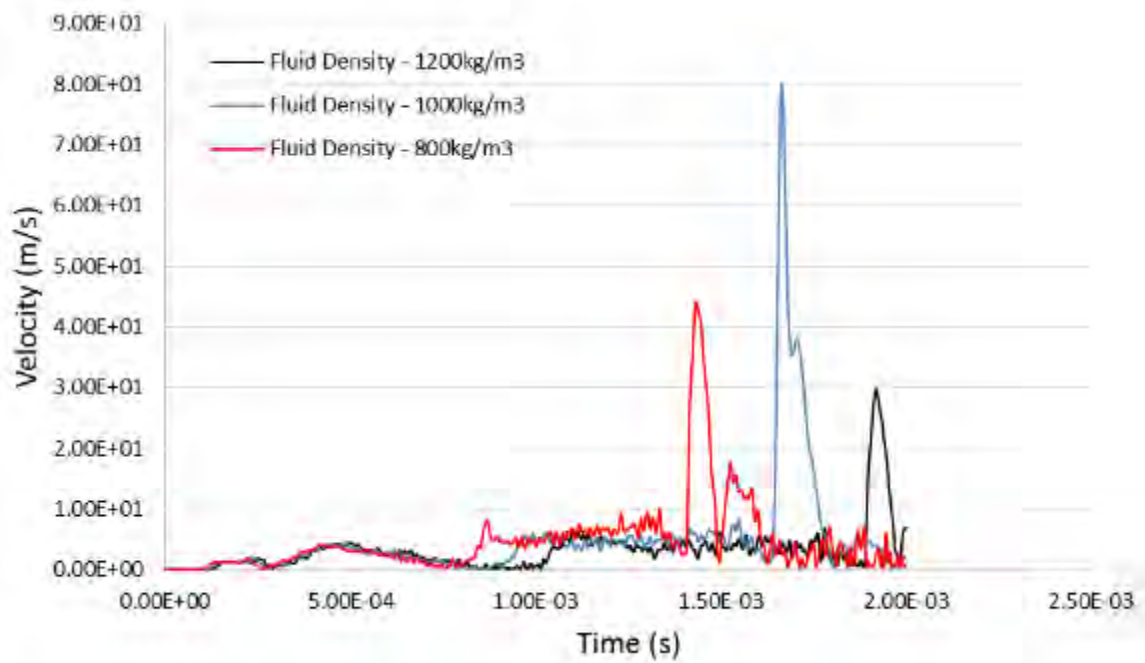


Figure 254. Exit wall resultant velocity for different fluid density (Model 2).

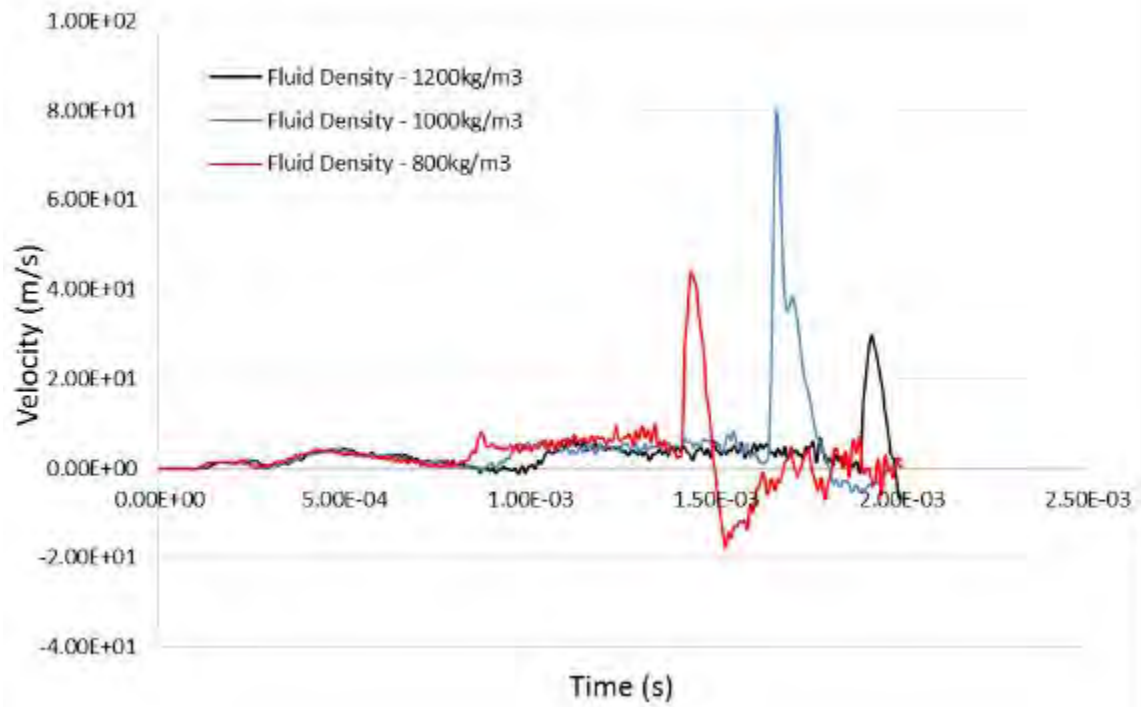


Figure 255. Exit wall X-Velocity for different fluid density (Model 2).

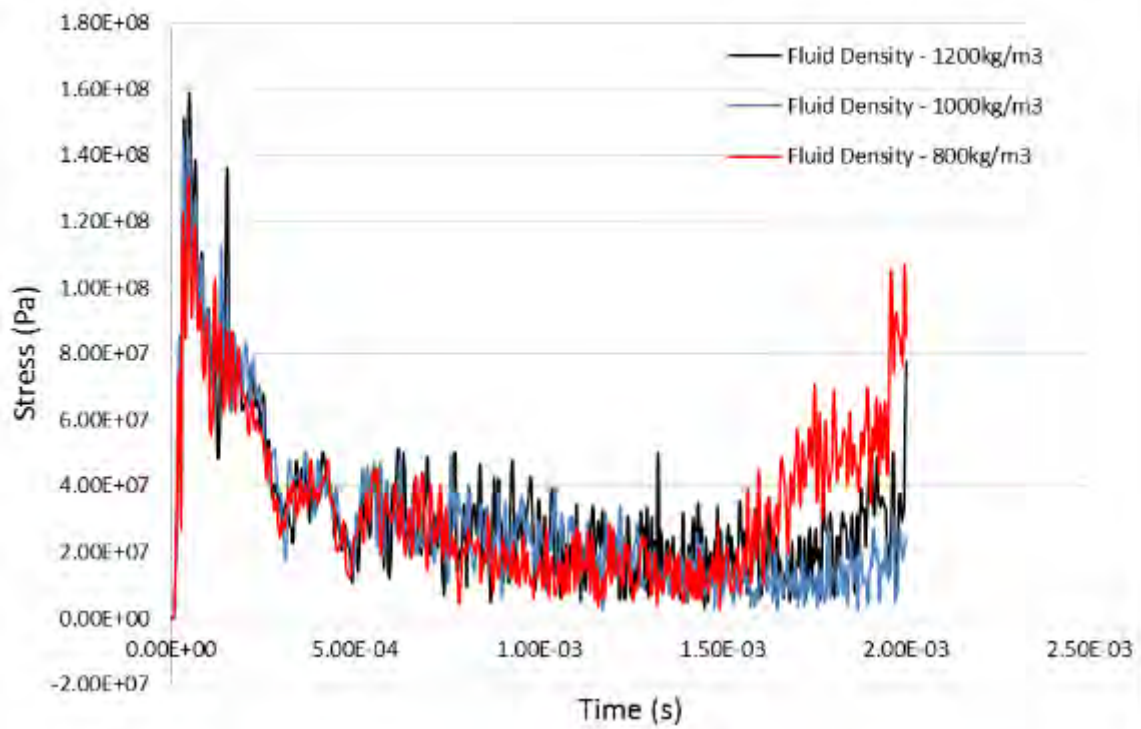


Figure 256. Entry wall effective stress for different fluid density (Model 2).

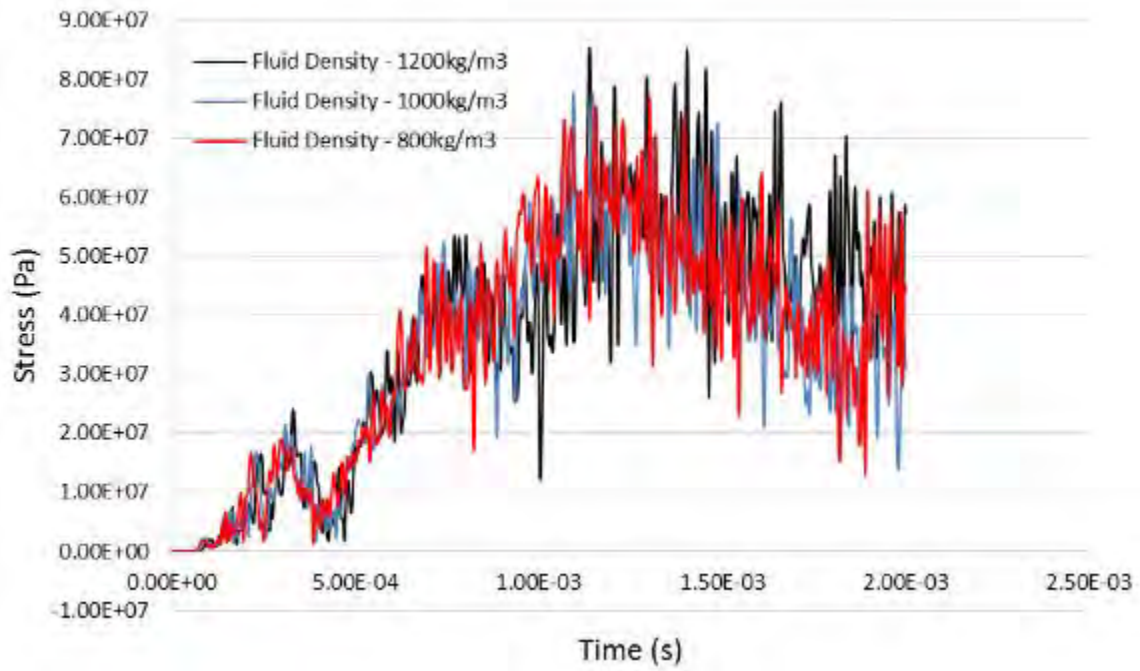


Figure 257. Left wall effective stress for different fluid density (Model 2).

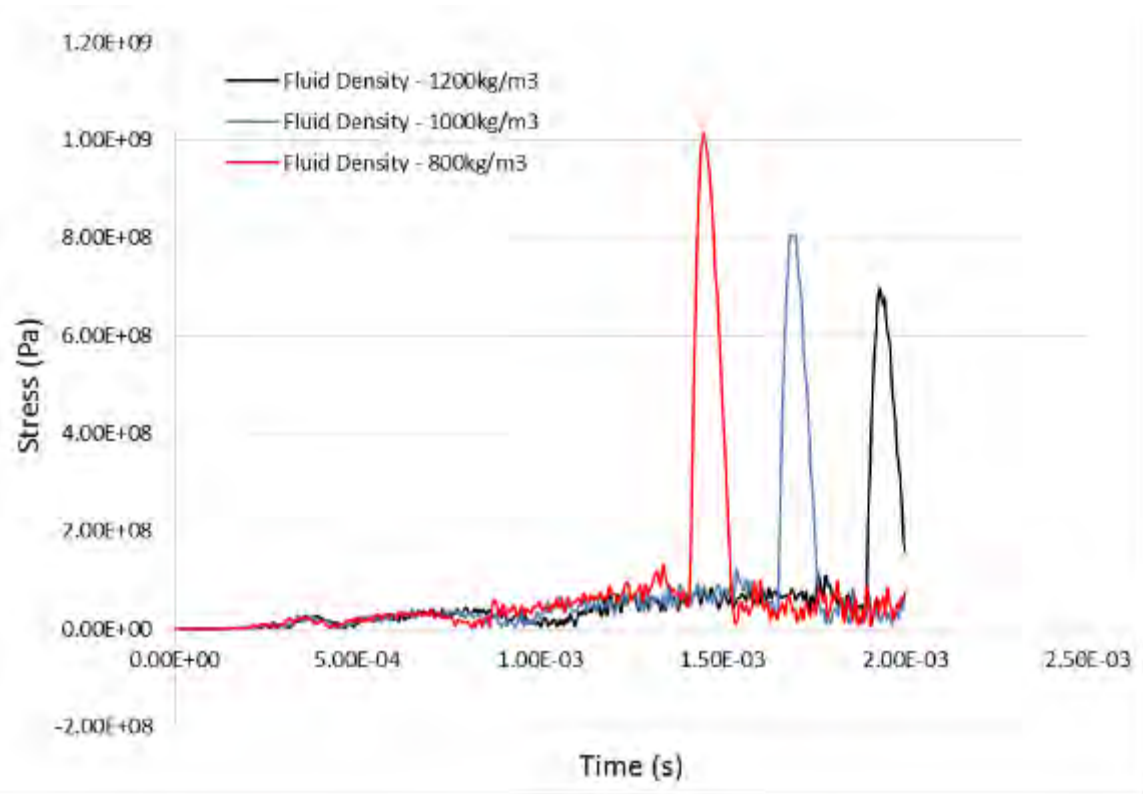


Figure 258. Exit wall effective stress for different fluid density (Model 2).

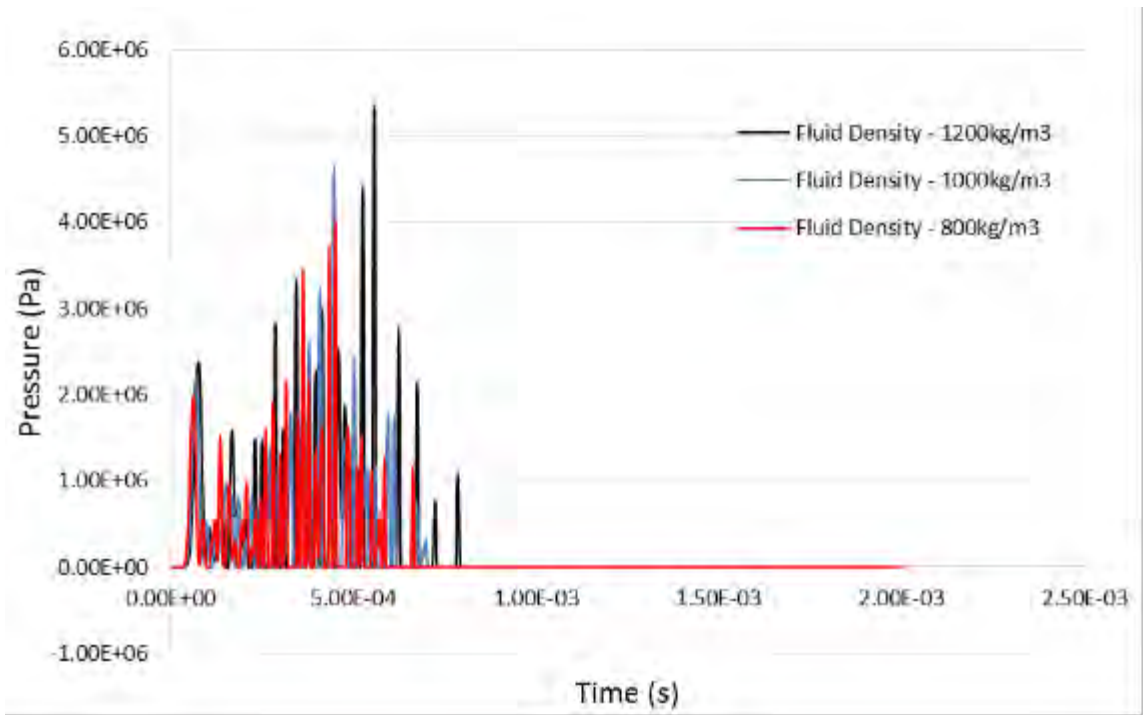


Figure 259. Drag phase pressure for different fluid density (Model 2).

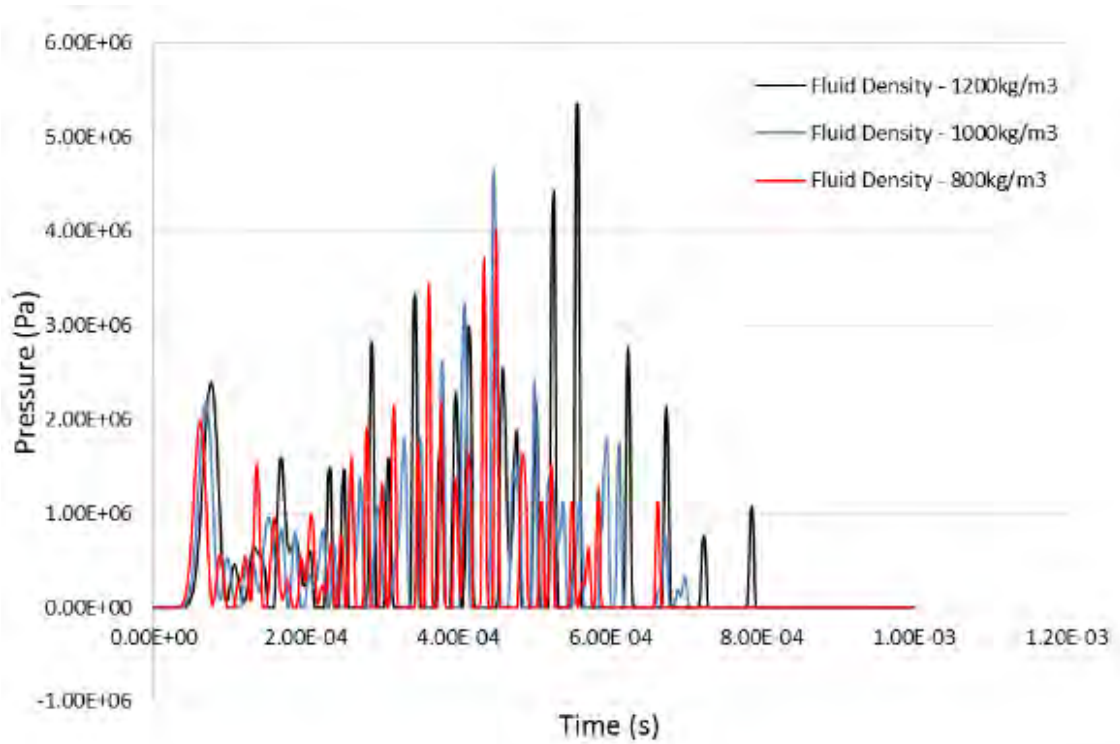


Figure 260. Drag phase pressure for different fluid density (Model 2) - Enlarged.

LIST OF REFERENCES

- [1] K. D. Kimsey, *Numerical Simulation Of Hydrodynamic Ram*, ARBRL-TR-02217, U.S. Army Ballistic Research Laboratory, USA, February 1980.
- [2] D. Varas, J. López-Puente and R. Zaera, “Experimental analysis of fluid-filled aluminium tubes subjected to high-velocity impact,” *Int. J. Impact Eng.*, vol. 36, pp. 81–91, 2009.
- [3] J. Bestard, M. Buck, B. Kocher and J. Murphy, “Hydrodynamic ram model Development–Survivability analysis requirements,” in 53rd AIAA/ASME/ASCE/AHS/ASC Structures, Structural Dynamics and Materials Conference 20th AIAA/ASME/AHS Adaptive Structures Conference 14th AIAA, 2012.
- [4] *Dytran 2010 Theory Manual*, MSC. Software Corporation, Santa Ana, CA, 2010.
- [5] R. E. Ball, “Missions, threats and threat effects,” in *The Fundamentals of Aircraft Combat Survivability Analysis and Design*, 2nd ed. Reston, AIAA, 2003, ch. 3, sec. 5, pp. 328–330.
- [6] J. H. McMillen, “Shock wave pressures in water produced by impact of small spheres,” *Physical Review*, vol. 68, pp. 198–209, 1945.
- [7] J. H. McMillen and E. N. Harvey, “A spark shadowgraphic study of body waves in water,” *J. Appl. Phys.*, vol. 17, pp. 541–555, 1946.
- [8] P. J. Disimile, L. A. Swanson and N. Toy, “The hydrodynamic ram pressure generated by spherical projectiles,” *Int. J. Impact Eng.*, vol. 36, pp. 821–829, 2009.
- [9] F. S. Stepka, R. P. Dengler and C. R. Morse, *Investigation of Characteristics of Pressure Waves Generated in Water Filled Tanks Impacted by High-Velocity Projectiles*, NASA TN D-3143, National Aeronautics and Space Administration, Washington, December 1965.
- [10] N. Lecysyn, A. Bony-Dandrieux, L. Aprin, F. Heymes, P. Slangen, G. Dusserre, L. Munier and C. Le Gallic, “Experimental study of hydraulic ram effects on a liquid storage tank: Analysis of overpressure and cavitation induced by a high-speed projectile,” *J. Hazard. Mater*, vol. 178, pp. 635–643, 2010.

- [11] R. E. Ball, "Structural response of fluid containing tanks to penetrating projectiles (hydraulic ram)-A comparison of experimental and analytical results," NPS-57Bp76051, Naval Postgraduate School, Monterey CA, 1976.
- [12] C. E. Sparks, R. L. Hinrichsen and D. Friedmann, "Comparison and validation of smooth particle hydrodynamic (SPH) and coupled euler lagrange (CEL) techniques for modelling hydrodynamic ram," in *46th AIAA ASME/ASCE/AHS/ASC Structures, Structural Dynamics and Materials Conf., Austin, Texas, 2005*, pp. 18–21.
- [13] D. Varas, R. Zaera and J. López-Puente, "Numerical modelling of the hydrodynamic ram phenomenon," *Int. J. Impact Eng.*, vol. 36, pp. 363–374, 2009.
- [14] G. Bharatram, S. Schimmels and V. Venkayya, "Application of MSC/DYTRAN to the hydrodynamic ram problem," in *MSC User's Conference, Universal City, California, 1995*, pp. 13–16.
- [15] C. Liang, S. Bifeng and P. Yang, "Simulation analysis of hydrodynamic ram phenomenon in composite fuel tank to fragment impact," in *Measuring Technology and Mechatronics Automation (ICMTMA), 2011 Third International Conference on*, 2011, pp. 241–244.
- [16] R. Vignjevic, V. T. De, J. C. Campbell and N. K. Bourne, "Modelling of impact on a fuel tank using smoothed particle hydrodynamics," presented at the Dynamics and Control of Systems and Structures in Space (DCSSS) 5th conference, Kings College, Cambridge, July 2002
- [17] M. Buyuk, C. S. Kan, N. E. Bedewi, A. Durmus and S. Ulku, "Moving beyond the finite elements, a comparison between the finite element methods and meshless methods for a ballistic impact simulation," in *Proceedings 8th International LS-DYNA Users Conference, 2004*, pp. 8-81–8-96.

INITIAL DISTRIBUTION LIST

1. Defense Technical Information Center
Ft. Belvoir, Virginia
2. Dudley Knox Library
Naval Postgraduate School
Monterey, California